

The Reactions of Dications with Neutral Species: Understanding Planetary Ionospheres

A thesis submitted for the degree of Doctor of Philosophy

By

Sam Armenta Butt

Department of Chemistry, UCL

2021



Signed Declaration

I, Sam Armenta Butt, confirm that the work presented in this thesis is my own. Where information has been derived from other sources, I confirm that this has been indicated in the thesis.

Signed,

Abstract

Doubly charged cations (dications) of molecular and atomic species are predicted to be influential in high-energy environments such as the interstellar medium, the ionospheres of planets and satellites, and plasmas. However, definitive detection of dications in these environments are not yet available and the presence of these ions is often overlooked. Early investigations of dication-neutral collisions, often at high collision energies, only resulted in the observation of electron-transfer reactivity. Modern experiments, using lower collision energies, have revealed a range of exotic chemistry such as bond-formation with rare gas elements. This chemistry, coupled with the significant abundance of dications predicted in ionospheres, suggests that these ions could play important roles in atmospheric processes. For example, dications could be involved in the chemistry of complex molecule assembly. The study of dications and their reactions is clearly important to understanding ionospheric processes in planets and satellites including the prebiotic Earth.

This thesis explores the bimolecular reactivity of various dications with neutral species in order to better understand the processes occurring in the ionospheres of planets and satellites. The position-sensitive coincidence mass spectrometry technique employed in this work utilises coincident, position-sensitive, detection of ions to reveal comprehensive information concerning the dynamics and energetics of the consequences of dication-neutral reactions.

Specifically, the reactions following collisions of Ar^{2+} , S^{2+} and $\text{CH}_2\text{CN}^{2+}$ with atoms and small molecules have been investigated. These dication-neutral collision systems exhibit intriguing reactivity clearly demonstrating the diversity of dication chemistry. For example, many of the electron-transfer reactions observed show evidence of proceeding *via* collision complexes, contrary to the orthodox (direct) mechanism. Of the bond-forming reactions detected, those generating molecular species containing a rare gas, such as ArO^+ and ArN^+ , are the most notable. Despite the observation of the involvement of collision complexes in electron-transfer, many of the bond-forming reactions described in this thesis have been shown to occur *via* direct mechanisms. The observation of bond-forming reactions and the involvement of collision complexes clearly shows the facility of dications to form associations despite their often-high potential energies.

Impact Statement

Space has captured human imagination since prehistory. We are at the beginning of the space age, where our knowledge of and use of space is exponentially increasing. However, we still do not understand many of the chemical processes occurring in space. This thesis hopes to, in part, address this deficiency. The aim of this research was to develop the overall picture of dication-neutral collisions to better understand processes occurring in high-energy environments, such as the ionospheres of planets and satellites. From studying a number of these systems, we have discovered a rich picture of the bimolecular reactivity of dications including the dynamics and energetics of the processes.

The $\text{Ar}^{2+} + \text{O}_2$ and $\text{Ar}^{2+} + \text{N}_2$ collision systems are representative of rare-gas-molecule systems and have been the subject of previous investigations. In this thesis we report a previously unknown reaction as well as unexpected dynamics and more comprehensive energetic information. One bond-forming channel, generating ArN^+ , potentially accounts for contamination observed in plasma-based mass spectrometry. We have also demonstrated the propensity for dication-neutral reactions to generate molecular species containing rare gas elements. This approach could be further utilised in syntheses of exotic species. The observation of both collision complexes in electron-transfer reactions, and bond-forming reactions occurring *via* direct mechanisms in these collision systems, challenges the current orthodoxy concerning these classes of reactions and is a valuable, and fundamental, result.

Observations from collisions of S^{2+} with the neutral species Ar, H_2 and N_2 are presented. The S^{2+} dication is one of few dications detected, to date, in the ionosphere of a planet or satellite. These results are therefore especially relevant to the studies of Io and Jupiter where S^{2+} has been observed. Moreover, S^{2+} is present in plasmas used in manufacturing. Thus, the reactions presented are of relevance to industry, aiding the research and development of new plasma-based techniques.

The reactions of the $\text{CH}_2\text{CN}^{2+}$ dication presented in this thesis are highly relevant to processes occurring in the ionosphere of nitrogen rich Titan. Therefore, these reactions are greatly pertinent to future studies of the satellite, including undoubtedly results of Titan's atmospheric composition from future explorations.

Each of the dications studied in this thesis are relevant to space, now that dications have been detected in the interstellar medium and planetary ionospheres. The reactions presented

here are therefore of use to the academic community. The results can be used to produce models describing and predicting the chemistry and chemical populations of these environments. Additionally, we suggest models of plasmas should include dications due to their significant reactivity. By broadening the database of dication-neutral reactions, we learn more about the chemistry of ionospheres and plasmas and how they evolve. Astronomers can now search for the products of the reactions observed in this thesis in the interstellar medium and ionospheres. Dications may hold the answers to questions of atmospheric erosion and the formation of complex molecules, potential precursors to life, which have been observed in atmospheres but cannot be accounted for with simple monocation-neutral chemistry.

Acknowledgements

This PhD has only been possible with contributions from many amazing people.

Firstly, I would like to thank my Supervisor, Professor Stephen Price. I have enjoyed working with a supervisor who is passionate about science, and I feel privileged to have been allowed the freedom to pursue what I find interesting. I greatly appreciate the time you have spent teaching me, especially in improving my scientific writing.

I am deeply indebted to Dr Mike Parkes, who has often gone out of his way to help me. Both in and out of the lab, your kindness has made my life easier many times, by explaining concepts and providing endless advice.

I express my gratitude to Dr Lily Ellis-Gibbins. I am lucky to have had such a great post doc to work alongside. You have helped me to no end, with the endless writing, and most importantly, keeping me motivated.

Thanks to Dr Catherine Higgins for being such a lovely group member, keeping me motivated, and generally being there to lend a hand.

I am grateful to Professor Claire Carmalt for helping me navigate my time at UCL, and the UCL Chemistry department for facilitating my studies. I appreciate Dr Chi-Lun Pang and Dr Yu Zhang for their time in my first year at UCL, teaching me invaluable skills. Also, to Dr Oscar Williams and Dr Michael Allan who both aided my scientific development as well as being lovely people to be friends with. I appreciate all the cake I had with Dr Isabelle Heath-Apostolopoulos and Alexander Tanner, giving a much-needed escape at times. I am grateful to Joseph Broughton for his help proofreading. I would also like to thank everyone else from the office for providing endless entertainment and distraction.

I am lucky to have such kind and inspirational family and friends who have been able to provide much needed relief from the PhD at crucial times. Thanks to my mum and Dave for everything you have done. Especially to my mum for introducing me to science in the first place and nurturing my curiosity. Thanks to my brother, Leo, and Kate for always being there when I need them. I am grateful for my dad and Lesley who have also been there for me at difficult times. Thanks to my lovely friends for all the great times away from the PhD and always being

there to support me, including Dan, Arthur, Hilary, Tim, Neha, Emily, and Ben. Finally, I want to thank Zero for being a good boy and reminding me what is important.

for Zero,

after all, dogs went to space before people

This is just another passing moment in a history over a billion years

Life's only purpose is life itself, exploring the endless sands

“I don't want to tempt fate, but I think everything is going to be totally great forever.”

Jeremy Usborne

List of Publications

The following publications are based on the work in this thesis:

Bond-forming and electron-transfer reactivity between Ar²⁺ and O₂

S. Armenta Butt and S. D. Price, *Phys. Chem. Chem. Phys.*, 2020, 22, 8391–8400.

Bond-forming and electron-transfer reactivity between Ar²⁺ and N₂

S. Armenta Butt and S. D. Price, *Phys. Chem. Chem. Phys.*, 2021, 23, 11287–11299.

Two further manuscripts are in preparation:

Reactivity of S²⁺ with Ar, H₂ and N₂

S. Armenta Butt and S. D. Price

Reactivity of CH₂CN²⁺ with Ar, N₂ and CO

S. Armenta Butt and S. D. Price

List of Abbreviations

CFD	Constant Fraction Discriminator
CID	Collision-Induced Dissociation
COLTRIMS	Cold Target Recoil Ion Momentum Spectroscopy
CM	Centre-Of-Mass
DCT	Double Charge Transfer Spectrometry
DET	Double Electron-Transfer
DFKER	Doppler Free Kinetic Energy Release Spectroscopy
DLA	Delay-Line Anode
DSET	Dissociative Single Electron-Transfer
E_{cm}	Centre-Of-Mass Collision Energy
EI	Electron Ionization
ESI	Electrospray Ionization
ET	Electron-Transfer
EUV	Extreme UltraViolet
FWHM	Full Width At Half Maximum
GIB	Guided Ion Beam
HEA	Hemispherical Energy Analyser
IF	Internal Frame
KER	Kinetic Energy Release
LAB	Laboratory
LZ	Landau-Zener
LZRW	Landau-Zener Reaction Window

ISM	Interstellar Medium
MCP	Microchannel Plate
MS	Mass Spectrometry
NDSET	Non-Dissociative Single Electron-Transfer
pCID	Pseudo Collision-Induced Dissociation
PEC	Potential Energy Curve
PEPECO	Photoelectron-Photoelectron Coincidence
PEPIPICO	Photoelectron-Photoion-Photoion Coincidence
PES	Potential Energy Surface
PIPICO	Photoion-Photoion Coincidence
PSCO-MS	Position-Sensitive Coincidence Mass Spectrometry
PSD	Position-Sensitive Detector
PT	Proton-Transfer
QQQ	Quadrupole-Octopole-Quadrupole
RIMS	Recoil Ion Momentum Spectroscopy
SET	Single Electron-Transfer
SIFT	Selected Ion Flow Tube
TDC	Time-To-Digital Convertor
TES	Translational Energy Spectrometry
TOF	Time-Of-Flight
TOF-MS	Time-Of-Flight Mass Spectrometry
TPEsCO	Threshold Photoelectrons Coincidence
VMI	Velocity Map Imaging

Table of Contents

Chapter 1: Introduction	25
1.1 Relevance of dications	26
1.1.1 Dications in the solar system	28
1.1.1.1 Dications detected and predicted in the solar system	28
1.1.1.2 Processes involving dications	31
1.2 Formation of dications	32
1.3 Properties of dications	33
1.4 Reactions of dications with neutral species	35
1.4.1 Collision-induced dissociation	36
1.4.2 Electron-transfer	37
1.4.2.1 Single electron-transfer	37
1.4.2.1.1 Reaction window theory	37
1.4.2.2 Double electron-transfer	39
1.4.3 Bond-formation	41
1.4.3.1 Herman model	42
1.5 Experimental techniques for investigating dications	43
1.5.1 Determining the properties of dications	44
1.5.1.1 Coincidence techniques	46
1.5.1.1.1 Coincidence techniques to investigate the dissociation of dications	48
1.5.2 Probing bimolecular dication reactions	52
1.5.2.1 Crossed-beam experiments	52
1.5.2.2 Guided ion-beam experiments	54
1.5.2.3 Selected ion flow tube experiments	56
1.5.3 Experimental outlook	57
1.6 Summary	57
1.7 References	59
Chapter 2: Experimental Methods and Data Analysis	75
2.1 Overview	75
2.2 PSCO-MS apparatus	76

2.2.1	Ion formation	76
2.2.1.1	Ions produced by electron ionization	77
2.2.2	Extraction and focussing	78
2.2.3	Energy selection	78
2.2.4	Pulsing	80
2.2.5	Acceleration and focussing lenses	80
2.2.6	Velocity selection	81
2.2.7	Deceleration	82
2.2.8	Interaction region	83
2.2.9	TOF-MS	83
2.2.9.1	Advantages of pulsing	86
2.2.10	Detector	88
2.2.11	Electronics and signal processing	89
2.3	Coincidence processing	89
2.3.1	Coincidence ‘pairs’ spectra	90
2.3.2	Errant counts	92
2.3.2.1	Background	93
2.3.2.2	Noise	93
2.3.2.3	False coincidences and the exclusion zone	93
2.4	Detailed event analysis	94
2.4.1	Product fragment velocities in the LAB frame	94
2.4.1.1	Calibration of the electric field strength in the TOF-MS source region	96
2.4.2	Product fragment velocities in the CM frame	97
2.4.2.1	Deriving the velocity of the CM	97
2.4.2.2	Converting the LAB frame velocities into the CM frame	98
2.4.2.3	Velocity of a third product	99
2.4.3	Scattering diagrams	99
2.4.3.1	CM scattering diagrams	100
2.4.3.2	IF scattering diagrams	103
2.4.4	Translational energy release	104
2.5	Summary	106
2.6	References	107

<i>Chapter 3: Bond-Forming and Electron-Transfer Reactivity Between</i>	
<i>Ar²⁺ and O₂</i>	109

3.1	Introduction	109
3.2	Experimental details	110
3.3	Results and discussion	110
3.3.1	Formation of Ar ⁺ and O ₂ ⁺	111
3.3.2	Formation of Ar ⁺ and O ⁺	114
3.3.3	Formation of ArO ⁺ and O ⁺	120
3.3.4	Formation of O ⁺ and O ⁺	122
3.4	Conclusions	124
3.5	References	125
	<i>Chapter 4: Bond-Forming and Electron-Transfer Reactivity Between Ar²⁺ and N₂</i>	129
4.1	Introduction	129
4.2	Experimental details	130
4.3	Results and discussion	130
4.3.1	Non-dissociative single electron-transfer	131
4.3.2	Dissociative single electron-transfer	137
4.3.3	Chemical bond-formation	143
4.3.4	Dissociative double electron-transfer	147
4.4	Conclusions	148
4.5	References	150
	<i>Chapter 5: Reactivity of S²⁺ with Ar, H₂ and N₂</i>	156
5.1	Introduction	156
5.2	Experimental details	158
5.3	Results and discussion	158
5.3.1	The collisions of S ²⁺ + Ar	158
5.3.2	The collisions of S ²⁺ + H ₂	161
5.3.2.1	Non-dissociative single electron-transfer	162
5.3.2.2	Dissociative single electron-transfer	165
5.3.3	The collisions of S ²⁺ + N ₂	170
5.3.3.1	Non-dissociative single electron-transfer	171

5.3.3.2	Dissociative single electron-transfer	173
5.3.3.3	Chemical bond-formation	175
5.4	Conclusions	178
5.5	References	179
<i>Chapter 6: Reactivity of CH₂CN²⁺ with Ar, N₂ and CO</i>		187
6.1	Introduction	187
6.2	Experimental details	189
6.3	Results and discussion	189
6.3.1	The formation of C ⁺ + CH ₂ N ⁺ (CID)	193
6.3.2	The formation of H ⁺ + HC ₂ N ⁺ (pCID)	197
6.3.2.1	The formation of H ⁺ + C ₂ N ⁺	202
6.3.3	Proton-transfer channels	203
6.3.4	Non-dissociative single electron-transfer channels	205
6.3.4.1	Dissociative single electron-transfer channels with CO and N ₂	211
6.4	Competition between proton-transfer and single electron-transfer	212
6.5	Conclusions	212
6.6	References	214
<i>Chapter 7: Conclusions and Further Work</i>		222
7.1	Conclusions	222
7.2	Further work	224
7.3	References	226
<i>Chapter 8: Appendix A</i>		229
8.1	References	232
<i>Chapter 9: Appendix B</i>		233
9.1	References	233

Table of Figures

<i>Figure 1.1: Picture of Ou4, known as the ‘Squid Nebula’. The turquoise light results from O^{2+} emission. Reproduced with permission.³⁹</i>	27
<i>Figure 1.2: Selected ion densities in the atmospheres of Venus, Earth, Mars, and Titan, calculated from numerical simulations. Reproduced from reference.⁴⁵</i>	30
<i>Figure 1.3: Schematic potential energy curves for a dication, AB^{2+}. The two limiting approaches to form AB^{2+} are from $A^+ + B^+$ or $A^{2+} + B$. (a) The diabatic model where the curves cross. (b) The adiabatic model where an avoided crossing results in a minimum in the potential energy curve.</i>	35
<i>Figure 1.4: Schematic showing the potential energy curves involved in the single electron-transfer reaction between AB^{2+} and CD. The reactant curve is dominated by attraction between the dication and neutral species. The product curve is dominated by Coulomb repulsion between the singly charged AB^+ and CD^+ ions. The curves cross at separation r_c. The ‘reaction window’ is also shown.</i>	38
<i>Figure 1.5: Schematic potential energy curves for double electron-transfer between a dication, AB^{2+}, and neutral species, C via (a) sequential and (b) concerted mechanisms. $r_{AB} - C$ is the interspecies separation between AB and C.</i>	40
<i>Figure 1.6: Schematic potential energy curves involved in complex formation and bond-forming reactivity between AB^{2+} and C. The $AB^{2+} + C$ curve is dominated by polarisation attraction. The $[ABC]^{2+}$ complex is found at the minimum, at short interspecies separations, r. The dication + neutral potential energy curves are crossed by the repulsive states corresponding to the SET products. Adapted from reference.¹¹³</i>	43
<i>Figure 1.7: Schematic of the electron ionization apparatus at UCL. MCP stands for microchannel plate, CFD stands for constant fraction discriminator, TDC stands for time-to-digital converter, ECL stands for emitter-coupled logic, and NIM stands for nuclear instrumentation mode. Reproduced from reference.¹⁶¹</i>	49
<i>Figure 1.8: Schematic of a typical reaction microscope apparatus. Reproduced from reference.¹⁸⁷</i>	51
<i>Figure 1.9: Schematic of the crossed-beam apparatus used by Price and co-workers. Reproduced from reference.⁹¹</i>	53
<i>Figure 1.10: Schematic of the EVA II apparatus. Reproduced from reference.¹¹³</i>	54
<i>Figure 1.11: Schematic of a guided ion beam apparatus, with typical quadrupole-octopole-quadrupole arrangement. Reproduced from reference.²¹¹</i>	55
<i>Figure 2.1 Schematic representation of the PSCO-MS apparatus. Reproduced from reference.¹</i>	76
<i>Figure 2.2: Schematic of the ion source, extraction lenses and deflectors before the hemispherical energy analyser.</i>	78
<i>Figure 2.3: Schematic of the hemispherical energy analyser.</i>	79

Figure 2.4: Retarding field analysis. a) Graph of dication counts recorded depending on retarding voltage applied. b) Normalised loss rate of the ions depending on retarding voltage. The error bars represent two standard deviations of the counts. _____	80
Figure 2.5: Schematic showing the deflectors, accelerating lenses, and focussing lenses between the hemispherical energy analyser and the velocity filter. _____	81
Figure 2.6: Schematic of the commercial decelerator. _____	82
Figure 2.7: Schematic of the TOF-MS (not to scale). _____	84
Figure 2.8: Schematic mass spectra recorded of a continuous ion beam (a) and a pulsed ion beam (b). When the ion beam is continuous, a high level of background counts are present at TOFs lower than the reactant ion due to ions from the acceleration and drift regions. Reproduced from reference. ¹¹ _____	87
Figure 2.9: (a) Schematic of the detector, (b) picture of the detector from above, looking down on the MCPs, (c) picture of the detector from below, looking up at the DLAs. _____	88
Figure 2.10: A coincidence spectrum recorded following the interactions of $\text{Ar}^{2+} + \text{O}_2$. Four peaks that correspond to pairs of product ions are labelled, (a) $\text{Ar}^+ + \text{O}_2^+$, (b) $\text{Ar}^+ + \text{O}^+$, (c) $\text{ArO}^+ + \text{O}^+$, and (d) $\text{O}^+ + \text{O}^+$. Magnifications of peaks (a), (c) and (d) are also shown. The exclusion zone is shown by the blank strip through the spectrum. _____	90
Figure 2.11: Calibration graph used to determine the electric field in the source region of the TOF-MS F . The gradient of the line of best fit, $-61.88 \text{ s J}^{-1/2}$, corresponds to a value of $F = 183.8 \text{ V cm}^{-1}$. _____	97
Figure 2.12: (a) A schematic diagram of the angle between the velocity vectors, Θ , of the ionic products A^+ and B^+ in the CM frame. The black dot indicates the position of the CM. (b) A schematic diagram of the scattering angle θ of the ionic product A^+ in the CM frame. _____	100
Figure 2.13: CM scattering diagram for the reaction $\text{S}^{2+} + \text{N}_2 \rightarrow \text{S}^+ + \text{N}_2^+$. The black dot indicates the position of the CM. _____	101
Figure 2.14: CM scattering diagram showing isotropic scattering of the SN^+ and N^+ products from the reaction $\text{S}^{2+} + \text{N}_2 \rightarrow \text{SN}^+ + \text{N}^+$. The black dot indicates the position of the CM. _____	102
Figure 2.15: Internal frame scattering diagrams for the products of the reaction $\text{Ar}^{2+} + \text{N}_2 \rightarrow \text{Ar}^+ + \text{N}^+ + \text{N}$. (a) the velocities of the N^+ and N products are shown relative to Ar^+ , (b) the velocities of the Ar^+ and N products are shown relative to N^+ , (c) the velocities of the Ar^+ and N^+ products are shown relative to N . In each scattering diagram the black dot indicates the position of the CM. _____	103
Figure 2.16: Schematic showing the exoergicity ΔE and kinetic energy release for a reaction. _____	105
Figure 2.17: Exoergicity spectrum for the reaction $\text{Ar}^{2+} + \text{O}_2 \rightarrow \text{Ar}^+ + \text{O}_2^+$. The error bars represent two standard deviations of the counts. _____	106
Figure 3.1: CM scattering diagram for the reaction $\text{Ar}^{2+} + \text{O}_2 \rightarrow \text{Ar}^+ + \text{O}_2^+$ at a CM collision energy of 4.4 eV. The black dot indicates the position of the CM. See text for details. _____	112

Figure 3.2: Experimental exoergicity spectrum for the reaction $\text{Ar}^{2+} + \text{O}_2 \rightarrow \text{Ar}^+ + \text{O}_2^+$. The exoergicities for potential SET pathways calculated from literature values are also shown: (3.a) $\text{Ar}^{2+}(^1S) + \text{O}_2(^3\Sigma_g^-) \rightarrow \text{Ar}^+(^4D) + \text{O}_2^+(X^2\Pi_g)$, (3.b) $\text{Ar}^{2+}(^1D) + \text{O}_2(^3\Sigma_g^-) \rightarrow \text{Ar}^+(^2S) + \text{O}_2^+(X^2\Pi_g)$, (3.c) $\text{Ar}^{2+}(^1S) + \text{O}_2(^3\Sigma_g^-) \rightarrow \text{Ar}^+(^2S) + \text{O}_2^+(X^2\Pi_g)$. The error bars represent two standard deviations of the associated counts. _____ 113

Figure 3.3: Scattering diagrams for the reaction $\text{Ar}^{2+} + \text{O}_2 \rightarrow \text{Ar}^+ + \text{O}^+ + \text{O}$ at a CM collision energy of 4.4 eV. (a) CM scattering diagram showing the scattering of O^+ and Ar^+ relative to the incident dication velocity, $w(\text{Ar}^{2+})$. (b) Internal frame scattering diagram showing the scattering of O^+ and O relative to the velocity of the Ar^+ product ion. In part (b) the labelled vector, (1), represents $0.55 \text{ cm } \mu\text{s}^{-1}$. _____ 115

Figure 3.4: Exoergicity spectrum for the initial electron-transfer reaction in the DSET channel, $\text{Ar}^{2+} + \text{O}_2 \rightarrow \text{Ar}^+ + \text{O}_2^{+*}$. The exoergicities for potential electron-transfer pathways calculated from literature values are also shown: (3.d) $\text{Ar}^{2+}(^3P) + \text{O}_2(^3\Sigma_g^-) \rightarrow \text{Ar}^+(^2P) + \text{O}_2^+(B^2\Sigma_g^-)$, (3.e) $\text{Ar}^{2+}(^3P) + \text{O}_2(^3\Sigma_g^-) \rightarrow \text{Ar}^+(^2P) + \text{O}_2^+(c^4\Sigma_u^-)$, (3.f) $\text{Ar}^{2+}(^1D) + \text{O}_2(^3\Sigma_g^-) \rightarrow \text{Ar}^+(^2P) + \text{O}_2^+(c^4\Sigma_u^-)$. The error bars represent two standard deviations of the counts. _____ 117

Figure 3.5: Experimental exoergicity spectrum for the dissociation of O_2^+ to form O^+ and O . The exoergicities for the potential dissociation pathways, calculated from literature values, are shown: (3.g) $\text{O}_2^+(B^2\Sigma_g^-) \rightarrow \text{O}(^1D) + \text{O}^+(^4S)$, (3.h) $\text{O}_2^+(B^2\Sigma_g^-) \rightarrow \text{O}(^3P) + \text{O}^+(^4S)$, (3.i) $\text{O}_2^+(c^4\Sigma_u^-) \rightarrow \text{O}(^1D) + \text{O}^+(^4S)$, (3.j) $\text{O}_2^+(c^4\Sigma_u^-) \rightarrow \text{O}(^3P) + \text{O}^+(^4S)$, (3.k) $\text{O}_2^+(E=27.5 \text{ eV}) \rightarrow \text{O}(^3P) + \text{O}^+(^4S)$. The arrows indicate the approximate range of exoergicities from the potential vibrational excitation of O_2^+ in a vertical transition. The error bars represent two standard deviation of the counts. See text for details. _____ 119

Figure 3.6: CM scattering diagram for the reaction $\text{Ar}^{2+} + \text{O}_2 \rightarrow \text{ArO}^+ + \text{O}^+$ at a CM collision energy of 4.4 eV. The scattering of O^+ and ArO^+ are shown relative to the incident dication velocity, $w(\text{Ar}^{2+})$. See text for details. _____ 120

Figure 3.7: Experimental exoergicity spectrum for the reaction producing ArO^+ and O^+ from Ar^{2+} and O_2 . The range of exoergicities indicated by (3.l) is determined from literature values for the pathway: $\text{Ar}^{2+}(^3P) + \text{O}_2(^3\Sigma_g^-) \rightarrow \text{ArO}^+(^2\Pi) + \text{O}^+(^4S)$. The arrow represents the possible range of exoergicity from the vibrational excitation of ArO^+ .^{35,42,43,51} The error bars represent two standard deviations of the counts. See text for details. _____ 121

Figure 4.1: CM scattering diagram for the reaction $\text{Ar}^{2+} + \text{N}_2 \rightarrow \text{Ar}^+ + \text{N}_2^+$ at a CM collision energy of 5.1 eV. The black dot indicates the position of the CM. See text for details. _____ 132

Figure 4.2: Histogram of the CM scattering angle θ for the product Ar^+ ion, relative to $w(\text{Ar}^{2+})$, for the reaction $\text{Ar}^{2+} + \text{N}_2 \rightarrow \text{Ar}^+ + \text{N}_2^+$ at a CM collision energy of 5.1 eV. The error bars represent two standard deviations of the counts. _____ 132

Figure 4.3: Experimental exoergicity spectrum for the reaction $\text{Ar}^{2+} + \text{N}_2 \rightarrow \text{Ar}^+ + \text{N}_2^+$. The exoergicities for potential SET pathways (reactions (4.a) – (4.e), discussed in the text) calculated from literature values are also shown. The error bars represent two standard deviations of the associated counts. _____ 133

Figure 4.4: Experimental exoergicity spectrum for the back scattered ($\theta(\text{Ar}^+) > 90^\circ$) counts of the NDSET reaction, $\text{Ar}^{2+} + \text{N}_2 \rightarrow \text{Ar}^+ + \text{N}_2^+$, in the low source field experiment. A comb is shown with a line spacing of 0.25 eV. The error bars represent two standard deviations of the associated counts. 136

Figure 4.5: Scattering diagrams for the reaction $\text{Ar}^{2+} + \text{N}_2 \rightarrow \text{Ar}^+ + \text{N}^+ + \text{N}$ at a CM collision energy of 5.1 eV. (a) CM scattering diagram showing the scattering of N^+ and Ar^+ relative to the incident dication velocity, $w(\text{Ar}^{2+})$. (b) Internal frame scattering diagram showing the scattering of N^+ and N relative to the velocity of the Ar^+ product ion. In part (b) the labelled vector, (1), represents $0.30 \text{ cm } \mu\text{s}^{-1}$. _____ 137

Figure 4.6: Histogram for the CM scattering angles for the product Ar^+ ion, relative to $w(\text{Ar}^{2+})$, for the reaction $\text{Ar}^{2+} + \text{N}_2 \rightarrow \text{Ar}^+ + \text{N}^+ + \text{N}$ at a CM collision energy of 5.1 eV. The error bars represent two standard deviations of the counts. _____ 138

Figure 4.7: Exoergicity spectrum for the initial electron-transfer reaction in the DSET channel, $\text{Ar}^{2+} + \text{N}_2 \rightarrow \text{Ar}^+ + \text{N}_2^{+*}$. The literature exoergicities are identified in Table 4.2. The error bars represent two standard deviations of the associated counts. _____ 140

Figure 4.8: Experimental exoergicity spectrum for the dissociation of the N_2^{+*} product to form N^+ and N . The literature exoergicities marked at the top are shown in Table 4.3. The error bars represent two standard deviation of the counts. See text for details. _____ 142

Figure 4.9: CM scattering diagram for the reaction $\text{Ar}^{2+} + \text{N}_2 \rightarrow \text{ArN}^+ + \text{N}^+$ at a CM collision energy of 5.1 eV. The scattering of N^+ and ArN^+ are shown relative to the incident dication velocity, $w(\text{Ar}^{2+})$. See text for details. _____ 145

Figure 4.10: Histogram of the CM scattering angles for the product ArN^+ ion, relative to $w(\text{Ar}^{2+})$, for the reaction $\text{Ar}^{2+} + \text{N}_2 \rightarrow \text{ArN}^+ + \text{N}^+$ at a CM collision energy of 5.1 eV. The error bars represent two standard deviations of the counts. _____ 145

Figure 4.11: Experimental exoergicity spectrum for the reaction producing ArN^+ and N^+ from Ar^{2+} and N_2 at a CM collision energy of 5.1 eV. The exoergicities for potential reaction pathways calculated from literature values are shown (reactions (4.r) – (4.t), discussed in the text).^{33,44} The error bars represent two standard deviations of the associated counts. See text for details. _____ 146

Figure 4.12: Experimental exoergicity spectrum for the dissociation of N_2^{2+} , formed in an initial DET reaction between Ar^{2+} and N_2 , to form N^+ and N^+ . The exoergicities for potential N_2^{2+} dissociation pathways calculated from literature values are also shown: (4.u) $\text{N}_2^{2+}(E = \text{Ar}^{2+}(^1D)) \rightarrow \text{N}^+(^3P) + \text{N}^+(^3P)$, (4.v) $\text{N}_2^{2+}(A^1\Pi_u, v = 7) \rightarrow \text{N}^+(^3P) + \text{N}^+(^3P)$, (4.w) $\text{N}_2^{2+}(D^3\Pi_g, v = 0) \rightarrow \text{N}^+(^3P) + \text{N}^+(^3P)$ and (4.x) $\text{N}_2^{2+}(E = \text{Ar}^{2+}(^1S)) \rightarrow \text{N}^+(^3P) + \text{N}^+(^3P)$. The error bars represent two standard deviation of the associated counts. See text for details. _____ 148

- Figure 5.1: CM scattering diagram for the reaction $S^{2+} + Ar \rightarrow S^+ + Ar^+$ at a CM collision energy of 5.3 eV. The black dot indicates the position of the CM. See text for details. _____ 159
- Figure 5.2: Experimental exoergicity spectrum for the reaction $S^{2+} + Ar \rightarrow S^+ + Ar^+$. Calculated exoergicities for the potential SET pathways are also shown (reactions (5.a) – (5.d), discussed in the text). The error bars represent two standard deviations of the associated counts. _____ 160
- Figure 5.3: CM scattering diagram for the reaction $S^{2+} + H_2 \rightarrow S^+ + H_2^+$ at a CM collision energy of 0.71 eV. The scattering of the S^+ product ion is enlarged for a clearer view. The black dot indicates the position of the CM. See text for details. _____ 163
- Figure 5.4: Experimental exoergicity spectrum for the reaction $S^{2+} + H_2 \rightarrow S^+ + H_2^+$. The error bars represent two standard deviations of the associated counts. The NDSET pathways indicated ((5.e) and (5.f)) are discussed in the text. _____ 164
- Figure 5.5: Scattering diagrams for the DSET reaction $S^{2+} + H_2 \rightarrow S^+ + H^+ + H$ at a CM collision energy of 0.71 eV. The black dot indicates the position of the CM. (a) CM scattering diagram showing the S^+ and H^+ products relative to the incident dication velocity, $w(S^{2+})$. The scattering of the S^+ product ion is enlarged for a clearer view. (b) Internal frame scattering diagram showing the scattering of H^+ and H relative to $w(S^+)$. The labelled vector (1) = $1.9 \text{ cm } \mu\text{s}^{-1}$. _____ 166
- Figure 5.6: Experimental exoergicity spectrum for the reaction $S^{2+} + H_2 \rightarrow S^+ + H^+ + H$. The error bars represent two standard deviations of the associated counts. _____ 167
- Figure 5.7: Experimental exoergicity spectrum for the dissociation of H_2^+ to form $H^+ + H$. The error bars represent two standard deviation of the counts. See text for details. _____ 168
- Figure 5.8: Exoergicity spectrum for the initial electron-transfer reaction in the DSET channel, $S^{2+} + H_2 \rightarrow S^+ + H_2^*$. The error bars represent two standard deviations of the associated counts. See text for details. _____ 170
- Figure 5.9: CM scattering diagram for the reaction $S^{2+} + N_2 \rightarrow S^+ + N_2^+$ at a CM collision energy of 4.7 eV. The black dot indicates the position of the CM. See text for details. _____ 172
- Figure 5.10: Experimental exoergicity spectrum for the reaction $S^{2+} + N_2 \rightarrow S^+ + N_2^+$. The error bars represent two standard deviations of the associated counts. The exoergicities resulting from the pathways (5.k) – (5.n) are indicated. See text for details. _____ 173
- Figure 5.11: Scattering diagrams for the DSET reaction $S^{2+} + N_2 \rightarrow S^+ + N^+ + N$ at a CM collision energy of 4.7 eV. The black dot indicates the position of the CM. (a) CM scattering diagram showing the S^+ and N^+ products relative to the incident dication velocity, $w(S^{2+})$. (b) Internal frame scattering diagram showing the scattering of N^+ and N relative to $w(S^+)$. In part (b) the labelled vector, (1), represents $0.44 \text{ cm } \mu\text{s}^{-1}$. _____ 175
- Figure 5.12: CM scattering diagram for the reaction $S^{2+} + N_2 \rightarrow SN^+ + N^+$ at a CM collision energy of 4.7 eV. The black dot indicates the position of the CM. See text for details. _____ 176

Figure 5.13: Experimental exoergicity spectrum for the reaction $S^{2+} + N_2 \rightarrow SN^+ + N^+$. The error bars represent two standard deviations of the associated counts. The exoergicities of potential reaction pathways (5.r) and (5.q) are indicated. See text for details. _____ 177

Figure 6.1: Minimum energy (metastable) structures of the reactant CH_2CN^{2+} dication, calculated using MP2(fc), with VTZ basis sets, using Gaussian16.⁶⁴ a) cyclic conformation, 2CD, b) Linear conformation, 2LD, c) linear isocyanide conformation, 2ID. _____ 192

Figure 6.2: CM scattering diagrams for the CID channel producing $CH_2N^+ + C^+$ resulting from the reactions of a) $CH_2CN^{2+} + Ar$ at a CM collision energy of 5.0 eV, b) $CH_2CN^{2+} + N_2$ at a CM collision energy of 4.5 eV, and c) $CH_2CN^{2+} + CO$ at a CM collision energy of 4.3 eV. _____ 194

Figure 6.3: Exoergicity distributions resulting from the CID channel $CH_2CN^{2+} + X \rightarrow CH_2N^+ + C^+ + X$, where $X = a) Ar, b) N_2,$ and c) CO . Dashed lines are marked at 6.2 eV and 6.9 eV in each of the distributions to show the predicted exoergicity with the involvement of the linear isocyanide dication 4ID and the cyclic quartet dication 4CD respectively. The error bars represent two standard deviations of the counts. _____ 196

Figure 6.4: Peaks in the coincidence ‘pairs’ spectrum following the collisions of $CH_2CN^{2+} + N_2$. (a) Peak and associated tail corresponding to the formation of $CH_2N^+ + C^+$. The faint peaks in the pairs spectrum centred at (3970,2420) and (3840,2500) are not due to real counts, but due to MS artifacts due to the similarity in the drift tube potential and the MCP potential. (b) Peak and associated tail corresponding to the formation of $HC_2N^+ + H^+$. The peak in the pairs spectrum centred at (4650,500) is due to the detection of $C_2N^+ + H^+$, discussed in Section 6.3.2.1. The faint peak in the pairs spectrum centred at (4590,490) is an artifact. _____ 198

Figure 6.5: IF scattering diagrams for the channel $CH_2CN^{2+} + N_2 \rightarrow HC_2N^+ + H^+ + N_2$ at a CM collision energy of 4.5 eV. a) The scattering of the H^+ and N_2 product fragments relative to the velocity of HC_2N^+ . b) The scattering of the N_2 and HC_2N^+ fragments relative to H^+ . c) The scattering of H^+ and HC_2N^+ relative to N_2 . _____ 200

Figure 6.6: CM scattering of the HC_2N^+ product for the channel $CH_2CN^{2+} + N_2 \rightarrow HC_2N^+ + H^+ + N_2$ at a CM collision energy of 4.5 eV. _____ 201

Figure 6.7: Exoergicity distributions resulting from the channel $CH_2CN^{2+} + X \rightarrow HC_2N^+ + H^+ + X$, where $X = a) Ar, b) N_2,$ and c) CO . Lines are marked at 3.5 eV and 5.0 eV in each of the distributions to show the predicted exoergicity with the involvement of the cyclic doublet dication 2CD and linear doublet dication 2LD respectively. The error bars represent two standard deviations of the counts. 202

Figure 6.8: CM scattering diagrams for the PT channel $CH_2CN^{2+} + X \rightarrow HC_2N^+ + XH^+$. a) $X = Ar$ at a CM collision energy of 5.0 eV, b) $X = N_2$ at a CM collision energy of 4.5 eV, and c) $X = CO$ at a CM collision energy of 4.3 eV. _____ 204

Figure 6.9: Exoergicity distributions resulting from the PT reactions $\text{CH}_2\text{CN}^{2+} + X \rightarrow \text{HC}_2\text{N}^+ + \text{XH}^+$. a) $X = \text{Ar}$, b) $X = \text{N}_2$, c) $X = \text{CO}$. Lines are marked on each distribution corresponding to the expected exoergicity from forming $\text{XH}^+ + \text{HC}_2\text{N}^+$ in their ground states from the ground state dication, 2CD . The error bars represent two standard deviations of the counts. _____ 205

Figure 6.10: CM scattering diagrams for the NDSET channel $\text{CH}_2\text{CN}^{2+} + X \rightarrow \text{CH}_2\text{CN}^+ + \text{X}^+$. a) $X = \text{N}_2$ at a CM collision energy of 4.5 eV b) $X = \text{CO}$ at a CM collision energy of 4.3 eV. _____ 206

Figure 6.11: Exoergicity distributions resulting from the NDSET reaction between $\text{CH}_2\text{CN}^{2+} + \text{N}_2$, resulting in the formation of $\text{CH}_2\text{CN}^+ + \text{N}_2^+$. The exoergicities resulting from pathways (6.a) – (6.i) are marked, see Table 6.6 for details. The error bars represent two standard deviations of the counts. 208

Figure 6.12: Exoergicity distributions resulting from the NDSET reaction between $\text{CH}_2\text{CN}^{2+} + \text{CO}$, resulting in the formation of $\text{CH}_2\text{CN}^+ + \text{CO}^+$. The exoergicities resulting from pathways (6.j) – (6.u) are marked, see Table 6.7 for details. The error bars represent two standard deviations of the counts. 210

Figure 8.1: Experimental exoergicity spectra for the reaction $\text{Ar}^{2+} + \text{O}_2 \rightarrow \text{Ar}^+ + \text{O}_2^+ \rightarrow \text{Ar}^+ + \text{O}^+ + \text{O}$ with source fields of (a) 28.5 V cm^{-1} and (b) 183 V cm^{-1} . The error bars represent two standard deviations of the counts. _____ 231

Figure 8.2: Total exoergicity spectrum for the DSET reaction, $\text{Ar}^{2+} + \text{N}_2 \rightarrow \text{Ar}^+ + \text{N}^+ + \text{N}$. The error bars represent two standard deviations of the associated counts. _____ 231

Chapter 1: Introduction

Ions are atoms or molecules possessing an imbalanced number of protons and electrons. Ionic properties are fundamental to many of the chemical processes that dictate the universe that we live in.^{1,2} A cation is a positively charged ion, with fewer electrons than protons. The properties of cationic species and their gas-phase bimolecular reactivity are especially important in understanding highly energised environments such as plasmas and planetary atmospheres.

The removal of two electrons from a neutral species results in the formation of a doubly charged cation, termed a ‘dication’. Chemists are familiar with dications in solution, where solvating effects (often from water) can stabilise two positive charges in close proximity. However, molecular dications can also be stable with respect to dissociation in the gas-phase, existing without the stabilising effects of solvation. The first detection and identification of a gas-phase molecular dication was of CO^{2+} in the early twentieth century, during the development of mass spectrometry (MS).^{3,4} Since their discovery, the intriguing properties of dications have inspired further research with implications that have challenged fundamental aspects of chemistry and bonding. One example is the dication of the helium dimer, He_2^{2+} , which is more strongly bound and has a shorter bond length than the corresponding monocation, He_2^+ .⁵⁻⁷ The stronger bond of the dicationic molecule compared to the monocation is counter to chemical intuition. Despite being discovered a century ago, dications have been largely neglected as an interesting but irrelevant species. However, in more recent times, dications have been investigated more intensely, due in part to the results from atmospheric modelling investigations that predict dications to be present in ionospheres with concentrations comparable with chemically significant monocations.⁸⁻¹⁰

Chemical intuition suggests that with two positive charges in close proximity, molecular dications should be unstable, with a high potential energy. One might expect molecular dications to spontaneously dissociate, resulting in the formation of two monocations, the ‘charge-separated’ products. Indeed, a typical energy release resulting from the dissociation of a molecular dication is ~ 6 eV, equivalent to ~ 580 kJ mol⁻¹.¹¹ Therefore, He_2^{2+} has been proposed as a candidate for an energy source due in part to its long lifetime, small mass and high energy release associated with dissociation.¹² Molecular dications are normally short lived, however,

they often have metastable states; minima in the potential energy surface (PES) that lie above the asymptote for charge separation. The fact that molecular dications can be detected by mass spectrometry experiments indicates that their lifetimes can be on at least the order of microseconds. In fact, the lifetimes of some molecular dications have been measured to be on the order of seconds; essentially such dications are stable to dissociation in collision-free conditions.¹³ Atomic dications are, of course, stable under collision free conditions. These metastable molecular dication states and stable atomic dications allow us to study dications and their interactions with other species.

This thesis presents an experimental investigation of the bimolecular reactivity of dications with neutral species. The experimental apparatus used in the studies presented throughout this thesis is described in detail in Chapter 2. The reactions following the collisions of the argon dication, Ar^{2+} , with molecular oxygen, O_2 , and molecular nitrogen, N_2 , are presented in Chapters 3 and 4 respectively. Chapter 5 presents a study of the bimolecular reactivity of the S^{2+} dication with the neutral species Ar, H_2 , and N_2 . An investigation of the reactivity of the molecular dication, $\text{CH}_2\text{CN}^{2+}$, with the neutral species Ar, N_2 , and CO is detailed in Chapter 6. The current chapter describes the relevant background information on the formation, properties, and prior experimental work on dications that are fundamental to the investigations of dication-neutral reactivity outlined in this thesis.

1.1 Relevance of dications

Dications can be formed from collisions between atoms or molecules and high energy particles or photons (described in Section 1.2). Dications have been detected in a range of high energy environments including in the ionospheres of planets and satellites, discussed in detail in Section 1.1.1.^{8–10,14–18} In the interstellar medium (ISM), dications can form in the proximity of high energy photon sources. Atomic dications including N^{2+} , O^{2+} , S^{2+} , Ar^{2+} , and Ne^{2+} have been identified in various nebulae, including in other galaxies, using emission spectroscopy.^{19–26} Spectral lines from nebulae observed as early as the 1860s were later identified as emission lines of O^{2+} .²⁷ Figure 1.1 shows Ou4, known as the ‘Squid Nebula’, which is a greenish colour due to the O^{2+} emission line at 500.7 nm.^{28,29} Moreover, in the ISM polyaromatic hydrocarbons can be sequentially ionized to make dications, which might contribute to the convoluted aromatic infrared bands observed in astronomy.^{30,31} The presence of dications could impact reactivity in these cold interstellar environments. For example, dications can undergo Coulomb

explosion, fragmenting into two monocations with a high potential energy. Coulomb explosion can result in the formation of monocations with high translational energies, enabling reaction barriers to be overcome at low temperatures.³² It is also suggested that metal ions, including Mg^{2+} , could be involved in mediating interstellar processes, lowering the barriers to reaction.³³ On Earth, dications have been observed to result from anthropogenic processes, such as the etching of semiconductors. For example, S^{2+} has been detected in plasma etching with SF_6 .³⁴ Additionally, as mentioned above, MS ionization techniques often result in the formation of dications such as CO^{2+} and Ar^{2+} .³⁵⁻³⁸

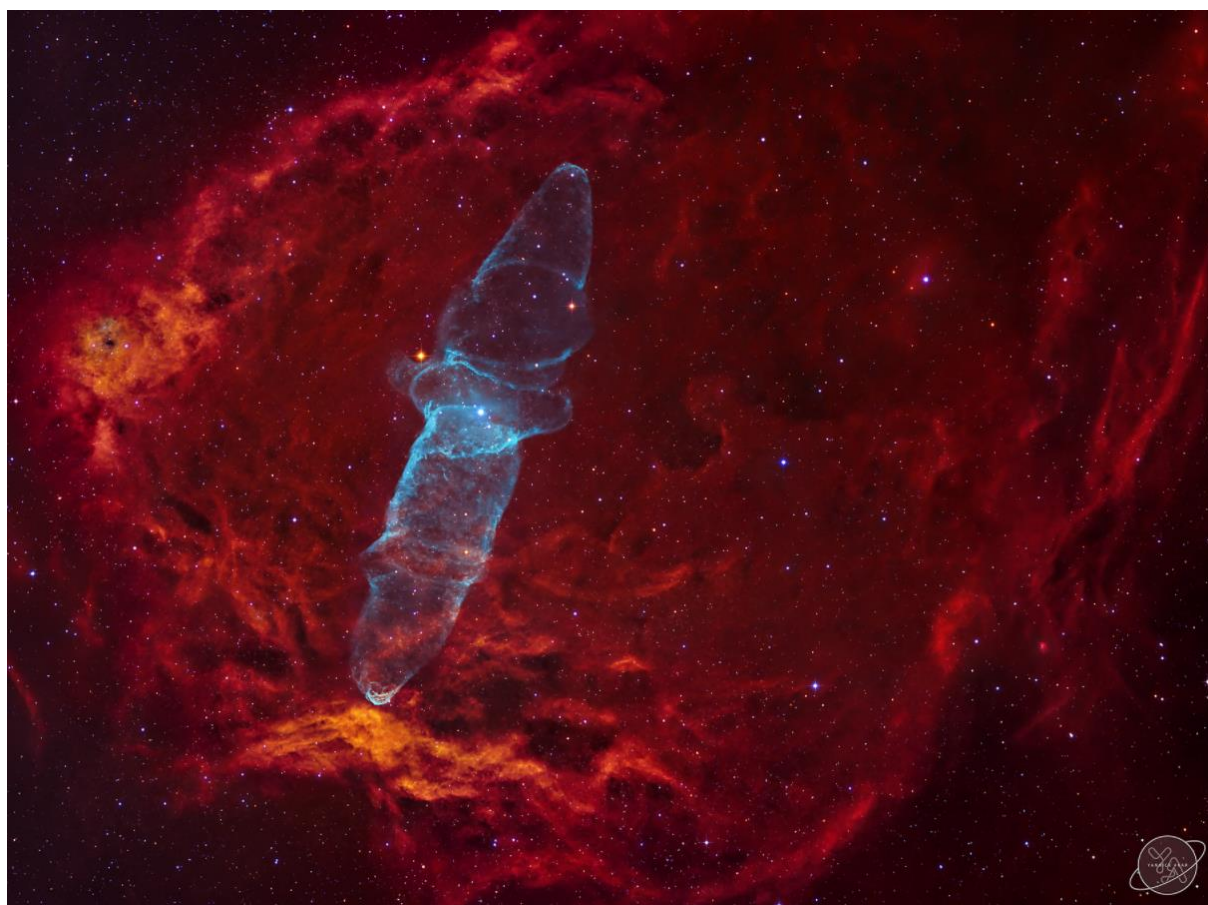


Figure 1.1: Picture of Ow4, known as the ‘Squid Nebula’. The turquoise light results from O^{2+} emission. Reproduced with permission.³⁹

Dications have also attracted interest due to their unusual properties. For example, the bimolecular reactivity of dications can lead to the generation of species involving rare gas bonds, including long-lived molecular dications such as ArN^{2+} ,⁴⁰ ArC^{2+} ,⁴¹ and HCCKr^{2+} .⁴² The bimolecular reactivity of dications with neutral species is discussed in detail in Section 1.4, and is a key focus of this thesis.

1.1.1 Dications in the solar system

Ionospheres are regions of the outer atmosphere of planets and satellites that contain significant concentrations of ionized species. The varied atomic and molecular species present are ionized by the absorption of energetic photons or collisional processes. Ionospheres have a relatively low density of species and experience a relatively high flux of radiation. Therefore, there is an increased chance of sequential ionization of neutral species to form dications, as at higher densities increased interspecies collisions act to neutralise the intermediate monocations.^{1,43,44} Modelling has indicated that atomic and molecular dications are present in ionospheres with concentrations similar to chemically important monocations and therefore should not be neglected from atmospheric chemistry models.⁸ The presence of dications in the ionospheres of planets and satellites in the solar system is reviewed by Thissen *et al.*,⁴⁵ considering C^{2+} , N^{2+} , O^{2+} , CH_4^{2+} , CO^{2+} , N_2^{2+} , NO^{2+} , O_2^{2+} , Ar^{2+} and CO_2^{2+} .

The few examples of dications that have been detected in planetary ionospheres are currently limited by the number and instrumentation of spacecraft sent to these environments. Dications in ionospheres are generally difficult to detect. In principle, mass spectrometry can be used for the detection of dications. However, homonuclear diatomic dications are impossible to distinguish from their corresponding atomic monocations. For example, N_2^{2+} and N^+ have identical mass-to-charge ratios. Spectroscopic methods of identifying dications have also been considered. Unfortunately, dications often exist in low concentrations in ionospheres compared to the other species present, making their identification difficult.⁴⁵ Additionally, only a handful of molecular dications have been well characterised spectroscopically.⁴⁶

1.1.1.1 Dications detected and predicted in the solar system

On Earth, MS analyses have detected O^{2+} and N^{2+} in the ionosphere and magnetosphere.^{16,47,48} Visible emission lines from O^{2+} have also been detected originating in the Earth's upper atmosphere.⁴⁹ Such spectroscopic identification of dications in ionospheres is important because it can be carried out remotely, removing the need to send instruments to these environments. As well as these atomic dications, modelling predicts that the molecular dications N_2^{2+} and O_2^{2+} are present in the Earth's ionosphere.⁸ These models show that the main loss mechanism for these dications is through collisions with neutral species.

Further afield, O^{2+} ions have been detected in the Venusian atmosphere by MS on the Pioneer Venus Orbiter spacecraft.^{15,50} The Mars Atmosphere and Volatile Evolution spacecraft

(MAVEN) detected O^{2+} in the Martian ionosphere with MS.⁵¹ Previous missions have shown that the Martian atmosphere is dominated by CO_2 ,^{52,53} and modelling has predicted the presence of a CO_2^{2+} layer in the upper atmosphere of Mars.¹⁰ Indeed CO_2^{2+} has recently been detected in the Martian ionosphere by MAVEN. This first detection of a molecular dication in a planetary atmosphere was possible utilising increased resolution MS on board MAVEN.⁵⁴ An analysis of the electrons in the outer atmosphere of Mars was also undertaken by MAVEN.⁵⁵ The electron energy distribution spans a wide range of energies. A distinctive peak is observed at ~ 27 eV, enough energy to result in the ionization of most monocations to form a dication, and for some, larger, molecules enough to form a dication directly from the neutral.

Io, one of the satellites of Jupiter, experiences intense volcanic activity, releasing SO_2 , resulting in an atmosphere dominated by S and O containing species. S^{2+} has been detected in the ionosphere of Io by the Galileo⁵⁶ and Voyager I^{57,58} spacecraft, as well as spectroscopically by the Hubble telescope.⁵⁹ O^{2+} and S^{2+} have been detected in the Jovian magnetosphere, likely emanating from Io.^{14,60} Additionally, UV-emission spectra of the Io plasma torus also exhibit transitions attributed to Cl^{2+} , C^{2+} and even the triply charged S^{3+} .⁶¹

Saturn's largest moon Titan has a dense atmosphere dominated by N_2 and CH_4 .^{62,63} Titan has a rich chemistry involving many organic species, initiated by photon absorption.⁶⁴ These organic species result in the 'haze' observed in photographs of the satellite. Titan is seen as a model for prebiotic chemistry, making it a proxy for exoplanets with atmospheres. Modelling predicts the presence of N_2^{2+} in the upper atmosphere of Titan, in chemically significant concentrations.^{9,17} Dutuit *et al.*⁶⁵ review the ionospherically relevant processes associated with N^{2+} and N_2^{2+} in Titan's atmosphere, including the bimolecular reactivity of these species with neutrals. The reactions of N_2^{2+} with neutrals relevant to the ionosphere of Titan have been the subject of previous studies in our group.⁶⁶⁻⁶⁹

The formation of dications can occur in other gaseous regions in the solar system which experience an appropriate flux of radiation. For example, the molecular dication CO_2^{2+} has been detected in the gas envelope of a comet, using MS on the Rosetta spacecraft.⁷⁰ Dications are also present in the stellar wind, which is partially comprised of He^{2+} .¹ These He^{2+} dications could interact with species in the outer atmosphere of planets and satellites, resulting in the formation of new species, including dications. For example, collisions between He^{2+} and hydantoin, a model biological molecule, resulted in the formation of new dications, among other

species.⁷¹ The effects of the He^{2+} dication in the solar wind interacting with comet comas have also been modelled and found to be a minor contribution to the source of ions in comets.⁷²

Modelling has indicated that dications should be an important trace species in the atmospheres of Mars, Titan, Earth and Venus, with chemical abundances comparable with chemically significant monocations in these ionospheres.^{8,9} Figure 1.2 illustrates calculated densities of dications in the atmospheres of Venus, Earth, Mars and Titan. For example, in Figure 1.2, the density of N_2^{2+} ions in Titan's atmosphere (panel D) is clearly greater than the monocations CH^+ , CN^+ , and C_2H^+ .

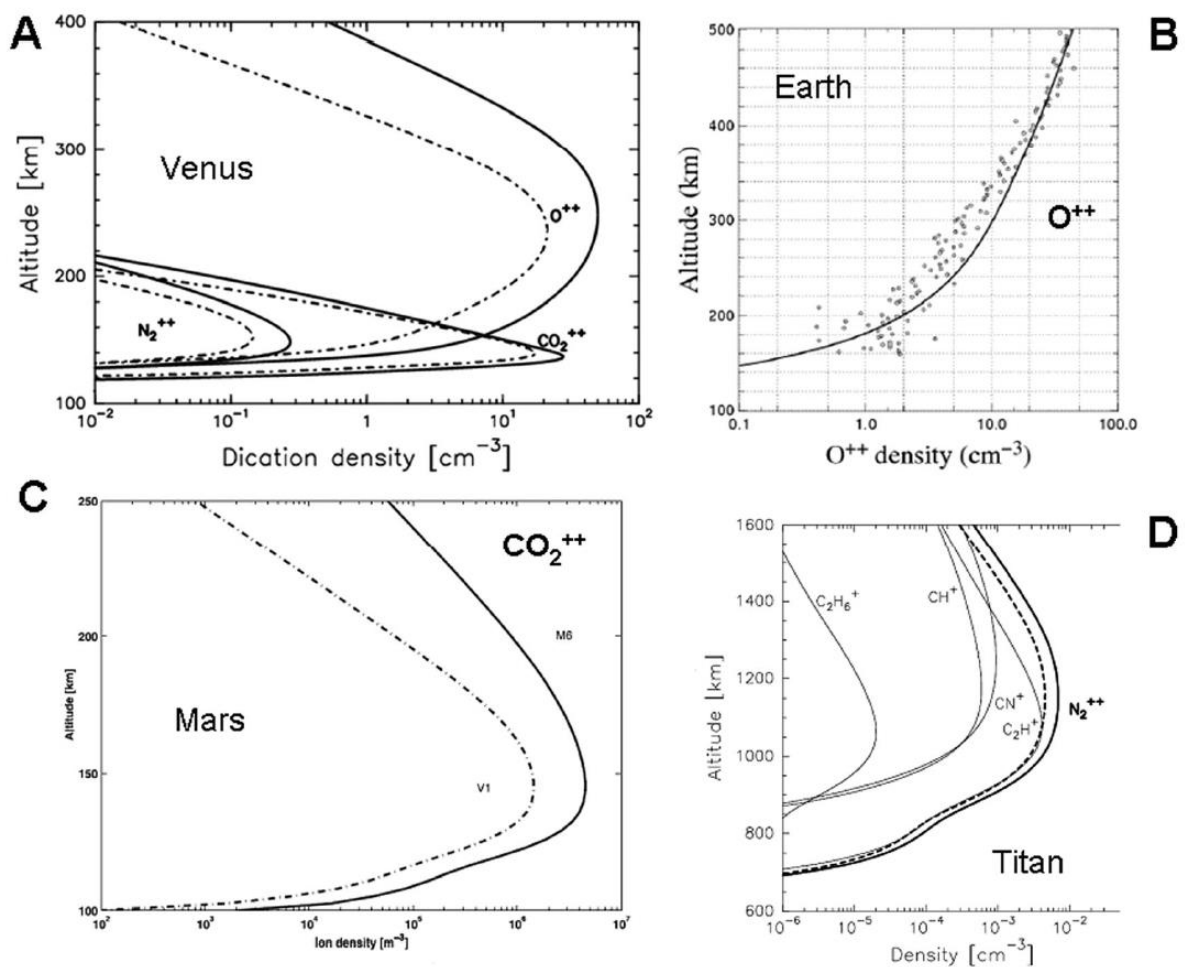


Figure 1.2: Selected ion densities in the atmospheres of Venus, Earth, Mars, and Titan, calculated from numerical simulations. Reproduced from reference.⁴⁵

The results of models suggesting that dications are present in chemically significant concentrations, as well as cases of detection in ionospheres, show that dications are an important

species in these environments. The recent detection of a molecular dication CO_2^{2+} by MAVEN could be the first of many molecular dications detected in ionospheres. Future missions with the capability to detect dications are clearly required.

1.1.1.2 Processes involving dications

As demonstrated in several studies, both atomic and molecular dications exhibit significant bimolecular reactivity following collisions with neutral species.^{37,73–76} Such collisional processes are expected to be the major route which limits the lifetimes of *atomic* dications in planetary ionospheres.⁴⁵ In addition, despite their inherent thermodynamic instability, compared to the charge separated products of dissociation, the metastable electronic states of many *molecular* dications have been shown to possess lifetimes sufficient to allow collisions with other species in planetary environments.³⁷ For example, the primary loss mechanisms of the CO_2^{2+} and O^{2+} dications detected in ionospheres are predicted to be *via* bimolecular reactivity.^{51,54} The reactive nature of dications, coupled with their significant abundance in ionospheres, suggests that the bimolecular chemistry of these species could play a role in ionospheric chemistry.⁶⁵ For example, dication reactions could be involved in the chemistry of complex molecule assembly.⁴⁵ Indeed, carbon-carbon coupling reactions have been observed following interactions of aromatic dications with methane,^{77,78} ethyne⁷⁹ and benzene.⁸⁰ Dications made from nitrogen containing compounds, such as pyridine and benzonitrile, were used in some of these bond-forming reactions.⁷⁸ These bond-forming reactions could therefore be of relevance to processes in Titan's nitrogen-rich atmosphere.

Another remarkable ionospheric phenomenon involving dications is atmospheric depletion. When a molecular dication dissociates, the kinetic energy released can be enough to allow the product ions to escape the atmosphere.⁸¹ Indeed, the influence of such unimolecular chemistry of molecular dications in atmospheric erosion has been recently recognized.^{44,81–83} Molecular dication dissociation and therefore atmosphere erosion are expected to be important for Mars and Titan.⁸³

Whilst there have been observations of dications in planetary ionospheres, including, encouragingly, the molecular dication CO_2^{2+} in the atmosphere of Mars, dications have been historically neglected in models of ionosphere chemistry, likely due to the difficulties mentioned above.⁴⁵ In order to identify dication reactions of ionospheric interest, laboratory-based experiments to probe dicationic reactivity, along with spectroscopic identification techniques, are vital.⁸⁴ By studying bimolecular processes involving dications, we can learn

about ionospheric phenomena, such as atmosphere depletion and complex molecule formation, elucidating processes of the ionospheres of planets and satellites including the prebiotic Earth. Greater understanding of the properties and reactivity of dications will also enhance our understanding of processes occurring in the ISM, and in anthropogenic manufacturing techniques involving plasmas.

1.2 Formation of dications

Dications can be formed *via* several different methods. A dication can be formed directly from a neutral species if an atom or molecule is given enough energy to overcome its double ionization energy, resulting in the loss of two electrons. Generally, the cross section for the direct formation of a dication from a neutral is at least an order of magnitude less than to form the corresponding monocation, making it sometimes challenging to study these species. Dications can also be formed sequentially, *via* a monocation. The two main methods of ionization are photoionization and electron ionization, discussed in more detail below. Additionally, dications can be formed from collisions between a neutral or monocation and other charged particles. For example, collisions with He^+ can result in the loss of an electron from a monocation through an electron-transfer (ET) process, forming a dication. Negative ions can also be used to ionize neutrals. For example, calcium-containing diatomic dications, such as CaP^{2+} , have been formed as a result of sputtering powder samples with high energy O^- ions.⁸⁵ New dications can also form as a result of dication-neutral reactions, the focus of this thesis.

Electron ionization (EI) can occur following inelastic collisions between electrons and an atom or molecule. If enough energy is transferred to the neutral species, an electron can be ejected, depicted in equation (1.1). Electron ionization is commonly used to produce ions experimentally, including in the experiments described in this thesis, due to its relative simplicity to implement.³⁷ A heated filament can be used to produce electrons *via* thermionic emission with tuneable energies capable of ionizing a target precursor gas. EI can result in the formation of dications with a range of internal energies. Some electronic states are unstable to dissociation, therefore EI of molecular precursor gases often results in a significant amount of fragmentation. An alternative ionization method that could be employed to aid the production of molecular dications is electrospray ionization (ESI) because it is ‘softer’ and limits

fragmentation. However, ESI is usually used to aid in the production of larger molecular dications that exist chemically in solution.



Photoionization (PI) involves the neutral species absorbing a photon with sufficient energy to cause ejection of an electron, shown in equation (1.2). Photoionization can be achieved with the use of a laser, which typically offers more control in the vibronic states of the dication accessed. The disadvantage with lasers is that they are expensive and complicated to use, as well as it being logistically difficult to incorporate a laser into the position-sensitive coincidence mass spectrometry (PSCO-MS) apparatus used for the experiments described in this thesis. For example, with a laser it is difficult to obtain high enough repetition rates to make coincidence experiments feasible whilst maintaining sufficient flux of ions.



1.3 Properties of dications

Molecular dications are often thermodynamically unstable due to Coulomb repulsion between the two positive charges. This repulsive force can result in dissociation and the formation of two separate monocations, shown in equation (1.3).



Some molecular dications have metastable states which are kinetically stable to dissociation with long lifetimes. One model to account for the existence of dicationic metastable states is with avoided crossings of the potential energy surfaces. In this model the metastable AB^{2+} dication state arises from an avoided crossing between an electronic state that converges to $A^{2+} + B$ at large interspecies separations and one that converges to $A^{+} + B^{+}$ at large interspecies separations. Such potential energy curves for a diatomic dication, AB^{2+} , are shown in Figure 1.3a. The potential energy curve for two monocations, $A^{+} + B^{+}$, is dominated by the inter-species Coulomb repulsion, shown in equation (1.4),

$$V(r) = \frac{q_1 q_2}{4\pi\epsilon_0 r}, \quad (1.4)$$

where q_1 and q_2 are the charges of the monocations, ϵ_0 is the permittivity of a vacuum, and r is the interspecies separation. At large interspecies separation, the potential curve for a dication

and neutral species, $A^{2+} + B$, is dominated by the polarisation attraction, shown in equation (1.5),

$$V(r) = -\frac{Z^2 e^2 \alpha}{32\pi^2 \epsilon_0^2 r^4}, \quad (1.5)$$

where Z is the nuclear charge number of the dication (+2), e is the electronic charge, and α is the polarizability of the neutral species. The $A^{2+} + B$ potential is dominated by electrostatic repulsion at short range. The dominance of repulsive forces at short range and attractive forces at long range leads to a minimum in the potential energy curve, resulting in a bound diatomic dication, AB^{2+} . As shown in Figure 1.3b, an avoided crossing results in a minimum in the PES that has a barrier to dissociation, therefore the dication is kinetically stable. Typically, this AB^{2+} minimum lies higher in energy than the asymptote of the repulsive potential of $A^+ + B^+$, therefore the dication is thermodynamically unstable to dissociation, but kinetically stable in the minimum (metastable), as shown in Figure 1.3b. If the AB^{2+} minimum is lower in energy than the repulsive $A^+ + B^+$ potential, then the dication can even be thermodynamically stable to dissociation. For example, computational studies have predicted that CrO^{2+} and BaO^{2+} are thermodynamically stable relative to their charge separated products of dissociation.^{86,87} Metastable dications can dissociate by tunnelling through the potential barrier to the charge dissociated monocation + monocation asymptote. However, the barrier to dissociation is often wide, and therefore the primary mechanism for the dissociation of dications is *via* curve crossings. The species can cross to a different curve that is either repulsive, or from which it can easily transition to a repulsive state, and then dissociate.

Dications can be stable with large well depths, for example, O_2^{2+} has a well depth of >2 eV, capable of supporting many vibrational levels.⁸⁸⁻⁹⁰ Polyatomic dications are more complex, yet still form metastable states *via* the same route - the formation of potential barriers in the PES resulting from avoided crossings. The presence of these long-lived metastable states means that a significant mode of decay for dications can be *via* bimolecular reactivity. Such dication reactions with neutral species, are discussed in the following section.

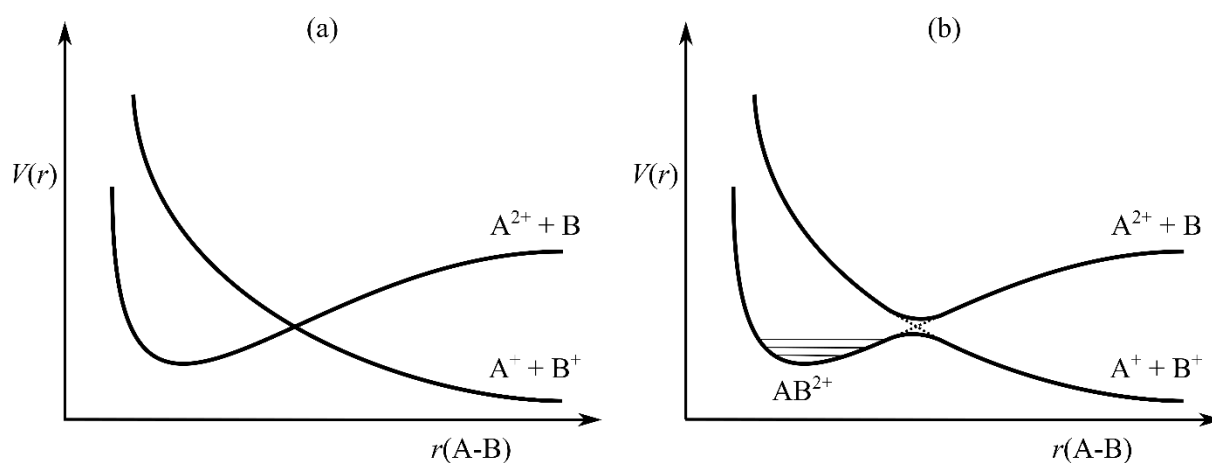


Figure 1.3: Schematic potential energy curves for a dication, AB^{2+} . The two limiting approaches to form AB^{2+} are from $\text{A}^+ + \text{B}^+$ or $\text{A}^{2+} + \text{B}$. (a) The diabatic model where the curves cross. (b) The adiabatic model where an avoided crossing results in a minimum in the potential energy curve.

1.4 Reactions of dications with neutral species

In high energy environments such as planetary ionospheres dications often have lifetimes long enough that their primary loss mechanism is through bimolecular reactions with neutral species.^{37,65} When a dication and a neutral species interact, there are a number of possible processes that can occur. Generalised forms of these processes are shown in Table 1 and are described below.

Table 1: Generalised reactivity that can occur following dication + neutral interactions.

Process	Equation
Collision-induced dissociation	$AB^{2+} + CD \rightarrow A^+ + B^+ + CD$ (1.a)
	$AB^{2+} + CD \rightarrow AB^{2+} + C + D$ (1.b)
Non-dissociative single electron-transfer	$AB^{2+} + CD \rightarrow AB^+ + CD^+$ (1.c)
Dissociative single electron-transfer	$AB^{2+} + CD \rightarrow AB^+ + C^+ + D$ (1.d)
	$AB^{2+} + CD \rightarrow A^+ + B + CD^+$ (1.e)
	$AB^{2+} + CD \rightarrow A^+ + B + C^+ + D$ (1.f)
Non-dissociative double electron-transfer	$AB^{2+} + CD \rightarrow AB + CD^{2+}$ (1.g)
Dissociative double electron-transfer	$AB^{2+} + CD \rightarrow AB + C^+ + D^+$ (1.h)
Bond-formation with charge separation	$AB^{2+} + CD \rightarrow ABC^+ + D^+$ (1.i)
Bond-formation forming a new dication	$AB^{2+} + CD \rightarrow ABC^{2+} + D$ (1.j)

1.4.1 Collision-induced dissociation

Collision-induced dissociation (CID) involves the dissociation of the dication or neutral species due to energy transfer in a collision. In Table 1 equations (1.a) and (1.b) represent this process. The key feature of CID is that there is no transfer of electrons between the reactants or new chemical bonds formed. In a collision, energy can be transferred from the rotational, vibrational, or electronic modes of one reactant to the other. This transfer of energy can result in one or both of the species transitioning to a state unstable to dissociation, or more easily tunnelling through a potential barrier due to inhabiting higher vibrational modes. Additionally, the translational energy of the reactant species could promote the internal energy of the reactants resulting in the population of dissociative states. CID is distinct from unimolecular dissociation, which does not require a collision to occur. CID and unimolecular dissociation can both lead to either charge separation, where two monocations are formed, or ‘neutral loss’, where a dication and a neutral are formed.

The formation of two monocations resulting from bimolecular collisions of *molecular* dications with neutral species is often observed because of the relative thermodynamic driving force of forming the charge separated products.^{91–93} Of course, the dication could also lose a neutral fragment. If CID results in the formation of new charged species (equation (1.a)) it is generally easy to study such a process, however, if just the neutral collision partner dissociates (equation (1.b)) it is less straightforward due to the difficulties associated with detecting neutral species. An example of a CID reaction is shown in equation (1.k).⁹⁴



1.4.2 Electron-transfer

1.4.2.1 Single electron-transfer

Electron-transfer (ET) processes are often found to dominate reactions between dications and neutral species.^{11,95} Single electron-transfer (SET) is the transfer of one electron from the neutral species to the dication, producing two monocations. Non-dissociative single electron-transfer (NDSET) is when SET does not result in the fragmentation of either of the monocationic products, as shown generally in equation (1.c). An example of a NDSET reaction observed experimentally is given in equation (1.l).⁹⁶



If either of the product monocations are formed in a dissociative state, fragmentation will follow, a process termed dissociative SET (DSET), shown in equations (1.d), (1.e), and (1.f). Due to the high potential energy of dications, when SET occurs, often one of the products is formed with enough vibronic excitation to cause dissociation. Example DSET reactions observed experimentally are shown in equations (1.m) and (1.n).^{97,98}



1.4.2.1.1 Reaction window theory

To describe the electron-transfer between a dication and neutral species, ‘reaction window’ theory is often employed.³⁷ Reaction window theory is an application of Landau-Zener (LZ) theory,⁹⁹ which offers a semi-classical description of the probability of transitioning

from one potential energy curve (PEC) to another (reactant to product), at their intersection. LZ reaction window (LZRW) theory is a semi-classical model which allows the probability of SET to be determined in dication-neutral systems.⁹³

Schematic potential energy curves for the dication + neutral reactants, and the monocation + monocation products for a SET reaction are shown in Figure 1.4. The product potential is dominated by the Coulomb repulsion between the two monocations, and the reactant potential is dominated by the polarisation attraction (ion-induced dipole interactions) between the dication and neutral species. Reaction window theory indicates that SET occurs near the curve crossing, r_c , the point where the reactant and product PECs intersect.

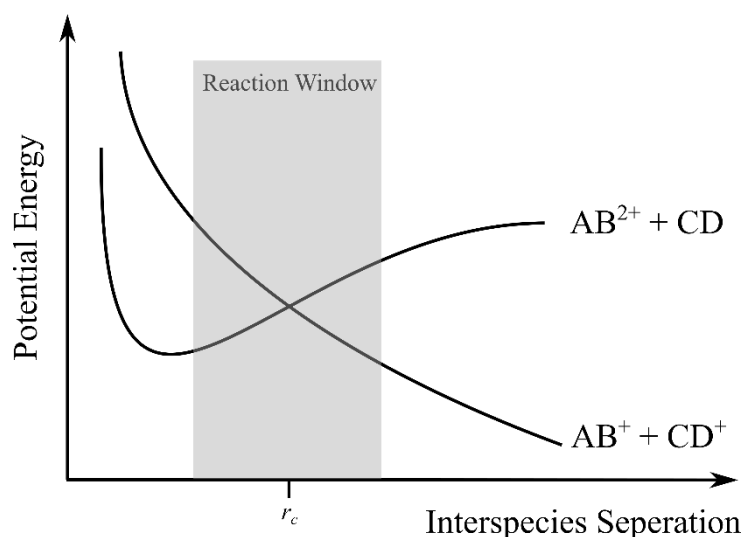


Figure 1.4: Schematic showing the potential energy curves involved in the single electron-transfer reaction between AB^{2+} and CD . The reactant curve is dominated by attraction between the dication and neutral species. The product curve is dominated by Coulomb repulsion between the singly charged AB^+ and CD^+ ions. The curves cross at separation r_c . The ‘reaction window’ is also shown.

The probability of the system remaining on the same surface as it passes through the curve crossing is given by δ , determined by the extent of the coupling between the curves. As the interspecies distance of the crossing decreases, the coupling between the two curves at the crossing increases. In a collision between a dication and a neutral, the system passes the curve crossing at r_c twice, once as the reactants approach each other and once as they depart. Thus, the probability of net SET occurring, P , is given by equation (1.6).

$$P = 2\delta(1 - \delta) \quad (1.6)$$

If the curve crossing occurs at a large interspecies separation, the coupling between the two potentials is poor and the electron is unable to move between them ($\delta \gg 0.5$, $P \rightarrow 0$). If the curve crossing occurs at a small interspecies separation, the potentials are coupled very strongly, and the electron is easily able to transfer between them ($\delta \ll 0.5$). However, the electron will, with high probability, transfer twice, as the species move towards each other and again as they move apart, resulting in no net electron-transfer ($P \rightarrow 0$). Therefore, efficient SET can only occur between these two limits, when the curve crossing is situated where the PECs are not too weakly or strongly coupled. This region is known as the ‘reaction window’ and in dication-neutral systems is typically where the interspecies separation is $\sim 2\text{--}6 \text{ \AA}$.^{11,100–102} Given the shapes of the potential curves in the $AB^{2+} + CD$ system, this interspecies separation corresponds to a reaction exothermicity of $\sim 2\text{--}6 \text{ eV}$. It should be noted that LZ theory is based on atomic species and therefore reaction window theory may be less appropriate for larger species with more internal modes and different geometries. For example, the orientation of the reactants is not considered.

1.4.2.2 Double electron-transfer

Double electron-transfer (DET) is a collisional process where two electrons move from the neutral species to the dication, shown by equation (1.g) in Table 1. This process results in the formation of a new neutral species and a new dication. Either of the products formed from DET could subsequently dissociate. The nascent dication often fragments into two monocations, shown in equation (1.h). An observed example of a DET reaction in which the nascent dication dissociates is shown in equation (1.o).⁹⁵



Typically, in dication-neutral systems, the reaction cross section for DET is smaller than that for SET. DET can, in theory, proceed *via* two mechanisms: sequential (*via* the SET products), or concerted. These mechanisms can be explained using simple, one-dimensional, electrostatic models for the reaction $AB^{2+} + C \rightarrow AB + C^{2+}$.⁹⁵ In sequential DET (Figure 1.5a), the reactant and product potentials are represented by simple polarization-attraction forces arising from dication-neutral interactions. The DET reaction proceeds *via* the SET products, $AB^+ + C^+$, the PEC for which is repulsive due to Coulombic repulsion, as discussed above. In order for DET to proceed *via* this sequential mechanism, both the product and reactant curves

must cross the monocation + monocation curve within the reaction window in order for an electron to transfer each time.

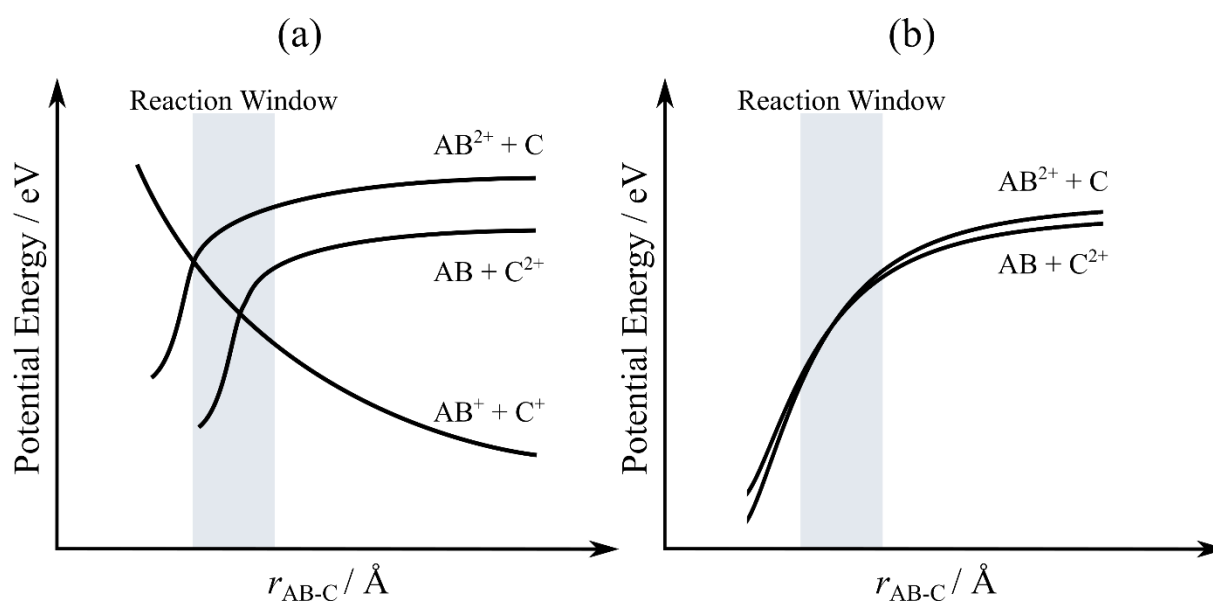


Figure 1.5: Schematic potential energy curves for double electron-transfer between a dication, AB^{2+} , and neutral species, C via (a) sequential and (b) concerted mechanisms. r_{AB-C} is the interspecies separation between AB and C .

In the concerted model (Figure 1.5b), the dication + neutral potential crosses the neutral + dication potential. In order for the reactant and product potentials to cross within the reaction window, centred on an interspecies separation of 4 \AA , the neutral reactant and neutral product must have different polarizabilities and the product asymptote must lie close in energy to the reactant asymptote ($<1 \text{ eV}$ difference). Indeed, previous work has shown that when a collision system exhibits a significant yield of DET, the reactant and product asymptotes conform to the above energetic constraints and appropriately favoured crossings in the Landau-Zener window exist.⁹⁵ The sequential mechanism proceeds *via* the SET products, and therefore there is an inherent competition between SET and DET. In theory, in the sequential mechanism, both sets of curve crossings can be within the reaction window over a wider range of reaction exothermicities than the range of exothermicities over which the concerted model allows efficient DET. It follows that if the sequential mechanism was favoured, DET should be a more common occurrence following the collisions of dications and neutral species at low collision energies. The relative scarcity of DET observed in studies of dication-neutral collision systems

suggests that concerted DET is indeed responsible for the majority of dication-neutral DET.^{95,103}

1.4.3 Bond-formation

Bond-forming reactions have been observed resulting from collisions of dications with neutral species at low collision energies (<10 eV).^{11,97,100} At these low energies the reactants can interact for longer, allowing new bonds to form. Additionally, at low collision energies bond-forming complexes, close-range associations between the reactants, will likely have less internal energy and therefore be more stable to dissociation. Thus, these bond-forming complexes can have longer lifetimes, increasing the likelihood of bond-formation. An example bond-forming reaction is shown in equation (1.p), involving the formation of a new S-O bond.¹⁰⁴



This bond-forming reactivity marks dications as potential precursors for the development of complex molecules in the ISM or planetary ionospheres. Dication-neutral interactions can result in carbon-carbon coupling reactions, as alluded to in Section 1.1.1.2.⁷⁷⁻⁸⁰ For example, equation (1.q) shows a carbon-carbon coupling reaction between $\text{C}_7\text{H}_6^{2+}$, formed from EI of toluene, and ethylene.¹⁰⁵ The reaction shown in (1.q) involves the addition of carbon atoms to the dication species, building on the original molecule. This reaction is especially interesting as a molecular dication is produced, despite the Coulomb repulsion of the double charge. Further addition reactions could be a pathway to the formation of the complex hydrocarbons observed in space.



The reaction of dications with neutrals also offers one of few pathways to form species that include rare gases. For example, Bassi and co-workers^{40,41,106} observed the formation of ArC^{2+} and ArN^{2+} resulting from reactions of Ar^{2+} with N_2 , CO and CO_2 . Ascenzi *et al.*¹⁰⁷ observed the formation of ArO^{2+} and ArO^+ following the collisions of Ar^{2+} with O_2 ; an investigation discussed in more detail in Chapter 3. The formation of ArN^+ and ArNH^+ was observed to result from the reaction of Ar^{2+} and NH_3 , proceeding *via* the formation of a complex, $[\text{ArNH}_3]^{2+}$.¹⁰⁸ HCCRg^{2+} dications ($\text{Rg} = \text{Ar}, \text{Kr}$) were observed resulting from $\text{C}_2\text{H}_2^{2+} + \text{Rg}$ collisions.⁴² Bonds with Ar, including with C and S, have also been formed by reacting

Ar gas with dications such as CF_3^{2+} .^{98,106,109} Additionally, Si-Ne and Si-Ar bonds have been observed to form resulting from $\text{SiF}_3^{2+} + \text{Ne/Ar}$ collisions.¹¹⁰ These examples of the formation of unusual species, involving rare gases, demonstrates the rich range of chemistry possible with dications.

1.4.3.1 Herman model

Experiments show that collision complexes are often involved in dication-neutral bond-forming reactions.^{66,67,111,112} Herman *et al.*¹¹³ developed a model for explaining dication-neutral bond-forming reactivity and its competition with SET. This model is shown in Figure 1.6, for a system with a dication, AB^{2+} , and neutral species, C. As the two species make their initial approach, starting on the left side of Figure 1.6, the potential energy surface is dominated by the polarisation attraction between the dication and neutral. This approach channel is crossed by a number of repulsive curves that result in SET, forming $\text{AB}^+ + \text{C}^+$ and their excited analogues. If the system does not cross onto one of these repulsive states then a collision complex, $[\text{ABC}]^{2+}$, can be formed at a small interspecies separation. In the collision complex, chemical bonds can be broken and made due to the close proximity of the atoms.

The collision complex can either dissociate back along the entrance pathway, or along a new reaction coordinate of $\text{A} + \text{BC}^{2+}$, with the A-B bond broken and B-C bond newly formed. The exit channel is also crossed by a number of (often more energetically favourable) repulsive states that result in SET, forming $\text{A}^+ + \text{BC}^+$. If the system does not cross to one of these repulsive states, then a new dication is formed, BC^{2+} . For example, the dication ArC^{2+} was observed following collisions between Ar^{2+} and CO .^{40,41,105,106}

In order to form a collision complex, the system must negotiate curve crossings with a number of different repulsive asymptotes leading to SET. Often, at least one of these curve crossings lies within the reaction window, making the formation of a collision complex difficult. As a result, reaction cross sections for bond-forming reactions are generally significantly lower than for competing SET reactions. Bond-forming reactions can also occur *via* more direct mechanisms,⁹⁵ including some of the bond-forming reactions studied in this thesis.¹¹⁴ For example, the $\text{ArO}^+ + \text{O}^+$ products resulting from collisions of Ar^{2+} and O_2 described in Chapter 3 are generated *via* a ‘stripping’ mechanism, where the Ar^{2+} abstracts an O^- from the O_2 at long range.¹¹⁵

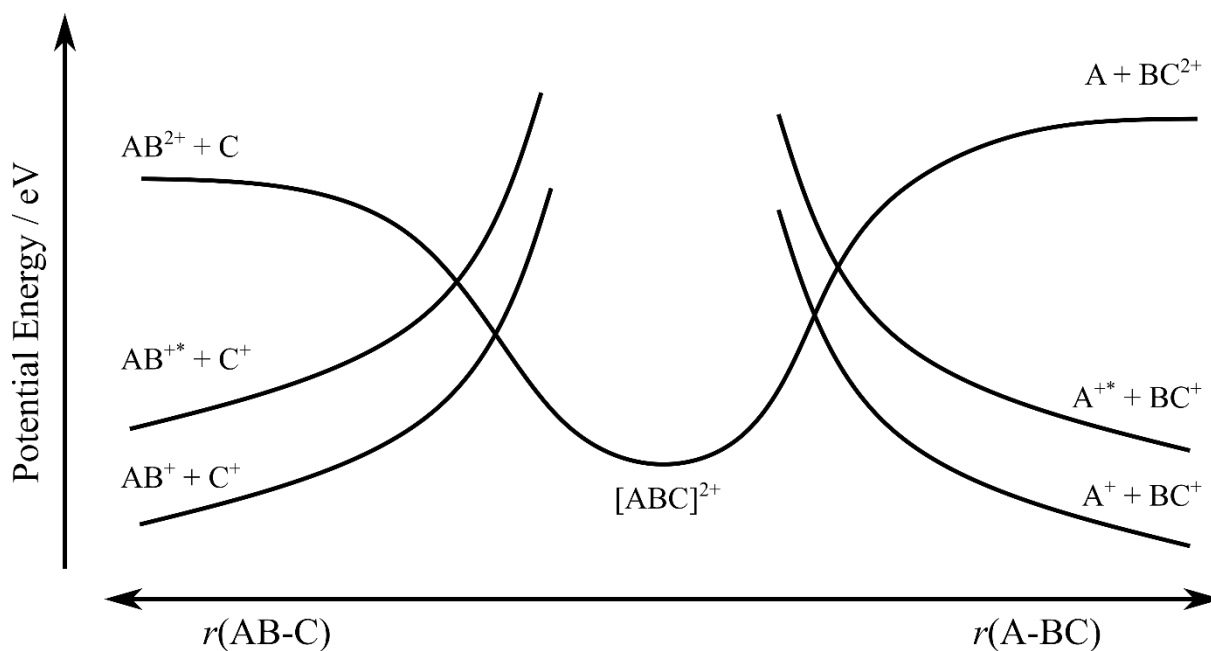


Figure 1.6: Schematic potential energy curves involved in complex formation and bond-forming reactivity between AB^{2+} and C. The $\text{AB}^{2+} + \text{C}$ curve is dominated by polarisation attraction. The $[\text{ABC}]^{2+}$ complex is found at the minimum, at short interspecies separations, r . The dication + neutral potential energy curves are crossed by the repulsive states corresponding to the SET products. Adapted from reference.¹¹³

1.5 Experimental techniques for investigating dications

Experimental investigations can provide vital information on the properties and reactivity of dications. The vibronic structure of a dication, or the double ionization energy of a neutral species are essential, among other details, when predicting which reactions may occur from the collisions of dications with neutral species. In this way we can predict if SET or DET is likely to occur. As will be seen for the dication + neutral systems presented in this thesis, relevant thermodynamic information such as the enthalpies of formation of the reactants and products can aid models that explain the observed reactions. The following sections address the experiments used to study the properties of dications and the interactions of dications with neutral species.

Of course, whilst we focus on experimental studies, computational techniques allow for the increasingly accurate determination of dicationic properties such as conformation and

energy, and therefore must be mentioned. Such computational studies often provide vital information to aid with the interpretation of experimental results, or even predict which molecular dications might be stable enough to generate in a laboratory experiment. Indeed, many of the experimental investigations of dications discussed throughout this thesis are supplemented with computational calculations to help rationalise the results. A variety of *ab initio* methods, based on solving the Schrödinger equation, have been applied to determine dicationic properties. Potential energy curves of many diatomic dications have been calculated, such as CrO^{2+} ,⁸⁶ HF^{2+} ,¹¹⁶ and HS^{2+} .¹¹⁷ Indeed, recent studies have predicted that the diatomic group 12 dications M_2^{2+} ($\text{M} = \text{Zn}, \text{Cd}, \text{Hg}$) are all kinetically stable with ~ 1 eV barriers to dissociation.¹¹⁸ BaO^{2+} and BaH^{2+} are predicted to have low lying electronic states that are thermodynamically stable.⁸⁷ Polyatomic dications have also been studied computationally, for example, the potential energy surface of $\text{CH}_3\text{Cl}^{2+}$ was recently calculated, in order to look at the formation of H_3^+ , an important astrochemical molecular ion.¹¹⁹ Calculations have also predicted that, curiously, the lowest energy structure of the dication of benzene is pyramidal, with a five-membered ring.¹²⁰

In the remainder of this section, the current and historical experimental techniques used to probe dication properties and their bimolecular reactivity are discussed.

1.5.1 Determining the properties of dications

Collisional techniques have been used to study dications including electron ionization (EI), translational energy spectrometry (TES), and double charge transfer spectrometry (DCT).

EI can be used to determine the energy threshold of formation for a particular ion, by measuring the onset of a product ion signal (typically detected with MS) as a function of electron energy. EI studies can therefore yield double ionization energies as well as which ionic products are formed as a result of electron bombardment. EI can also be used to determine ionization cross sections. In order to be detected using conventional MS methods, the lifetime of a species needs to be on the order of ~ 10 μs .^{117,121} The lifetimes of molecular dications generated by EI have also been determined using a storage ring.¹³ Several molecular dications, including N_2^{2+} and CS_2^{2+} , were found to have lifetimes greater than a few seconds, limited by collisions with the background gas in the apparatus. Recent investigations utilised EI in a systematic search of metastable dications derived from benzene, resulting in the detection of several $\text{C}_6\text{H}_n^{2+}$ dications.¹²²

Auger spectroscopy involves the detection of secondary electrons emitted accompanying the relaxation of an outer electron to fill a core vacancy. The detection of secondary Auger electrons after EI or PI of a species can reveal the energies of the electronic states of dications. Particularly when these Auger electrons are detected in coincidence with the dication.^{123–125} High resolution (with vibrational structure) spectra of molecular dications can be obtained from the detection of Auger electrons in coincidence with threshold photoelectrons.¹²⁶ For example, the PECs of CO^{2+} states have been determined with the aid of synchrotron experiments detecting the Auger electrons from photoionization.¹²⁷

TES involves collisions of a high energy ion with a neutral target in a collision cell followed by the measurement of the translational energy (E_T) loss (or gain) of the fast ion as a result of the collision.¹²⁸ This loss or gain of E_T allows electronic and vibrational states of an ion to be determined. For example, Jonathan *et al.* employed TES to study the lowest energy electronic states of NO^{2+} .¹²⁹ TES is especially useful for determining information on the mutual positions of the ground and excited electronic states of molecular dications.

DCT is similar to TES except it involves collisions between cations, usually protons, and a neutral species. The collision results in the transfer of two electrons from the neutral to the monocation, forming a dication (from the neutral) and an anion (from the monocation). Translational energy loss from the nascent anion is therefore used to determine the double ionization energy of the neutral species.¹³⁰ Typically performed using MS apparatus with a collision chamber, previous investigations utilising DCT with high energy ($\sim\text{keV}$) H^+ ions have been used to determine double ionization energies of CH_4 ,¹³¹ allene (C_3H_4),¹³² N_2 , O_2 , NO , and others.^{133,134}

Ionization techniques involving PI typically offer greater selectivity in the dication states accessed than electron ionization. This is because in PI all of the energy from the photon is absorbed compared with a collision with an electron which will cause excitation with a range of energies. The spread (full width at half maximum, FWHM) of ionizing energy is also generally larger for electrons than the spread of ionizing photon energy. To this end, synchrotron radiation offers a highly tuneable photon source, for example the CERISES apparatus on the DESIRS beamline at the synchrotron SOLEIL has been used to probe dication formation, determining the double-ionization energy of cycloheptatriene (C_7H_8) and the appearance energy of $\text{C}_7\text{H}_6^{2+}$.⁷³

Dications are commonly identified using MS, however, spectroscopic identification techniques are a valuable tool to detect dications in faraway astrophysical environments.^{23,25,59,61} Atomic dications are well characterised spectroscopically, however, the same cannot be said about the corresponding molecular species. Spectroscopy can also reveal information on the specific states of a dication as well as their identity. Excited dication states can sometimes fluoresce, for example, a N_2^{2+} fluorescence band was observed in rotationally resolved spectra as early as 1958.^{135,136} While some work is ongoing,¹³⁷ in order to detect more dications in space, laboratory based spectroscopic studies of dications are required, as well as more sensitive spectroscopic techniques to aid detection.

The auto-dissociation dynamics of molecular dications have been studied, often using velocity map imaging (VMI) which can reveal the velocity distribution of the product fragments and therefore energetic information. PI coupled with VMI detection has been recently employed to study the dissociation of dications generated from 1,2-bromochloroethane¹³⁸ and CD_3OD .¹³⁹ A statistical technique has been developed to study the fragmentation of multiply charged molecular cations, termed covariance-map imaging, often used with PI-VMI.¹⁴⁰ Covariance-map imaging quantifies the correlation between two product fragments in order to determine if they are formed in the same process. For example, the fragmentation of CF_3I^{2+} has been recently studied with this technique, revealing mechanisms of the various dissociation channels.¹⁴¹ The dissociation dynamics of doubly ionized adamantane, a proxy for interstellar carbonaceous species, has also recently been investigated using covariance techniques coupling extreme UV (EUV) radiation and VMI detection.¹⁴² Whilst the use of covariance mapping can provide information on the pathways and energetics of the fragmentation of dications, the use of coincidence techniques removes the need for statistical methods and can offer greater sensitivity.

1.5.1.1 Coincidence techniques

Coincidence techniques involve the detection of two or more products from a single event. From a coincidence experiment, we can unambiguously assign products, and infer the dynamics and mechanisms of reactions. To demonstrate the power of coincidence techniques, consider the following reaction:



The dication AB^{2+} reacts with a neutral species, C , resulting in the formation of three products: A^+ , B^+ and C . However, the formation of each of these individual products could also proceed *via* multiple pathways. A traditional mass spectrometry experiment would detect A^+ and B^+ , however, either of these products could also form from dissociative SET along with C^+ . Therefore, in conventional experiments, the products of dicationic dissociation are largely indistinguishable from the products of single ionization or other processes. With the application of a coincidence method that detects pairs of cations, the simultaneous formation of A^+ and B^+ in this channel can be distinguished from two parallel dissociative SET reactions.

As discussed above, statistical methods (such as covariance-map imaging) have also been developed to study the dissociation of a molecule without the coincident detection of product fragments.¹⁴³ However, coincidence techniques detect the products of single reactive events and allows the complete and direct reconstruction of the correlation between the particles. While covariance-map techniques are statistical and hence still look at ensemble processes with the inherent averaging that involves. Covariance-map techniques will also struggle to detect weak channels. Coincidence measurements are powerful as they are unambiguous, without using averaging or statistical methods. Thus, coincidence experiments can give comprehensive insight into the dynamics of processes involving dications.

Ion coincidence experiments typically involve there being fewer than one event per detection cycle, to ensure that any products detected originate from a single reactive event. The experiments are therefore repeated over many cycles to build a statistically significant distribution of the correlation between the variables of interest. A high repetition rate is required to mitigate for the low count rate and allow for reasonable experimental run times. This need for a high repetition rate makes the use of lasers in coincidence experiments difficult. Most laboratory based high power lasers have low repetition rates of a few Hz. The use of lasers with coincidence experiments is now more feasible with the availability of high-power Ti:sapphire laser systems. However, the need for multiphoton ionization schemes makes the use of lasers in coincidence challenging.

Coincidence techniques were first applied to the study of dications by McCulloh *et al.*¹⁴⁴ to investigate the decomposition of isolated multiply charged ions, including CO_2^{2+} and CH_4^{2+} . Positive ions or ion pairs generated by EI were detected in coincidence with an ejected electron. Subsequently, a variety of coincidence techniques have been developed, especially by Eland^{66,145–147} and co-workers, to encompass many ionization and detection methods.

Coincidence techniques involving photoionization are especially informative because of the control over ionizing energy. For example, the state selective ionization of neutrals to dications is possible with photoionization.

Photoelectron-photoelectron coincidence (PEPECO), involving the coincident detection of two photoelectrons, has been used to obtain double photoionization spectra, equivalent to photoelectron spectra for a dication, of many small molecules.^{145,148,149} The detection of threshold electrons, with near zero kinetic energy, in coincidence (TPEsCO) allows for enhanced resolution spectra to be obtained.^{150,151}

Time-of-flight (TOF) MS is ideally suited for coincidence experiments as it allows the detection of more than one ion in the same TOF cycle of the same detector. In pioneering experiments, Curtis and Eland¹⁵² used a photoion-photoion coincidence (PIPICO) technique to probe the dicationic states of several molecules. This first PIPICO study of double photoionization revealed the dissociation pathways and energetics of a number of small dications for the first time. PIPICO has been performed with synchrotron radiation, for example, in investigations of the fragmentation of SO_2^{2+} generated from ionization of SO_2 .^{153,154} Techniques such as these, involving the detection of more than one product ion in coincidence, have allowed the dissociation of dications to be explored in more detail.

1.5.1.1.1 Coincidence techniques to investigate the dissociation of dications

The EI apparatus at UCL, shown in Figure 1.7, is capable of detecting multiple ions in coincidence following electron ionization of a neutral species. The cross sections for the formation of ions resulting from EI of neutrals, as well as the corresponding fragmentation pathways resulting from ionization are easily determined.¹⁵⁵⁻¹⁵⁷ Recent work investigating the EI of PF_3 has shown that F^+ ions are, in fact, primarily formed as a result of processes involving multiple ionization.¹⁵⁸ Indeed, multiple ionization processes generally account for a large proportion of the total ion yields from collisions of molecules by 200 eV electrons. Ion-ion coincidence techniques have also been used to study the fragmentation dynamics of the doubly ionized amino acids glycine and alanine, formed from collisions of the neutral amino acids with Xe^{25+} and O^{6+} respectively.^{159,160}

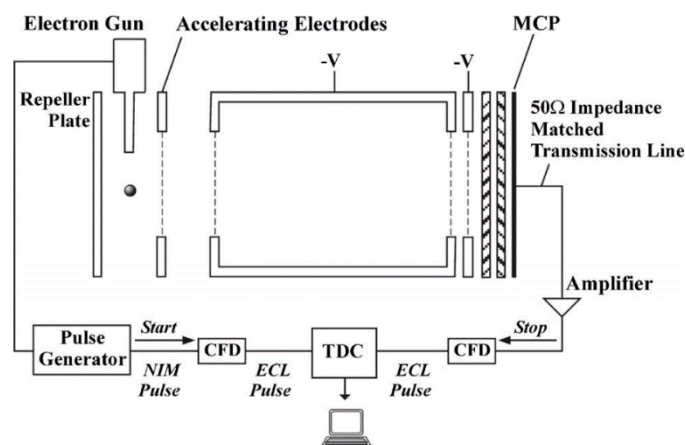


Figure 1.7: Schematic of the electron ionization apparatus at UCL. MCP stands for microchannel plate, CFD stands for constant fraction discriminator, TDC stands for time-to-digital converter, ECL stands for emitter-coupled logic, and NIM stands for nuclear instrumentation mode. Reproduced from reference.¹⁶¹

The use of time- and position-sensitive detectors with multi-ion detection can allow the determination of the dynamics and kinetic energy releases of a reaction, as demonstrated by the investigations presented in this thesis.^{146,162} Additionally, the momentum of a third, neutral, fragment can be determined using conservation of momentum. For example, in this way the two and three body Coulomb explosion of N_2O^{2+} was studied, revealing the dynamics and branching ratios of the competing N-NO and NN-O bond cleavages.¹⁶³ Such set ups are sometimes described as ‘momentum imaging’, other examples of the applications of such experiments include a study of the fragmentation of $\text{C}_2\text{H}_2^{2+}$.¹⁶⁴

Coincident cation detection was employed by Lundqvist *et al.* in 1995 to study the dissociation of dications with a technique termed ‘doppler free kinetic energy release spectroscopy’ (DFKER).¹⁶⁵ CO_2 was ionized by EI in the middle of two TOF tubes, with a detector at each end. By detecting each product monocation resulting from a two-body Coulomb explosion the energy of each fragment can be determined. The centre-of-mass (CM) can then be accurately determined using conservation of momentum. The CM kinetic energy can then be subtracted from the fragment energies, thus eliminating any error arising from thermal motion of the reactant. Using DFKER, it is possible to obtain kinetic energy release spectra of dicationic dissociation with vibrational structure, also demonstrated with N_2^{2+} ,¹⁶⁶ and O_2^{2+} .¹⁶⁷

In photoelectron-photoion-photoion coincidence (PEPIPICO) spectroscopy the flight times of the two product ions can be measured relative to the ejected electron. Thus, the masses of ions generated from dication dissociation are directly determined, a capability especially useful when studying dications with multiple fragmentation pathways. The use of PEPIPICO, especially when coupled with position-sensitive ion detection, means that the three-body decays of dications are better characterised than for three-body decays of neutrals or monocations.^{146,147} Recently, PEPIPICO has been used to investigate the fragmentation of doubly ionized water, D_2O^{2+} .¹⁶⁸ Similarly, an electron-ion-ion coincidence technique has been used to show that after double ionization by EI, the ethanol dication can undergo significant rearrangement before Coulomb explosion.¹⁶⁹

The Elettra synchrotron, in Trieste, has been used in various coincidence experiments involving dications. Elettra gives tuneable and intense UV and EUV photons. The double ionization of HBr was studied at Elettra using PEPICO and PEPIPICO.¹⁷⁰ TPEsCO was also used to obtain high resolution spectra resulting from double ionization of HBr,¹⁷¹ HI,¹⁷² HCl,¹⁷³ and more recently, H_2O .¹⁷⁴ At Elettra, PEPIPICO coupled with position-sensitive ion detection has been used to characterise the dications of atmospheric species including CO_2^{2+} ,^{175,176} N_2O^{2+} ,^{177,178} benzene,^{179,180} acetylene,^{181,182} and other species relevant to astrochemical environments.^{183–185} These studies involved the determination of the kinetic energy releases accompanying Coulomb explosion, concluding that processes involving dications could be important in atmospheric erosion.

Another class of apparatus used to study the dissociation of dications are termed ‘reaction microscopes’ where the products are ‘imaged’. This term is used to describe methodologies which involve the coincident detection of several product fragments (ions and electrons) generated from interactions between molecules and particles or photons, often with full solid angle detection, and with high momentum resolution.^{186,187} These experiments are also known as recoil ion momentum spectroscopy (RIMS), and the low temperature analogue cold target recoil ion momentum spectroscopy (COLTRIMS). A schematic of a typical reaction microscope experiment is shown in Figure 1.8. Typically, a collimated beam of cold atoms or molecules is crossed with a beam of photons, electrons, or charged particles in the interaction region. A weak electrostatic field is applied to the interaction region to extract the product fragments, often resulting from a Coulomb explosion after multiple ionization. At each end of the electrostatic field is a position-sensitive detector, one side for positive ions and the other

side for electrons. The side for electrons often has an extra magnetic field applied to ensure that electrons with high transverse velocities are detected. The momentum of each ion is determined from the TOFs and detector hit positions. Energetic information can be calculated from the ion momenta information. Reaction microscopes are able to reveal branching ratios, and the dynamics of dissociation, for example, rearrangements after excitation can be detected. Due to the precise imaging of the product ions, the energetics of dissociation can also be determined.

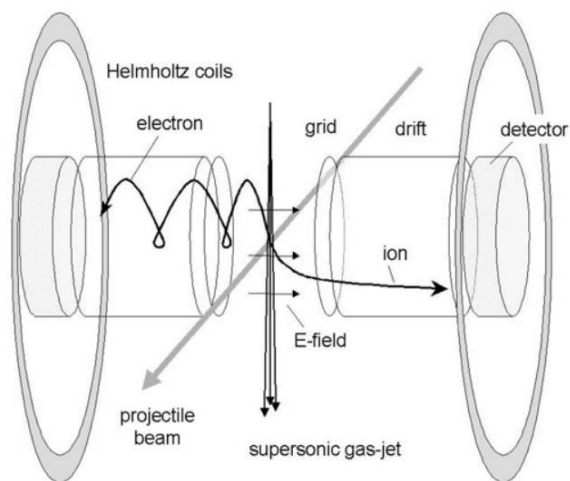


Figure 1.8: Schematic of a typical reaction microscope apparatus. Reproduced from reference.¹⁸⁷

Reaction microscopes using EI as the ionization method have been used to study the formation of H_3^+ resulting from the double ionization of ethane¹⁸⁸ and methanol.¹⁸⁹ The fragmentation of ethylene, allene and CS_2 , induced by multiple ionization *via* EI, have also been investigated.^{190,191} The reaction microscope methodology has led to the determination of which specific NH_3^{2+} dication states are populated from PI of NH_3 .¹⁹² The kinetic energy releases accompanying dissociation of N_2 and O_2 molecules following multiple ionization by EUV radiation from a free electron laser have also been reported.¹⁹³ Finally, collisions with multiply charged ions have been used to ionize neutral species in COLTRIMS experiments. Energetic Ar^{8+} and Ne^{8+} ions have been used to form dications ionized from methane, ethene, propyne, and allene.^{194,195} These studies elucidated fragmentation dynamics of the dications involved, for example, the formation of H_3^+ from methane and ethene dications proceeds *via* a ‘ H_2 roaming’ mechanism.

The techniques described above have contributed to an increasingly detailed picture of dicationic properties. Many small dications are now well characterised with accurate double

ionization energies, and even dicationic electronic structures with vibrational resolution, being available for a number of small molecules. Kinetic energy releases accompanying the unimolecular fragmentation of dications, and their corresponding lifetimes are also available for an increasing number of small molecules. Knowledge of these properties allows for the accurate determination of the dynamics and energetics of reactions between dications and neutrals, such as those presented in Chapters 3 – 6. The bimolecular reactivity of dications has been less explored. There have been several methods applied to the study of dication-neutral reactions, typically appropriating apparatuses designed for the investigation of monocation-neutral reactivity. These experiments are described in the following section.

1.5.2 Probing bimolecular dication reactions

1.5.2.1 Crossed-beam experiments

The first gas-phase ion-molecule reactions were carried out in the ionization chambers of MS instruments before the development of specialist apparatus.¹⁹⁶ To study the reactivity of dications, generally, the dications of interest need to be generated and selected before interacting with another species within a short time-frame to prevent unimolecular dissociation. Dications are typically generated by electron ionization before being mass filtered and passed through a collision cell containing the target species. The products of dication-neutral interactions occurring in the collision cell are then usually detected by MS. Early experiments studying the interaction of dications and neutrals used dication beams with high collision energies (~ 1 keV), and the experiments therefore only identified ET and CID products, without the observation of bond-formation.^{96,197–200} Recent examples of the application of this method include a study of the dissociation of peptide dications following collisions with Na and Cs atoms,²⁰¹ and the fragmentation of the amino acid alanine following collisions with He²⁺.²⁰² A crossed-beam methodology has also been coupled with luminescence spectroscopy.²⁰³ Fluorescence was detected from CO⁺ monocations formed from collisions of CO²⁺ with various neutrals, showing that the CO⁺ *B* state was primarily involved.

Later, crossed-beam apparatus, including the PSCO-MS apparatus used for the experiments presented in this thesis, were used to study dication-neutral collisions at lower collision energies (a few eV). These experiments involve the production of a mass-selected beam of dications, crossing this ion beam perpendicularly with a neutral collision gas, and then extracting and identifying the charged products, typically with MS. Price and others^{91,93} studied

the reactions of dications with neutrals including CO^{2+} , OSC^{2+} and CO_2^{2+} with rare gases using the apparatus shown in Figure 1.9. These collision systems involved CID and SET, with the total reaction cross section increasing with the atomic mass of the rare gas. Importantly, the use of these lower collision energies allowed bond-forming reactions to occur.²⁰⁴ For example, the collisions of $\text{CF}_2^{2+} + \text{Xe}$ resulted in the generation of XeF^+ . More recent studies using the crossed-beam apparatus at UCL investigated the bimolecular reactivity of PF_3^{2+} with Ar, O_2 , CO, and Ne.¹⁵⁸ The collisions of PF_3^{2+} with Ar resulted in the formation of ArF^+ .

The use of crossed-beams allows for a more localised interaction region, compared to a collision cell, and therefore allows for more dynamical information about the dication-neutral interaction to be determined.¹⁹⁶ If the spread in collision energy can be minimised, informative data on the angular and energy distributions of the product ions can be obtained. However, by localising the reaction to such a small area, the ion yield is dramatically reduced, and determining the absolute neutral reactant concentration is also problematic. Therefore, it is difficult to obtain absolute reaction cross sections using the crossed-beam methodology.

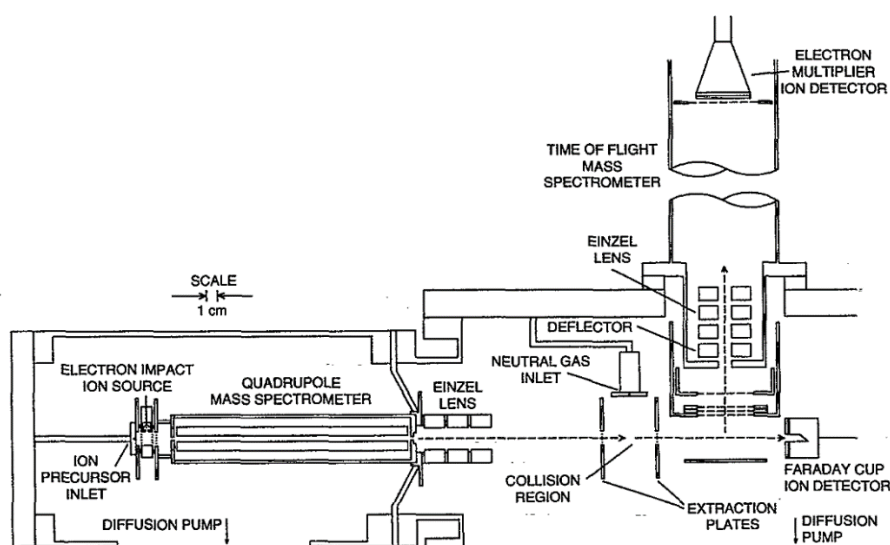


Figure 1.9: Schematic of the crossed-beam apparatus used by Price and co-workers. Reproduced from reference.⁹¹

EVA II is a crossed-beam apparatus built by the Herman group, shown in Figure 1.10.^{205–207} By rotating the two beams around the scattering centre, the angular distribution of the product ions is obtained. Therefore, the dynamics of the reaction and the relative differential cross section of products following collisions of atomic dications with atomic neutrals can be

determined. The reaction dynamics can be interpreted to indicate the mechanisms involved. The dynamics and energetics of charge transfer and chemical reactions resulting from collisions of many dication-neutral systems have been studied with EVA II, including $\text{CHCl}_2^{2+} + \text{D}_2$,²⁰⁵ $\text{CF}_2^{2+} + \text{D}_2/\text{H}_2$,¹¹³ $\text{CO}_2^{2+} + \text{D}_2$,²⁰⁸ $\text{CF}_3^{2+} + \text{D}_2$,²⁰⁹ and $\text{CO}_2^{2+} + \text{CO}_2$.²¹⁰

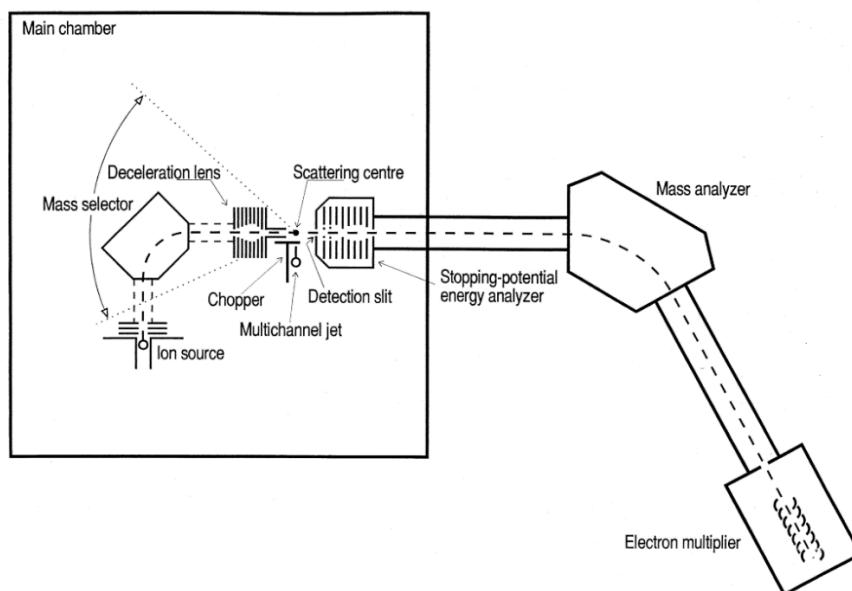


Figure 1.10: Schematic of the EVA II apparatus. Reproduced from reference.¹¹³

1.5.2.2 Guided ion-beam experiments

Another experimental method used to study the interactions between dications and neutrals involves guided ion-beams (GIB). In a GIB experiment, a mass selected beam of dications interacts with a neutral species in a collision region. However, unlike a crossed-beam experiment, this collision region is electrostatically constrained by a multipole ion guide. The products are then identified with a subsequent quadrupole MS. GIB apparatuses therefore tend to have a linear configuration. The guide acting on the collision region helps to prevent the loss of ions formed with transverse velocities; therefore, ions are more efficiently collected to the detector. The measurement of precise ion yields with GIB experiments allows for the determination of accurate reaction cross sections and branching ratios. The collision energy of a GIB experiment is simply controlled by varying the potential of the octopole and CM collision energies of close to 0 eV are attainable. Therefore, the collision energy dependence of reaction cross sections can be easily quantified. Results from GIB experiments have revealed that the cross sections for bond-forming reactions resulting from dication-neutral collisions decrease rapidly with increasing collision energy. However, because all of the ions are directed into the

final quadrupole regardless of their velocity, most of the dynamical information (the angular distribution of the velocities) is removed. Therefore, the crossed-beam and GIB methodologies can be used in tandem to get a more complete picture of dication neutral reactions.

The Trento group have used the GIB methodology to study dication-neutral collisions.⁴⁰ Dications are generated by EI before being selected by a quadrupole. The ions then pass through an octopole collision cell where the dications can interact with the neutral species before being detected by a channeltron following a second quadrupole. The quadrupole-octopole-quadrupole (QOQ) arrangement, shown in Figure 1.11, is typical for a GIB apparatus. Amongst other studies, the Trento GIB has been used to investigate reactivity following the collisions of $\text{Ar}^{2+} + \text{O}_2$,¹⁰⁷ discussed in Chapter 3, and also $\text{CO}_2^{2+} + \text{Ar}$,¹⁰⁶ with both systems resulting in bond-forming reactions. The Trento GIB was also used to investigate the collisions of $\text{C}_7\text{H}_6^{2+}$ with N_2 and Xe , resulting in the generation of the adducts $\text{C}_7\text{H}_6\text{N}_2^{2+}$ and $\text{C}_7\text{H}_6\text{Xe}^{2+}$ respectively.⁷³

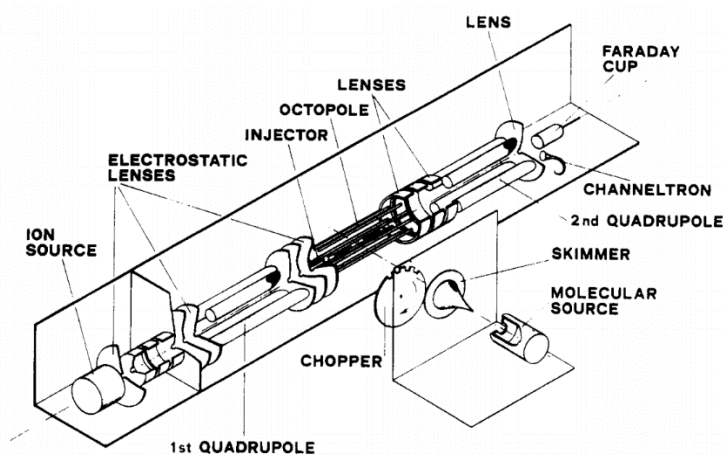


Figure 1.11: Schematic of a guided ion beam apparatus, with typical quadrupole-octopole-quadrupole arrangement. Reproduced from reference.²¹¹

Roithová and co-workers have also used the GIB methodology extensively.²¹² Dications are generated by EI before being guided by an octupole into a QOQ arrangement, similar to that of the apparatus used by the Trento group. The apparatus also has the option to couple the GIB technique with a selected ion flow tube (discussed further in Section 1.5.2.3). After generation, the ions can be directed into a flow tube before the QOQ section. In the high-pressure flow tube collisions with a buffer gas act to thermalise the ions. Differential pumping is required to maintain the balance of pressures throughout the apparatus. Roithová and Schröder^{79,105} studied the collisions of various aromatic hydrocarbon dications, $\text{C}_m\text{H}_n^{2+}$ ($m = 6-$

14, $n = 6-10$), with acetylene, which resulted in the formation of new carbon-carbon bonds, mentioned in Sections 1.1.1.2 and 1.4.3. The bimolecular reactivity of SiF_3^{2+} , generated *via* EI of SiF_4 , has also been studied.⁷⁴ Several species with new bonds were observed. For example, at low collision energies, $\text{SiF}_2\text{N}_2^{2+}$ was the most abundant product following the collisions of SiF_3^{2+} with N_2 .

The CERISES experiment also employs the GIB methodology. Dications are generated *via* photoionization from synchrotron radiation, allowing for the generation of energy selected dications. After the dications are generated, there is the familiar QOQ GIB arrangement. CERISES has been employed to investigate the collision energy dependence of the reaction cross sections of charge transfer and bond-forming reactions following the collisions of CHCl^{2+} with Ar and D_2 ,²¹³ and CO_2^{2+} with CO_2 and CO .²¹⁴ The GIB methodology has also been used to study dication-neutral collisions in other laboratories, such as at Utah, where the energy dependence of the reactivity of $\text{Ta}^{2+} + \text{CH}_4$ was investigated.²¹⁵

1.5.2.3 Selected ion flow tube experiments

The selected ion flow tube (SIFT) methodology involves a beam of mass selected ions injected into a flow of buffer gas.²¹⁶ The neutral reactant is also injected later in the flow. Ion-neutral reactions can occur, and the products are detected at the end of the tube with quadrupole MS. By including multiple injection points, consecutive reactions can be studied. Due to interactions with the buffer gas, the reactant species are thermalised. The SIFT technique can be described as a ‘swarm’ experiment because a reactant ion can undergo multiple collisions, typically in a high-pressure environment.

The SIFT technique has been used to determine rate constants and branching ratios for dication-neutral reactions. Early SIFT experiments resulted in the determination of the rate coefficients for the SET and DET reactions of rare gas dications, Rg^{2+} ($\text{Rg} = \text{Ne}, \text{Ar}, \text{Kr}, \text{Xe}$), with atoms and small molecules, including $\text{Rg}, \text{H}_2, \text{N}_2, \text{CO}, \text{CO}_2$, and C_2H_2 .^{103,217–220} Curiously, the reactions of $\text{Ar}^{2+} + \text{C}_{60}$, studied using a SIFT technique, resulted in formation of C_{60}^{3+} , undoubtedly due to there being multiple collisions and low triple ionization energy of C_{60} .²²¹ Reactions of the oxygen dication, O_2^{2+} , with $\text{O}_2, \text{N}_2, \text{CO}_2, \text{NO}$ and Ne have also been studied using the SIFT methodology.²²² The low collision energies accessible with this technique resulted in the first observation of a bond-forming dication-neutral reaction: $\text{O}_2^{2+} + \text{NO} \rightarrow \text{NO}_2^+ + \text{O}^+$.

1.5.3 Experimental outlook

Since the discovery of dications there have been numerous studies of their properties and reactivity, aided by the development of a number of experimental methodologies and enhanced computational power. Another technique recently applied to dication-neutral reactions involves trapping C^{2+} ions at 20 K before introducing H_2 , to look for the formation of new C-H bonds.²²³

The methodologies applied to studies of dication-neutral reactions, discussed in the above sections, namely the GIB and crossed-beam techniques generally only result in one-dimensional data, therefore, it is difficult to differentiate which processes lead to the observation of any product monocations. Thus, the use of a methodology employing coincident detection of product ions is required to unambiguously assign reaction pathways.

There are examples of dication-neutral collisions studied employing coincidence methodologies, but these typically involve high collision energies (>100 keV), and therefore bond-forming chemistry is unlikely to be observed. For example, the dynamics and energetics of the dissociation of NH_3 and H_2O following collisions with Ar^{2+} and C^{2+} respectively has been investigated.^{75,76} Whilst these studies revealed the fragmentation dynamics of the neutrals after ionization, as expected, no bond-forming chemistry was observed.

The PSCO-MS apparatus used for the experiments described in this thesis couples the crossed-beam methodology with the position-sensitive coincident detection of ions. This setup allows for the kinematics of dication-neutral reactions to be characterised more thoroughly than before. For example, evidence for the formation of a short lived complex, $[NeN_2]^{2+}$, was observed in the DSET reaction following the collisions of $Ne^{2+} + N_2$.⁹⁷ The use of low collision energies (<10 eV) allows for bond-forming chemistry to occur following dication-neutral collisions. The PSCO-MS methodology is discussed in detail in Chapter 2.

1.6 Summary

This chapter has introduced dications, discussing their formation and properties. The reactivity of dications with neutrals has been discussed in a general sense, including the description of models used to rationalise dication-neutral reactivity that involve potential energy surfaces. The relevance of dications has been discussed, especially to planetary ionospheres. A thorough review of the current techniques used to study the properties and

reactions of dications, and the outcomes of these studies has been presented. This thesis helps to address the need to study dication-neutral reactions in order to reveal information on processes occurring in ionospheres, as well as other high energy environments. The following chapter provides a comprehensive description of the PSCO-MS apparatus. Chapters 3 – 6 detail the bimolecular reactions of three ionospherically relevant dications with several neutral species.

1.7 References

- 1 M. Larsson, W. D. Geppert and G. Nyman, *Reports Prog. Phys.*, 2012, **75**, 66901.
- 2 K. P. Kirby, *Phys. Scr.*, 1995, **1995**, 59–64.
- 3 A. L. Vaughan, *Phys. Rev.*, 1931, **38**, 1687–1695.
- 4 R. Conrad, *Phys. Z.*, 1930, **31**, 888–892.
- 5 F. Fantuzzi, T. M. Cardozo and M. A. C. Nascimento, *Phys. Chem. Chem. Phys.*, 2017, **19**, 19352–19359.
- 6 P. M. W. Gill and L. Radom, *J. Am. Chem. Soc.*, 1989, **111**, 4613–4622.
- 7 L. Pauling, *J. Chem. Phys.*, 1933, **1**, 56–59.
- 8 C. Simon, J. Lilensten, O. Dutuit, R. Thissen, O. Witasse, C. Alcaraz and H. Soldi-Lose, *Ann. Geophys.*, 2005, **23**, 781–797.
- 9 J. Lilensten, O. Witasse, C. Simon, H. Soldi-Lose, O. Dutuit, R. Thissen and C. Alcaraz, *Geophys. Res. Lett.*, 2005, **32**, L03203.
- 10 O. Witasse, O. Dutuit, J. Lilensten, R. Thissen, J. Zabka, C. Alcaraz, P.-L. Blelly, S. W. Bougher, S. Engel, L. H. Andersen and K. Seiersen, *Geophys. Res. Lett.*, 2002, **29**, 104.
- 11 S. D. Price, *J. Chem. Soc., Faraday Trans.*, 1997, **93**, 2451–2460.
- 12 C. A. Nicolaides, *Chem. Phys. Lett.*, 1989, **161**, 547–553.
- 13 D. Mathur, L. H. Andersen, P. Hvelplund, D. Kella and C. P. Safvan, *J. Phys. B At. Mol. Opt. Phys.*, 1995, **28**, 3415–3426.
- 14 H. S. Bridge, J. W. Belcher, A. J. Lazarus, J. D. Sullivan, R. L. McNutt, F. Bagenal, J. D. Scudder, E. C. Sittler, G. L. Siscoe, V. M. Vasyliunas, C. K. Goertz and C. M. Yeates, *Science*, 1979, **204**, 987–991.
- 15 S. Ghosh, K. K. Mahajan, J. M. Grebowsky and N. Nath, *J. Geophys. Res.*, 1995, **100**, 23983–23991.

- 16 J. H. Hoffman, C. Y. Johnson, J. C. Holmes and J. M. Young, *J. Geophys. Res.*, 1969, **74**, 6281–6290.
- 17 J. Liliensten, C. Simon, O. Witasse, O. Dutuit, R. Thissen and C. Alcaraz, *Icarus*, 2005, **174**, 285–288.
- 18 S. Falcinelli and M. Rosi, *Molecules*, 2020, **25**, 4157.
- 19 B. J. Wilkes, G. J. Ferland, D. Hanes and J. W. Truran, *Mon. Not. R. Astron. Soc.*, 1981, **197**, 1–6.
- 20 L. N. Kondrat'eva, *Sov. Astron.*, 1978, **22**, 194–199.
- 21 M. Perinotto, *Astron. Astrophys.*, 1977, **61**, 247–249.
- 22 J. P. Simpson, R. H. Rubin, E. F. Erickson and M. R. Haas, *Astrophys. J.*, 1986, **311**, 895–908.
- 23 A. L. Strom, C. C. Steidel, G. C. Rudie, R. F. Trainor, M. Pettini and N. A. Reddy, *Astrophys. J.*, 2017, **836**, 164.
- 24 T. Barker, *Astrophys. J.*, 1980, **240**, 99–104.
- 25 S. Rappaport, E. Chiang, T. Kallman and R. Malina, *Astrophys. J.*, 1994, **431**, 237–246.
- 26 L. T. Greenberg, P. Dyal and T. R. Geballe, *Astrophys. J. Lett.*, 1977, **213**, L71–L74.
- 27 I. S. Bowen, *Nature*, 1927, **120**, 473.
- 28 A. Acker, H. M. J. Boffin, N. Outters, B. Miszalski, L. Sabin, P. Le Dû and F. Alves, *Rev. Mex. Astron. y astrofísica*, 2012, **48**, 223–233.
- 29 S. Lombardo, F. Prada, E. Hugot, S. Basa, J. M. Bautista, S. Boissier, A. Boselli, A. Bosma, J. C. Cuillandre, P. A. Duc, M. Ferrari, N. Grosso, L. Izzo, K. Joaquina, Junais, J. Koda, A. Lamberts, G. R. Lemaitre, A. Longobardi, D. Martínez-Delgado, E. Muslimov, J. L. Ortiz, E. Perez, D. Porquet, B. Sicardy and P. Vola, CASTLE: performances and science cases, <http://arxiv.org/abs/2006.13956>, (accessed 2 April 2021).
- 30 G. Wenzel, C. Joblin, A. Giuliani, S. Rodriguez Castillo, G. Mulas, M. Ji, H. Sabbah, S.

- Quiroga, D. Peña, L. Nahon, S. R. Castillo, G. Mulas, M. Ji, H. Sabbah, S. Quiroga, D. Peña and L. Nahon, *Astron. Astrophys.*, 2020, **641**, A98.
- 31 J. Roithová, J. Jašík, J. J. Del Pozo Mellado and D. Gerlich, *Faraday Discuss.*, 2019, **217**, 98–113.
- 32 D. K. Böhme, *Phys. Chem. Chem. Phys.*, 2011, **13**, 18253–18263.
- 33 S. Thripati and R. O. Ramabhadran, *J. Phys. Chem. A*, 2021, **125**, 3457–3472.
- 34 J. N. Bull, J. W. L. Lee and C. Vallance, *Phys. Rev. A*, 2017, **96**, 042704.
- 35 K. Hu and R. S. Houk, *J. Am. Soc. Mass Spectrom.*, 1993, **4**, 28–37.
- 36 J. S. Becker, G. Seifert, A. I. Saprykin and H.-J. Dietze, *J. Anal. At. Spectrom.*, 1996, **11**, 643–648.
- 37 S. D. Price, J. D. Fletcher, F. E. Gossan and M. A. Parkes, *Int. Rev. Phys. Chem.*, 2017, **36**, 145–183.
- 38 R. S. Houk, *Anal. Chem.*, 1980, **52**, 2283–2289.
- 39 Y. Akar, Sh2-129 & Ou4 - The Flying Bat and Giant Squid Nebula (Yannick Akar) - AstroBin, <https://astrophotomannheim.de/images/sh2-129-ou4/>, (accessed 10 May 2021).
- 40 P. Tosi, R. Correale, W. Lu, S. Falcinelli and D. Bassi, *Phys. Rev. Lett.*, 1999, **82**, 450–452.
- 41 P. Tosi, W. Lu, R. Correale and D. Bassi, *Chem. Phys. Lett.*, 1999, **310**, 180–182.
- 42 D. Ascenzi, P. Tosi, J. Roithová, C. L. Ricketts, D. Schröder, J. F. Lockyear, M. A. Parkes and S. D. Price, *Phys. Chem. Chem. Phys.*, 2008, **10**, 7121–7128.
- 43 D. Smith and P. Spanel, *Mass Spectrom. Rev.*, 1995, **14**, 255–278.
- 44 M. Alagia, N. Balucani, P. Candori, S. Falcinelli, F. Pirani, R. Richter, M. Rosi, S. Stranges and F. Vecchiocattivi, *Rend. Lincei*, 2013, **24**, 53–65.
- 45 R. Thissen, O. Witasse, O. Dutuit, C. S. Wedlund, G. Gronoff and J. Liliensten, *Phys.*

- Chem. Chem. Phys.*, 2011, **13**, 18264–18287.
- 46 D. Wehrli, M. Génévriez and F. Merkt, *Phys. Chem. Chem. Phys.*, 2021, **23**, 10978–10987.
- 47 C. R. Chappell, R. C. Olsen, J. L. Green, J. F. E. Johnson and J. H. Waite, *Geophys. Res. Lett.*, 1982, **9**, 937–940.
- 48 A. W. Yau, B. A. Whalen and E. Sagawa, *Geophys. Res. Lett.*, 1991, **18**, 345–348.
- 49 O. Witasse, T. Slinger and R. Thissen, *Ann. Geophys.*, 2011, **29**, 2235–2238.
- 50 H. A. Taylor, H. C. Brintor, T. C. G. Wagner, B. H. Blackwell and G. R. Cordier, *IEEE Trans. Geosci. Remote Sens.*, 1980, **GE-18**, 44–49.
- 51 H. Gu, J. Cui, Z. He and J. Zhong, *Earth Planet. Phys.*, 2020, **4**, 11–16.
- 52 A. O. Nier, W. B. Hanson, A. Seiff, M. B. McElroy, N. W. Spencer, R. J. Duckett, T. C. Knight and W. S. Cook, *Science*, 1976, **193**, 786–788.
- 53 A. O. Nier, M. B. McElroy, S. K. Atreya, H. Franz, M. Wong, P. G. Conrad, D. Harpold, J. J. Jones, L. A. Leshin, H. Manning, T. Owen, R. O. Pepin, S. Squyres, M. Trainer and M. S. Team, *Science*, 1976, **194**, 1298–300.
- 54 H. Gu, J. Cui, D. Niu, L. Dai, J. Huang, X. Wu, Y. Hao and Y. Wei, *Earth Planet. Phys.*, 2020, **4**, 396–402.
- 55 X. Wu, J. Cui, Y. Cao, W. Sun, Q. Luo and B. Ni, *Earth Planet. Phys.*, 2020, **4**, 390–395.
- 56 L. A. Frank, W. R. Paterson, K. L. Ackerson, V. M. Vasyliunas, F. V. Coroniti and S. J. Bolton, *Science*, 1996, **274**, 394–395.
- 57 D. E. Shemansky and G. R. Smith, *J. Geophys. Res.*, 1981, **86**, 9179–9192.
- 58 F. Bagenal and J. D. Sullivan, *J. Geophys. Res. Sp. Phys.*, 1981, **86**, 8447–8466.
- 59 F. Herbert, N. M. Schneider, A. R. Hendrix and F. Bagenal, *J. Geophys. Res. Sp. Phys.*, 2003, **108**, 1167.

- 60 B. R. Sandel, D. E. Shemansky, A. L. Broadfoot, J. L. Bertaux, J. E. Blamont, M. J. S. Belton, J. M. Ajello, J. B. Holberg, S. K. Atreya, T. M. Donahue, H. W. Moos, D. F. Strobel, J. C. McConnell, A. Dalgarno, R. Goody, M. B. Mcelroy and P. Z. Takacs, *Science*, 1979, **206**, 962–966.
- 61 P. D. Feldman, D. F. Strobel, H. W. Moos and H. A. Weaver, *Astrophys. J.*, 2004, **601**, 583–591.
- 62 R. L. Hudson and M. H. Moore, *Icarus*, 2004, **172**, 466–478.
- 63 H. B. Niemann, S. K. Atreya, S. J. Bauer, G. R. Carignan, J. E. Demick, R. L. Frost, D. Gautier, J. A. Haberman, D. N. Harpold, D. M. Hunten, G. Israel, J. I. Lunine, W. T. Kasprzak, T. C. Owen, M. Paulkovich, F. Raulin, E. Raaen and S. H. Way, *Nature*, 2005, **438**, 779–784.
- 64 J. Bourgalais, N. Carrasco, L. Vettier, A. Comby, D. Descamps, S. Petit, V. Blanchet, J. Gaudin, Y. Mairesse and B. Marty, *J. Phys. Chem. A*, 2021, **125**, 3159–3168.
- 65 O. Dutuit, N. Carrasco, R. Thissen, V. Vuitton, C. Alcaraz, P. Pernot, N. Balucani, P. Casavecchia, A. Canosa, S. Le Picard, J.-C. Loison, Z. Herman, J. Zabka, D. Ascenzi, P. Tosi, P. Franceschi, S. D. Price and P. Lavvas, *Astrophys. J. Suppl. Ser.*, 2013, **204**, 20.
- 66 S. D. Price, *Int. J. Mass Spectrom.*, 2007, **260**, 1–19.
- 67 J. D. Fletcher, M. A. Parkes and S. D. Price, *Int. J. Mass Spectrom.*, 2015, **377**, 101–108.
- 68 C. L. Ricketts, S. M. Harper, S. W. P. Hu and S. D. Price, *J. Chem. Phys.*, 2005, **123**, 134322.
- 69 J. F. Lockyear, C. L. Ricketts, M. A. Parkes and S. D. Price, *Chem. Sci.*, 2011, **2**, 150–156.
- 70 A. Beth, K. Altwegg, H. Balsiger, J.-J. Berthelier, M. R. Combi, J. De Keyser, B. Fiethe, S. A. Fuselier, M. Galand, T. I. Gombosi, M. Rubin and T. Sémon, *Astron. Astrophys.*, 2020, **642**, A27.
- 71 J. Renoud, S. Indrajith, A. Domaracka, P. Rousseau, P. Moretto-Capelle, B. A. Huber and J.-P. Champeaux, *Phys. Chem. Chem. Phys.*, 2020, **22**, 5785–5796.

- 72 C. Simon Wedlund, E. Behar, H. Nilsson, M. Alho, E. Kallio, H. Gunell, D. Bodewits, K. Heritier, M. Galand, A. Beth, M. Rubin, K. Altwegg, M. Volwerk, G. Gronoff and R. Hoekstra, *Astron. Astrophys.*, 2019, **630**, A37.
- 73 D. Ascenzi, J. Aysina, E. L. Zins, D. Schröder, J. Žabka, C. Alcaraz, S. D. Price and J. Roithová, *Phys. Chem. Chem. Phys.*, 2011, **13**, 18330–18338.
- 74 J. Roithová, H. Schwarz and D. Schröder, *Chem. Eur. J.*, 2009, **15**, 9995–9999.
- 75 W. Wolff, H. Luna, R. Schuch, N. D. Cariatore, S. Otranto, F. Turco, D. Fregenal, G. Bernardi and S. Suárez, *Phys. Rev. A*, 2016, **94**, 022712.
- 76 P. Bhatt, T. Sairam, A. Kumar, H. Kumar and C. P. Safvan, *Phys. Rev. A*, 2017, **96**, 022710.
- 77 C. L. Ricketts, D. Schröder, C. Alcaraz and J. Roithová, *Chem. Eur. J.*, 2008, **14**, 4779–4783.
- 78 E.-L. Zins and D. Schröder, *J. Phys. Chem. A*, 2010, **114**, 5989–5996.
- 79 J. Roithová and D. Schröder, *Chem. Eur. J.*, 2007, **13**, 2893–2902.
- 80 J. Roithová and D. Schröder, *Phys. Chem. Chem. Phys.*, 2007, **9**, 731–738.
- 81 J. Liliensten, C. Simon Wedlund, M. Barthélémy, R. Thissen, D. Ehrenreich, G. Gronoff and O. Witasse, *Icarus*, 2013, **222**, 169–187.
- 82 S. Falcinelli, F. Pirani, M. Alagia, L. Schio, R. Richter, S. Stranges, N. Balucani and F. Vecchiocattivi, *Atmosphere*, 2016, **7**, 112.
- 83 S. Falcinelli, M. Rosi, P. Candori, F. Vecchiocattivi, J. M. Farrar, F. Pirani, N. Balucani, M. Alagia, R. Richter and S. Stranges, *Planet. Space Sci.*, 2014, **99**, 149–157.
- 84 H. Sabzyan, E. Keshavarz and Z. Noorisafa, *J. Iran. Chem. Soc.*, 2014, **11**, 871–945.
- 85 T. V. Alves, W. Hermoso, K. Franzreb and F. R. Ornellas, *Phys. Chem. Chem. Phys.*, 2011, **13**, 18297–18306.
- 86 L. Gonçalves dos Santos, K. Franzreb and F. R. Ornellas, *Chem. Phys. Lett.*, 2021, 138525.

- 87 L. G. dos Santos and F. R. Ornellas, *Chem. Phys.*, 2019, **520**, 32–39.
- 88 M. Larsson, P. Baltzer, S. Svensson, B. Wannberg, N. Martensson, A. N. de Brito, N. Correia, M. P. Keane, M. Carlsson-Gothe and L. Karlsson, *J. Phys. B At. Mol. Opt. Phys.*, 1990, **23**, 1175–1195.
- 89 R. I. Hall, G. Dawber, A. Mcconkey, M. A. MacDonald and G. C. King, *Phys. Rev. Lett.*, 1992, **68**, 2751–2754.
- 90 M. Fu, S. Pan, L. Zhao and G. Frenking, *J. Phys. Chem. A*, 2020, **124**, 1087–1092.
- 91 S. D. Price, S. A. Rogers and S. R. Leone, *J. Chem. Phys.*, 1993, **98**, 9455–9465.
- 92 C. L. Ricketts, D. Schröder, J. Roithová, H. Schwarz, R. Thissen, O. Dutuit, J. Žabka, Z. Herman and S. D. Price, *Phys. Chem. Chem. Phys.*, 2008, **10**, 5135–5143.
- 93 S. A. Rogers, S. D. Price and S. R. Leone, *J. Chem. Phys.*, 1993, **98**, 280–289.
- 94 S. D. Price, M. Manning and S. R. Leone, *Chem. Phys. Lett.*, 1993, **214**, 553–558.
- 95 M. A. Parkes, J. F. Lockyear and S. D. Price, *Int. J. Mass Spectrom.*, 2009, **280**, 85–92.
- 96 Z. Herman, P. Jonathan, A. G. Brenton and J. H. Beynon, *Chem. Phys. Lett.*, 1987, **141**, 433–442.
- 97 S. M. Harper, S. W.-P. Hu and S. D. Price, *J. Chem. Phys.*, 2004, **120**, 7245–7248.
- 98 P. W. Burnside and S. D. Price, *Int. J. Mass Spectrom.*, 2006, **249–250**, 279–288.
- 99 C. Zener, *Proc. R. Soc. London. Ser. A, Contain. Pap. a Math. Phys. Character*, 1932, **137**, 696–702.
- 100 Z. Herman, *Int. Rev. Phys. Chem.*, 1996, **15**, 299–324.
- 101 W.-P. Hu, S. M. Harper and S. D. Price, *Mol. Phys.*, 2005, **103**, 1809–1819.
- 102 S. M. Harper, W.-P. Hu and S. D. Price, *J. Phys. B At. Mol. Opt. Phys.*, 2002, **35**, 4409–4423.
- 103 D. Smith, N. G. Adams, E. Alge, H. Villinger and W. Lindinger, *J. Phys. B At. Mol.*

- Phys.*, 1980, **13**, 2787–2799.
- 104 M. A. Parkes, J. F. Lockyear and S. D. Price, *Int. J. Mass Spectrom.*, 2013, **354–355**, 39–45.
- 105 J. Roithová and D. Schröder, *J. Am. Chem. Soc.*, 2006, **128**, 4208–4209.
- 106 W. Lu, P. Tosi and D. Bassi, *J. Chem. Phys.*, 2000, **112**, 4648–4651.
- 107 D. Ascenzi, P. Franceschi, P. Tosi, D. Bassi, M. Kaczorowska and J. N. Harvey, *J. Chem. Phys.*, 2003, **118**, 2159–2163.
- 108 N. Lambert, D. Kearney, N. Kaltsoyannis and S. D. Price, *J. Am. Chem. Soc.*, 2004, **126**, 3658–3663.
- 109 J. F. Lockyear, K. Douglas, S. D. Price, M. Karwowska, K. J. Fijalkowski, W. Grochala, M. Remeš, J. Roithová and D. Schröder, *J. Phys. Chem. Lett.*, 2010, **1**, 358–362.
- 110 J. Roithová and D. Schröder, *Angew. Chemie Int. Ed.*, 2009, **48**, 8788–8790.
- 111 M. A. Parkes, J. F. Lockyear and S. D. Price, *Int. J. Mass Spectrom.*, 2014, **365–366**, 68–74.
- 112 J. Roithová, C. L. Ricketts, D. Schröder and S. D. Price, *Angew. Chemie Int. Ed.*, 2007, **46**, 9316–9319.
- 113 Z. Herman, J. Žabka, Z. Dolejšek, M. Fárník and M. Fárník, *Int. J. Mass Spectrom.*, 1999, **192**, 191–203.
- 114 S. Armenta Butt and S. D. Price, *Phys. Chem. Chem. Phys.*, 2021, **23**, 11287–11299.
- 115 S. Armenta Butt and S. D. Price, *Phys. Chem. Chem. Phys.*, 2020, **22**, 8391–8400.
- 116 D. Liu, R. Li, J. Ren, Y. Cheng, B. Yan, Y. Wu, J. G. Wang and S. Bin Zhang, *RSC Adv.*, 2021, **11**, 9600–9607.
- 117 P. J. Miller, S. A. Rogers, J. Senekowitsch, S. V Oneil, S. R. Leone, H.-J. Werner and P. J. Knowles, *Int. J. Mass Spectrom. Ion Process.*, 1990, **100**, 505–519.
- 118 S. Sadjadi, C. F. Matta and I. P. Hamilton, *J. Comput. Chem.*, 2020, **42**, 40–49.

- 119 J. Palaudoux and M. Hochlaf, *ACS Earth Space Chem.*, 2019, **3**, 980–985.
- 120 P. Pozo-Guerron, L. E. Seijas, J. L. Burgos, L. Rincon, F. J. Torres, J. R. Mora, C. Zambrano and R. Almeida, *Chem. Phys. Lett.*, 2020, **758**, 137912.
- 121 S. A. Rogers, P. J. Miller, S. R. Leone and B. Brehm, *Chem. Phys. Lett.*, 1990, **166**, 137–140.
- 122 W. Wolff, A. Perlin, R. R. Oliveira, F. Fantuzzi, L. H. Coutinho, F. de A Ribeiro and G. Hilgers, *J. Phys. Chem. A*, 2020, **124**, 9261–9271.
- 123 E. Fainelli, F. Maracci, R. Platania and L. Avaldi, *J. Electron Spectros. Relat. Phenomena*, 1998, **87**, 169–176.
- 124 W. E. Moddeman, T. A. Carlson, M. O. Krause, B. P. Pullen, W. E. Bull and G. K. Schweitzer, *J. Chem. Phys.*, 1971, **55**, 2317–2336.
- 125 P. Lablanquie, F. Penent, R. I. Hall, H. Kjeldsen, J. H. D. Eland, A. Muehleisen, P. Pelicon, Šmit, M. Žitnik and F. Koike, *Phys. Rev. Lett.*, 2000, **84**, 47–50.
- 126 Y. Hikosaka, F. Penent, P. Lablanquie, R. Hall and K. Ito, *Meas. Sci. Technol.*, 2000, **11**, 1697–1702.
- 127 R. Püttner, X. J. Liu, H. Fukuzawa, T. Tanaka, M. Hoshino, H. Tanaka, J. Harries, Y. Tamenori, V. Carravetta and K. Ueda, *Chem. Phys. Lett.*, 2007, **445**, 6–11.
- 128 C. P. Safvan and D. Mathur, *J. Phys. B At. Mol. Opt. Phys.*, 1993, **26**, L793–L798.
- 129 P. Jonathan, Z. Herman, M. Hamdan and A. G. Brenton, *Chem. Phys. Lett.*, 1987, **141**, 511–514.
- 130 K. Lammertsma, P. von Ragué Schleyer and H. Schwarz, *Angew. Chemie Int. Ed. English*, 1989, **28**, 1321–1341.
- 131 P. G. Fournier, J. Fournier, F. Salama, P. J. Richardson and J. H. D. Eland, *J. Chem. Phys.*, 1985, **83**, 241–246.
- 132 S. R. Andrews, D. E. Parry and F. M. Harris, *J. Chem. Soc., Faraday Trans.*, 1995, **91**, 1181–1183.

- 133 J. Appell, J. Durup, F. C. Fehsenfeld and P. Fournier, *J. Phys. B At. Mol. Phys.*, 1973, **6**, 197–205.
- 134 O. Furuhashi, T. Kinugawa, N. Nakamura, S. Masuda, C. Yamada and S. Ohtani, *J. Chinese Chem. Soc.*, 2001, **48**, 531–534.
- 135 P. K. Carroll, *Can. J. Phys.*, 1958, **36**, 1585–1587.
- 136 D. Cossart, F. Launay, J. M. Robbe and G. Gandara, *J. Mol. Spectrosc.*, 1985, **113**, 142–158.
- 137 S. Banhatti, J. Palotás, P. Jusko, B. Redlich, J. Oomens, S. Schlemmer and S. Brünken, *Astron. Astrophys.*, 2021, **648**, A61.
- 138 H. Wu, Y. Xue, J. Wen, H. Wang, L. Bai, W. He, R. Sun and W. Zheng, *RSC Adv.*, 2019, **9**, 31853–31859.
- 139 N. Iwamoto, C. J. Schwartz, B. Jochim, K. Raju P., P. Feizollah, J. L. Napierala, T. Severt, S. N. Tegegn, A. Solomon, S. Zhao, H. Lam, T. N. Wangjam, V. Kumarappan, K. D. Carnes, I. Ben-Itzhak and E. Wells, *J. Chem. Phys.*, 2020, **152**, 054302.
- 140 C. Vallance, D. Heathcote and J. W. L. Lee, *J. Phys. Chem. A*, 2021, **125**, 1117–1133.
- 141 H. Köckert, D. Heathcote, J. W. L. L. Lee and C. Vallance, *Mol. Phys.*, 2021, **119**, e1811909.
- 142 S. Maclot, J. Lahl, J. Peschel, H. Wikmark, P. Rudawski, F. Brunner, H. Coudert-Alteirac, S. Indrajith, B. A. Huber, S. Díaz-Tendero, N. F. Aguirre, P. Rousseau and P. Johnsson, *Sci. Rep.*, 2020, **10**, 2884.
- 143 C. E. M. Strauss and P. L. Houston, *J. Phys. Chem.*, 1990, **94**, 8751–8762.
- 144 K. E. McCulloh, T. E. Sharp and H. M. Rosenstock, *J. Chem. Phys.*, 1965, **42**, 3501–3509.
- 145 J. H. . Eland, *Chem. Phys.*, 2003, **294**, 171–186.
- 146 S. Hsieh and J. H. D. D. Eland, *J. Phys. B At. Mol. Opt. Phys.*, 1997, **30**, 4515–4534.
- 147 J. H. D. Eland, *Mol. Phys.*, 1987, **61**, 725–745.

- 148 S. D. Price and J. H. D. Eland, *J. Phys. B At. Mol. Opt. Phys.*, 1991, **24**, 4379–4389.
- 149 R. D. Molloy, A. Danielsson, L. Karlsson and J. H. D. Eland, *Chem. Phys.*, 2007, **335**, 49–54.
- 150 G. Dawber, A. G. McConkey, L. Avaldi, M. A. Macdonald, G. C. King and R. I. Hall, *J. Phys. B At. Mol. Opt. Phys.*, 1994, **27**, 2191–2209.
- 151 M. Hochlaf, R. I. Hall, F. Penent, H. Kjeldsen, P. Lablanquie, M. Lavollée and J. H. D. Eland, *Chem. Phys.*, 1996, **207**, 159–165.
- 152 D. M. Curtis and J. H. D. Eland, *Int. J. Mass Spectrom. Ion Process.*, 1985, **63**, 241–264.
- 153 G. Dujardin, S. Leach, O. Dutuit, P.-M. Guyon and M. Richard-Viard, *Chem. Phys.*, 1984, **88**, 339–353.
- 154 T. Masuoka, A. Okaji and A. Kobayashi, *Int. J. Mass Spectrom.*, 2002, **218**, 11–18.
- 155 K. M. Douglas and S. D. Price, *Int. J. Mass Spectrom.*, 2011, **303**, 147–153.
- 156 M. A. Parkes, K. M. Douglas and S. D. Price, *Int. J. Mass Spectrom.*, 2019, **438**, 97–106.
- 157 J. D. Fletcher, M. A. Parkes and S. D. Price, *J. Chem. Phys.*, 2013, **138**, 184309.
- 158 L. K. Ellis-Gibblings, W. G. Fortune, B. Cooper, J. Tennyson and S. D. Price, *Phys. Chem. Chem. Phys.*, 2021, **23**, 11424–11437.
- 159 D. G. Piekarski, R. Delaunay, S. Maclot, L. Adoui, F. Martín, M. Alcamí, B. A. Huber, P. Rousseau, A. Domaracka and S. Díaz-Tendero, *Phys. Chem. Chem. Phys.*, 2015, **17**, 16767–16778.
- 160 S. MacLot, D. G. Piekarski, A. Domaracka, A. Méry, V. Vizcaino, L. Adoui, F. Martín, M. Alcamí, B. A. Huber, P. Rousseau and S. Díaz-Tendero, *J. Phys. Chem. Lett.*, 2013, **4**, 3903–3909.
- 161 S. J. King and S. D. Price, *J. Chem. Phys.*, 2007, **127**, 174307.
- 162 W.-P. Hu, S. M. Harper and S. D. Price, *Meas. Sci. Technol.*, 2002, **13**, 1512–1522.
- 163 K. Gope, I. Luzon and D. Strasser, *Phys. Chem. Chem. Phys.*, 2019, **21**, 13730–13737.

- 164 B. Jochim, M. Zohrabi, T. Severt, B. Berry, K. J. Betsch, P. Feizollah, J. Rajput, E. Wells, K. D. Carnes and I. Ben-Itzhak, *Phys. Rev. A*, 2020, **101**, 013406.
- 165 M. Lundqvist, P. Baltzer, D. Edvardsson, L. Karlsson and B. Wannberg, *Phys. Rev. Lett.*, 1995, **75**, 1058–1061.
- 166 M. Lundqvist, D. Edvardsson, P. Baltzer and B. Wannberg, *J. Phys. B At. Mol. Opt. Phys.*, 1996, **29**, 1489–1499.
- 167 M. Lundqvist, D. Edvardsson, P. Baltzer, M. Larsson and B. Wannberg, *J. Phys. B At. Mol. Opt. Phys.*, 1996, **29**, 499–514.
- 168 C. Cheng, Z. L. Streeter, A. J. Howard, M. Spanner, R. R. Lucchese, C. W. McCurdy, T. Weinacht, P. H. Bucksbaum and R. Forbes, Strong Field Ionization of Water II: Electronic and Nuclear Dynamics En Route to Double Ionization, <http://arxiv.org/abs/2104.05869>, (accessed 19 April 2021).
- 169 E. Wang, X. Shan, L. Chen, T. Pfeifer, X. Chen, X. Ren and A. Dorn, *J. Phys. Chem. A*, 2020, **124**, 2785–2791.
- 170 M. Alagia, M. Boustimi, B. G. Brunetti, P. Candori, S. Falcinelli, R. Richter, S. Stranges and F. Vecchiocattivi, *J. Chem. Phys.*, 2002, **117**, 1098–1102.
- 171 M. Alagia, B. G. Brunetti, P. Candori, S. Falcinelli, M. M. Teixidor, F. Pirani, R. Richter, S. Stranges and F. Vecchiocattivi, *J. Chem. Phys.*, 2004, **120**, 6980–6984.
- 172 M. Alagia, B. G. Brunetti, P. Candori, S. Falcinelli, M. Moix Teixidor, F. Pirani, R. Richter, S. Stranges and F. Vecchiocattivi, *J. Chem. Phys.*, 2006, **124**, 204318.
- 173 M. Alagia, F. Biondini, B. G. Brunetti, P. Candori, S. Falcinelli, M. Moix Teixidor, F. Pirani, R. Richter, S. Stranges and F. Vecchiocattivi, *J. Chem. Phys.*, 2004, **121**, 10508–10512.
- 174 P. Bolognesi, J. M. Randazzo, G. Turri, J. E. Mathis, C. Penson, L. U. Ancarani and L. Avaldi, *J. Phys. B At. Mol. Opt. Phys.*, 2021, **54**, 034002.
- 175 M. Alagia, P. Candori, S. Falcinelli, M. Lavollée, F. Pirani, R. Richter, S. Stranges and F. Vecchiocattivi, *J. Phys. Chem. A*, 2009, **113**, 14755–14759.

- 176 M. Alagia, P. Candori, S. Falcinelli, M. Lavollée, F. Pirani, R. Richter, S. Stranges and F. Vecchiocattivi, *Phys. Chem. Chem. Phys.*, 2010, **12**, 5389–5395.
- 177 M. Alagia, P. Candori, S. Falcinelli, M. Lavollée, F. Pirani, R. Richter, S. Stranges and F. Vecchiocattivi, *Chem. Phys. Lett.*, 2006, **432**, 398–402.
- 178 M. Alagia, P. Candori, S. Falcinelli, M. Lavollée, F. Pirani, R. Richter, S. Stranges and F. Vecchiocattivi, *J. Chem. Phys.*, 2007, **126**, 201101.
- 179 M. Alagia, P. Candori, S. Falcinelli, M. S. P. Mundim, F. Pirani, R. Richter, M. Rosi, S. Stranges and F. Vecchiocattivi, *J. Chem. Phys.*, 2011, **135**, 144304.
- 180 M. Alagia, P. Candori, S. Falcinelli, F. Pirani, M. S. P. Mundim, R. Richter, M. Rosi, S. Stranges and F. Vecchiocattivi, *Phys. Chem. Chem. Phys.*, 2011, **13**, 8245–8250.
- 181 S. Falcinelli, M. Alagia, J. M. Farrar, K. S. Kalogerakis, F. Pirani, R. Richter, L. Schio, S. Stranges, M. Rosi and F. Vecchiocattivi, *J. Chem. Phys.*, 2016, **145**, 114308.
- 182 M. Alagia, C. Callegari, P. Candori, S. Falcinelli, F. Pirani, R. Richter, S. Stranges and F. Vecchiocattivi, *J. Chem. Phys.*, 2012, **136**, 204302.
- 183 S. Falcinelli, F. Vecchiocattivi, M. Alagia, L. Schio, R. Richter, S. Stranges, D. Catone, M. S. Arruda, L. A. V. Mendes, F. Palazzetti, V. Aquilanti and F. Pirani, *J. Chem. Phys.*, 2018, **148**, 114302.
- 184 S. Falcinelli, M. Rosi, F. Pirani, D. Bassi, M. Alagia, L. Schio, R. Richter, S. Stranges, N. Balucani, V. Lorent and F. Vecchiocattivi, *Front. Chem.*, 2019, **7**, 621.
- 185 S. Falcinelli, F. Vecchiocattivi, F. Pirani, M. Alagia, L. Schio, R. Richter, S. Stranges, V. Zhaunerchyk, N. Balucani and M. Rosi, *ACS Earth Space Chem.*, 2019, **3**, 1862–1872.
- 186 C. Wu, Y. Yang, Z. Wu, B. Chen, H. Dong, X. Liu, Y. Deng, H. Liu, Y. Liu and Q. Gong, *Phys. Chem. Chem. Phys.*, 2011, **13**, 18398.
- 187 J. Ullrich, R. Moshhammer, A. Dorn, R. Dörner, L. P. H. Schmidt and H. Schmidt-Böcking, *Reports Prog. Phys.*, 2003, **66**, 1463–1545.
- 188 Y. Zhang, B. Ren, C.-L. Yang, L. Wei, B. Wang, J. Han, W. Yu, Y. Qi, Y. Zou, L. Chen,

- E. Wang and B. Wei, *Commun. Chem.*, 2020, **3**, 160.
- 189 E. Wang, X. Ren and A. Dorn, *Phys. Rev. Lett.*, 2021, **126**, 103402.
- 190 L. Wei, B. Ren, Y. Zhang, J. Wang, B. Wang, J. Han, W. Yu, Y. Zou, L. Chen and B. Wei, *Phys. Rev. A*, 2021, **103**, 012810.
- 191 E. Wang, M. Gong, Z. Shen, X. Shan, X. Ren, A. Dorn and X. Chen, *J. Chem. Phys.*, 2018, **149**, 204301.
- 192 K. A. Larsen, T. N. Rescigno, Z. L. Streeter, W. Iskandar, S. Heck, A. Gatton, E. G. Champenois, T. Severt, R. Strom, B. Jochim, D. Reedy, D. Call, R. Moshhammer, R. Dörner, A. L. Landers, J. B. Williams, C. W. Mccurdy, R. R. Lucchese, I. Ben-Itzhak, D. S. Slaughter and T. Weber, *J. Phys. B At. Mol. Opt. Phys.*, 2020, **53**, 244003.
- 193 A. Yamada, H. Fukuzawa, K. Motomura, X.-J. Liu, L. Foucar, M. Kurka, M. Okunishi, K. Ueda, N. Saito, H. Iwayama, K. Nagaya, A. Sugishima, H. Murakami, M. Yao, A. Rudenko, K. U. Kühnel, J. Ullrich, R. Feifel, A. Czasch, R. Dörner, M. Nagasono, A. Higashiya, M. Yabashi, T. Ishikawa, H. Ohashi, H. Kimura and T. Togashi, *J. Chem. Phys.*, 2010, **132**, 204305.
- 194 Y. Zhang, L. Wei, C. L. Yang, W. Yu, B. Wang, B. Yan, Y. Zou, L. Chen and B. Wei, *Phys. Rev. A*, 2019, **100**, 052706.
- 195 H. Yuan, S. Xu, T. Li, Y. Liu, D. Qian, D. Guo, X. Zhu and X. Ma, *Phys. Rev. A*, 2020, **102**, 062808.
- 196 Z. Herman, *Int. J. Mass Spectrom.*, 2001, **212**, 413–443.
- 197 W. B. Maier, *J. Chem. Phys.*, 1974, **60**, 3588–3598.
- 198 W. B. Maier and B. Stewart, *J. Chem. Phys.*, 1978, **68**, 4228–4232.
- 199 R. K. Janev and H. Winter, *Phys. Rep.*, 1985, **117**, 265–387.
- 200 J. H. Agee, J. B. Wilcox, L. E. Abbey and T. F. Moran, *Chem. Phys.*, 1981, **61**, 171–179.
- 201 C. S. Jensen, J. A. Wyer, J. Houmøller, P. Hvelplund and S. B. Nielsen, *Phys. Chem. Chem. Phys.*, 2011, **13**, 18373–18378.

- 202 S. Bari, P. Sobocinski, J. Postma, F. Alvarado, R. Hoekstra, V. Bernigaud, B. Manil, J. Rangama, B. Huber and T. Schlathölter, *J. Chem. Phys.*, 2008, **128**, 074306.
- 203 A. Ehbrecht, N. Mustafa, C. Ottinger and Z. Herman, *J. Chem. Phys.*, 1996, **105**, 9833–9846.
- 204 S. D. Price, M. Manning and S. R. Leone, *J. Am. Chem. Soc.*, 1994, **116**, 8673–8680.
- 205 J. Roithová, J. Žabka, J. Hrušák, R. Thissen and Z. Herman, *J. Phys. Chem. A*, 2003, **107**, 7347–7354.
- 206 J. Roithová, J. Žabka, Z. Herman, R. Thissen, D. Schröder and H. Schwarz, *J. Phys. Chem. A*, 2006, **110**, 6447–6453.
- 207 Z. Herman, *Int. J. Mass Spectrom.*, 2015, **378**, 113–126.
- 208 L. Mrázek, J. Žabka, Z. Dolejšek, J. Hrušák and Z. Herman, *J. Phys. Chem. A*, 2000, **104**, 7294–7303.
- 209 N. Lambert, N. Kaltsoyannis, S. D. Price, J. Žabka and Z. Herman, *J. Phys. Chem. A*, 2006, **110**, 2898–2905.
- 210 J. Žabka, C. L. Ricketts, D. Schröder, J. Roithová, H. Schwarz, R. Thissen, O. Dutuit, S. D. Price and Z. Herman, *J. Phys. Chem. A*, 2010, **114**, 6463–6471.
- 211 P. Tosi, *Chem. Rev.*, 1992, **92**, 1667–1684.
- 212 J. Roithová, D. Schröder, P. Gruene, T. Weiske and H. Schwarz, *J. Phys. Chem. A*, 2006, **110**, 2970–2978.
- 213 J. Roithová, R. Thissen, J. Žabka, P. Franceschi, O. Dutuit and Z. Herman, *Int. J. Mass Spectrom.*, 2003, **228**, 487–495.
- 214 P. Franceschi, R. Thissen, J. Žabka, J. Roithová, Z. Herman and O. Dutuit, *Int. J. Mass Spectrom.*, 2003, **228**, 507–516.
- 215 L. G. Parke, C. S. Hinton and P. B. Armentrout, *J. Phys. Chem. A*, 2008, **112**, 10469–10480.
- 216 N. G. Adams and D. Smith, *Int. J. Mass Spectrom. Ion Phys.*, 1976, **21**, 349–359.

- 217 N. G. Adams and D. Smith, *Int. J. Mass Spectrom. Ion Phys.*, 1980, **35**, 335–342.
- 218 N. G. Adams, D. Smith and D. Grief, *J. Phys. B At. Mol. Phys.*, 1979, **12**, 791–800.
- 219 H. Störi, E. Alge, H. Villinger, F. Egger and W. Lindinger, *Int. J. Mass Spectrom. Ion Phys.*, 1979, **30**, 263–270.
- 220 G. Dupeyrat, J. B. Marquette, B. R. Rowe and C. Rebrion, *Int. J. Mass Spectrom. Ion Process.*, 1991, **103**, 149–156.
- 221 V. Blagojevic, S. Petrie and D. K. Bohme, *Int. J. Mass Spectrom.*, 2004, **233**, 33–37.
- 222 B. K. Chatterjee and R. Johnsen, *J. Chem. Phys.*, 1989, **91**, 1378–1379.
- 223 R. Plašil, A. Kovalenko, T. D. Tran, S. Rednyk, P. Dohnal, Š. Roučka and J. Glosík, *J. Phys. Conf. Ser.*, 2020, **1412**, 122007.

Chapter 2: Experimental Methods and Data Analysis

This chapter provides a detailed description of the position-sensitive coincidence time-of-flight mass spectrometry (PSCO-MS) apparatus that was used to carry out the experiments reported in this thesis. Following the physical description of the apparatus, this chapter then describes how the raw data is processed to give insight into dication-neutral reactivity using scattering diagrams and kinetic energy release histograms. The PSCO-MS apparatus has been specifically designed to study dication-neutral reactions that produce pairs of monocations, detecting them, in coincidence, with a position-sensitive detector. As well as the identity of the products, position-sensitive detection allows for the determination of the velocity vectors of the product ions. These velocity vectors can be used to determine reaction dynamics as will be explained in this chapter. The PSCO-MS apparatus has been described in detail in the literature.¹⁻³

2.1 Overview

Bimolecular reactions of dications with neutral species often generate pairs of monocations; the PSCO-MS apparatus detects these pairs of ions in coincidence. A schematic of the experimental apparatus is shown in Figure 2.1. Briefly, a pulsed beam of dications is produced and directed into the field-free source region of a time-of-flight mass spectrometer (TOF-MS). In the TOF-MS source region, the dications interact with an effusive jet of the neutral reactant species. Subsequent application of an extraction voltage to this source region allows the TOF-MS to detect the cation pairs generated in the dication-neutral interactions. The detection of these ions involves recording their time of flight and arrival position at a large microchannel-plate detector. The raw data consists of a list of flight times and arrival positions of the ions detected in pairs. From the time of flight data two-dimensional mass spectra are prepared, revealing various reactive channels. The positional data accompanying the ionic detections can be processed to reveal the relative motion of the products of each reactive event, providing a detailed event by event insight into the mechanisms of each reactive channel.³

Cations are formed in the ion source region before being extracted and focussed into the hemispherical energy analyser (HEA). The HEA energy-selects the ions before the ions are periodically swept across an aperture, dividing the continuous beam into packets of ions: ion ‘pulses’. A set of accelerating and focussing lenses then guide the monoenergetic ions into a

commercial velocity filter, that effectively selects the ions based on their m/z ratios. The ions are then decelerated to <10 eV before entering the interaction region where they can react with the desired neutral species. The unreacted dications, and the charged products from any reactions, are detected in coincidence by a TOF-MS.

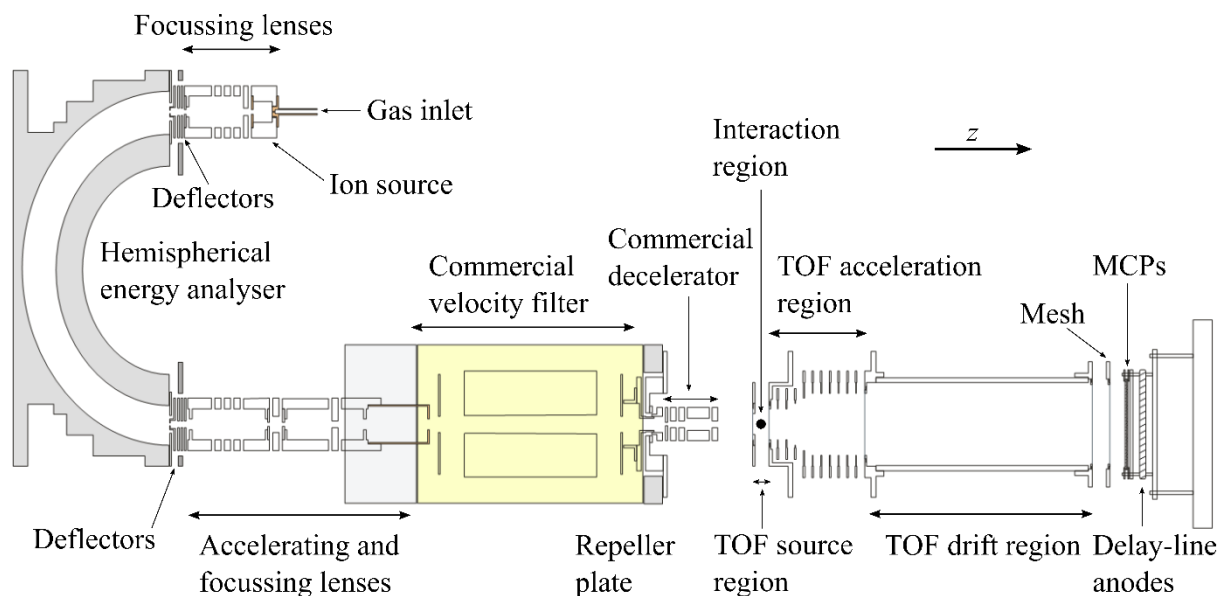


Figure 2.1 Schematic representation of the PSCO-MS apparatus. Reproduced from reference.¹

The PSCO-MS setup described above is contained in a series of stainless-steel chambers in which high-vacuum conditions ($\sim 10^{-8}$ Torr) are maintained to minimise collisions of the dications, or product ions, with background gases. Such low pressures are realised by three diffusion pumps and a turbomolecular pump that are all backed by rotary pumps. The following sections provide a detailed description of each stage of the PSCO-MS experiment including the data processing and analysis.

2.2 PSCO-MS apparatus

2.2.1 Ion formation

In the PSCO-MS apparatus, the ions are formed by electron ionization (EI). A filament operating at a current of ~ 4 A ejects electrons by the process of thermionic emission. A tungsten or yttria-coated tungsten filament is typically used. The electron energy is typically between 100 eV – 200 eV, set to maximise the cross section for the production of the desired dication. In this work all the dications were produced using an electron energy of 100 eV. These electrons

are accelerated into the ion source region, the inside of the ‘source block’, to collide with the chosen precursor gas. The precursor gas is effusively admitted to the ion source region *via* a needle valve. The pressure inside the chamber that houses the ion source is kept below $\sim 2 \times 10^{-6}$ Torr, however the pressure inside the source block is likely to be at least two orders of magnitude higher. The precursors for the Ar^{2+} , S^{2+} , and $\text{CH}_2\text{CN}^{2+}$ dications used in the experiments described in this thesis were Ar (BOC, 99.998 %), H_2S (CKgas, 99.5 %), and CH_3CN (BDH, >99.9 %, purified by the freeze-pump-thaw method using liquid nitrogen) respectively.

A potential, V_{sb} , is applied to the source block that defines the ‘rest potential’ of the ions that are formed. The rest potential determines the kinetic energy that the ions have as they ultimately enter the interaction region and, therefore, the collision energy of the experiment. By manipulating V_{sb} , the collision energy of the experiment can be tuned. V_{sb} typically has values between 2 V – 6 V.

2.2.1.1 Ions produced by electron ionization

EI is a simple and robust method of making ions. The obvious alternative, photoionization with a laser, can offer more control of the dication states accessed but is not appropriate for the PSCO-MS setup. For example, lasers are expensive and coincidence experiments require high repetition rates, which are challenging. A disadvantage of EI is that ions are formed in a wide range of electronic and vibrational states, and molecular dications can be formed in more than one conformation. Such a broad population is undesirable as it increases the spread of exoergicities observed from reactions. However, collisions in the high-pressure ion source can result in vibrational and electronic relaxation. Additionally, it takes on the order of 100s of μs for an ion to reach the interaction region after being created in the ion source. This flight time is sufficiently long enough that radiative electronic relaxation can occur, reducing the amount of excitation that a dication has when it arrives in the interaction region. Furthermore, ions in states that are unstable to dissociation with lifetimes of less than $\sim 100 \mu\text{s}$ will dissociate before reaching the interaction region. Despite this relaxation, the reactant dication is usually present in more than one electronic state with potentially non-thermal internal energy when it arrives at the interaction region.

2.2.2 Extraction and focussing

The ions formed in the ion source region are extracted and focussed by a series of electrostatic lenses, see Figure 2.2. The first lens extracts the cations with an applied voltage of -250 V. A series of three lenses (E1, E2 and E3) then guide the ions into an accelerating lens. These three lenses have applied potentials between -10 V and +10 V. The acceleration lens is typically set in the vicinity of 0 V. The ions are then passed through a set of vertical deflectors and a set of horizontal deflectors which are adjusted to align the trajectory of the ions with the entrance to the hemispherical energy analyser.

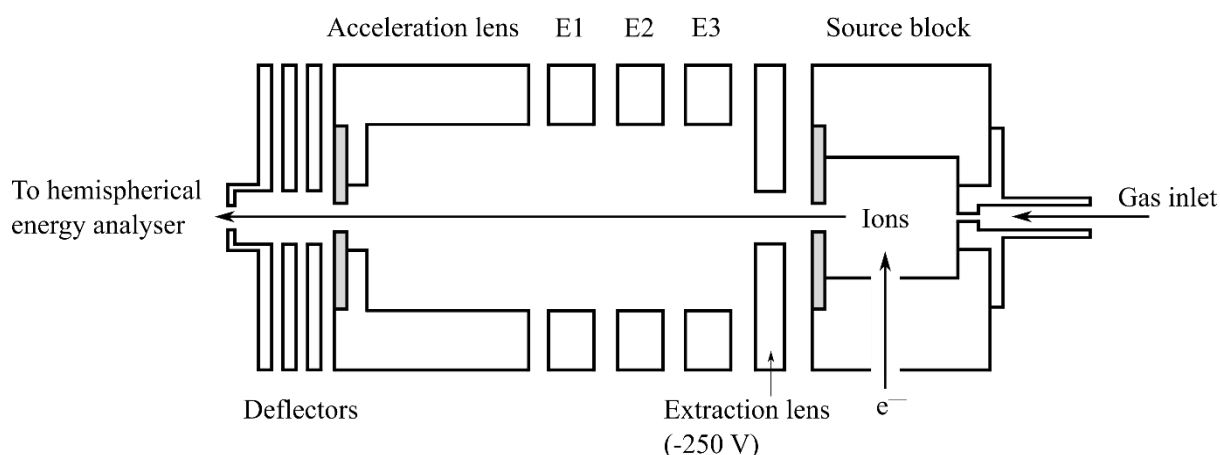


Figure 2.2: Schematic of the ion source, extraction lenses and deflectors before the hemispherical energy analyser.

2.2.3 Energy selection

Ions in the ion source region are formed with a range of translational energies centred around the ‘rest potential’ (V_{sb}). In order to improve the energy resolution of our data, and allow the formation of well-defined ion pulses, we need to select ions with as small of a range of translational energies as practical. After the focussing lenses and deflectors, the ions pass around a hemispherical energy analyser (HEA), that filters the ions, only allowing the transmission of ions in a specific kinetic energy range. A schematic of the hemispherical energy analyser in the PSCO-MS apparatus is shown in Figure 2.3. The analyser is comprised of an outer hemisphere H2 (radius, $r_2 = 170$ mm) and an inner hemisphere H1 (radius, $r_1 = 130$ mm). The mean radius of the analyser, r_0 , the path an ion will take in the middle of the two hemispheres is 150 mm, therefore the average pathlength an ion takes to travel through the hemispherical energy analyser is 471 mm.

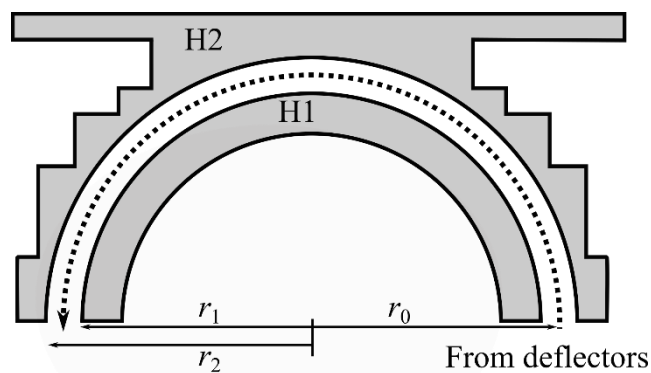


Figure 2.3: Schematic of the hemispherical energy analyser.

The pass energy, E_0 , is defined as the translational energy that an ion must have in order to travel through the hemispherical energy analyser. The pass energy is determined by the potentials applied to the outer and inner hemispheres. There is an intrinsic spread in the kinetic energy of the ions which are transmitted, ΔE . The rate of ion transmission and ΔE must be balanced to achieve practical ion fluxes. The energy resolution of the dication beam is defined as the ratio between the full width at half maximum (FWHM) of the energy distribution of the dications ($\Delta E_{1/2}$) and E_0 : $\Delta E_{1/2} / E_0$. Generally, the PSCO-MS apparatus is run with an E_0 of ~ 4 V to give a good energy resolution whilst maintaining enough ion transmission. This potential translates to an energy of ~ 8 eV for a dication. The theoretical value of $\Delta E_{1/2} / E_0$ of the HEA is ~ 1 %, which is defined by its dimensions and assumes that the angular acceptance for incoming ions is small. In our case, we increase the angular acceptance of the ions to enhance transmission, resulting in an increased value of $\Delta E_{1/2} / E_0$. Due to the angular spread of the ion beam, the dication energy resolution achieved by the HEA is ~ 4 %.

The energy distribution of the ions in the beam is determined by retarding field analysis, for example shown in Figure 2.4. The measured ion flux is plotted against an applied positive ‘retarding’ voltage (Figure 1.4a). Therefore, the decrease in the number of ions between two voltages is effectively the number of ions with $E_T = qV$, where q is the charge of the ion and V is the voltage. This is more easily interpreted with a normalised ion loss rate, shown in Figure 2.4b. Figure 2.4b shows that the mode of the energy distribution of the ions is ~ 4.4 V, which translates to 8.8 eV, and has a FWHM of ~ 0.16 V, which translates to 0.32 eV. Therefore, $\Delta E_{1/2} / E_0 = 0.037$, equivalent to ~ 4 %.

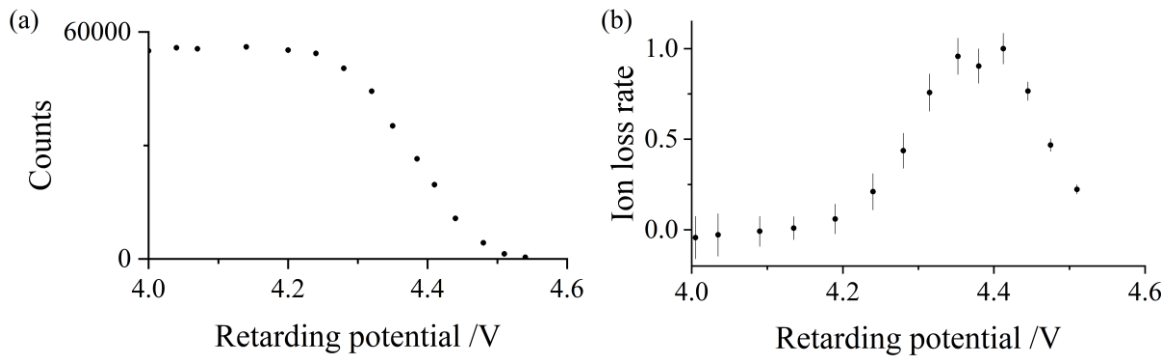


Figure 2.4: Retarding field analysis. a) Graph of dication counts recorded depending on retarding voltage applied. b) Normalised loss rate of the ions depending on retarding voltage. The error bars represent two standard deviations of the counts.

2.2.4 Pulsing

The continuous beam of ions exiting the HEA then passes through another set of horizontal and vertical deflectors. The vertical deflectors tune the trajectory of the beam whereas the horizontal deflectors' primary function is to 'pulse' the beam, dividing it into well defined 'packets' of ions. Voltages which follow oscillating triangular waveforms are applied to each of the horizontal deflectors. The oscillating waveforms are 180° out of phase with each other. The application of these oscillating voltages causes the ion beam to oscillate around the central aperture of the next set of lenses. Therefore, the ions are only periodically able to pass through the lenses, so the ions are temporally separated into pulses. The amplitude and frequency of the waveforms determines the length of the ion pulse and separation between the pulses respectively. Typically, the waveforms involve amplitudes of ~ 10 V and frequencies of ~ 30 kHz. The oscillating waveforms must be perfectly 180° out of phase otherwise asymmetrical ion pulses will be formed. The reasons for pulsing will be discussed in more detail in section 2.2.9.1.

2.2.5 Acceleration and focussing lenses

After the ion beam is pulsed by the deflectors at the exit of the HEA, the ion pulses are passed through a series of lenses which have potentials optimised to accelerate and focus the ions. By manipulating the potentials applied to these lenses, the angular spread (shape) and transmission of the beam can be optimised. After this section of lenses, shown in Figure 2.5, the ions pass through a velocity filter.

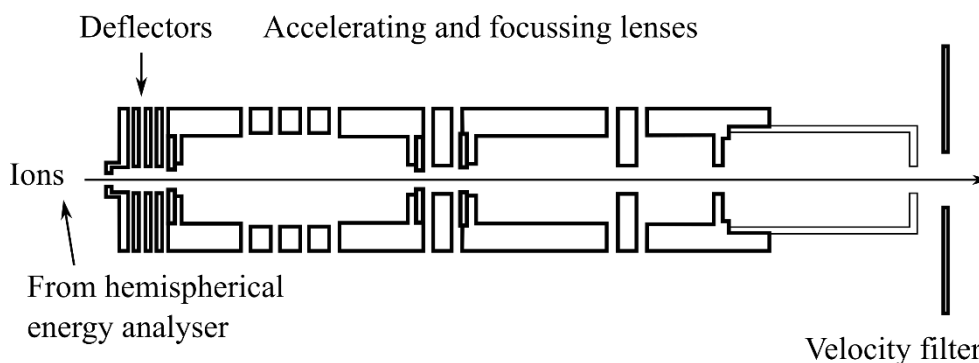


Figure 2.5: Schematic showing the deflectors, accelerating lenses, and focussing lenses between the hemispherical energy analyser and the velocity filter.

2.2.6 Velocity selection

After the acceleration and focussing lenses the ions are energy selected, however, the ion source produces a range of different ions which must be filtered to allow only the transmission of the desired reactant ions. For example, EI of the atomic precursor Ar forms Ar^+ , Ar^{2+} and Ar^{3+} ions. Because the different ions have equal translational energies, filtering by the velocity is the same as filtering by a specific m/z (remembering $E_t = \frac{1}{2}mv^2$).

Velocity selection is achieved with a commercial velocity filter. This filter consists of an electro-magnet and a pair of electrostatic deflection plates. The components generate perpendicular magnetic and electric fields. The force exerted on an ion moving through a magnetic field, F_B , is equal to the magnitude of the field multiplied by the charge of the particle and the velocity of the ion, $F_B = Bqv$. The force exerted on an ion in an electric field, F_E , is determined by the magnitude of the electric field multiplied by the charge of the ion, $F_E = Eq$. The electric and magnetic fields in the velocity filter are set up to act in opposing directions. In order for an ion to traverse the velocity filter unperturbed, F_E must be equal to F_B , therefore, $Bv = E$. The magnetic field strength, B , is kept constant, thus changing the electric field strength E determines the velocity v with which an ion will pass unperturbed through the filter.

The velocity filter selects for m/z (and not m), therefore, ions with the same m/z ratio cannot be separated, for example, S^{2+} and O^+ ($m/z = 16$). Obviously, reactions involving monocations cannot produce pairs of product ions, so will generally not be detected by coincidence experiments such as the PSCO-MS apparatus that detect pairs of cations. However, in some cases monocations can lead to the detection of errant coincidences, explained in Section

2.3.2. These errant coincidences can generally be easily distinguished from those resulting from those resulting from real dication + neutral reactions, however, in some cases the events resulting from the reactions of monocations can obscure real events the coincidence spectra.

2.2.7 Deceleration

After the velocity filter, the pulses of ions are decelerated to the desired collision energy using a commercial decelerator. Typical collision energies are <10 eV in the laboratory frame. These collision energies are employed because dication-neutral reactions have been shown to have higher cross sections for bond-forming reactions at lower collision energies.⁴ A schematic of the decelerator is shown in Figure 2.6.

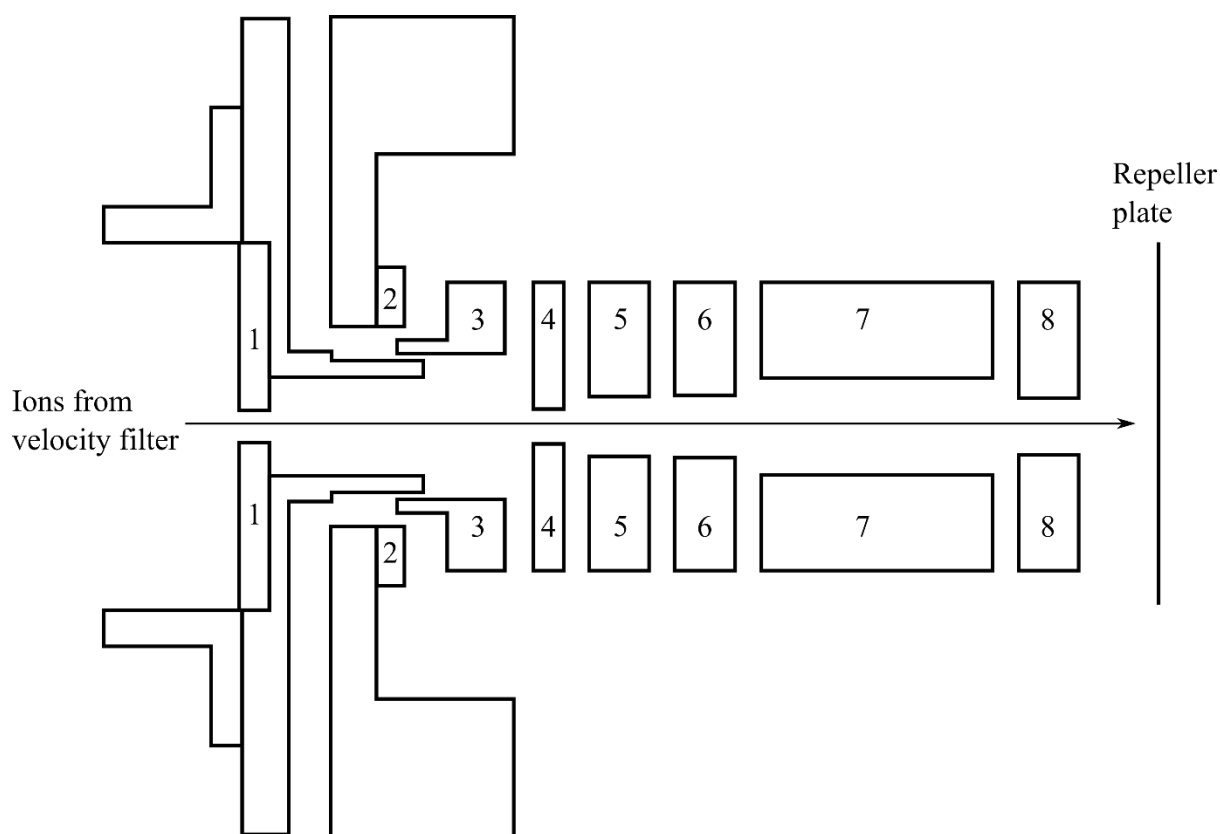


Figure 2.6: Schematic of the commercial decelerator.

The first two lenses, 1 and 2, are held at the beam potential as it exits the velocity filter, -250 V. Lenses 3, 4 and 5 decelerate the ions, with typical voltages of -250 V, -250 V, and -150 V respectively. The final lenses the ions pass through in the decelerator, 6, 7, and 8 are operated as an Einzel lens. Lenses 6 and 8 are held at close to 0 V, whilst 7 is changed to result in optimal focussing. Lens 7 typically has a potential of 5 V – 20 V applied.

2.2.8 Interaction region

Following deceleration, the reactant dications pass through a small grid-covered aperture in the repeller plate, and then enter the source region of the TOF-MS, which is also the ‘interaction region’. In the interaction region, the dications can interact with the neutral species. The neutral species is admitted to the interaction region as an effusive jet that is perpendicular to the dication beam, *via* a leak valve. The neutral gases used for the experiments outlined in this thesis were O₂ (BOC, >99.5 %), CO (Aldrich, >99.0 %), H₂ (BOC, >99.995 %), N₂ (BOC, >99.998 %), and Ar (BOC, 99.998 %). Single-collision conditions⁵ are achieved by employing a low pressure of the neutral gas. Hence, most dications do not undergo a collision, whilst only a small percentage experience one collision. Such a pressure regime ensures that no reactivity due to successive collisions with two neutral species influences the dication reactivity we observe.

The interaction region is initially kept field free to ensure the dication-neutral interactions occur at a constant and fixed collision energy. When the dication pulse reaches the centre of the interaction region, a positive potential is applied to the repeller plate, which pushes any positive species (unreacted dications or product dications / monocations) into the acceleration and drift regions of the MS. At the end of the MS recording cycle (the duration of which is adjusted to include the heaviest possible products from the reactions of the specific reactants involved) the repeller plate is set back to 0 V, so the region is returned to its field-free state, ready for the next pulse of dications.

2.2.9 TOF-MS

As discussed above, the interaction region is also the source region of the TOF-MS of the apparatus. The TOF-MS consists of three regions: the source region, the acceleration region, and the field-free drift region. A schematic of the TOF-MS is shown in Figure 2.7. As the dication pulse reaches the centre of the source region, a positive potential is applied to the repeller plate, creating a potential gradient that accelerates the ions towards the acceleration region. The electronic trigger pulse sent to the pulser that applies the voltage to the source region also starts the ion timing circuitry, to which the signals from the detector provide stop pulses, as discussed below. The guard rings in the acceleration region ensure the ions experience a uniform electric field. After the acceleration region, the ions pass through the drift region. At the end of the drift region the ions are accelerated further and impinge on the detector, resulting in detection.

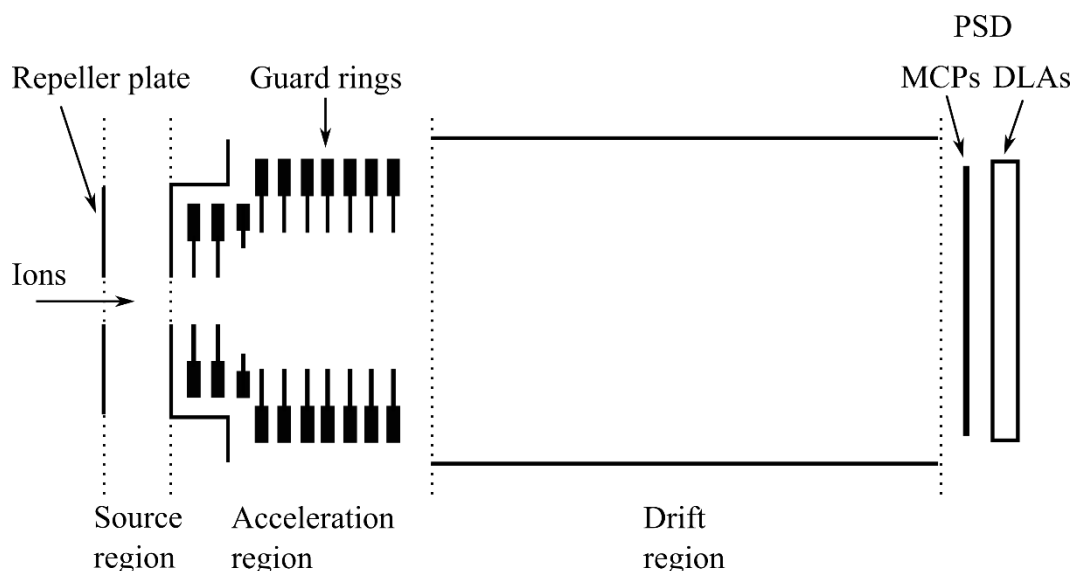


Figure 2.7: Schematic of the TOF-MS (not to scale).

The fundamental principle of TOF-MS is that ions with different m/z ratios take different lengths of time to traverse a field-free distance when they are accelerated to the same kinetic energy.⁶⁻⁸ Therefore the m/z of an ion can be determined by its flight time over a known distance.

The first TOF-MS machines used a single acceleration region: the source region, and then a drift region. Thus, these early pieces of apparatus were called ‘single-field’ TOF-MS.⁶⁻⁸ In these early experiments, the ions at different points in the source region experienced different levels of acceleration and therefore were accelerated to different maximum velocities as they reached the start of the drift region. However, the spread in initial positions is compensated by the difference in acceleration that the ions in different initial positions experience. Ions formed further back, nearer the repeller plate, will experience more acceleration in the source region and therefore will have higher velocities when they reach the drift region. These ions ‘catch-up’ with the ions formed nearer the drift region, resulting in a single TOF for ions of the same m/z . When ions are formed in different positions in the source region but arrive at the detector at the same time, this is called ‘space-focussing’.

In 1955 Wiley and McLaren⁹ found that space-focussing could also be achieved by employing two distinct accelerating fields with magnitudes set in a specific ratio, termed a ‘two-field’ TOF-MS. In single-field TOF-MS, in order to achieve space-focussing conditions so that ions of the same m/z arrive at a single flight time, the lengths of the source and acceleration regions need to be precisely engineered. The focussing conditions of a single-field TOF-MS

are constrained by its geometry, and only a specific magnitude of the electric field can be used. In two-field TOF-MS the applied fields can be varied to achieve optimal focussing conditions. Therefore, in two-field TOF-MS, the dimensions are not as important as for single-field TOF-MS meaning that the two-field TOF-MS design is more versatile and practical.

Newtonian mechanics can be used to determine the flight time t for each MS region. The resulting equations show that the TOF of an ion is proportional to the square root of its m/z , shown in (2.1).

$$TOF = c\sqrt{m/z} \quad (2.1)$$

where c is a constant encompassing the dimensions of the TOF-MS as well as the magnitudes of the source and acceleration fields.

Both the single-field TOF-MS and the two-field TOF-MS proposed by Wiley and McLaren achieve ‘first-order’ space focusing conditions. First-order space focusing means that, to the first order, the spread in the TOF of ions with the same m/z ratio is independent of source position S from the centre of the source region ($S = 0$):

$$\left(\frac{d(TOF)}{dS}\right)_{S=0} = 0 \quad (2.2)$$

In 1993, Eland¹⁰ discovered that further improvements to TOF-MS space focussing were possible. If the geometry and magnitudes of the fields of the two acceleration regions in the two-field apparatus are constrained, it is possible that both the first and second order derivatives of the TOF of an ion relative to its initial source position become zero. This ‘second-order’ focussing results in an even smaller spread of TOFs for ions with the same m/z that have different initial source positions compared to first-order focussing. Moreover, second-order focussing conditions apply over a larger range of S , again increasing the versatility of the design. However, to achieve second-order focussing, longer acceleration regions are required to limit the use of impractical voltages.

The PSCO-MS apparatus employs two-field, second-order space focussing, with source, acceleration and drift lengths of 1.63 cm, 11 cm and 27.5 cm respectively.¹ The second-order space focussing specifically allows for a significantly smaller temporal distribution of the focussed reactant dications. When the repeller plate is operated with a voltage of 300 V, the accelerating voltage used is approximately –1900 V. These conditions typically result in parent

ion peaks in the mass spectrum with FWHMs of ~ 3 ns. The resultant TOF-MS source field, F , is typically ~ 200 V cm $^{-1}$ and is determined from the calibration in Section 2.4.1.1. Experiments can be run with varying TOF-MS source fields. The experiments in this thesis employed either high (183 V cm $^{-1}$) or low (28.5 V cm $^{-1}$) TOF-MS source fields. The lower source field experiments result in better energy resolution in the resulting PSCO-MS data because the ions travel in the drift region for longer and therefore their x and y velocities are determined from larger distances. However, in these low field spectra ions with high transverse (off-axis) velocities do not reach the detector, which can result in ions scattered with angles around 90° not being detected. To overcome the individual limitations of each of the high and low TOF-MS source fields, each dication-neutral system is often studied at both field values, allowing a more complete representation of the dynamics and energetics respectively.

2.2.9.1 Advantages of pulsing

The primary reason for the pulsing of the dication beam is to reduce background signal in the TOF spectra. As shown in Figure 2.8, the operation of a continuous dication beam results in a high level of background counts at TOFs shorter than the ion of interest. This high level of background counts results from ions which are in the acceleration and drift regions of the MS when the repeller plate is pulsed. The ions which are in the source region when the repeller is pulsed will be correctly accelerated to the same potential and will therefore have the same TOF as other ions of the same m/z . However, ions already in the acceleration and drift regions when the repeller is pulsed are not appropriately accelerated and arrive at the detector earlier than ions with the same m/z from the TOF-MS source when the repeller is pulsed. This effect would affect the pairs spectrum with false coincidences involving TOFs shorter than the reactant dication. Conversely, when the beam is pulsed, the packets of ions are finite in length and the repeller plate pulse is optimised to trigger only when the whole of the packet of ions is in the TOF-MS source region. The ions are therefore appropriately accelerated and focussed to form a sharp peak in the spectrum, resulting in a significant decrease in background counts with TOFs lower than the reactant dication. There will, of course, still be a small number of errant counts, discussed in Section 2.3.2, that are evenly distributed over all TOFs.

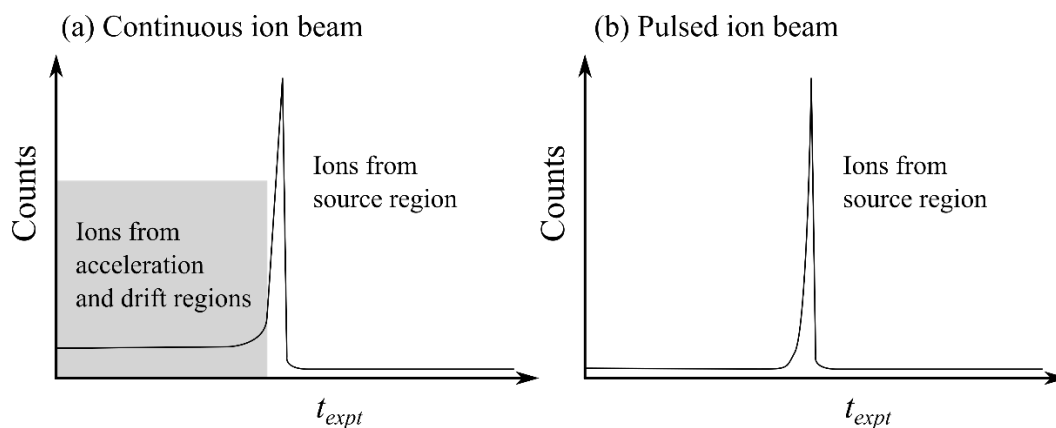


Figure 2.8: Schematic mass spectra recorded of a continuous ion beam (a) and a pulsed ion beam (b). When the ion beam is continuous, a high level of background counts are present at TOFs lower than the reactant ion due to ions from the acceleration and drift regions. Reproduced from reference.¹¹

During the data processing, it is assumed that interactions happen at a single point in the interaction region. Therefore, the more localised the interaction region is, the more accurate the resulting data processing. The FWHM of the temporal distribution (the width) of the ion pulses can be determined. For example, using the formula relating kinetic energy E_T and velocity v of a particle, $E_t = \frac{1}{2}mv^2$, where m is mass, an Ar^{2+} dication with $E_T \sim 10$ eV gives a velocity v of $\sim 0.7 \text{ cm } \mu\text{s}^{-1}$. The FWHM of the pulsed ion beam is generally $\sim 1.5 \mu\text{s}$, corresponding to a length of ~ 1 cm. Therefore, the interaction region is reduced in one dimension. This reduction in length results in the determination of more accurate product ion velocities and, subsequently, a better energy resolution.

If the amplitude or the frequency of the waveforms that pulse the beam (Section 2.2.4) is too large, the translational energy of the ions in the beam can be altered. When the ions do not have sufficient time to adjust to the changing voltages, when the rate of change of the deflector voltage is similar to the transit time of the lenses, the ion energies can be perturbed. To ensure that the kinetic energies of the ions remain unchanged, the TOF of the ions is carefully monitored when implementing the pulsing. Generally, the pulsing frequency is set to be as high as possible, to result in the temporal length of the pulse being as short as possible (~ 1 cm), whilst ensuring that the ions are not perturbed. Waveform frequencies of < 50 kHz are typically utilised for the pulsing in the PSCO-MS apparatus.

2.2.10 Detector

After traversing the TOF-MS, the ions are detected by a position-sensitive detector (PSD) mounted at the end of the drift region. The PSD is a commercial device (Roentdek), comprising a chevron-pair of microchannel plates (MCPs) located in front of a dual delay-line anode (DLA), shown in Figure 2.9.¹²⁻¹⁴ This setup coupling DLAs and MCPs typically gives maximum spatial resolutions with FWHM of $\sim 18 \mu\text{m}$.¹⁵

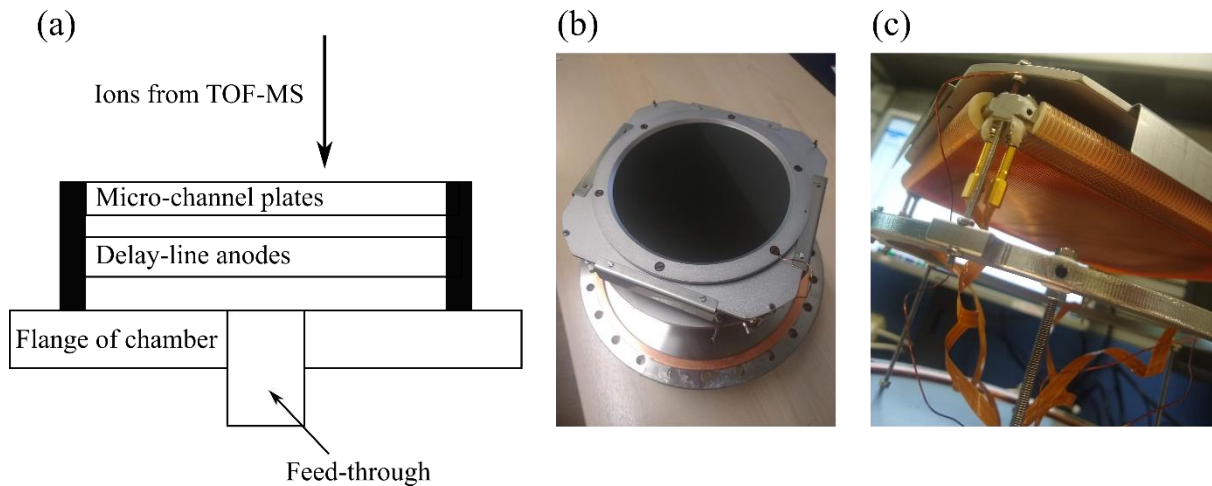


Figure 2.9: (a) Schematic of the detector, (b) picture of the detector from above, looking down on the MCPs, (c) picture of the detector from below, looking up at the DLAs.

MCPs consist of a plate with channels running through that are $\sim 10 \mu\text{m}$ in diameter. When an ion impinges on the front of the plate, a cascade of electrons is emitted from the other end of the channel which gives the timing signal for an ion arriving. To ensure that an ion hit causes a cascade of electrons, the ions are accelerated before they reach the PSD by applying a potential of approximately -2 kV to a grid before the MCP and to the front of the MCP. The rear of the MCP is connected to ground. The time between the start of the repeller plate pulse and the voltage distortion detected from the MCP gives the experimental TOF of an ion, $t_{\text{expt}}(i)$, where $i = 1$ or 2 for events where a pair of ions are detected in coincidence.

The electron cascade produced by the MCP then impinges on the DLA, which consists of two wires wound around a ceramic support, one in the x direction and one in the y direction, perpendicular to the axis of the TOF-MS. A potential of 550 V is applied to the DLAs to attract the electrons produced by the MCP. When the electrons impinge on the DLA, charge propagates along each direction of the x -oriented and y -oriented delay-lines. Each wire therefore generates

two signals, so the DLA generates four signals for each ion hit. These signals $\{t_{xa}(i), t_{xb}(i), t_{ya}(i), t_{yb}(i)\}$ are recorded as times relative to the start of the repeller plate pulse. The difference between these times can be used to determine where on the anode the pulse of electrons hit.

The time recorded from the MCP hit and the four times recorded from the DLA give a set of five distinct times for each ion hit. Therefore, the detection of a pair of product ions resulting from a dication + neutral reaction will result in ten times being recorded.

2.2.11 Electronics and signal processing

The signals from the MCPs and DLA are sent to a commercial (Roentdek ATR-19) constant fraction discriminator (CFD) that discriminates and amplifies each signal. Each of the CFD's five input channels has a threshold and electronic delays that need to be appropriately set to ensure optimal collection conditions: maximising the probability of detecting 'real' ions whilst rejecting electrical noise. The discriminated signal is then sent to a commercial (Roentdek TDC8HP) single-start multi-stop time-to-digital convertor (TDC).

The start signal to the TDC is given by the delayed trigger pulse sent to the repeller pulser. This trigger pulse starts a TOF window, any stop signals registered from the CFD in this time are transferred to a PC for further, rapid, online analysis. For an ion hit to be classed as real it must consist of 5 times (one from the MCP and four from the separate delay line channels) for each detected ion. Events that involve the detection of one ion after the repeller plate pulse are termed 'singles' and the TOF of each single is added to a 1D mass spectrum. Events where a pair of ions (with five times for each ion) are detected following the repeller plate pulse are termed 'pairs' and all ten times are subsequently stored in a list of pairs data to be analysed as described below. Higher order coincidences can also be recorded (for example triples where three ions are detected) but are not relevant when only considering dication-neutral interactions.

2.3 Coincidence processing

The raw data consists of lists of ten times for each coincidence event. The data is first plotted as a 'coincidence' spectrum. Then, after identifying the reaction and further processing, scattering diagrams can be produced to reveal dynamical information about each reaction channel. Kinetic energy releases can also be determined that give energetic information about a reaction.

2.3.1 Coincidence ‘pairs’ spectra

The first step of the analysis procedure is to plot the time-of-flight of each ion ($t_{\text{expt}}(1)$ and $t_{\text{expt}}(2)$) in a coincidence spectrum. A coincidence spectrum is a two-dimensional histogram, where $t_{\text{expt}}(1)$ is plotted on the x -axis and $t_{\text{expt}}(2)$ is plotted on the y -axis for each ion pair detected, as shown in Figure 2.10. Peaks in the coincidence spectrum readily identify bimolecular reaction channels that result in a pair of positively charged product ions. The group of events from each peak corresponding to a specific pair of ions (an individual reaction channel) can then be selected for further off-line analysis, as described in Section 2.4.

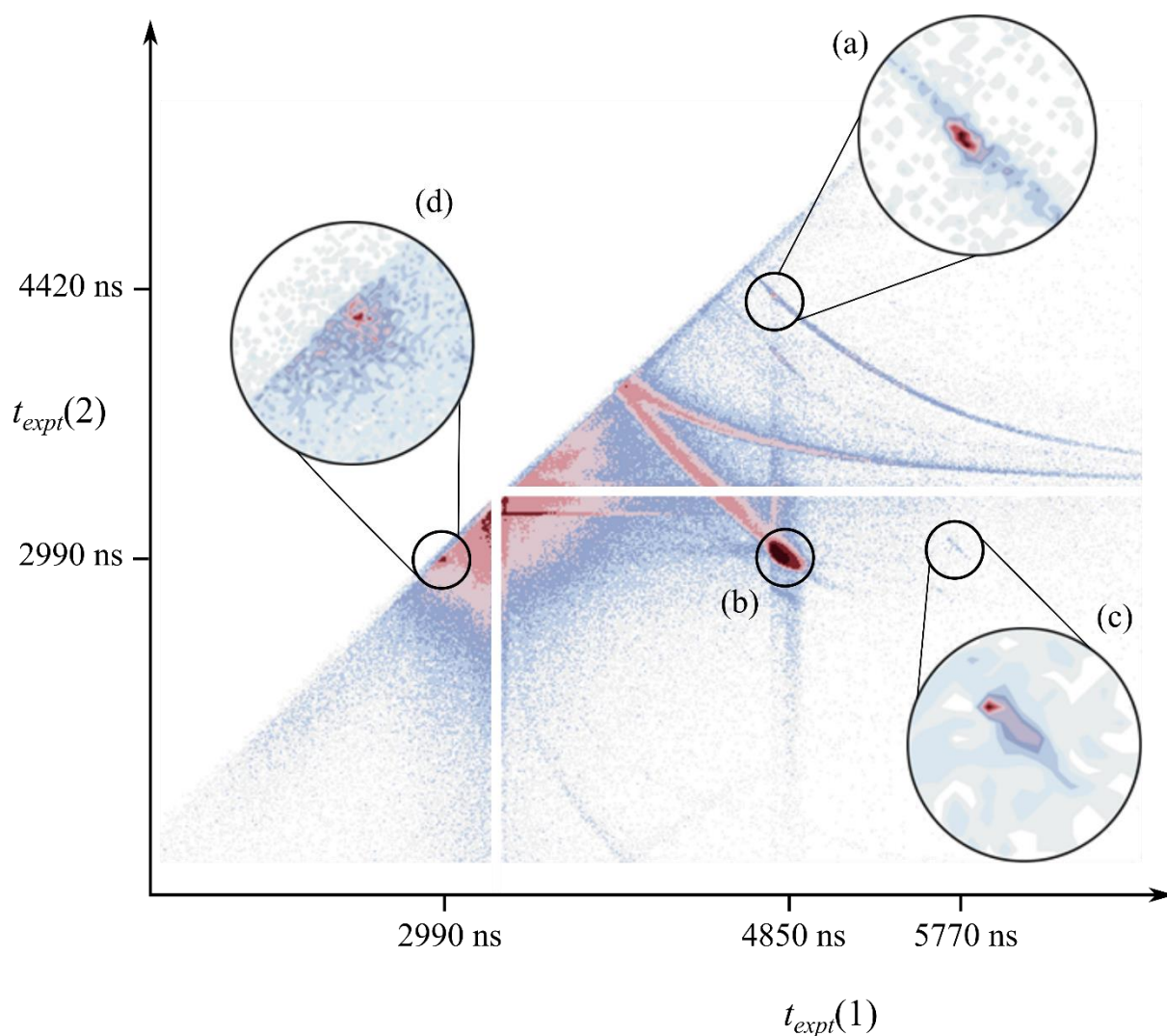


Figure 2.10: A coincidence spectrum recorded following the interactions of $\text{Ar}^{2+} + \text{O}_2$. Four peaks that correspond to pairs of product ions are labelled, (a) $\text{Ar}^+ + \text{O}_2^+$, (b) $\text{Ar}^+ + \text{O}^+$, (c) $\text{ArO}^+ + \text{O}^+$, and (d) $\text{O}^+ + \text{O}^+$. Magnifications of peaks (a), (c) and (d) are also shown. The exclusion zone is shown by the blank strip through the spectrum.

Figure 2.10 shows the coincidence spectrum collected following the interactions of Ar^{2+} with O_2 . Half of the coincidence spectrum is blank, simply because it is symmetrical; by convention ion 1 is heavier than ion 2, therefore, $t_{\text{expt}}(1) > t_{\text{expt}}(2)$.

The well-defined, intense peaks in the coincidence spectra arise from dication-neutral reactions occurring in the interaction region. These well-defined peaks are indicative of accurate second-order space focussing of the cations from the two-field set up described in Section 2.2.9. However, the peaks arising from reactions occurring in the interaction region are still bigger than perhaps would be expected, considering that the FWHM of a TOF for a single ion is typically ~ 3 ns. The peaks are lozenge shaped and their major axis is ‘extended’ due to the kinetic energy releases accompanying the reactions. The specific shape of the peak is due to the momentum sharing between the products: peaks resulting from two-body reactions should have gradients of -1, the same as peaks resulting from the detection of two monocations following the unimolecular dissociation of dications in PIPICO spectra.^{16,17}

Additionally, some reaction channels have long, curved tails such as peak (b) in Figure 2.10. These tails originate from dication-neutral reactions producing the same two product ions, but from reactions that occur in the acceleration region of the TOF-MS, rather than the interaction region. The neutral reactant is admitted to the apparatus as an effusive jet which travels through the interaction region. The neutral reactant will also be present in a low concentration throughout the apparatus, as a residual gas, including in the acceleration region. As dications enter the acceleration region they can react with neutral species that are present there. The subsequent products will not be appropriately focussed, and their TOFs will be different to the same product ions formed in the interaction region. The differing TOFs recorded from coincidences resulting from reactions happening in the acceleration region result in these pairs being plotted away from the main peak in the coincidence spectrum. The relative masses of the reactants and products determine the direction of the tail and the further from the interaction region that the dication-neutral reaction occurs, the further away from the original peak the event will appear in the coincidence spectrum. For example, for the reaction $\text{A}^{2+} + \text{BC} \rightarrow \text{A}^+ + \text{BC}^+$, if the reaction occurs in the acceleration region, then the A^+ product will have spent more time as A^{2+} and the BC^+ will have spent more time unaccelerated as BC compared to those products formed in the interaction region. The m/z of A^{2+} is, obviously, less than A^+ , so the A^+ will have experienced greater acceleration and therefore its flight-time will be shorter than that of an A^+ formed in the interaction region. Conversely, BC^+ formed in the acceleration

region will have experienced less acceleration than a BC^+ ion formed in the interaction region and will therefore have a longer flight-time. In the above scenario, if $m(A) > m(BC)$, since the heavier product ion is plotted on the x -axis, the tail would therefore curve to the high t_2 , low t_1 direction (top-left) from the main peak, as seen in Figure 2.10 (b). Conversely, if $m(A) < m(BC)$, a tail would be formed to the low t_2 , high t_1 direction (bottom-right) from the main peak. Given that these tails result from reactions happening in the acceleration region, where the dications have increased translational energy, these reactions are also occurring at a significantly higher collision energy than those in the interaction region. Therefore, it follows that the intensity of the tails is convolved with the CM collision energy dependence of the reaction cross-section.

Sometimes, peaks are observed that do not have any accompanying tails, for example, peak (c) in Figure 2.10. Peaks without tails are indicative of reactions in which the cross-section sharply declines with increasing collision energy. These reactions cannot occur in the acceleration region because the CM collision energy is too high. As discussed above, the reaction cross-sections for dication-neutral reactions that involve the formation of new chemical bonds usually decrease strongly at collision energies higher than several eV. Therefore, peaks in the coincidence spectrum without tails are generally due to reactions that involve the formation of new chemical bonds.

2.3.2 Errant counts

Like any dataset, there are counts in coincidence spectra that do not result from reactions of the dication and neutral species of interest. These can be broadly defined as ‘false coincidences’, ‘background counts’ or ‘noise’ and are discussed in more detail here. All of these counts convolve the spectrum and make it appear more ‘noisy’.

Additional counts can also result from further reactions of the products formed in a dication + neutral reaction. For example, in the reaction $A^{2+} + BC \rightarrow A^+ + BC^+$, the A^+ product could react with another BC species, to form $A + BC^+$, giving the final ionic products as $BC^+ + BC^+$. These counts can only occur as a result of multiple collisions occurring, a higher likelihood of which there is occurring if the pressure of neutral species is too high. As discussed in section 2.2.8, single-collision conditions⁵ are maintained in the interaction region to prevent a significant number of events resulting from multiple collisions.

2.3.2.1 Background

Background counts are real ion coincidences that do not result from interactions between the dication and neutral species that we are interested in. For example, if the dication reacts with one of the background gases in the chamber, instead of the intended target species, to produce two monocations, the detection of the products would result in a count in the coincidence spectrum. Background counts can also result from impurities in the beam; for example, other dications and monocations that are not removed from the beam, especially, for example, a monocation with the same m/z ratio as the dication. Despite only having a charge of +1, monocations can result in the detection of coincidences. For example, if an unreacted monocation enters the drift tube, and then gains an electron from a neutral species, the nascent neutral species can have enough kinetic energy to be detected by the MCP. This newly generated neutral species can be detected in coincidence with the nascent monocation, thereby resulting in a count in the coincidence spectrum.¹¹ However, because these reactions do not occur in the interaction region the counts resulting from reactions with monocations usually only contribute to diffuse tail structures in coincidence spectra. The counts arising from monocation reactions can therefore generally be easily distinguished from structures resulting from the reaction channels of interest.

2.3.2.2 Noise

Noise does not result from a real ion signal, but from another source such as electrical noise, or cosmic radiation. An errant count can therefore be recorded resulting from the detection of two noise events or a noise event coupled with the detection of a single ion, most likely the dication. The effects of noise are minimised by ensuring the apparatus is well grounded and the electrical signals are well shielded. Furthermore, the signal to noise ratio for real ions from the detector is high and the discrimination level of the CFD is correctly set.

2.3.2.3 False coincidences and the exclusion zone

A ‘false coincidence’ is a count in the coincidence spectrum that is not the result of two ions produced by the same reactive event. False coincidences are uncorrelated, arising from statistical effects, and are especially prevalent when there are high counts of a specific ion. False coincidences resulting from two abundant ions can give localised peaks in coincidence spectra much like you expect from real peaks, however, peaks arising from false coincidences are not lozenge shaped nor have discrete gradients that would be expected.^{1,18} Instead they appear as lines in the 2D spectra at the mass of the abundant ions. The operating conditions of

the PSCO-MS apparatus are set to reduce false coincidences and maximise real counts. Optimal conditions are obtained by the use of a high repetition rate and low dication flux. Therefore, most cycles will have no dications in them, however the probability of there being two dications in the same cycle is significantly diminished.

Despite the relatively low intensity of false coincidences, there is still an intense strip of false coincidences in the area of the TOF of the dication, resulting from unreacted dications. In spite of the relatively low dication intensity (there are on average ~ 0.1 dications per pulse), the unreacted dication signal vastly outweighs the signal from all product ions. Therefore, unreacted dications are likely to cause false coincidences by being detected in coincidence with another ion. The false coincidences in the region of the TOF of the dication have a significant intensity that would overwhelm the spectrum, therefore, an ‘exclusion zone’ is set up around the TOF of the unreacted dication, within which signals are not appended to the data. This exclusion zone is visible in the coincidence spectrum in Figure 2.10. The implementation of an exclusion zone does not result in the loss of many ‘real’ product ions and at the normal operating conditions, the number of remaining false coincidences in coincidence spectra are negligible. In some dication + neutral systems, the exclusion zone can be problematic if the m/z of the dication is similar to the m/z of one of the product ions, resulting in a partial obscuration of these product peaks. Background ions can also contribute to the detection of false coincidences, either coupled with the dication of interest or another background ion.

2.4 Detailed event analysis

A specific region (peak) of the coincidence spectrum that corresponds to a reaction channel can be selected for further analysis. To get information about the dynamics and energetics of a reaction we need the velocity vectors of the product species. The velocity vectors are determined from the sets of ten times, five each for a pair of product ions detected in coincidence. We start by determining the x , y , and z components of the velocity vectors in the laboratory (LAB) frame.

2.4.1 Product fragment velocities in the LAB frame

In the lab frame, the movement of the ions is defined relative to the axes of the PSCO-MS apparatus, where z is defined as the axis along which the dication beam travels, from the interaction region towards the detector.¹

The four times from the DLA signals of each ion are used to derive the x and y components of a product ion's velocity. The DLA signals are the times that the separate electrical signals reach the ends of each delay line (t_{xa} and t_{xb} are the times from one delay line, which runs in the x direction, and t_{ya} and t_{yb} are the times from the other delay line running in the y direction) and can be converted to the $x(i)$ and $y(i)$ position that the ion impacts on the detector relative to the centre of the detector, using (2.3) and (2.4).¹

$$x(i) = [t_{xa}(i) - t_{xb}(i)]/s_x \quad (2.3)$$

$$y(i) = [t_{ya}(i) - t_{yb}(i)]/s_y \quad (2.4)$$

where s_x and s_y are the propagation speeds of the charge pulse along the x - and y -oriented delay-lines respectively. The propagation speeds are determined by calibration and are intrinsic to the specific DLA. To determine how far the ions have moved in the x and y directions, the x and y coordinates of the reactant dications in the reaction region (x_0 and y_0) must also be accounted for, approximated by the impact position on the detector of the unreacted dication beam. Finally, the TOF of the ion, $t_{\text{expt}}(i)$, with a correction compensating for the electronic delay between the start of the repeller plate pulse and the start of the data collection, c , is required. To determine the x and y components of the product ion velocities, $v_x(i)$ and $v_y(i)$, equations (2.5) and (2.6) are used respectively.

$$v_x(i) = \frac{x(i) - x_0}{t_{\text{expt}}(i) + c} \quad (2.5)$$

$$v_y(i) = \frac{y(i) - y_0}{t_{\text{expt}}(i) + c} \quad (2.6)$$

The z component of the product ion velocity, $v_z(i)$, is determined from the deviation of $t_{\text{expt}}(i)$ from the TOF of an ion with the same m/z but with zero initial kinetic energy, $t_0(i)$. The value of $v_z(i)$ is particularly important for transposing to the CM frame, explored in Section 2.4.2. The Wiley-McLaren 'braking-time' relationship, shown in (2.7), is used to determine $v_z(i)$.^{1,9}

$$v_z(i) = \frac{-(t_{\text{expt}}(i) - t_0(i))eZF}{m_i} \quad (2.7)$$

where e is the charge of an electron, Z is the magnitude of the charge of the ion, m_i is the mass of the ion, and F is the electric field strength in the TOF-MS source region. During the analysis

procedure $t_0(i)$ is determined on a case by case basis using the Wiley-McLaren formula with the known energy of the ions in the beam, E_T , and the electric field strength in the TOF-MS source region, F . The values of E_T and F can be determined in two ways. Firstly, use of the calibration experiment described in Section 2.4.1.1 provides the approximately correct values. These values are then finely adjusted in a self-consistent manner as part of the analysis of a two-body decay. The values of E_T and F are adjusted so that the experimentally determined and expected values of the velocity of the CM of the system (v_{cm} , explained in Section 2.4.2.1) agree and that the curvature in the experimental scattering diagrams are correct.

Using the above procedure, the LAB frame velocity vectors, $v(i) = (v_x, v_y, v_z)$, for each product ion are derived for every pair of ions selected in a reaction channel.

2.4.1.1 Calibration of the electric field strength in the TOF-MS source region

Calibration of the electric field strength in the TOF-MS source region, F , is carried out by measuring the flight-time of a known ion ($t_{expt}(i)$) at different rest potentials (V_{sb}) and applying the following procedure. By rearranging the Wiley-McLaren braking formula, (2.7), and substituting in $v_i = \sqrt{\frac{2E_T}{m_i}}$ (a rearrangement of $E_T = \frac{1}{2}mv^2$), where E_T is the translational energy of the dication in the beam which is equal to $2V_{sb}$, we get the following:

$$t_{expt}(i) = t_0(i) - \frac{\sqrt{2m_i}}{eZF} \sqrt{E_T} \quad (2.8)$$

By plotting a graph with $t_{expt}(i)$ vs $\sqrt{E_T}$, as shown in Figure 2.11, the gradient, Δt , is equal to $-\frac{\sqrt{2m_i}}{eZF}$. Considering that the values of m_i , e and Z are known, we can obtain the value of F from the gradient using formula (2.9). The calibration graph shown in Figure 2.11 has a line of best fit of $-61.88 \text{ s J}^{1/2}$, which corresponds to $F = 183.8 \text{ V cm}^{-1}$.

$$F = -\frac{\sqrt{m_i}}{eZ\Delta t} \quad (2.9)$$

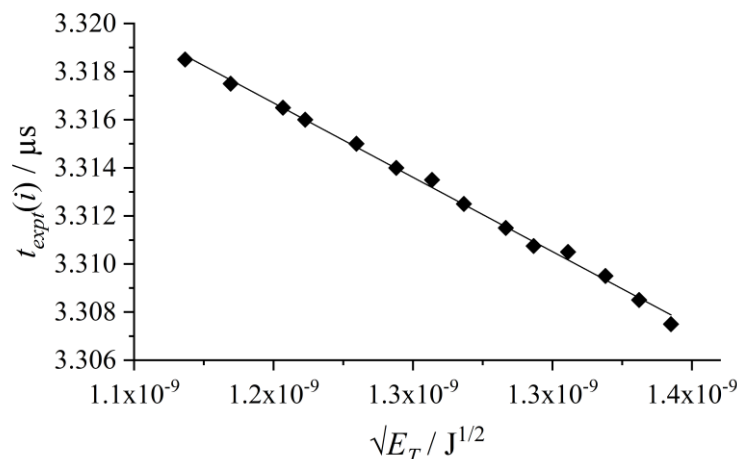


Figure 2.11: Calibration graph used to determine the electric field in the source region of the TOF-MS F . The gradient of the line of best fit, $-61.88 \text{ s J}^{-1/2}$, corresponds to a value of $F = 183.8 \text{ V cm}^{-1}$.

From equation (2.8) it is also clear that the TOF of an ion with the same m/z but with zero initial kinetic energy, $t_0(i)$, is the y-axis intercept

2.4.2 Product fragment velocities in the CM frame

The overwhelming momentum of the reactant dication means that, in the LAB frame, the products will travel in the same direction as the reactant dication, and therefore it is difficult to easily determine the dynamics. Therefore, in order to aid the interpretation of the dynamics, the product velocities are converted into the centre-of-mass (CM) frame. That is, the velocity vectors are expressed relative to the motion of the CM of the reactants. In the LAB frame the reactant dication travels with a large velocity in the z direction, and the neutral reactant is stationary. In the CM frame the reactants travel towards each other and have equal and opposite momenta, therefore, the sum of the momenta of the reactant species is equal to zero. The CM frame is the universal frame for a chemical reaction, the dynamics are simplified and the energy of the collision in the CM frame is the energy available for chemical processes to occur. The CM frame is therefore a more natural frame to work in, removing the effect of experimental choices.

2.4.2.1 Deriving the velocity of the CM

In order to convert the LAB frame velocities into the CM frame, the velocity of the CM of the system must first be determined. The CM of the reactants can be determined in two ways. The first method uses the velocities of the reactant dication, v_d , and reactant neutral species, v_n .

Given that the angular spread of the dication beam is negligible, the x and y components of v_d are assumed to be equal to zero, and therefore v_d is equal to the z component of the dication velocity, v_{dz} . The velocity of the CM of the system, v_{cm} , can be calculated using equation (2.10).

$$v_{cm} = \frac{m_d v_d + m_n v_n}{m_d + m_n} \quad (2.10)$$

where m_n and m_d are the masses of the neutral and dication species respectively. In our experiment, the momentum ($p = mv$) of the reactant neutral species is negligible compared to the momentum of the dication. Therefore, equation (2.10) reduces to (2.11) and can be used to calculate a single value for v_{cm} that can be subsequently used to process every reactive event.

$$v_{cm} = \frac{m_d v_d}{m_d + m_n} \quad (2.11)$$

The second method for determining the CM velocity of the collision system involves calculating v_{cm} separately for each product ion pair. Calculation of v_{cm} using this second method is only possible for two-body reactions, those dication + neutral reactions that result in the generation of two ionic fragments, without the generation of an additional neutral species. The second method requires knowledge of the LAB frame velocities, $v(i)$ $i=1$ or 2 , and masses, $m(i)$ $i=1$ or 2 , of the two ionic products. The CM velocity of the system can then be calculated using equation (2.12). Conservation of momentum dictates that the CM velocity of the system remains constant throughout the reaction, therefore, the product velocities can be used to determine v_{cm} . Both methods are used in conjunction to corroborate the calibration of the PSCOMS data and are in good agreement.^{1,19}

$$v_{cm} = \frac{v(1)m(1) + v(2)m(2)}{m(1) + m(2)} \quad (2.12)$$

2.4.2.2 Converting the LAB frame velocities into the CM frame

The CM velocities of the product ions, $w(i)$, can be calculated using equation (2.13) with the newly calculated v_{cm} .

$$w(i) = v(i) - v_{cm} \quad (2.13)$$

By further analysis of the product ion velocities in the CM frame, angular scattering information and kinetic energy release (KER) distributions can be extracted from the data with ease. Henceforth after the above conversions, the data set consists of pairs of velocity vectors in the CM frame for the product monocations.

2.4.2.3 Velocity of a third product

Often the reaction between a dication and a neutral produces a pair of detected monocations accompanied by a neutral species: a ‘three-body reaction’. These neutral products are generally not detected by the detector. However, using the momenta of the ionic products, the velocity of the neutral species can be determined in the CM frame *via* conservation of momentum using equation (2.14):¹

$$w(3) = -\frac{[m(1)w(1)+m(2)w(2)]}{m(3)} \quad (2.14)$$

Hence the CM frame velocity vectors and therefore the full dynamics and energetics can be determined for all products of two-body and three-body reactions.

2.4.3 Scattering diagrams

In order to examine the relationships between the velocity vectors of the product species and give insight into the mechanisms involved, we display the product ion velocities pictorially in the form of scattering diagrams. Scattering diagrams display the velocity vectors of the products relative to a specific frame of reference, either the CM frame or an internal frame. Note that scattering diagrams are also known as ‘Newton’ diagrams because Newton’s laws govern the asymptotic behaviour of the reacting species.²⁰

The angle between the velocity vectors of the ionic products Θ (shown in Figure 2.12a) can be determined from the dot product of the two CM velocity vectors:

$$\cos(\Theta) = \frac{w(1) \cdot w(2)}{|w(1)||w(2)|} \quad (2.15)$$

Note that for a two-body reaction, conservation of momentum dictates that $\Theta = 180^\circ$. In order to construct a scattering diagram, the angle θ between the velocity vector of the ionic product $w(i)$ and the CM velocity of the system v_{cm} must also be determined (shown in Figure 2.12b). The angle θ is determined by using the dot product of $w(i)$ and v_{cm} .

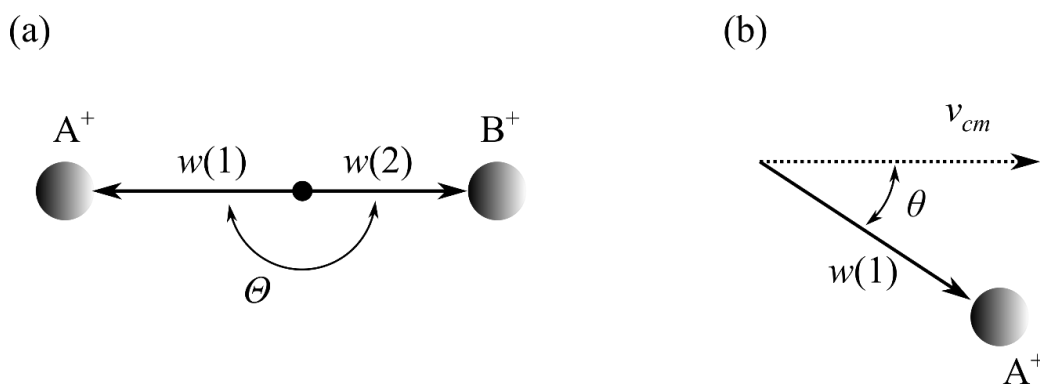


Figure 2.12: (a) A schematic diagram of the angle between the velocity vectors, θ , of the ionic products A⁺ and B⁺ in the CM frame. The black dot indicates the position of the CM. (b) A schematic diagram of the scattering angle θ of the ionic product A⁺ in the CM frame.

2.4.3.1 CM scattering diagrams

A CM scattering diagram is a polar histogram including each event collected for a given reaction channel. For each product ion, the diagram plots the magnitude of the CM velocity $|w_i|$ as the radial co-ordinate, and the scattering angle θ between w_i and the v_{cm} as the angular coordinate. From our assumptions, v_{cm} has the same direction as the velocity vector of the reactant dication, so the velocity vectors of the product species are expressed relative to the direction of the reactant dication. An example of a CM scattering diagram is shown in Figure 2.13, with the local density displayed as a heat map; the areas with the highest density of ions are dark red in colour. The scattering of each ion is azimuthally symmetric about v_{cm} , therefore, we plot the data for one product in the upper semicircle of the figure and the data for another product in the lower semicircle. Therefore, the scattering velocity vectors of both products can be displayed simultaneously. Correlations between the reactant and product velocity vectors are readily identified in scattering diagrams of this type.

There are two commonly observed scattering diagram motifs which are due to mechanisms involving ‘forward scattering’ and ‘isotropic scattering’ of the product species. The scattering diagram shown in Figure 2.13, which shows the scattering of the S⁺ and N₂⁺ products of a SET reaction between S²⁺ and N₂, displays strong forward scattering. That is, the velocity of the S⁺ product ion is strongly oriented with the incident dication velocity, $w(S^{2+})$. Conversely the velocity of the N₂⁺ product ion is directed anti-parallel to $w(S^{2+})$ and strongly oriented with the velocity vector of the neutral reactant $w(N_2)$. This forward scattering occurs because the reaction (the transfer of an electron from the neutral species to the dication)

occurred at a relatively large interspecies separation. As discussed in Section 1.4.2.1.1, LZ reaction window theory suggests that dication + neutral SET reactions are generally more likely to occur at interspecies separations of $2 \text{ \AA} - 6 \text{ \AA}$. At these large interspecies separations, there is no long-term association between the reactant species and they simply travel past each other allowing an electron to transfer. The product monocations therefore largely retain the directions of their reactant precursors, resulting in the scattering observed in Figure 2.13. As well as commonly occurring for SET reactions, forward scattering can be seen in reactions that involve the formation of new chemical bonds.

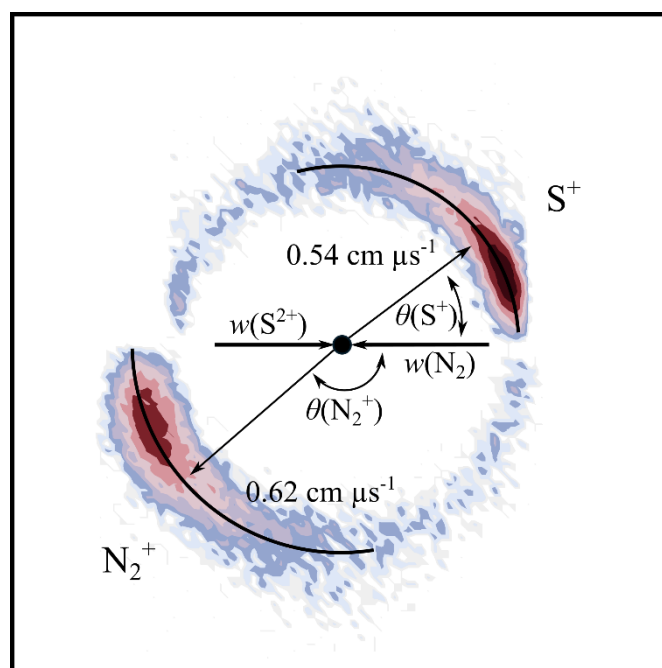


Figure 2.13: CM scattering diagram for the reaction $S^{2+} + N_2 \rightarrow S^+ + N_2^+$. The black dot indicates the position of the CM.

Whilst the bulk of LZ style SET reactions result in product ion velocity vectors being oriented with their reactant precursors, the events form a distribution. Despite the prominence of forward scattering in Figure 2.13, there are some events where the S^+ product ion is scattered to higher angles, near 180° . These events arise from ‘head-on’ collisions and result in the S^+ product ion reversing direction towards where the S^{2+} reactant came from. There are also very few events that result in S^+ scattering of near 0° , where the reaction causes no change in direction. The reduced probability of events resulting in scattering at 0° and 180° is because there are not many reactant trajectories that can result in these scattering angles. The angular distributions of the scattering data are also distorted by the data presentation. We transform all scattering events over three dimensions, $4\pi \text{ sr}$, into a simple two-dimensional $0^\circ - 180^\circ$

projection. This transformation results in a sinusoidal distribution, with less intensity towards 0 and 180 degrees. Therefore, even for strongly forward scattered reactions, there is still usually a tail towards higher scattering angles.

The second commonly observed scattering diagram motif is isotropic scattering, as seen in Figure 2.14. Both the SN^+ and N^+ product ions are scattered throughout $\theta = 0^\circ - 180^\circ$. This form of scattering occurs when the reactant species form a complex. The complex survives for at least the period of several rotations before fragmenting into the observed products. These rotations scramble the direction of approach of the reactants, resulting in the product fragments being ejected with equal probability throughout 4π sr in space. Due to the conversion of the three-dimensional scattering data into the two-dimensional diagrams, discussed above, in our projection ($0^\circ < \theta < 180^\circ$) truly isotropic scattering throughout 4π sr in space results in scattering that is sinusoidal in shape. A true isotropic distribution in our projection can therefore be obtained by dividing the angular distribution by $\sin(\theta)$.

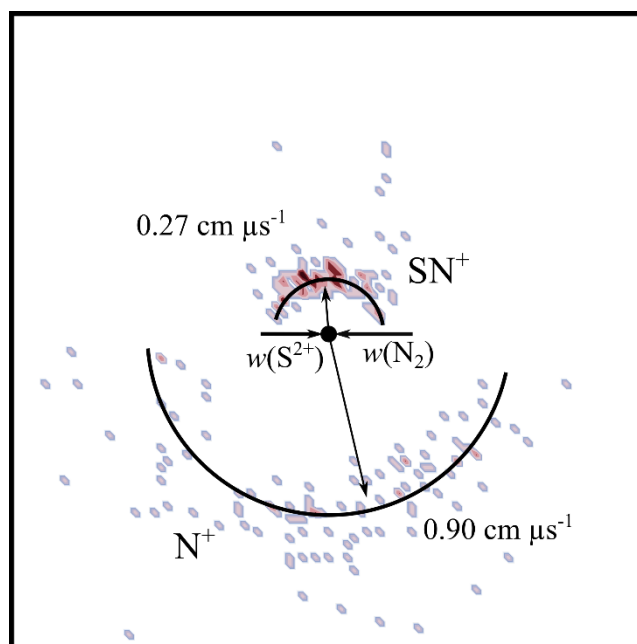


Figure 2.14: CM scattering diagram showing isotropic scattering of the SN^+ and N^+ products from the reaction $\text{S}^{2+} + \text{N}_2 \rightarrow \text{SN}^+ + \text{N}^+$. The black dot indicates the position of the CM.

When there are more than two product species, the CM frame may not always be the most helpful in interpreting the relationships between the species, instead we use internal frame (IF) scattering diagrams.

2.4.3.2 IF scattering diagrams

As discussed in Section 2.4.2.3, for reactions where a third, neutral, fragment is produced as well as two monocations, each of their velocity vectors can be determined. Internal-frame (IF) scattering diagrams can be used to help interpret the dynamics of these three-body reactions. In this class of scattering diagram $|w_i|$ is again the radial coordinate, but the angular coordinate is now the CM scattering angle with respect to the CM velocity of one of the other product species (determined from the dot product of the CM velocities). The data for one of the product species is plotted in the upper half of the figure and the data for a second product is plotted in the lower half of the figure, both relative to the CM velocity of the third fragment. Thus, IF scattering diagrams offer a method to examine the relative motions of three different products in the same figure. In IF scattering diagrams, any of the three products can be used as the reference. Figure 2.15 shows the possible IF scattering diagrams plotted for the products of the three-body reaction $\text{Ar}^{2+} + \text{N}_2 \rightarrow \text{Ar}^+ + \text{N}^+ + \text{N}$. Here, for example, (a) shows the scattering of N^+ and N relative to Ar^+ . In all three of the scattering diagrams in Figure 2.15 the motion of the Ar^+ fragment is anti-correlated with the motions of the N^+ and N fragments. This correlation is indicative of an association between the N^+ and N fragments, indicative of DSET. First, a SET reaction occurs, forming Ar^+ and N_2^+ , and then, after some time, the N_2^+ fragment dissociates to form $\text{N}^+ + \text{N}$, resulting in the scattering shown where the N^+ and N fragments are correlated.

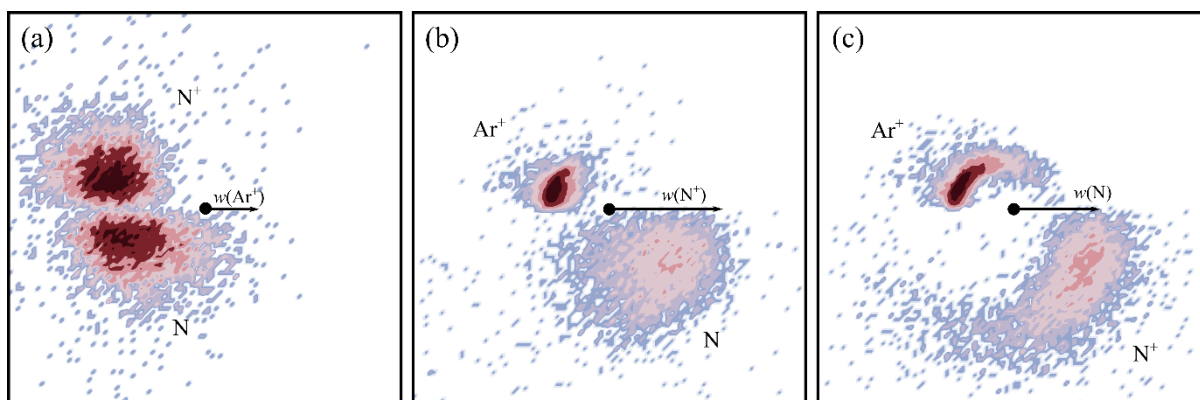


Figure 2.15: Internal frame scattering diagrams for the products of the reaction $\text{Ar}^{2+} + \text{N}_2 \rightarrow \text{Ar}^+ + \text{N}^+ + \text{N}$. (a) the velocities of the N^+ and N products are shown relative to Ar^+ , (b) the velocities of the Ar^+ and N products are shown relative to N^+ , (c) the velocities of the Ar^+ and N^+ products are shown relative to N . In each scattering diagram the black dot indicates the position of the CM.

In the field of reaction dynamics understanding three-body reactions can be complex and has long been an experimental issue, resulting in a limited understanding of these processes.²¹ For example, monocation-neutral three-body reactions are hard to probe because there are two neutral products which are generally difficult to detect. As discussed, reactions involving dications often result in the formation of two monocations, allowing the momentum of a third, neutral, body to be determined by detecting the two monocation products in coincidence. Thus, we can obtain the complete momenta information of the products from three-body reactions involving dications. The use of coincidence measurements involving the detection of two particles resulting from a single event eliminates the need for statistical models and has allowed for a more comprehensive understanding of chemical reaction dynamics. Three-body reactions involving dications are therefore understood more thoroughly than in other fields.

2.4.4 Translational energy release

The total kinetic energy release (KER) in the CM frame, T , for a given reactive event can also be determined from further analysis of the product ion velocities.¹ The LAB frame velocities, calculated in Section 2.4, are used to determine T for a two-body reaction by using equation (2.16).

$$T = \frac{1}{2}\mu_p \left[(v_x(1) - v_x(2))^2 + (v_y(1) - v_y(2))^2 + (v_z(1) - v_z(2))^2 \right] \quad (2.16)$$

where μ_p is the reduced mass of the product ions and $v_{x,y,z}(i)$ are the x , y and z components of the velocity vectors for ion i . For a three-body reaction, equation (2.17) is used to determine T .

$$T = \frac{1}{2}[m_1v_1^2 + m_2v_2^2 + m_3v_3^2] \quad (2.17)$$

Where m_i and v_i are the mass and velocity of fragment i respectively. The exoergicity of the reaction ΔE can then be determined from T and the CM collision energy, E_{cm} using equation (2.18), where $E_{products}$ and $E_{reactants}$ are the relative energies of the product and reactant states respectively. E_{cm} can be determined using equation (2.19) where μ_r is the reduced mass of the reactants. Again, the velocity of the neutral reactant is negligible compared to that of the dication.

$$\Delta E = T - E_{cm} = E_{products} - E_{reactants} \quad (2.18)$$

$$E_{cm} = \frac{1}{2} \mu_r v_d^2 \quad (2.19)$$

Obtaining ΔE for all the events collected for a given reaction channel provides a histogram of the exoergicity of the detected reactive events. A schematic diagram showing ΔE , T , and E_{cm} is shown in Figure 2.16. From Figure 2.16, it is clear that ΔE is intrinsic to the reactants and is independent of E_{cm} . An example exoergicity spectrum is shown in Figure 2.17 for the SET reaction between Ar^{2+} and O_2 . From knowledge of the available electronic states of the reactants and products of a reaction, the exoergicity spectrum can reveal the electronic states, and even the vibrational states, involved in the reaction, as will be shown throughout this thesis.

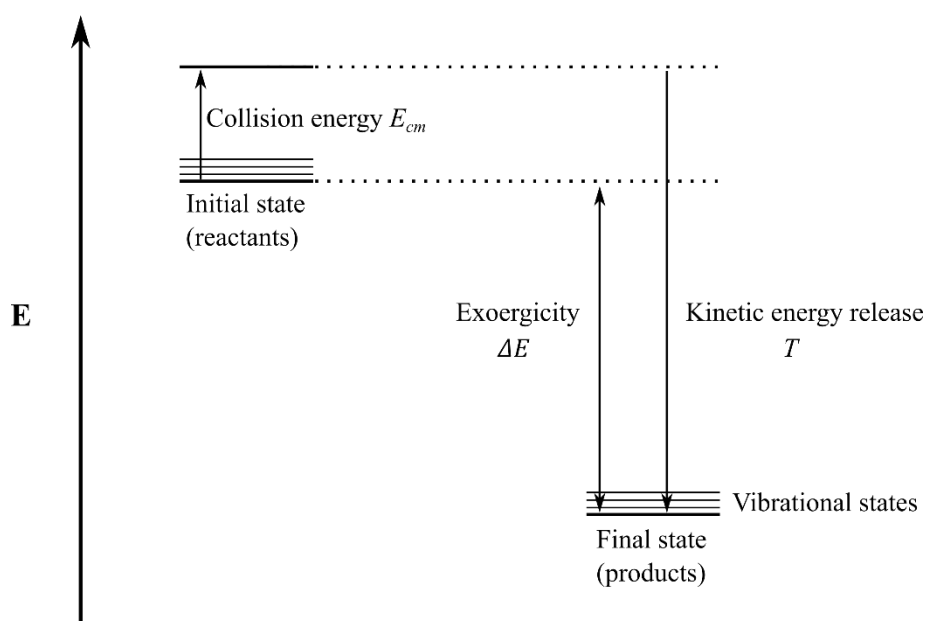


Figure 2.16: Schematic showing the exoergicity ΔE and kinetic energy release for a reaction.

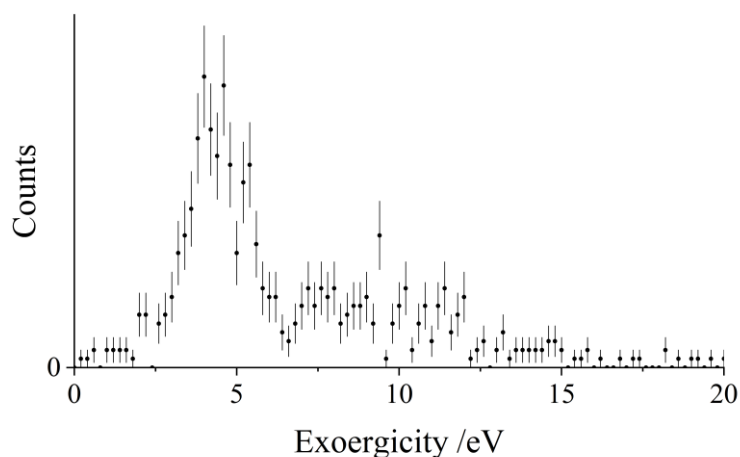


Figure 2.17: Exoergicity spectrum for the reaction $\text{Ar}^{2+} + \text{O}_2 \rightarrow \text{Ar}^+ + \text{O}_2^+$. The error bars represent two standard deviations of the counts.

2.5 Summary

This chapter has described in detail the PSCO-MS experimental setup at UCL that has been used to investigate dication-neutral reactions presented in this thesis. The data processing and analysis methods have also been explained in detail. It has been shown that the PSCO-MS apparatus can yield rich data, offering detailed insights into the dynamics and energetics of dication + neutral reactions, such as the exoergicities and electronic states involved, and if collision complexes are formed.

2.6 References

- 1 W.-P. Hu, S. M. Harper and S. D. Price, *Meas. Sci. Technol.*, 2002, **13**, 1512–1522.
- 2 W.-P. Hu, S. M. Harper and S. D. Price, *Mol. Phys.*, 2005, **103**, 1809–1819.
- 3 S. D. Price, *Int. J. Mass Spectrom.*, 2007, **260**, 1–19.
- 4 S. D. Price, J. D. Fletcher, F. E. Gossan and M. A. Parkes, *Int. Rev. Phys. Chem.*, 2017, **36**, 145–183.
- 5 K. Yamasaki and S. R. Leone, *J. Chem. Phys.*, 1989, **90**, 964–976.
- 6 V. H. Dibeler, *Anal. Chem.*, 1955, **26**, 58–65.
- 7 B. A. Mamyryn, *Int. J. Mass Spectrom.*, 2001, **206**, 251–266.
- 8 C. J. Brais, J. O. Ibañez, A. J. Schwartz and S. J. Ray, *Mass Spectrom. Rev.*, 2020, mas.21650.
- 9 W. C. Wiley and I. H. McLaren, *Rev. Sci. Instrum.*, 1955, **26**, 1150–1157.
- 10 J. H. D. Eland, *Meas. Sci. Technol.*, 1993, **4**, 1522–1524.
- 11 J. F. Lockyear, PhD thesis, UCL, 2011.
- 12 I. Ali, R. Dörner, O. Jagutzki, S. Nüttgens, V. Mergel, L. Spielberger, K. Khayyat, T. Vogt, H. Bräuning, K. Ullmann, R. Moshhammer, J. Ullrich, S. Hagmann, K. O. Groeneveld, C. L. Cocke and H. Schmidt-Böcking, *Nucl. Instruments Methods Phys. Res. Sect. B Beam Interact. with Mater. Atoms*, 1999, **149**, 490–500.
- 13 A. Oelsner, O. Schmidt, M. Schicketanz, M. Klais, G. Schönhense, V. Mergel, O. Jagutzki and H. Schmidt-Böcking, *Rev. Sci. Instrum.*, 2001, **72**, 3968–3974.
- 14 J. H. D. Eland, *Meas. Sci. Technol.*, 1994, **5**, 1501–1504.
- 15 M. B. Williams and S. E. Sobottka, *IEEE Trans. Nucl. Sci.*, 1989, **36**, 227–230.
- 16 J. H. D. Eland, *Mol. Phys.*, 1987, **61**, 725–745.
- 17 M. A. Parkes, K. M. Douglas and S. D. Price, *Int. J. Mass Spectrom.*, 2019, **438**, 97–106.

- 18 J. D. Fletcher, M. A. Parkes and S. D. Price, *Int. J. Mass Spectrom.*, 2015, **377**, 101–108.
- 19 W. P.-P. Hu, S. M. Harper and S. D. Price, *Mol. Phys.*, 2005, **103**, 1809–1819.
- 20 P. R. Brooks, *J. Phys. Chem.*, 1993, **97**, 2153–2157.
- 21 C. Maul and K.-H. Gericke, *J. Phys. Chem. A*, 2000, **104**, 2531–2541.

Chapter 3: Bond-Forming and Electron-Transfer Reactivity Between Ar²⁺ and O₂

3.1 Introduction

This chapter presents a thorough investigation of the interactions between Ar²⁺ and O₂, giving information on dicationic energetics, reactivity, and the associated reaction mechanisms. This detailed information allows a better understanding of the relevance and influence of Ar²⁺/O₂ collisions in planetary environments. Argon constitutes ~1 % of the Earth's atmosphere and is one of the most abundant elements in the universe.^{1,2} Argon is also abundant in the atmospheres of the Moon, Mercury and Mars.³⁻⁵ In these atmospheres, the formation of the Ar²⁺ dication is likely, as recognised by Thissen *et al.*⁶ The bimolecular reactivity of Ar²⁺ was one of the first such dicationic collision systems to be investigated, as beams of Ar²⁺ are relatively easy to generate using electron ionization.⁷⁻¹⁰ In most of these early investigations of Ar²⁺-neutral collisions, only the dominant single electron-transfer (SET) and double electron-transfer (DET) channels were observed. These early experiments were usually carried out at high laboratory translational energies (0.1 – 20 keV) and involved rare gases or simple molecules as the neutral collision partner (e.g. He, H₂, N₂, CO₂, C₂H₆, C₆H₆).^{8,9,11-13} More recent experiments, at lower collision energies (<100 eV), led to the observation of bond-forming chemistry following the interactions of Ar²⁺ with various neutral species, revealing, for example, the formation of Ar-O, Ar-N and Ar-C bonds.¹⁴⁻¹⁹ Indeed, the bimolecular reactivity of rare gas dications is now recognised as an effective route to forming these unusual chemical bonds.

Oxygen is the third most abundant element in the universe, it is a major component of the atmosphere of the Earth and is also present in the atmosphere of other planets and satellites.^{2,3} The reactions between Ar²⁺ and O₂ have been studied in experiments over a range of supra-thermal energies.^{8,9,11-13} In the earliest work, no chemical bond-formation was observed, and the ion yields were explained using models involving varying contributions from SET and DET. In later work, Ascenzi *et al.*¹⁷ studied the reaction of Ar²⁺ with O₂ using a combination of experiments and *ab initio* calculations. This work revealed a reactivity involving SET as well as the formation of two different products involving Ar-O bonds: ArO²⁺ and ArO⁺.

Whilst the ionic products of the reaction between Ar²⁺ and O₂ are now reasonably well established,¹⁷ there has been little investigation of the dynamics and kinematics of these chemical processes. To address this issue, this chapter reports an investigation of the reactivity of Ar²⁺ and O₂, at collision energies of 2.7 eV and 4.4 eV in the centre-of-mass frame, using position-sensitive coincidence mass spectrometry (PSCO-MS). As discussed in Chapter 2, the PSCO-MS technique couples a crossed-beam collisional methodology with the coincident detection of the cationic products of dication-neutral collisions, providing a comprehensive insight into the reactivity and dynamics involved in dication-neutral interactions.²⁰

In the study of Ar²⁺/O₂ collisions detailed in this chapter we observe that chemical bond-formation occurs *via* a direct mechanism rather than complexation. Conversely, we find strong evidence of complex formation ([ArO₂]²⁺) in the dynamics of the dissociative SET channel; a reaction that typically occurs *via* long-range electron-transfer.

3.2 Experimental details

In the work described in this chapter the Ar²⁺ ions were generated *via* electron ionization of Ar (BOC, 99.998 %) by 100 eV electrons in the ion source. In the TOF-MS source region the beam of dications was crossed with an effusive jet of O₂ (BOC, 99.5 %). The experiments in this work employed both high (183 V cm⁻¹) and low (28.5 V cm⁻¹) TOF-MS source fields. As discussed in more detail below, the lower source field results in better energy resolution in the resulting PSCO-MS data. However, in these low field spectra ions with high transverse (off-axis) velocities do not reach the detector.

3.3 Results and discussion

PSCO-MS spectra were recorded following the collisions of Ar²⁺ with O₂ at $E_{\text{cm}} = 4.4$ eV. Four significant product ions were detected in the coincidence spectrum: Ar⁺, O₂⁺, O⁺ and ArO⁺. Of course, O₂²⁺ could also be present, although no sharp peak indicative of a dication is visible in the $m/z = 16$ region of the mass spectrum. The experiments were repeated at $E_{\text{cm}} = 2.7$ eV and no significant differences in the ratios of products or the derived reaction dynamics were apparent.

Table 3.1 lists the product channels observed in the coincidence spectrum following the collisions of Ar²⁺ with O₂. The most intense channel (Rxn. 3.II) is dissociative single electron-

transfer (DSET), producing $\text{Ar}^+ + \text{O}^+ + \text{O}$. Non-dissociative SET (NDSET) is also observed (Rxn. 3.I), albeit with only 1 % of the intensity of the DSET channel. The second most intense channel involves the production of $\text{O}^+ + \text{O}^+$ (Rxn. 3.IV) and results from double electron-transfer (DET): the dissociation of a nascent O_2^{2+} ion into O^+ and O^+ . Finally, a bond-forming reaction forming $\text{ArO}^+ + \text{O}^+$ is also observed at low intensity (Rxn. 3.III). Reaction II makes up 94.5 % of the total counts, indicating a significantly larger reaction cross section for this (DSET) reaction than the other channels, in agreement with previous experiments.¹⁷

Table 3.1: Reaction channels following collisions of Ar^{2+} with O_2 at a CM collision energy of 4.4 eV, with relative intensities. The modal experimental values of the total exoergicity ΔE from each reaction are reported.

Reaction	Products	Relative intensity/%	Modal experimental ΔE / eV
3.I	$\text{Ar}^+ + \text{O}_2^+$	0.9	4.0
3.II	$\text{Ar}^+ + \text{O}^+ + \text{O}$	94.5	9.5
3.III	$\text{ArO}^+ + \text{O}^+$	0.2	10.5
3.IV	$\text{Ar} + \text{O}^+ + \text{O}^+$	4.4	8.5 [†]

[†]The exoergicity given for Rxn. 3.IV is the value for the $\text{O}_2^{2+} \rightarrow \text{O}^+ + \text{O}^+$ dissociation.

As noted above, PSCO-MS data were also recorded at a low TOF-MS source field to yield a higher energy resolution in the exoergicity spectrum ($E_{\text{cm}} = 4.0$ eV). As discussed below, these experiments reveal that Reaction II initially involves the population of a number of electronic states of the product Ar^+ and O_2^{+*} ions, the O_2^{+*} states then dissociating to $\text{O}^+ + \text{O}$.

3.3.1 Formation of Ar^+ and O_2^+

Figure 3.1 shows a CM scattering diagram for the Ar^+ and O_2^+ products of the NDSET reaction (Rxn. 3.I). Figure 3.1 reveals strong forward scattering, where the velocity of the Ar^+ ion is strongly oriented with the incident dication velocity, $w(\text{Ar}^{2+})$. This strong forward scattering results in the O_2^+ product ion's velocity being directed anti-parallel to $w(\text{Ar}^{2+})$, and strongly oriented with $w(\text{O}_2)$. This form of scattering has been commonly observed for other

NDSET processes and arises from a direct electron-transfer mechanism, where the electron is transferred between the reactants at a significant interspecies separation (3-6 Å).²¹⁻²⁴ Such electron-transfer processes are well-represented by a Landau-Zener formalism, discussed in Section 1.4.2.1.1.²⁵

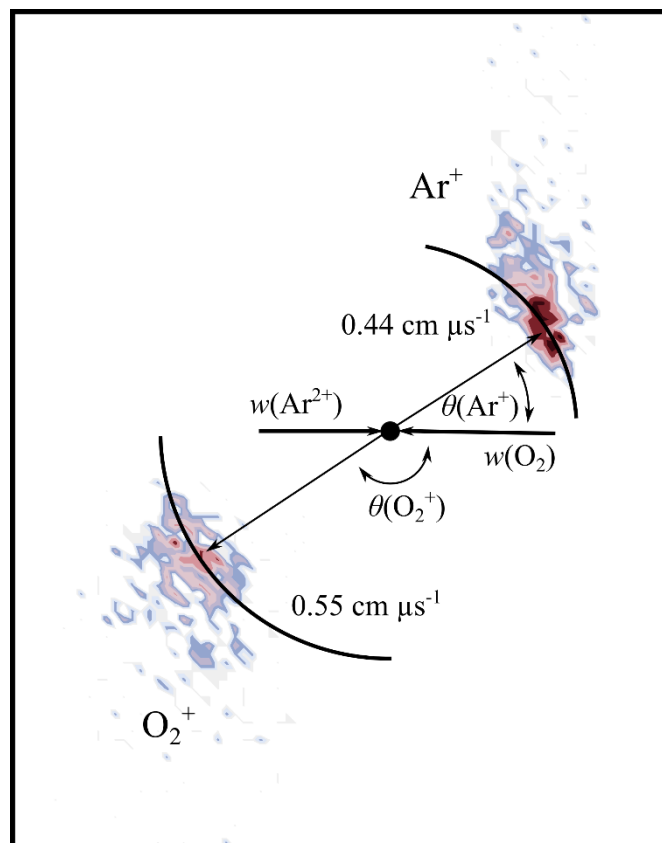


Figure 3.1: CM scattering diagram for the reaction $\text{Ar}^{2+} + \text{O}_2 \rightarrow \text{Ar}^+ + \text{O}_2^+$ at a CM collision energy of 4.4 eV. The black dot indicates the position of the CM. See text for details.

From analysis of the product ion velocities, as previously discussed, the exoergicity distribution of Reaction 3.I can be determined (Figure 3.2). The exoergicity for the formation of Ar^+ and O_2^+ ($E_{\text{cm}} = 4.4$ eV) is found to be centred at ~ 4.7 eV, with a full width at half maximum (FWHM) of 2.1 eV. The experiments performed at a lower TOF-MS source field, to give a higher energy resolution, revealed no new structures in this exoergicity spectrum.

To interpret the exoergicity spectrum for Reaction A (Figure 3.2) we need to determine the relative energies of the reactant and product states that could be involved in the reaction. For this collision system this energetic data is readily accessible. Previous studies have shown that Ar^{2+} beams, generated in a similar manner to those in our experiments, are composed of

ions in all three electronic states (^3P , ^1D and ^1S) arising from the Ar^{2+} p^4 configuration;²⁶ the relative abundance of these states appears approximately statistical in these previous investigations.²⁷ The reactant O_2 molecule, admitted as an effusive beam, will be in its ground vibronic state, $^3\Sigma_g^- \nu=0$. The accessible states of the O_2^+ product are well studied.²⁸ The ground state of O_2^+ ($X^2\Pi_g$) lies 12.07 eV above the ground state of the neutral molecule and requires an additional 6.7 eV to break the O-O bond to form $\text{O}^+ + \text{O}$.²⁹ All O_2^+ states lying above this $\text{O}^+ + \text{O}$ asymptote are unstable to dissociation within the lifetime of our experiment and therefore cannot contribute to the formation of the O_2^+ observed in this NDSET channel.³⁰ For example, metastable minima in the O_2^+ $c^4\Sigma_u^-$ state, and levels of the $b^4\Sigma_g^-$ state above $\nu=3$ are expected to dissociate before they are detected in our experiments.³¹⁻³⁴ There are three energetically accessible electronic levels for the product Ar^+ ions (^2P , ^2S and ^4D).³⁵

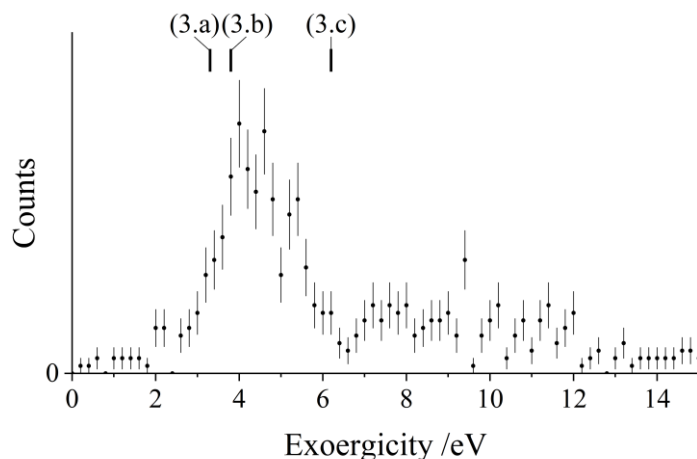
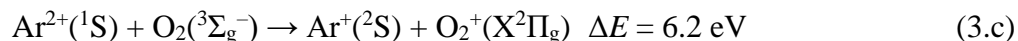
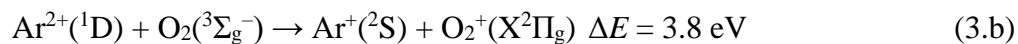
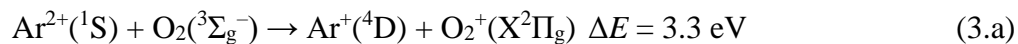


Figure 3.2: Experimental exoergicity spectrum for the reaction $\text{Ar}^{2+} + \text{O}_2 \rightarrow \text{Ar}^+ + \text{O}_2^+$. The exoergicities for potential SET pathways calculated from literature values are also shown: (3.a) $\text{Ar}^{2+}(^1\text{S}) + \text{O}_2(^3\Sigma_g^-) \rightarrow \text{Ar}^+(^4\text{D}) + \text{O}_2^+(X^2\Pi_g)$, (3.b) $\text{Ar}^{2+}(^1\text{D}) + \text{O}_2(^3\Sigma_g^-) \rightarrow \text{Ar}^+(^2\text{S}) + \text{O}_2^+(X^2\Pi_g)$, (3.c) $\text{Ar}^{2+}(^1\text{S}) + \text{O}_2(^3\Sigma_g^-) \rightarrow \text{Ar}^+(^2\text{S}) + \text{O}_2^+(X^2\Pi_g)$. The error bars represent two standard deviations of the associated counts.

From the above energetic considerations (see Table 8.1 in Appendix A) we find that there are three possible reaction pathways that match the favoured 3-6.5 eV range of exoergicities we see in Figure 3.2: reactions (3.a), (3.b) and (3.c). These three pathways all involve the formation of O_2^+ in its ground electronic state, $X^2\Pi_g$, which is stable to dissociation. The exoergicities of these three channels are indicated in Figure 3.2. The match of the calculated

exoergicities with the experimental spectrum (Figure 3.2) is good but not perfect due to the neglect of product vibrational excitation and the distribution of centre of mass collision energies.



Pathway (3.b) involves Ar²⁺ in its first excited state, ({}¹D) and, as noted above, the abundance of this state in the incident beam is expected to be larger by a factor of 5 than the second ({}¹S) excited state involved in pathways (3.a) and (3.c). Therefore pathway (3.b) is likely to be the dominant pathway for this channel. Pathway (3.b) involves an exoergicity that should result in a favoured Landau-Zener style electron-transfer.²⁵ However, despite these favourable factors the relative intensity of this channel (Rxn. 3.I) is low (Table 3.1); specifically, this SET channel has only ~1 % of the intensity of the DSET channel. The low propensity for this channel is most likely because pathways (3.a), (3.b) and (3.c) all involve two-electron processes when the Ar²⁺ accepts the transferred electron.

3.3.2 Formation of Ar⁺ and O⁺

The most intense product channel we observe following the reaction of Ar²⁺ with O₂ is dissociative single electron-transfer (DSET), in agreement with Ascenzi *et al.*¹⁷ The well-established mechanism of such dicationic DSET reactions, in this collision energy regime, is that initial Landau-Zener (LZ) style electron-transfer occurs, at significant interspecies separations, forming one or both of the nascent product ions in dissociative states. These dissociative state(s) subsequently fragment to yield the detected products.⁷ These dynamics, given the LZ curve crossing is favoured in a “reaction window” centred at an inter-reactant separation of around 4 Å, result in strong forward scattering. Such strong forward scattering has been observed in several different collision systems.^{7,24,36,37} In this specific reaction channel, the nascent O₂^{+*} ion formed in the initial electron-transfer would subsequently dissociate, resulting in the formation of Ar⁺ + O⁺ + O.

Figure 3.3a shows the CM scattering diagram for the Ar⁺ and O⁺ product ions from this DSET channel. The Ar⁺ is primarily forward scattered but has a significant tail to higher scattering angles. Such a tail is indicative of a short-lived association, a collision complex,

between the O_2 and Ar^{2+} : $[\text{ArO}_2]^{2+}$. Clearly, this collision complex does not live long enough for a complete loss of the correlation between the Ar^+ velocity and the initial velocity of the Ar^{2+} reactant before fragmenting into O_2^{+*} and Ar^+ . The observed scattering shows that this DSET reaction does not follow the standard (direct) mechanism of dicationic electron-transfer outlined above. Dynamics supporting the standard (direct) model of dication SET have been revealed, using the PSCO experiment and other angularly resolved techniques, for SET in many other collision systems.^{7,24,36,37} However, other isolated cases of dicationic electron-transfer involving significant complexation, as we see for this reaction, have also been previously reported.^{38,39}

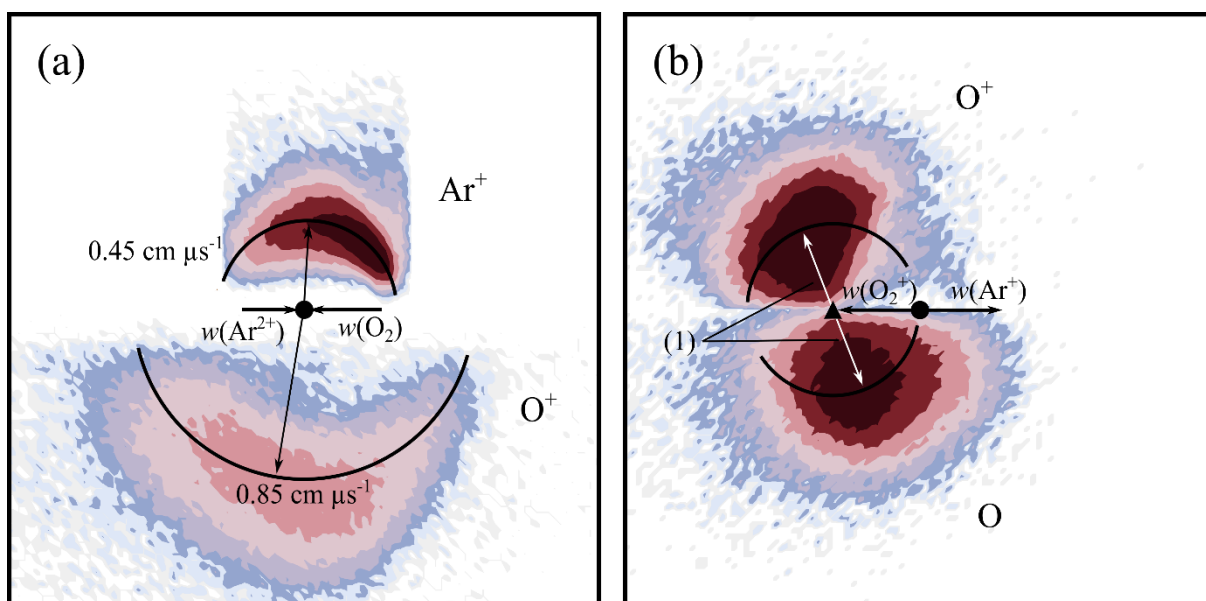


Figure 3.3: Scattering diagrams for the reaction $\text{Ar}^{2+} + \text{O}_2 \rightarrow \text{Ar}^+ + \text{O}^+ + \text{O}$ at a CM collision energy of 4.4 eV. (a) CM scattering diagram showing the scattering of O^+ and Ar^+ relative to the incident dication velocity, $w(\text{Ar}^{2+})$. (b) Internal frame scattering diagram showing the scattering of O^+ and O relative to the velocity of the Ar^+ product ion. In part (b) the labelled vector, (1), represents $0.55 \text{ cm } \mu\text{s}^{-1}$.

Figure 3.3 shows the internal frame scattering of O^+ and O , relative to the Ar^+ ion. The diagram clearly shows the O and O^+ fragments are both backward scattered relative to the Ar^+ ion, clearly indicating that the $[\text{ArO}_2]^{2+}$ complex dissociates into O_2^{+*} and Ar^+ *before the molecular ion subsequently fragments*. A similar case of DSET *via* a collision complex was observed following collisions between Ne^{2+} and N_2 .³⁸ In the $\text{Ne}^{2+}/\text{N}_2$ collision system the

dissociative SET reaction proceeded along two competing routes, *via* a collision complex, [NeN₂]²⁺, and *via* a fast-sequential pathway. The two different pathways could be distinguished by distinct peaks in the product ions' angular distributions. In the current Ar²⁺/O₂ collision system, such peaks are not observed, implying a single mechanism, involving short-lived complexation, is responsible for the DSET reaction.

The internal frame scattering (Figure 3.3b) has a symmetrical character, but the O⁺ is slightly more strongly backward scattered, relative to the Ar⁺, than the O. This additional acceleration of the O⁺ product is very likely due to Coulombic repulsion with the Ar⁺. That is the scattering indicates that the O₂⁺ dissociates relatively rapidly, before it leaves the electric field of its Ar⁺ partner. Dissociation of the O₂⁺ within the electric field of the Ar⁺ gives the O⁺ a larger velocity away from the Ar⁺ than the O fragment. By looking at the extra velocity of the O⁺ ion, the point of O₂^{+*} dissociation can be estimated. The difference in velocities between the O⁺ and O fragments corresponds to an energy difference of 3 ± 0.2 eV. The extra kinetic energy of the O⁺ fragment would result from O₂^{+*} dissociation at an interspecies separation of about 5 Å between the Ar⁺ and O₂⁺. This distance corresponds to an O₂^{+*} lifetime of approximately 50 fs, which is comparable to lifetimes of O₂⁺ dissociative states determined from the rotational bandwidths of photoelectron spectra,^{32,40} and calculated potential curves.⁴¹ DSET reactions where the dissociation of one of the product ions occurs within the field of the other have been previously observed, for example in the reaction between Ar²⁺ and C₂H₂.⁷ Here the C₂H₂^{+*} fragment formed from the initial electron-transfer dissociates into CH⁺ and CH, and the CH⁺ fragment is backscattered with a larger velocity than the CH fragment relative to the Ar⁺ ion. In this earlier work dissociation of C₂H₂^{+*} was estimated to occur at a distance of about 20 Å from the Ar⁺ ion, involving a C₂H₂^{+*} lifetime of about 500 fs, values compatible those derived for the current collision system.

The modal total exoergicity of the DSET reaction (Rxn. 3.II) determined experimentally is ~9.5 eV with a FWHM of 6-15 eV (see Figure 8.1 in Appendix A). This range of exoergicities encompasses a large number of accessible combinations of reactant and product electronic states: permutations of the Ar²⁺ (³P, ¹D and ¹S) states and the first five dissociation limits of O₂⁺.^{35,42,43}

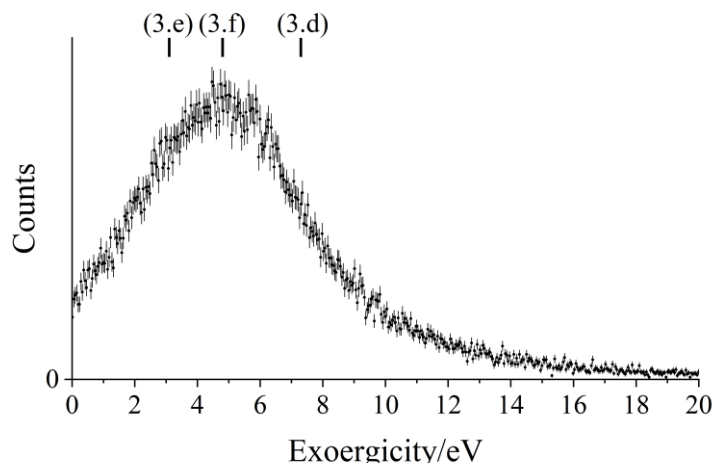
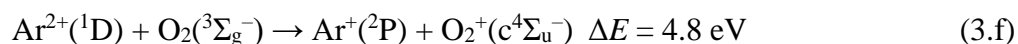
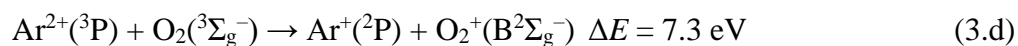


Figure 3.4: Exoergicity spectrum for the initial electron-transfer reaction in the DSET channel, $\text{Ar}^{2+} + \text{O}_2 \rightarrow \text{Ar}^+ + \text{O}_2^{+*}$. The exoergicities for potential electron-transfer pathways calculated from literature values are also shown: (3.d) $\text{Ar}^{2+}(^3\text{P}) + \text{O}_2(^3\Sigma_g^-) \rightarrow \text{Ar}^+(^2\text{P}) + \text{O}_2^+(\text{B}^2\Sigma_g^-)$, (3.e) $\text{Ar}^{2+}(^3\text{P}) + \text{O}_2(^3\Sigma_g^-) \rightarrow \text{Ar}^+(^2\text{P}) + \text{O}_2^+(\text{c}^4\Sigma_u^-)$, (3.f) $\text{Ar}^{2+}(^1\text{D}) + \text{O}_2(^3\Sigma_g^-) \rightarrow \text{Ar}^+(^2\text{P}) + \text{O}_2^+(\text{c}^4\Sigma_u^-)$. The error bars represent two standard deviations of the counts.

Considering the DSET reaction to be stepwise, an approximation given the above analysis of the O and O⁺ velocities, we can derive the O₂^{+*} precursor velocity from the Ar⁺ velocity. Using this approximation, we find an exoergicity distribution for the initial electron-transfer step ($\text{Ar}^{2+} + \text{O}_2 \rightarrow \text{Ar}^+ + \text{O}_2^{+*}$) centred at ~5.7 eV with a FWHM of ~1.5 – 7.7 eV (Figure 3.4). The broad distribution is indicative of a number of product and reactant electronic states being involved in this initial electron-transfer. Considering the accessible reactant and product electronic states, specifically the dissociative states of O₂⁺, and excluding some transitions due to poor Frank-Condon overlap, pathways (3.d), (3.e) and (3.f) nicely match the peak of the exoergicity distribution for the initial electron-transfer step (Figure 3.4).⁴⁴



Looking at the photoelectron intensities of transitions to the excited states of O₂⁺ involved in pathways (3.d)-(3.f), for a vertical transition the O₂⁺(B²Σ_g⁻) state will likely be formed in a range of vibrational levels, from $\nu = 0$ to $\nu = 6$, and O₂⁺(c⁴Σ_u⁻) will likely be formed

in its lowest two vibrational levels. This range of vibrational excitation contributes to the spread of energies in the exoergicity spectrum.⁴⁴ There are also accessible O_2^+ states higher in energy than the $c^4\Sigma_u^-$ state; population of such states will give exoergicities of less than 3.1 eV for the initial electron-transfer step.^{45,46}

When the PSCO-MS data was recorded at a lower source field, to achieve higher energy resolution, peaks at lower energies in the total exoergicity spectrum were revealed. Specifically, a distinct peak at around 4 eV is visible (see Figure 8.1 in Appendix A), with another broad peak at 5 – 8 eV. In this higher energy resolution experiment, sideways-scattered ions from reactions with higher exoergicities are not detected. The exoergicity for the initial electron-transfer step, determined from the precursor velocity of Ar^+ in this low source field experiment, shows a broad peak centred at 4 eV and a FWHM from 1.8 – 5.7 eV. This distribution is in good general agreement with that derived from the high source field experiments (Figure 3.4). The high energy resolution experiment supports the population of $\text{O}_2^+(c^4\Sigma_u^-)$, shown by the exoergicities of reactions (3.e) and (3.f); these pathways have exoergicities of 3.1 eV and 4.8 eV respectively.

To summarise, there are multiple pathways for the initial electron-transfer reaction in the DSET channel. The major pathways are likely (3.d), (3.e) and (3.f), however there may be contributions from higher energy O_2^{+*} states. The higher energy resolution experiments confirm the presence of pathways (3.e) and (3.f).

Using the O_2^{+*} precursor velocity, the KER for the dissociation of O_2^{+*} into $\text{O}^+ + \text{O}$ can also be extracted from our data.⁴⁷ This exoergicity for the O_2^+ dissociation, from the high source field experiment, is shown in Figure 3.5. The broad maximum of the exoergicity distribution is at 1.5 – 6.5 eV, with the FWHM from 0.2 – 10.3 eV. Previous work studying the dissociation of O_2^{+*} formed from neutral O_2 *via* electron-transfer with O_2^{2+} , in a similar experiment, revealed a dominant peak in the exoergicity spectrum at 1.5 – 3.0 eV, this overlaps with the lower end of the maximum exoergicity observed in this study.⁴⁷ Dissociation energies for O_2^{+*} of up to ~5.8 eV have been previously observed, resulting from dissociation of $\text{O}_2^+(c^4\Sigma_u^-)$ to the lowest energy dissociation limit of $\text{O}^+ + \text{O}$.^{30,31,44,48} In order to explain the higher energy exoergicities, higher lying states of O_2^+ must be involved. Higher lying states of O_2^+ have been observed, including one at ~27.5 eV, potentially accounting for the higher exoergicities we observe.^{45,46} The broad maximum observed in the current study results from the presence of multiple dissociation pathways, derived from the range of O_2^+ states, identified above, formed in the

initial electron-transfer step which fragment to the first dissociation limit, $\text{O}({}^3\text{P}) + \text{O}^+({}^4\text{S})$ (L1), and second dissociation limit, $\text{O}({}^1\text{D}) + \text{O}^+({}^4\text{S})$ (L2). The pathways, shown in Figure 3.5, are (3.g) $\text{B}^2\Sigma_g^- \rightarrow \text{L2}$, (3.h) $\text{B}^2\Sigma_g^- \rightarrow \text{L1}$, (3.i) $\text{c}^4\Sigma_u^- \rightarrow \text{L2}$, (3.j) $\text{c}^4\Sigma_u^- \rightarrow \text{L1}$, (3.k) $\text{O}_2^{+*} (E = 27.5 \text{ eV}) \rightarrow \text{L1}$. The range of exoergicities attributable to each pathway is estimated by considering the possible vibrational excitation of the O_2^+ product, and these ranges are indicated in Figure 3.5. As well as the first two dissociation limits, there are many additional minor O_2^+ dissociation pathways to higher dissociation limits that have been reported.^{30,31,48,49} The possibility of dissociation to higher energy $\text{O} + \text{O}^+$ asymptotes, and the array of dissociative states of O_2^+ available, further broaden the kinetic energy release observed from the O_2^{+*} dissociation, shown in Figure 3.5.

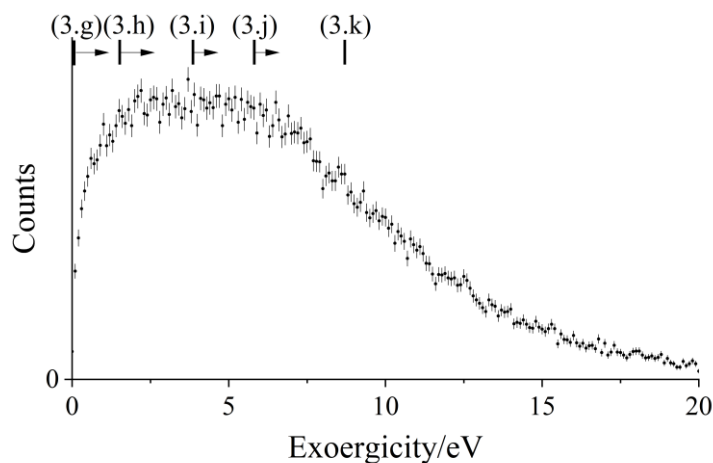


Figure 3.5: Experimental exoergicity spectrum for the dissociation of O_2^+ to form O^+ and O . The exoergicities for the potential dissociation pathways, calculated from literature values, are shown: (3.g) $\text{O}_2^+(\text{B}^2\Sigma_g^-) \rightarrow \text{O}({}^1\text{D}) + \text{O}^+({}^4\text{S})$, (3.h) $\text{O}_2^+(\text{B}^2\Sigma_g^-) \rightarrow \text{O}({}^3\text{P}) + \text{O}^+({}^4\text{S})$, (3.i) $\text{O}_2^+(\text{c}^4\Sigma_u^-) \rightarrow \text{O}({}^1\text{D}) + \text{O}^+({}^4\text{S})$, (3.j) $\text{O}_2^+(\text{c}^4\Sigma_u^-) \rightarrow \text{O}({}^3\text{P}) + \text{O}^+({}^4\text{S})$, (3.k) $\text{O}_2^+(E=27.5 \text{ eV}) \rightarrow \text{O}({}^3\text{P}) + \text{O}^+({}^4\text{S})$. The arrows indicate the approximate range of exoergicities from the potential vibrational excitation of O_2^+ in a vertical transition. The error bars represent two standard deviation of the counts. See text for details.

Whilst DSET resulting from the reaction of Ar^{2+} with O_2 has previously been observed,^{12,17} the current work provides much additional information on the dynamics and energetics of the reaction. The tail to higher scattering angles in the CM scattering diagram of Ar^+ and O^+ (Figure 3.3a) is evidence for the formation of a short-lived $[\text{ArO}_2]^{2+}$ complex. This

collision complex then dissociates into the nascent electron-transfer products Ar^+ and O_2^{+*} ($\text{B}^2\Sigma_g^-$ and $\text{c}^4\Sigma_u^-$), with the O_2^{+*} subsequently fragmenting within the field of the Ar^+ ion.

3.3.3 Formation of ArO^+ and O^+

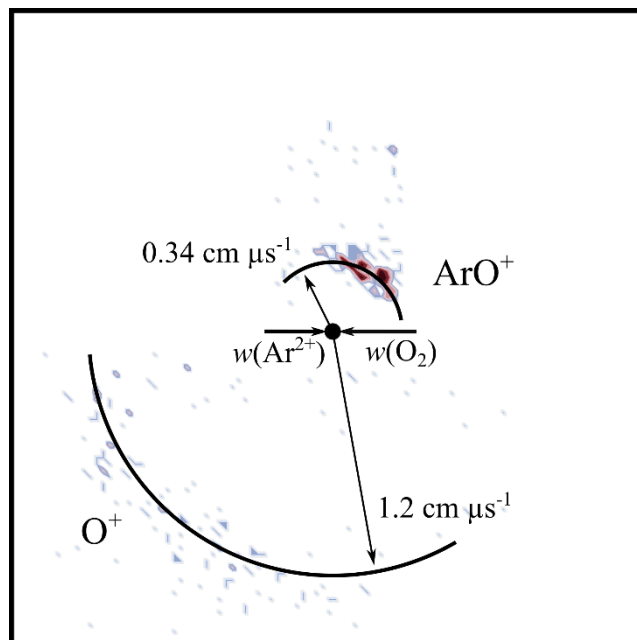


Figure 3.6: CM scattering diagram for the reaction $\text{Ar}^{2+} + \text{O}_2 \rightarrow \text{ArO}^+ + \text{O}^+$ at a CM collision energy of 4.4 eV. The scattering of O^+ and ArO^+ are shown relative to the incident direction velocity, $w(\text{Ar}^{2+})$. See text for details.

Figure 3.6 shows the CM scattering for $\text{ArO}^+ + \text{O}^+$, the products of the bond-forming reaction we detect in this collision system. Scattering that is distinctly forward is apparent, where the velocity of the ArO^+ ion is broadly oriented with the velocity of the incident direction, $w(\text{Ar}^{2+})$. This form of scattering suggests a stripping-style mechanism, where an O^- is transferred between the O_2 and Ar^{2+} at a relatively large interspecies separation. Such dynamics for bond-forming reactions involving atom transfer have been observed before.⁷ In their earlier work, where this unusual reaction was first observed, Ascenzi *et al.*¹⁷ suggest that this bond-forming reaction proceeds *via* a collision complex, ArO_2^{2+} . The scattering data we report here shows little evidence for any long-lived association between the reactants. If the channel proceeded *via* a long-lived collision complex, which survived for several rotational periods, prominent forward scattering would not be observed, and the scattering would have a more

isotropic nature. Such a signature of long-lived collision complexes has been reported in other dicationic collision systems.^{23,50}

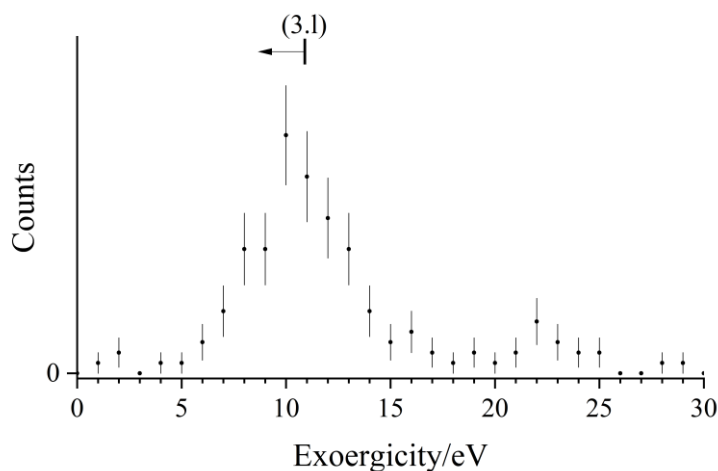
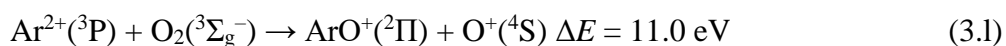


Figure 3.7: Experimental exoergicity spectrum for the reaction producing ArO^+ and O^+ from Ar^{2+} and O_2 . The range of exoergicities indicated by (3.1) is determined from literature values for the pathway: $\text{Ar}^{2+}({}^3\text{P}) + \text{O}_2({}^3\Sigma_g^-) \rightarrow \text{ArO}^+({}^2\Pi) + \text{O}^+({}^4\text{S})$. The arrow represents the possible range of exoergicity from the vibrational excitation of ArO^+ .^{35,42,43,51} The error bars represent two standard deviations of the counts. See text for details.

The exoergicity distribution of the bond-forming reaction, which is determined from the velocities of the product ions, is shown in Figure 3.7. The exoergicity distribution has a maximum at 10.5 eV, with a FWHM of 5 eV. As above, the exoergicity spectrum can be rationalised by considering the possible electronic states of the products. Energetic calculations involving ArO^+ usually consider the two lowest-bound electronic states: the ground state (${}^4\Sigma^-$) and the first excited state (${}^2\Pi$).^{51,52} The minimum of the ${}^2\Pi$ state lies ~ 0.4 eV higher in energy than the ${}^4\Sigma^-$ state minimum, but at a markedly different equilibrium geometry.

The exoergicity for forming $\text{ArO}^+({}^4\Sigma^-) + \text{O}^+({}^4\text{S})$ from the ground states of $\text{Ar}^{2+} + \text{O}_2$ is 11.4 eV, whilst populating $\text{ArO}^+({}^2\Pi) + \text{O}^+({}^4\text{S})$ would have an exoergicity of 11.0 eV. Both of these exoergicities coincide well with the peak in the experimental exoergicity distribution (shown in Figure 3.7). We note access to both these asymptotes is spin-allowed from $\text{Ar}^{2+}({}^3\text{P}) + \text{O}_2({}^3\Sigma_g^-)$.

In interpreting the results of their experiments, Ascenzi *et al.*¹⁷ suggest this reaction involves ArO⁺ formed in its ground ⁴Σ⁻ state along with O⁺(⁴S). Considering the formation of ArO⁺ at these two lowest energy product asymptotes, it is perhaps unlikely that a significant proportion of any ArO⁺(⁴Σ⁻) products would be long-lived enough to be detected by our experiment. Specifically, the ArO⁺ product is likely to be formed with significant vibrational excitation due to the long-range O⁻ abstraction from the O₂ by the Ar²⁺. However, the ArO⁺(⁴Σ⁻) ground state has only a shallow potential well (~0.4 eV)⁵¹ and is most likely to be formed at an unstable geometry due to the expected level of vibrational excitation. Conversely, the first excited state of ArO⁺, ²Π, has a well depth of ~2.0 eV, thus would more readily accommodate the expected significant vibrational excitation. Given these considerations, we suggest pathway (3.1) as the dominant route for this bond-forming reaction:



Of course, contributions from the excited p⁴ states of Ar²⁺ may also be present and cannot be resolved in the exoergicity spectrum (Figure 3.7).

Ascenzi *et al.*¹⁷ also proposed the operation of a markedly less exoergic channel, ArO⁺(²Π) + O⁺(²P), involving the formation of an excited state of the product oxygen monocation. A hint of the involvement of such a channel came from evidence of a threshold in their cross sections for the formation of ArO⁺. The pathway to ArO⁺(²Π) + O⁺(²P) (ΔE = 6.0 eV) was considered a possible candidate for such a threshold due to a Coulombic barrier in the exit channel.¹⁷ Our exoergicity spectrum (Figure 3.7) shows that such a channel, if present at this collision energy, makes only a minor contribution to the ArO⁺ yield.

PSCO-MS experiments using a lower source field to achieve a higher energy resolution in the exoergicity spectrum for this reaction are impractical as the lower source field dramatically reduces the collection efficiency for the translationally energetic O⁺ ions.

3.3.4 Formation of O⁺ and O⁺

Analysis of the dynamics of the product channel generating a pair of O⁺ ions shows these charged species are effectively isotropically scattered about the velocity of the O₂ reactant. Such scattering dynamics confirm that the source of these ion pairs is double electron-transfer (DET). That is, two electrons are transferred from the oxygen molecule to the argon dication, at a significant interspecies separation, resulting in the formation of neutral argon and O₂²⁺. The

O_2^{2+} then dissociates to form O^+ and O^+ . The dissociation of the resulting O_2^{2+} ion should be uniformly distributed in the molecular (O_2) frame, resulting in the scattering of O^+ ions we observe.

As discussed in Section 1.4.2.2, previous experiments indicate that dicationic DET generally occurs *via* a concerted (two-electron-transfer) mechanism in which the product asymptote lies close in energy to the reactant asymptote (<1 eV difference).⁷ To apply this model to the $\text{Ar}^{2+}/\text{O}_2$ collision system we note that the Ar^{2+} ground state (^3P) and first two excited states (^1D and ^1S) have energies of 43.4, 45.1 and 47.5 eV above the ground state of Ar. Considering the products, there are several dissociative states of O_2^{2+} lying between 42 and 46 eV above the ground state of O_2 .⁵³ From these simple energetic considerations we can immediately see that the $\text{Ar}^{2+}/\text{O}_2$ collision system is likely to involve DET as we have product and reactant asymptotes lying close in energy. However, since the polarizability of Ar ($\alpha = 1.6411 \times 10^{-24} \text{ cm}^3$) is slightly larger than the polarizability of O_2 ($\alpha = 1.5689 \times 10^{-24} \text{ cm}^3$) if the DET process is exoergic overall, that is the $\text{Ar} + \text{O}_2^{2+}$ limit lies below the $\text{Ar}^{2+} + \text{O}_2$ asymptote, the reactant and product potentials will not cross in the simple polarization-attraction model outlined above.⁵⁴ Of course, this simple model, with its additional assumption of spherical symmetry, will only provide an approximation to the true potentials, and of course no repulsive character is included. Indeed, there are potential $\text{Ar}^{2+}(^1\text{D}) + \text{O}_2$ and $\text{Ar} + \text{O}_2^{2+}(1^1\Pi_g$ and $1^1\Delta_g)$ reactant and product asymptotes which lie very close in energy. Hence, it is quite possible, since the polarizabilities of O_2 and Ar are very similar, that, given these close lying asymptotes, the potentials cross in the real collision system, particularly when the influence of differing repulsive terms, and the anisotropy, of the true interaction potentials are taken into account. Alternatively, it is possible that this DET reaction is an endothermic process, for which situation the differing polarizabilities will allow a simple curve crossing. Such an endothermic process would have to be facilitated by the collision energy. Such coupling of E_{cm} to the potential energy surface could, for example, allow the formation of $\text{O}_2^{2+}(\text{B}^3\Pi_g)$ from $\text{Ar}^{2+}(^3\text{P})$ ($\Delta E = +0.2$ eV).

Once formed, the O_2^{2+} dissociates to $\text{O}^+ + \text{O}^+$. Lundqvist *et al.*⁵³ studied the formation and dissociation of O_2^{2+} and found O_2^{2+} states that result in dissociation to the first and second dissociation asymptotes ($\text{O}^+ + \text{O}^+$), with kinetic energy releases of 6.9 – 12.7 eV. From analysis of the O^+ ion velocities, the exoergicity of the dissociation of the O_2^{2+} formed in the DET channel (Rxn. 3.IV) was determined to have a broad maximum centred at ~ 8.5 eV with a

FWHM from 6.3 – 11.6 eV. This KER is in good agreement with that determined by Lundqvist *et al.*⁵³

3.4 Conclusions

The collisions of Ar^{2+} and O_2 have been studied using coincidence methods at a collision energy of 4.4 eV. Four bimolecular reaction channels generating pairs of product ions are observed forming: $\text{Ar}^+ + \text{O}_2^+$, $\text{Ar}^+ + \text{O}^+$, $\text{ArO}^+ + \text{O}^+$ and $\text{O}^+ + \text{O}^+$.

The formation of $\text{Ar}^+ + \text{O}_2^+$ is a minor channel involving strong forward scattering and generates O_2^+ in its ground electronic state. This single electron-transfer process is expected to be facile by Landau-Zener arguments, but the relative intensity of this channel is low because the electron-transfer pathways involve multi-electron processes.

The formation of $\text{Ar}^+ + \text{O}^+ + \text{O}$, is the most intense channel resulting from the reaction of Ar^{2+} with O_2 , in agreement with previous experiments. Many different combinations of Ar^{2+} and product electronic states contribute to the flux in this reaction. Major dissociation pathways of the nascent O_2^+ ion involve the first ($\text{O}(^3\text{P}) + \text{O}^+(^4\text{S})$), and second ($\text{O}(^1\text{D}) + \text{O}^+(^4\text{S})$) dissociation limits. Unusually, the experimental results clearly show the involvement of a short-lived collision complex $[\text{ArO}_2]^{2+}$ in this channel.

The formation of O^+ and ArO^+ involves direct abstraction of O^- from O_2 by Ar^{2+} . Scant evidence of the involvement of a collision complex in this bond-forming pathway is apparent. The formation of the first excited state of $\text{ArO}^+(^2\Pi)$, accompanied by $\text{O}^+(^4\text{S})$ is the likely product channel.

The formation of $\text{O}^+ + \text{O}^+$ results from dissociative double electron-transfer *via* the formation of O_2^{2+} . The exoergicity of the O_2^{2+} dissociation, which we can extract from our data, is in good agreement with previous work investigating the unimolecular dissociation of this dication.

3.5 References

- 1 D. F. Mark, F. M. Stuart and M. de Podesta, *Geochim. Cosmochim. Acta*, 2011, **75**, 7494–7501.
- 2 A. G. W. Cameron, *Space Sci. Rev.*, 1973, **15**, 121–146.
- 3 S. A. Stern, *Rev. Geophys.*, 1999, **37**, 453–491.
- 4 A. O. Nier, W. B. Hanson, A. Seiff, M. B. McElroy, N. W. Spencer, R. J. Duckett, T. C. Knight and W. S. Cook, *Science*, 1976, **193**, 786–788.
- 5 D. D. Bogard, R. N. Clayton, K. Marti, T. Owen and G. Turner, in *Space Science Reviews*, eds. R. Kallenbach, J. Geiss and W. K. Hartmann, Springer, Dordrecht, 2001, vol. 12, pp. 425–458.
- 6 R. Thissen, O. Witasse, O. Dutuit, C. S. Wedlund, G. Gronoff and J. Lilensten, *Phys. Chem. Chem. Phys.*, 2011, **13**, 18264–18287.
- 7 M. A. Parkes, J. F. Lockyear and S. D. Price, *Int. J. Mass Spectrom.*, 2009, **280**, 85–92.
- 8 G. Dupeyrat, J. B. Marquette, B. R. Rowe and C. Rebrion, *Int. J. Mass Spectrom. Ion Process.*, 1991, **103**, 149–156.
- 9 H. Störi, E. Alge, H. Villinger, F. Egger and W. Lindinger, *Int. J. Mass Spectrom. Ion Phys.*, 1979, **30**, 263–270.
- 10 B. Friedrich and Z. Herman, *Chem. Phys. Lett.*, 1984, **107**, 375–380.
- 11 W. Lindinger, E. Alge, H. Störi, M. Pahl and R. N. Varney, *J. Chem. Phys.*, 1977, **67**, 3495–3499.
- 12 E. Y. Kamber, P. Jonathan, A. G. Brenton and J. H. Beynon, *J. Phys. B At. Mol. Phys.*, 1987, **20**, 4129–4142.
- 13 G. C. Shields and T. F. Moran, *J. Phys. B At. Mol. Phys.*, 1983, **16**, 3591–3607.
- 14 P. Tosi, R. Correale, W. Lu, S. Falcinelli and D. Bassi, *Phys. Rev. Lett.*, 1999, **82**, 450–452.

- 15 P. Tosi, W. Lu, R. Correale and D. Bassi, *Chem. Phys. Lett.*, 1999, **310**, 180–182.
- 16 W. Lu, P. Tosi and D. Bassi, *J. Chem. Phys.*, 2000, **112**, 4648–4651.
- 17 D. Ascenzi, P. Franceschi, P. Tosi, D. Bassi, M. Kaczorowska and J. N. Harvey, *J. Chem. Phys.*, 2003, **118**, 2159–2163.
- 18 N. Lambert, D. Kearney, N. Kaltsoyannis and S. D. Price, *J. Am. Chem. Soc.*, 2004, **126**, 3658–3663.
- 19 J. F. Lockyear, K. Douglas, S. D. Price, M. Karwowska, K. J. Fijalkowski, W. Grochala, M. Remeš, J. Roithová and D. Schröder, *J. Phys. Chem. Lett.*, 2010, **1**, 358–362.
- 20 W.-P. Hu, S. M. Harper and S. D. Price, *Meas. Sci. Technol.*, 2002, **13**, 1512–1522.
- 21 W.-P. Hu, S. M. Harper and S. D. Price, *Mol. Phys.*, 2005, **103**, 1809–1819.
- 22 S. M. Harper, W.-P. Hu and S. D. Price, *J. Phys. B At. Mol. Opt. Phys.*, 2002, **35**, 4409–4423.
- 23 S. D. Price, *Int. J. Mass Spectrom.*, 2007, **260**, 1–19.
- 24 Z. Herman, *Int. Rev. Phys. Chem.*, 1996, **15**, 299–324.
- 25 S. A. Rogers, S. D. Price and S. R. Leone, *J. Chem. Phys.*, 1993, **98**, 280–289.
- 26 T. Nakamura, N. Kobayashi and Y. Kaneko, *J. Phys. Soc. Japan*, 1985, **54**, 2774–2775.
- 27 J. F. Lockyear, M. A. Parkes and S. D. Price, *J. Phys. B At. Mol. Opt. Phys.*, 2009, **42**, 145201.
- 28 O. Edqvist, E. Lindholm, L. E. Selin and L. Asbrink, *Phys. Scr. Phys. Scr.*, 1970, **1**, 25–30.
- 29 P. M. Guyon, T. Baer, L. F. A. Ferreira, I. Nenner, A. Tabche-Fouhaile, R. Botter and T. R. Govers, *J. Phys. B At. Mol. Phys.*, 1978, **11**, L141–L144.
- 30 T. Akahori, Y. Morioka, M. Watanabe, T. Hayaishi, K. Ito and M. Nakamura, *J. Phys. B At. Mol. Phys.*, 1985, **18**, 2219–2229.

- 31 X. Tang, G. A. Garcia and L. Nahon, *J. Chem. Phys.*, 2018, **148**, 124309.
- 32 A. Padmanabhan, M. A. MacDonald, C. H. Ryan, L. Zuin and T. J. Reddish, *J. Phys. B At. Mol. Opt. Phys.*, 2010, **43**, 165204.
- 33 A. Mitrushenkov, P. Palmieri, G. Chambaud and P. Rosmus, *Chem. Phys. Lett.*, 2003, **378**, 463–469.
- 34 J. T. Moseley, P. C. Cosby, J. B. Ozenne and J. Durup, *J. Chem. Phys.*, 1979, **70**, 1474–1481.
- 35 A. Kramida, Y. Ralchenko, J. Reader and NIST ASD Team, Eds., *NIST Atomic Spectra Database (version 5.6.1)*, National Institute of Standards and Technology, Gaithersburg, MD, 2020.
- 36 M. A. Parkes, J. F. Lockyear, D. Schröder, J. Roithová and S. D. Price, *Phys. Chem. Chem. Phys.*, 2011, **13**, 18386–18392.
- 37 S. D. Price, *J. Chem. Soc., Faraday Trans.*, 1997, **93**, 2451–2460.
- 38 S. M. Harper, S. W.-P. Hu and S. D. Price, *J. Chem. Phys.*, 2004, **120**, 7245–7248.
- 39 C. L. Ricketts, D. Schröder, J. Roithová, H. Schwarz, R. Thissen, O. Dutuit, J. Žabka, Z. Herman and S. D. Price, *Phys. Chem. Chem. Phys.*, 2008, **10**, 5135–5143.
- 40 M. Evans, S. Stimson, C. Y. Ng and C.-W. Hsu, *J. Chem. Phys.*, 1998, **109**, 1285–1292.
- 41 K. Tanakaa and M. Yoshimine, *J. Chem. Phys.*, 1979, **70**, 1626–1633.
- 42 J. E. Sansonetti and W. C. Martin, *J. Phys. Chem. Ref. Data*, 2005, **34**, 1559–2259.
- 43 I. Velchev, W. Hogervorst and W. Ubachs, *J. Phys. B At. Mol. Opt. Phys.*, 1999, **32**, L511–L516.
- 44 M. Richard-Viard, O. Dutuit, M. Lavollée, T. Govers, P. M. Guyon and J. Durup, *J. Chem. Phys.*, 1985, **82**, 4054–4063.
- 45 P. Baltzer, B. Wannberg, L. Karlsson, M. Carlsson Göthe and M. Larsson, *Phys. Rev. A*, 1992, **45**, 4374–4384.

- 46 K. Ellis, R. I. Hall, L. Avaldi, G. Dawber, A. McConkey, L. Andric and G. C. King, *J. Phys. B At. Mol. Opt. Phys.*, 1994, **27**, 3415–3426.
- 47 M. A. Parkes, J. F. Lockyear, S. D. Price, D. Schröder, J. Roithová and Z. Herman, *Phys. Chem. Chem. Phys.*, 2010, **12**, 6233–6243.
- 48 A. Lafosse, J. C. Brenot, A. V Golovin, P. M. Guyon, K. Hoejrup, J. C. Houver, M. Lebech and D. Dowek, *J. Chem. Phys.*, 2001, **114**, 6605–6617.
- 49 L. J. Frasinski, K. J. Randall and K. Codling, *J. Phys. B At. Mol. Phys*, 1985, **18**, 129–135.
- 50 Z. Herman, *Int. J. Mass Spectrom.*, 2015, **378**, 113–126.
- 51 S. M. McIntyre, J. W. Ferguson and R. S. Houk, *Spectrochim. Acta Part B At. Spectrosc.*, 2011, **66**, 581–587.
- 52 G. Frenking, W. Koch, D. Cremer, J. Gauss and J. F. Liebman, *J. Phys. Chem.*, 1989, **93**, 3410–3418.
- 53 M. Lundqvist, D. Edvardsson, P. Baltzer, M. Larsson and B. Wannberg, *J. Phys. B At. Mol. Opt. Phys.*, 1996, **29**, 499–514.
- 54 J. R. Rumble, Ed., *CRC Handbook of Chemistry and Physics*, CRC Press/Taylor & Francis, Boca Raton, FL, 100th Edit., 2020.

Chapter 4: Bond-Forming and Electron-Transfer Reactivity Between Ar^{2+} and N_2

4.1 Introduction

Following the study of the reactions of $\text{Ar}^{2+} + \text{O}_2$ discussed in Chapter 3,¹ this chapter presents a detailed investigation of the interactions between Ar^{2+} and N_2 . As described previously argon is present in the atmospheres of planets and satellites including the Earth, the Moon and Mars.²⁻⁶ In the upper reaches of these atmospheres, the formation of the Ar^{2+} dication is also likely.⁷ The reactivity of Ar^{2+} -neutral collisions have been studied previously,⁸⁻¹⁴ with most early investigations (carried out at high collision energies) only resulting in the observation of electron-transfer reactivity. In contrast, more recent experiments, utilising lower collision energies (<100 eV) revealed bond-forming chemistry following the interactions of Ar^{2+} with various neutral species.^{1,15-20}

Nitrogen (N_2) is the dominant species in the atmospheres of the Earth and Titan, and is present in the atmospheres of other planets and satellites.^{3-7,21-24} The reactions resulting from collisions of Ar^{2+} with N_2 have been the subject of previous investigation. As noted above, at high collision energies (keV), SET and DET pathways were identified, as expected, although these studies did not probe the reactivity at an electronic state selective level.^{8,10-12,25,26} However, in 1999, Tosi *et al.*¹⁵ observed the formation of ArN^{2+} following the collisions of Ar^{2+} with N_2 , demonstrating a more complex chemistry in this collision system than the earlier studies had indicated. Indeed, molecular ions of ArN have attracted interest due to their rare gas bond and ArN^+ is a well-known contaminant in plasma-based mass spectrometry.²⁷⁻²⁹ The formation of ArN^+ has also been observed as a product of monocation-neutral^{30,31} and dication-neutral reactions.¹⁹ In the latter case, the production of ArN^+ and ArNH^+ was observed following reactions of Ar^{2+} with NH_3 ; the reaction proceeding *via* the formation of a collision complex $[\text{ArNH}_3]^{2+}$. Computational investigations predict ArN^{2+} to be kinetically stable³² whilst ArN^+ is found to have the highest binding energy of the ArX^+ ($\text{X} = \text{Li-Ne}$) species.³³ The stability of ArN^{n+} species, and the facility of dication-neutral reactions to form new bonds, suggests that there is perhaps a richer chemistry resulting from the collisions of Ar^{2+} and N_2 than has been previously reported.

In this investigation we study collisions between Ar^{2+} and N_2 , at a centre-of-mass (CM) collision energy of 5.1 eV, using position-sensitive coincidence mass spectrometry (PSCO-MS). This experimental technique has been shown to provide comprehensive information on the dynamics and energetics of dicationic bimolecular reactions that generate pairs of monocationic products.^{13,34,35} For the $\text{Ar}^{2+}/\text{N}_2$ collision system our experiments reveal the dynamics and energetics of the SET and DET channels, including both dissociative and non-dissociative SET reactions. We see clearly that the dissociative SET reaction proceeds *via* two mechanisms: a long-range direct process, and a process involving the formation of a collision complex, $[\text{Ar-N}_2]^{2+}$. We also report, for the first time, to the best of our knowledge, a bond-forming channel that generates $\text{ArN}^+ + \text{N}^+$ *via* a direct mechanism.

4.2 Experimental details

In the work described in this chapter the Ar^{2+} ions were generated *via* electron ionization of Ar (BOC, 99.998 %) by 100 eV electrons in the ion source. In the TOF-MS source region the beam of dications was crossed with an effusive jet of N_2 (BOC, 99.998 %). The experiments in this work employed both high (183 V cm^{-1}) and low (28.5 V cm^{-1}) TOF-MS source fields. As discussed in more detail below, the lower source field results in better energy resolution in the resulting PSCO-MS data. However, in these low field spectra ions with high transverse (off-axis) velocities do not reach the detector.

4.3 Results and discussion

PSCO-MS spectra were recorded following the collisions of Ar^{2+} with N_2 at $E_{\text{cm}} = 5.1 \text{ eV}$. The ‘pairs’ spectrum revealed the four reaction channels shown in Table 4.1. The most intense channel (Rxn. 4.I) is a non-dissociative single electron-transfer process (NDSET), producing $\text{Ar}^+ + \text{N}_2^+$. A dissociative SET (DSET) reaction, forming $\text{Ar}^+ + \text{N}^+ + \text{N}$ is also observed (Rxn. 4.II) with a slightly lower intensity than the NDSET channel. A bond-forming channel (Rxn. 4.III) is also observed, producing $\text{ArN}^+ + \text{N}^+$. To our knowledge, the formation of ArN^+ from the interactions of Ar^{2+} and N_2 has not been previously observed. Finally, double electron-transfer (DET) is observed resulting in the formation of $\text{N}^+ + \text{N}^+$ *via* N_2^{2+} (Rxn. 4.IV).

PSCO-MS experiments were also repeated at a low TOF-MS source field to yield a higher energy resolution in the exoergicity spectrum ($E_{\text{cm}} = 4.5 \text{ eV}$). As discussed below, these

low source field experiments reveal a minor, low energy release, pathway in the NDSET channel (Rxn. 4.I).

Table 4.1: Reaction channels, following the collisions of Ar^{2+} with N_2 at a CM collision energy of 5.1 eV, with associated relative intensities (branching ratios). The modal experimental values of the total exoergicity ΔE from each reaction are reported. See text for details.

Reaction	Products	Relative intensity / %	Modal experimental ΔE / eV
4.I	$\text{Ar}^+ + \text{N}_2^+$	43.2	5.4
4.II	$\text{Ar}^+ + \text{N}^+ + \text{N}$	41.7	6.5
4.III	$\text{ArN}^+ + \text{N}^+$	4.3	5.5
4.IV	$\text{Ar} + \text{N}^+ + \text{N}^+$	10.8	6.8 [†]

[†]The exoergicity given for Rxn. 4.IV is the value for the $\text{N}_2^{2+} \rightarrow \text{N}^+ + \text{N}^+$ dissociation.

4.3.1 Non-dissociative single electron-transfer

Figure 4.1 shows the CM scattering diagram for the $\text{Ar}^+ + \text{N}_2^+$ product ions observed from the NDSET reaction, $\text{Ar}^{2+} + \text{N}_2 \rightarrow \text{Ar}^+ + \text{N}_2^+$. A forward scattering pattern, typical of that reported before for this class of reaction is observed.^{13,36,37} Forward scattering indicates that the velocity of the Ar^+ product ion is predominantly oriented in the same direction as the velocity of the reactant Ar^{2+} , $w(\text{Ar}^{2+})$, while the velocity of the N_2^+ product ion is directed anti-parallel to $w(\text{Ar}^{2+})$. This scattering pattern is typical of a direct process, where the electron-transfer occurs at a relatively large interspecies separation (3 – 6 Å), and is generally well represented by a Landau-Zener (LZ) formalism.³⁸⁻⁴¹ The scattering angles of the Ar^+ ion (the angle between the velocity of the reactant dication $w(\text{Ar}^{2+})$ and the velocity of the Ar^+ product ion) are shown more clearly in Figure 4.2. Figure 4.2 reveals that whilst the scattering is dominated by $\theta < 90^\circ$, the scattering is not concentrated as intensely at lower angles as might be expected for a typical forward scattered NDSET reaction.^{13,36,37} For example, in the SET reaction between $\text{Ne}^{2+} + \text{Ar}$, also investigated with PSCO-MS, the Ne^+ product was forward scattered with an angular distribution peaked at $\sim 15^\circ$.⁴⁰ There is also a tail in our data, to higher scattering angles, manifested in the scattering diagram (Figure 4.1) by the extra ‘bumps’ involving higher velocity ions scattered between $70 < \theta < 110$. Both of these observations hint strongly that there is a

distinct contribution to the scattering in this channel involving longer-lived association, or a ‘sticky collision’, between the reactant species, in addition to the usual direct (LZ) mechanism. As we will see below, the analysis of the N_2^+ electronic states populated in this NDSET channel, and the dynamics exhibited by the DSET channel, also point towards a contribution from such a non-direct reaction pathway.

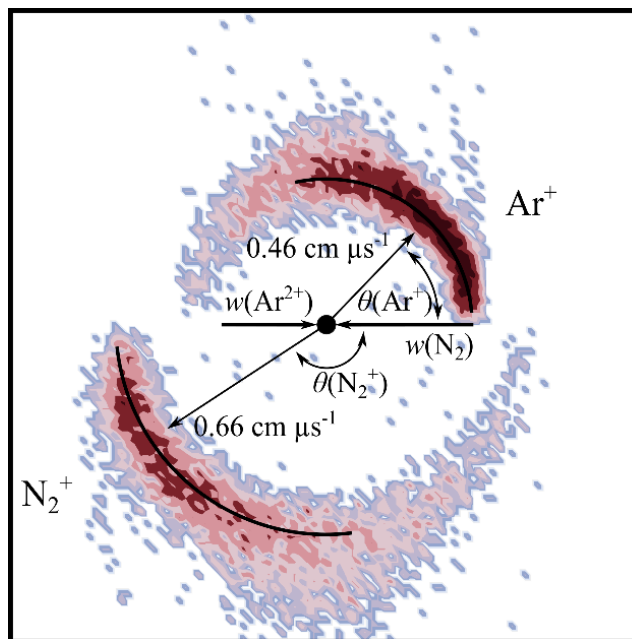


Figure 4.1: CM scattering diagram for the reaction $\text{Ar}^{2+} + \text{N}_2 \rightarrow \text{Ar}^+ + \text{N}_2^+$ at a CM collision energy of 5.1 eV. The black dot indicates the position of the CM. See text for details.

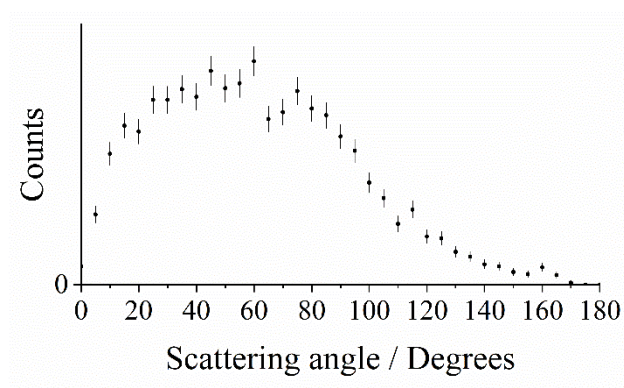


Figure 4.2: Histogram of the CM scattering angle θ for the product Ar^+ ion, relative to $w(\text{Ar}^{2+})$, for the reaction $\text{Ar}^{2+} + \text{N}_2 \rightarrow \text{Ar}^+ + \text{N}_2^+$ at a CM collision energy of 5.1 eV. The error bars represent two standard deviations of the counts.

Figure 4.3 shows a histogram of the exoergicities recorded in the NDSET reaction channel, $\text{Ar}^{2+} + \text{N}_2 \rightarrow \text{Ar}^+ + \text{N}_2^+$. In the exoergicity distribution, there is a maximum centred around 5.8 eV, with a full width at half maximum (FWHM) from 4.1 – 7.2 eV. To interpret the exoergicity spectrum for this channel, we need to consider the accessible electronic states of the reactant and product species. For these species the relevant energetic data is readily available. The Ar^{2+} beam used in this experiment has been shown to be composed of ions in the three electronic states derived from the $\text{Ar}^{2+} p^4$ configuration (^3P , ^1D and ^1S), with relative abundances that are approximately statistical.^{1,42,43} There are two energetically accessible electronic states for the Ar^+ product (^2P and ^2S).⁴⁴ The reactant N_2 molecule, admitted as an effusive beam, will be in its ground vibronic state, $\text{X}^1\Sigma_g^+ \nu = 0$. The ground state of N_2^+ ($\text{X}^2\Sigma_g^+$) lies 15.58 eV above the ground state of N_2 .^{45,46} The lowest energy dissociation asymptote of N_2^+ ($\text{N}^+(^3\text{P}) + \text{N}(^4\text{S})$) lies at 24.3 eV relative to $\text{N}_2(\text{X}^1\Sigma_g^+)$, which corresponds energetically to the energy of $\text{N}_2^+(\text{C}^2\Sigma_u^+ \nu = 3)$.^{44,47} Photoionization studies have shown that N_2^+ states generated with a higher internal energy than 24.3 eV have dissociation lifetimes less than the timescale of our experiment and therefore will not contribute to the N_2^+ counts observed in this channel.^{47–}

50

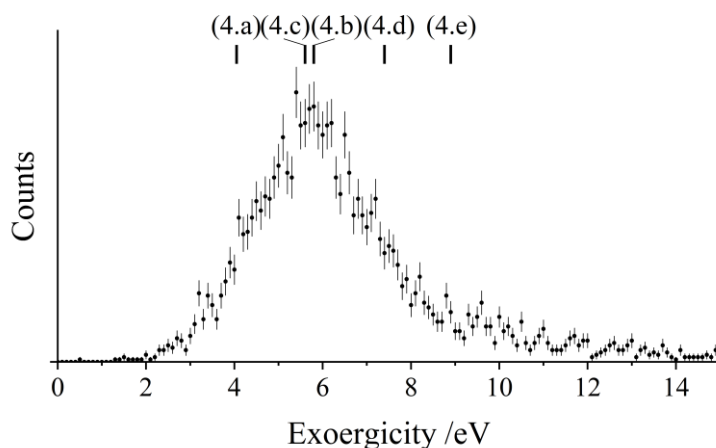
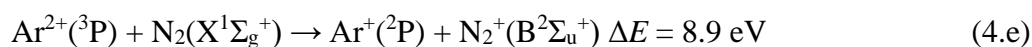
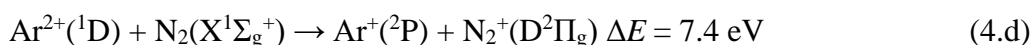
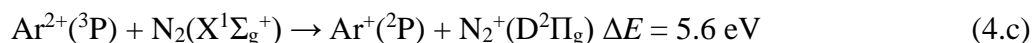
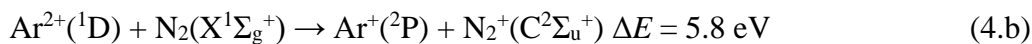
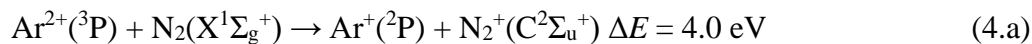


Figure 4.3: Experimental exoergicity spectrum for the reaction $\text{Ar}^{2+} + \text{N}_2 \rightarrow \text{Ar}^+ + \text{N}_2^+$. The exoergicities for potential SET pathways (reactions (4.a) – (4.e), discussed in the text) calculated from literature values are also shown. The error bars represent two standard deviations of the associated counts.

From the above energetic considerations, we find that there are four possible NDSET reaction pathways that match the range of exergicities^{45,46} shown in Figure 4.3: (4.a) – (4.d).

Additionally, whilst pathway (4.e) has an exoergicity (8.9 eV) clearly outside of the observed range, if the N₂⁺(B²Σ_u⁺) product is formed with significant vibrational excitation, it could yield exoergicities in accord with our experimental observations.



The match of the calculated exoergicities of pathways (4.a) – (4.e) with the experimental spectrum is good, particularly when allowing for potential vibrational excitation of the N₂⁺ product ion. Pathways (4.a) – (4.e) are all spin-allowed and involve the formation of the Ar⁺ ion in its ground ²P state; their exoergicities are indicated in Figure 4.3. Reviewing what is known of the N₂⁺ electronic states involved in these pathways is instructive. Photoelectron spectra show low intensities for the formation of N₂⁺(D²Π_g) from N₂ in this energy range due to Franck-Condon effects; in fact the D state is only stable to dissociation at significantly longer bond lengths than that of the neutral molecule. Pathway (4.e) involves ground state Ar²⁺(³P) and forms N₂⁺ in its B²Σ_u⁺ state. As noted above, populating the B²Σ_u⁺ state and giving an exoergicity within the observed range necessitates the state being formed with a high vibrational quantum number. The potential energy surface of the N₂⁺(B²Σ_u⁺) state has a deep well and therefore could support vibrational excitation, however, photoelectron spectra show that the first two vibrational levels, *v* = 0 and *v* = 1, are predominantly populated in a vertical transition.^{45,46}

In our spectra it is not possible to resolve the different N₂⁺ channels potentially involved in this NDSET reaction. Pathways (4.c) – (4.e) involve the formation of N₂⁺(D²Π_g) or vibrationally excited levels of N₂⁺(B²Σ_u⁺). As noted above, such transitions are not favoured in a vertical transition from N₂(X¹Σ_g⁺) and previous experiments studying dicationic electron-transfer have shown that the ionizing transitions in the neutral are often vertical in nature.^{51,52} However, ionizing transitions in the neutral collision partner that produce monocations in vibrational states well outside the Franck-Condon zone have also been reported.⁵³ Additionally, the longer-lived association observed between the reactant species in this channel (identified

above) will facilitate the formation of N_2^+ states away from the equilibrium geometry of N_2 . However, in contrast to pathways (4.c) - (4.e), pathways (4.a) and (4.b) involve the population of the lower vibrational levels of $\text{N}_2^+(\text{C}^2\Sigma_u^+)$, transitions which are favoured in the photoelectron spectra of N_2 , inherently more probable than transitions to the $\text{D}^2\Pi_g$ state or higher vibrational levels of the $\text{B}^2\Sigma_u^+$ state. Thus pathways (4.a) and (4.b), involving $\text{N}_2^+(\text{C}^2\Sigma_u^+)$, are most likely the dominant pathways in the NDSET reaction, but a minor contribution from pathways (4.c) – (4.e) is also possible.

As discussed before in the literature, higher resolution energetic information is obtainable from the PSCO-MS experiment using a low TOF-MS source field.^{13,35,40} In low source field experiments conducted as part of this study, the counts where the Ar^+ ions were forward scattered relative to Ar^{2+} were masked by reactions occurring away from the source region. Thus, only events where the Ar^+ ions were backwards scattered could be selected for analysis. Figure 4.4 shows the resulting exoergicity spectrum of these back-scattered events for the NDSET channel. As previously noted, low source field experiments do not collect product ions with high transverse velocities. Therefore, exoergicity spectra from low source field experiments discriminate in favour of events with lower exoergicities. The exoergicity of the back-scattered events in the low source field experiment (Figure 4.4) ranges from ~2.5 eV – 4.5 eV. The range of exoergicities revealed in Figure 4.4 are clearly present at the low energy extreme of the exoergicity distribution generated by the high source field experiment (Figure 4.3). One way to account for these low exoergicities is to invoke the population of higher energy, long-lived, N_2^+ states than those involved in pathways (4.a) – (4.e). However, given the extensive studies of N_2^+ it is unlikely that there are previously unknown long-lived metastable states of N_2^+ lying above the dissociation asymptote to $\text{N}^+ + \text{N}$.

The formation of stable states of $\text{N}_2^+(\text{X}, \text{A})$ in processes involving low exoergicities (2.7 eV, 1.6 eV) is possible from reactions of $\text{Ar}^{2+}(^1\text{S})$ with N_2 , if $\text{Ar}^+(^2\text{S})$ is generated as the second monocation. However, such processes cannot account for the signals around 3 eV in Figure 4.4. Indeed, $\text{Ar}^{2+}(^1\text{S})$ is a minor component of the dication beam and formation of $\text{Ar}^+(^2\text{S})$ from $\text{Ar}^{2+}(^1\text{S})$ involves a two-electron transition usually a strong indication of a disfavoured process. Thus, we do not feel such reactions can explain the form of the exoergicity spectrum (Figure 4.4) at low exoergicities. A more likely explanation of these low exoergicity processes, generating long-lived N_2^+ ions, is that the $\text{N}_2^+(\text{C}^2\Sigma_u^+)$ state is formed with an energy above the first dissociation limit, before fluorescing to a N_2^+ bound state, most likely $\text{X}^2\Sigma_g^+$.

Populating these higher vibrational levels of the C state will result in the reduced exoergicity we observe. Several of the electronic excited states of N_2^+ higher in energy than $X^2\Sigma_g^+$, including the $\text{N}_2^+(\text{C}^2\Sigma_u^+)$ state, are known to fluoresce to lower-lying electronic states.⁵⁴⁻⁵⁶ Since our energetic analysis above clearly shows population of bound levels of the C state, it is not unreasonable to propose higher levels of the C state are also populated, and these levels then, in competition with their dissociation, fluoresce to result in long-lived N_2^+ ions. In Figure 4.4, there is perhaps a hint of fine structure that could result from the vibrational structure of the N_2^+ state populated in this low exoergicity region. The spacings of these features (Figure 4.4) appear to be of the order of ~ 0.25 eV which is the vibrational spacing of the $\text{N}_2^+(\text{C}^2\Sigma_u^+)$ state.⁴⁵ The competition between fluorescence and predissociation has been studied in depth for $\text{N}_2^+(\text{C}^2\Sigma_u^+)$.^{47,57,58} Predissociation dominates over fluorescence when N_2^+ is formed with more energy than the lowest energy dissociation asymptote (24.3 eV).⁵⁸⁻⁶⁰ However, predissociation of the C state will not generate counts in this NDSET channel, but instead contributes to the counts in the DSET channel, Rxn 4.II., as discussed below. So although the yield of the C state fluorescence is low, the long-lived N_2^+ ions resulting from this emissive process will be sensitively detected in the low-field spectrum.

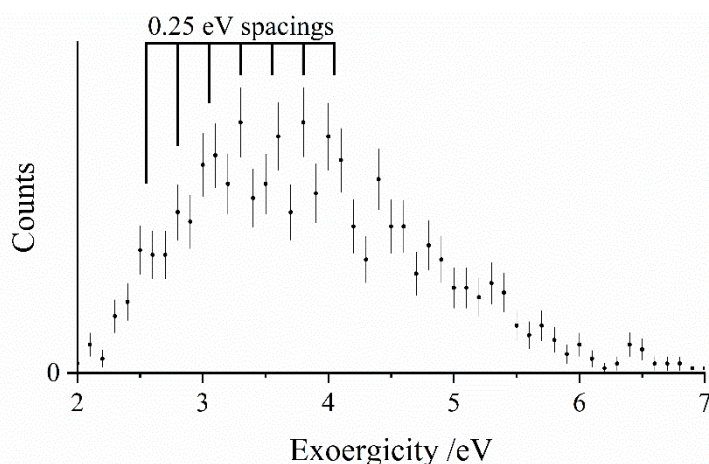


Figure 4.4: Experimental exoergicity spectrum for the back scattered ($\theta(\text{Ar}^+) > 90^\circ$) counts of the NDSET reaction, $\text{Ar}^{2+} + \text{N}_2 \rightarrow \text{Ar}^+ + \text{N}_2^+$, in the low source field experiment. A comb is shown with a line spacing of 0.25 eV. The error bars represent two standard deviations of the associated counts.

To summarise, the NDSET reaction forming $\text{Ar}^+ + \text{N}_2^+$ is the dominant channel resulting from the collisions of Ar^{2+} and N_2 . A broadly forward scattering dynamic was observed,

indicative of a direct, long-range electron-transfer, but with a significant tail to higher scattering angles, indicative of a competitive mechanism involving a longer-lived association between the reactant species. After the electron-transfer, Ar^+ is generated in its ground (^2P) state and N_2^+ is likely predominantly generated in its $\text{C}^2\Sigma_u^+$ state, with perhaps a minor contribution from the $\text{B}^2\Sigma_u^+$ and $\text{D}^2\Pi_g$ states. The high dissociation threshold of N_2^+ and the involvement of the most abundant Ar^{2+} states present in the beam explain why this NDSET reaction is the most intense product channel in the $\text{Ar}^{2+} + \text{N}_2$ collision system.

4.3.2 Dissociative single electron-transfer

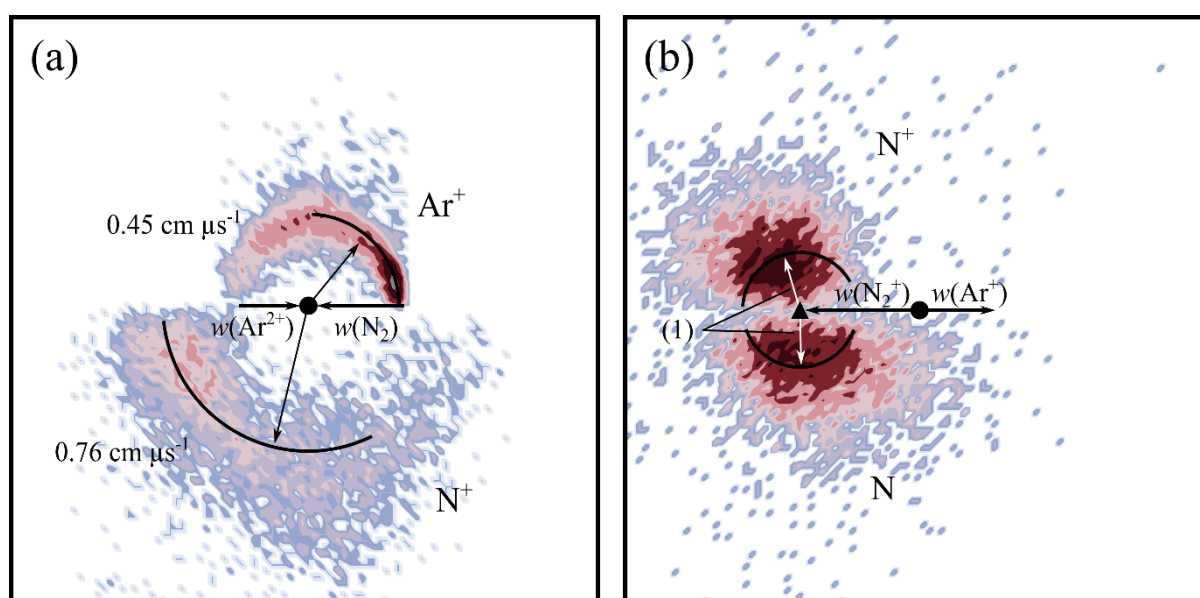


Figure 4.5: Scattering diagrams for the reaction $\text{Ar}^{2+} + \text{N}_2 \rightarrow \text{Ar}^+ + \text{N}^+ + \text{N}$ at a CM collision energy of 5.1 eV. (a) CM scattering diagram showing the scattering of N^+ and Ar^+ relative to the incident dication velocity, $w(\text{Ar}^{2+})$. (b) Internal frame scattering diagram showing the scattering of N^+ and N relative to the velocity of the Ar^+ product ion. In part (b) the labelled vector, (1), represents $0.30 \text{ cm } \mu\text{s}^{-1}$.

The pairs spectrum we record following collisions of Ar^{2+} with N_2 shows a clear peak corresponding to the formation of $\text{Ar}^+ + \text{N}^+$: a DSET reaction. The general mechanism for dicationic DSET reactions has been well investigated,^{13,39,61–63} and involves an initial LZ style single electron-transfer, populating a product cation in a dissociative state (e.g. N_2^{+*}), followed by subsequent dissociation of that ion. In the CM scattering diagram these dynamics result in

strong forward scattering (Figure 4.5a), with the velocity of the Ar^+ product $w(\text{Ar}^+)$ strongly oriented with $w(\text{Ar}^{2+})$. The scattering angles of the Ar^+ ions are shown in more detail in Figure 4.6 which reveals a bimodal distribution: a large peak at low scattering angles, consistent with a direct mechanism, along with an additional broad peak at higher scattering angles. This secondary peak has a broad maximum close to 90° , typical of processes involving isotropic scattering associated with a longer temporal association between the Ar^{2+} and N_2 species. That is, the involvement of a collision complex, as also suggested by the NDSET data discussed above. Again, it seems clear that both a direct mechanism and a mechanism involving complexation are operating in this channel.

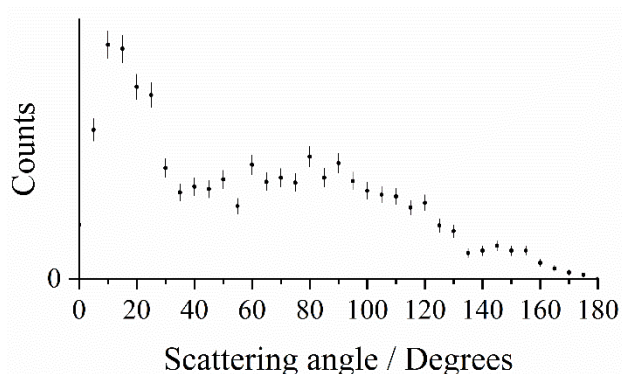


Figure 4.6: Histogram for the CM scattering angles for the product Ar^+ ion, relative to $w(\text{Ar}^{2+})$, for the reaction $\text{Ar}^{2+} + \text{N}_2 \rightarrow \text{Ar}^+ + \text{N}^+ + \text{N}$ at a CM collision energy of 5.1 eV. The error bars represent two standard deviations of the counts.

Figure 4.5b shows the internal frame scattering of the N^+ and N products, relative to the velocity of the Ar^+ product. The N^+ and N fragments are clearly both back-scattered, away from the Ar^+ product ion, confirming that any complex between the N_2 and Ar^{2+} species initially dissociates into $\text{N}_2^{+*} + \text{Ar}^+$. Figure 4.5b also clearly shows that the N^+ ion flies away from the Ar^+ ion with a greater velocity than the N product. Such a signature has been observed before in DSET reactions,^{1,13} and indicates the N_2^{+*} ion dissociates in the Coulomb field of the Ar^+ , and the N^+ product is subsequently further accelerated. An estimate of the lifetime of the N_2^{+*} species generated in this DSET reaction can be determined by a simple electrostatic model to reproduce the additional velocity of the N^+ species with respect to the nitrogen atom. The difference in the velocities of the N^+ and N fragments corresponds to dissociation of the N_2^{+*} at an average distance of $11 \pm 0.5 \text{ \AA}$ from the Ar^+ , equating to an N_2^{+*} lifetime of approximately 100 fs. The N_2^{+*} lifetime value calculated here is comparable to our previous estimates of the

lifetime of N_2^{+*} formed from collisions of Ne^{2+} with N_2 ,⁶¹ as well as that of O_2^{+*} formed in the $\text{Ar}^{2+} + \text{O}_2$ system (Section 3.3.2).¹

The experimentally determined total exoergicity of the DSET reaction, (see Figure 8.2 in Appendix A) for forming $\text{Ar}^+ + \text{N}^+ + \text{N}$, has a peak at 6.5 eV with a FWHM from 4.4 eV – 8.0 eV. The bulk of the counts in this spectrum can be accounted for by contributions from the first and second excited states of Ar^{2+} (^1D and ^1S) forming $\text{N}^+ + \text{N}$ at the three lowest energy dissociation limits of N_2^+ together with an $\text{Ar}^+(^2\text{P})$.^{44,64} The three channels involving $\text{Ar}^{2+}(^1\text{S})$ result in nominal exoergicities of 7.4 eV, 5.5 eV, and 5.0 eV, in good accord with the bulk of the exoergicity distribution. Additionally, minor structure towards lower exoergicities could point to the involvement of $\text{Ar}^{2+}(^3\text{P})$ or $\text{N}^+(^1\text{S})$.

Considering the higher energy events in the exoergicity spectrum (Figure 8.2) we note that, as previously discussed, if N_2^+ is formed with an energy of over 24.33 eV relative to the ground state of N_2 (equivalent to $\text{N}_2^+(\text{C}^2\Sigma_u^+ \nu=3)$) and does not fluoresce, it will dissociate within the lifetime of our experiment and therefore can contribute the DSET channel.⁴⁷⁻⁵⁰ The maximum energy that can be released from $\text{Ar}^{2+}(^1\text{S})$ accepting an electron to form the ground state monocation, $\text{Ar}^+(^2\text{P})$, is 31.75 eV. Therefore, the maximum exoergicity in this channel is 7.42 eV if we restrict ourselves to the p^4 states of Ar^{2+} . There are a significant number of counts observed in this channel above this theoretical maximum of 7.4 eV (~30%, Figure 8.2). These higher energy events are too numerous and extend to too high an energy to be explained by the spread in the translation energy of the Ar^{2+} ions in the beam (FWHM = 0.3 eV). One possible source for these higher energy events is higher lying excited Ar^{2+} energy states in the beam. However, we see little evidence of such states in other channels in this collision system, or in our previous work involving Ar^{2+} .^{1,13,43} However, the clear observation of a significant complexation pathway in this reaction channel provides an explanation for these high energy events. Specifically, if the translational energy of the Ar^{2+} in the beam can be coupled into the reaction, a process that is not normally involved in the direct SET mechanism,³⁴ but is perfectly feasible when complexation is involved, exoergicities of up to ~12.5 eV are perfectly possible. The Ar^+ scattering angle distribution of the high exoergicity events (>7.4 eV) is dominated by the peak centered at 90° , indicating a link with the complexation pathway. Thus, it seems highly likely that the high energy tail in the exoergicity distribution is (yet) another signature of complexation competing with direct electron-transfer in this collision system.

If we consider the DSET reaction to be predominantly stepwise, the exoergicity of the initial electron-transfer step (forming Ar^+ and N_2^{+*}) can be estimated using the N_2^{+*} precursor velocity. The N_2^{+*} precursor velocity is determined, on an event-wise basis, *via* conservation of momentum from the Ar^+ velocity. Using this method, which neglects any small contribution to the Ar^+ velocity from interaction with the final N^+ product, we find the exoergicity for the initial electron-transfer step to have a broad peak centred at 5.0 eV and with a FWHM from 2.9 eV – 6.4 eV, as shown in Figure 4.7. Exoergicity distributions for such primary electron-transfer reactions of dications are commonly peaked between 2 and 6 eV due to such exoergicities favouring the net curve crossing probability as predicted in the LZ model.^{39,65}

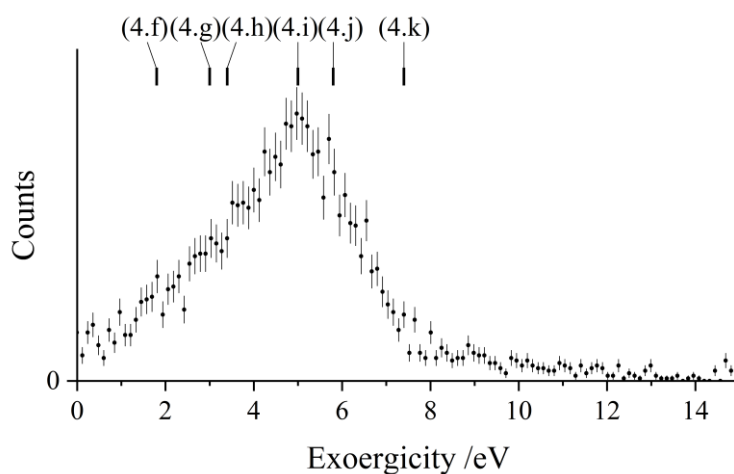


Figure 4.7: Exoergicity spectrum for the initial electron-transfer reaction in the DSET channel, $\text{Ar}^{2+} + \text{N}_2 \rightarrow \text{Ar}^+ + \text{N}_2^{+*}$. The literature exoergicities are identified in Table 4.2. The error bars represent two standard deviations of the associated counts.

As discussed above, this DSET channel, producing $\text{Ar}^+ + \text{N}^+ + \text{N}$, mostly involves $\text{Ar}^{2+}({}^1\text{D}$ and ${}^1\text{S})$, and results in the formation of N_2^{+*} in a dissociative state. The dissociative states of N_2^{+*} that best fit the exoergicity data in Figure 4.7 are: the $\text{C}^2\Sigma_u^+$ state ($v > 2$), the $2^2\Pi_g$ state, and the continuum of the $\text{D}^2\Pi_g$ state ($E \sim 26$ eV), all of which lie in the Franck-Condon region of the N_2 ground state.⁴⁶ Photoelectron spectra from Baltzer *et al.*⁴⁶ show that the $2^2\Pi_g$ state overlaps with the $\text{C}^2\Sigma_u^+$ state around the Franck-Condon region, overlying the D continuum, and these states are therefore indistinguishable in our experiment. We detail in Table 4.2 the possible pathways contributing to this channel, the exoergicities of which are marked on Figure 4.7. Pathways (4.i) and (4.j) match well with the peak of the observed experimental exoergicity distribution, and involve the formation of $\text{N}_2^+(\text{C}^2\Sigma_u^+)$ and $\text{N}_2^+(\text{D}^2\Pi_g)$

respectively. Pathway (4.h) also involves the formation of D²Π_g with Ar²⁺(¹D). There are also possible smaller contributions from pathways (4.f) and (4.g), which populate the higher lying F²Σ_g⁺ and G²Π_u or H²Π_u states of N₂⁺; structures that hint at these reactions can be seen in the exoergicity spectrum (Figure 4.7). Additionally, pathway (4.k) could contribute to this channel, involving Ar²⁺(¹S) generating N₂⁺(C²Σ_u⁺). Of course, the observed exoergicities will be broadened by the population of the N₂⁺ species in a range of vibrational states.

Table 4.2: Exoergicities for primary electron-transfer reactions in the DSET channel, Ar²⁺ + N₂(X¹Σ_g⁺) → Ar⁺(²P) + N₂⁺*, this electron-transfer populates a dissociative state of the molecular nitrogen cation.

Pathway	Ar ²⁺ state	N ₂ ⁺ state	Exoergicity / eV
(4.f)	¹ S	G ² Π _u or H ² Π _u	1.8
(4.g)	¹ S	F ² Σ _g ⁺	3.0
(4.h)	¹ D	D ² Π _g	3.4
(4.i)	¹ D	C ² Σ _u ⁺ at predissociation limit	5.0
(4.j)	¹ S	D ² Π _g	5.8
(4.k)	¹ S	C ² Σ _u ⁺ at predissociation limit	7.4

The exoergicity of the final N₂⁺* dissociation can also be evaluated by determining the velocities of the N⁺ and N products, on an event by event basis, in the frame of the N₂⁺* precursor velocity.¹ This exoergicity spectrum (Figure 4.8) has a maximum at 0.9 eV with a FWHM extending from 0.1 eV – 2.3 eV. To interpret this exoergicity, we must consider previous studies of N₂⁺ dissociation. As noted above, the dissociation threshold, corresponding to the lowest energy N⁺ + N asymptote, L1 (N⁺(³P) + N(⁴S)), Table 4.3), lies at ~24.3 eV above the molecular ground state and corresponds to N₂⁺(C²Σ_u⁺ ν = 3).^{47–49} At energies above the second dissociation limit, L2 (N⁺(¹D) + N(⁴S)), ~26.2 eV, Table 4.3), there is competition between dissociation to L1 and L2.^{64,66,67} In studies of N₂ excitation, at the energies involved in the processes we see in our experiment (24.3 – 32 eV), the C²Σ_u⁺ state is the dominant state populated in photoelectron spectra and dissociation to the three lowest energy dissociation asymptotes is observed, with lifetimes of the order of nanoseconds.^{45,46,50,55,68–71} The

predissociation of N₂⁺(C²Σ_u⁺) is thought to occur *via* several mechanisms including by spin orbit coupling to the ²Σ_u⁻ state then transition to the continuum of ⁴Π_u.^{47,69,72–74}

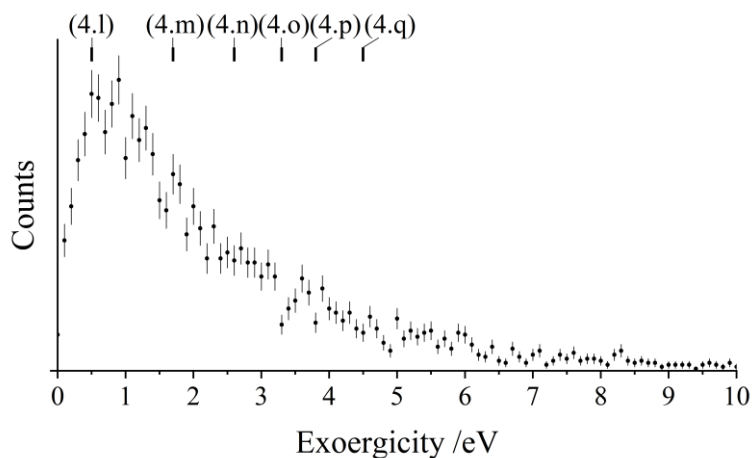


Figure 4.8: Experimental exoergicity spectrum for the dissociation of the N₂⁺* product to form N⁺ and N. The literature exoergicities marked at the top are shown in Table 4.3. The error bars represent two standard deviation of the counts. See text for details.

In previous experiments probing the dissociation of N₂⁺*, produced *via* electron impact or photoionization, kinetic energy releases of 0.5 eV – 8 eV were observed.^{66,75} The maximum theoretical exoergicity for N₂⁺* dissociation in this channel, under the energy constraints of the current study, is 7.4 eV, arising when Ar²⁺(¹S) is involved and N₂⁺* dissociates to the lowest energy dissociation limit, L1. Considering the maximum theoretical exoergicity available in this system (7.4 eV), the exoergicity observed in this study matches nicely with the previous experiments characterising N₂⁺* dissociation.

The shape of the exoergicity spectrum we see for the dissociation of N₂⁺* (Figure 4.8) can be associated with the pathways shown in Table 4.3. The main contributions are clearly from the C²Σ_u⁺ / 2²Π_g or the D²Π_g states dissociating to L1, in satisfying accord with the assignment made above that the initial electron-transfer step populates these ionic states. Additionally there are potentially minor contributions from the involvement some of the higher energy excited states of N₂⁺. These states were also implicated in the above analysis of the initial electron-transfer, showing a coherent description of the electron-transfer state selectivity is emerging.

To summarise, dissociative single electron-transfer is the second most intense channel following the collisions of Ar²⁺ and N₂ at a collision energy of 5.1 eV. The scattering angles of the Ar⁺ product ion (Figure 4.6) show that two mechanisms are involved in the initial electron-transfer: a direct, Landau-Zener process where the electron-transfer occurs at long range, and a process involving the formation of a complex [Ar-N₂]²⁺. In this channel, electron-transfer predominantly involves N₂ and Ar²⁺ (¹D and ¹S), forming Ar⁺(²P), and N₂^{+*} formed in the dissociative C²Σ_u⁺, 2²Π_g and D²Π_g states. These N₂^{+*} ions then fragment, a dissociation slightly perturbed by the field of the Ar⁺ product, primarily to the lowest energy dissociation asymptote, N⁺(³P) + N(⁴S). The lifetime of N₂^{+*} before it dissociates was determined to be ~100 fs, comparable to estimates for N₂^{+*} generated in similar experiments.⁶¹ There is a spread in the observed exoergicities due to minor contributions from the involvement of Ar²⁺(³P), N₂⁺(F²Σ_g⁺) and N₂⁺(G²Π_u or H²Π_u) and higher energy dissociation limits of N⁺ + N.

Table 4.3: Possible exoergicities calculated from literature values for the dissociation of N₂^{+*}. L1, L2 and L3 are the three lowest energy dissociation asymptotes forming N⁺ + N.

Pathway	N ₂ ⁺ state	N ⁺ + N states	Exoergicity / eV
(4.l)	C ² Σ _u ⁺ or 2 ² Π _g at (E = 24.8eV)	N ⁺ (³ P) + N(⁴ S) (L1)	0.5
(4.m)	D ² Π _g	N ⁺ (³ P) + N(⁴ S) (L1)	1.7
(4.n)	F ² Σ _g ⁺	N ⁺ (¹ D) + N(⁴ S) (L2)	2.6
(4.o)	G ² Π _u or H ² Π _u	N ⁺ (³ P) + N(² D) (L3)	3.3
(4.p)	G ² Π _u or H ² Π _u	N ⁺ (¹ D) + N(⁴ S) (L2)	3.8
(4.q)	F ² Σ _g ⁺	N ⁺ (³ P) + N(⁴ S) (L1)	4.5

4.3.3 Chemical bond-formation

Figure 4.9 shows the CM scattering of the ArN⁺ and N⁺ products observed from the previously unreported bond-forming channel, Rxn. 4.III. Figure 4.9 shows that the ArN⁺ product ion is scattered with a marked bias towards lower scattering angles. This bias can be

seen more clearly in the histogram of ArN^+ scattering angles, shown in Figure 4.10. This form of the scattering suggests a stripping-style mechanism where an N^- is transferred between the N_2 and Ar^{2+} species at a relatively large interspecies separation. This style of direct mechanism is similar to that found in our previous work with the analogous channel in the $\text{Ar}^{2+} + \text{O}_2$ system, forming ArO^+ (Section 3.3.3).¹ The more usual mechanism observed for a chemical bond-forming reaction between a dication and neutral species involves a ‘long-lived’ association between the reactant species with a lifetime of at least several rotations of this collision complex.^{36,41} However, direct mechanisms for bond-forming reactions between dications and neutral species have been previously reported.¹³ The scattering data shown here shows little evidence for a long-lived association between the reactants. If such a complex survived for long enough to undergo several rotations, the relationship of the direction of approach of the reactant species would be scrambled and both product fragments would be scattered effectively isotropically about the CM, as has been observed before in other collision systems.^{37,76} It is interesting that formation of ArN^+ from the $\text{Ar}^{2+} + \text{N}_2$ system proceeds *via* a direct mechanism rather than complexation, particularly given the clear evidence of complexation observed in the SET channels. The formation of new chemical bonds via direct processes is well-established in dication reactions and the experimental data clearly imply that complexation does not provide a viable route to populate long-lived states of ArN^+ .

Figure 4.11 shows the experimental exoergicity distribution observed for the bond-forming reaction (Rxn. 4.III). The exoergicity maximum is at 5.5 eV, and the FWHM is from 3.5 eV – 9.0 eV. To interpret this exoergicity we note that several states of ArN^+ have been identified theoretically.^{28,33,77} The ground state, $\text{X}^3\Sigma^-$, and first excited state, $\text{A}^3\Pi$, are both lower in energy than the $\text{Ar}(^1\text{S}) + \text{N}^+(^3\text{P})$ dissociation asymptote and their formation has been reported from the reactions of $\text{N}_2^+ + \text{Ar}$ and $\text{Ar}^+ + \text{N}_2$ respectively.³⁰ Here we will consider just the ground state, $\text{X}^3\Sigma^-$, which is well bound with a significant dissociation energy (~ 2.1 eV). The minimum of the $\text{ArN}^+(\text{A}^3\Pi)$ state lies just below the $\text{Ar}(^1\text{S}) + \text{N}^+(^3\text{P})$ dissociation asymptote. Thus, we would not expect to populate long-lived, and hence detectable, $\text{ArN}^+(\text{A}^3\Pi)$ states with the level of vibrational excitation that we expect to result from a long-range N^- abstraction from N_2 by Ar^{2+} .

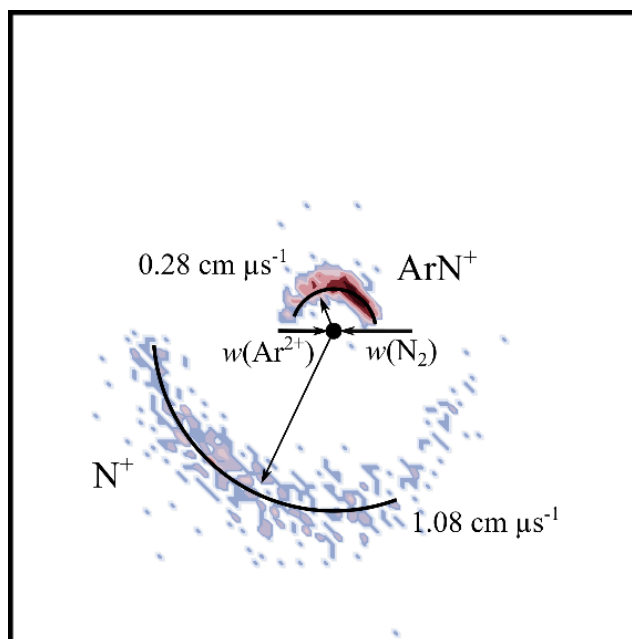


Figure 4.9: CM scattering diagram for the reaction $\text{Ar}^{2+} + \text{N}_2 \rightarrow \text{ArN}^+ + \text{N}^+$ at a CM collision energy of 5.1 eV. The scattering of N^+ and ArN^+ are shown relative to the incident direction velocity, $w(\text{Ar}^{2+})$. See text for details.

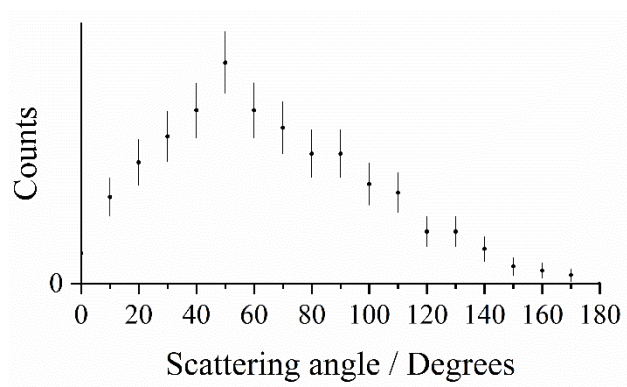


Figure 4.10: Histogram of the CM scattering angles for the product ArN^+ ion, relative to $w(\text{Ar}^{2+})$, for the reaction $\text{Ar}^{2+} + \text{N}_2 \rightarrow \text{ArN}^+ + \text{N}^+$ at a CM collision energy of 5.1 eV. The error bars represent two standard deviations of the counts.

From consideration of the calculated ArN^+ energies and literature values for known N^+ and Ar^{2+} states, reaction pathways (4.r) – (4.t) provide a very good match to the exoergicity distribution observed for this channel.^{33,44} Pathways (4.s) and (4.t) result from the production of $\text{ArN}^+(\text{X}^3\Sigma^-)$ and N^+ in its ground state (^3P) from the two lowest energy Ar^{2+} states in our

beam (³P and ¹D). Pathway (4.r) results in the formation of N⁺ in its first excited state, ¹D. Note that these pathways are all spin allowed. Of course, the formation of vibrationally excited ArN⁺, which we expect due to the long-range N⁻ abstraction from N₂ by Ar²⁺, will act to spread (decrease) the nominal exoergicity of the reaction, in accord with the spread in the exoergicity data in Figure 4.11.

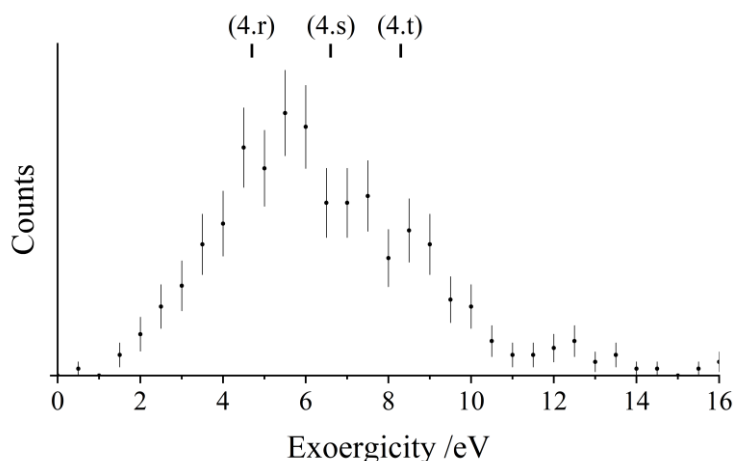
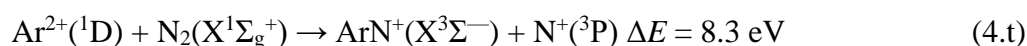
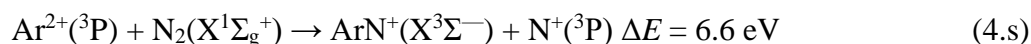
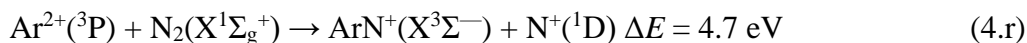


Figure 4.11: Experimental exoergicity spectrum for the reaction producing ArN⁺ and N⁺ from Ar²⁺ and N₂ at a CM collision energy of 5.1 eV. The exoergicities for potential reaction pathways calculated from literature values are shown (reactions (4.r) – (4.t), discussed in the text).^{33,44} The error bars represent two standard deviations of the associated counts. See text for details.

The formation of ArN⁺ from the collisions of Ar²⁺ and N₂ has not been previously reported, to the best of our knowledge. This study therefore offers another potential source for the formation of ArN⁺ species detected in Ar/N₂ plasmas.^{27,28} The scattering shows that, unusually, this reaction proceeds *via* a direct mechanism. The relative intensity for this channel is high (4.3 %) compared with typical bond-forming dication-neutral reactions, showing an affinity to form the Ar-N bond.^{17–19,78–83}

4.3.4 Dissociative double electron-transfer

Rxn. 4.IV from the Ar²⁺/N₂ collision system results in the formation of N⁺ + N⁺ and has a relative intensity of 12.8 %. From the dynamics it is clear that this channel originates from double electron-transfer (DET), *via* the formation of N₂²⁺, as the N⁺ + N⁺ ions are effectively isotropically scattered about the velocity of the N₂ reactant. Such DET reactions are commonly observed in dicationic collision systems,^{13,84,85} where two electrons transfer from N₂ to the Ar²⁺ ion and the nascent N₂²⁺ ion then dissociates. As discussed in Section 1.4.2.2, dicationic DET usually favours a concerted mechanism in which the product and reactant asymptotes lie close in energy (<1 eV).¹³ The Ar²⁺ ground state (³P) and first two excited states (¹D and ¹S) have energies of 43.4 eV, 45.1 eV and 47.5 eV above the ground state of Ar respectively.⁴⁴ There are several dissociative states of N₂²⁺ that lie at a comparable energy to these Ar²⁺ states relative to the ground state of N₂.^{45,86,87} Therefore, concerted DET would be expected to occur in the Ar²⁺ + N₂ system. The dissociation of N₂²⁺ into N⁺ + N⁺ has been well studied. In 1996, Lundqvist *et al.*⁸⁶ reported the kinetic energies of N₂²⁺ dissociation revealing energy releases of 6.7 – 7 eV corresponding to the $\nu = 7-10$ levels of the A¹Π_u state dissociating to the lowest energy N⁺ + N⁺ asymptote, D1(N⁺(³P) + N⁺(³P)). Lundqvist *et al.* also observed peaks at 7.6 and 7.7 eV, corresponding to the N₂²⁺(D³Π_g) $\nu = 0$ and $\nu = 1$ levels dissociating to D1. In Lundqvist's study of the dissociation of N₂²⁺ the dominant contribution is from the lowest energy N⁺ + N⁺ dissociation asymptote.

From analysis of the N⁺ ion velocities, we see the exoergicity for the dissociation of N₂²⁺ in the DET channel has a maximum centred at 7.2 eV with a FWHM from 6.2 – 8.6 eV, shown in Figure 4.12. The experimental exoergicity distribution is a good match with the observations of Lundqvist *et al.*⁸⁶ (see Figure 4.12) and also agrees well with energy releases reported in other studies of N₂²⁺ dissociation.⁸⁸⁻⁹² Therefore, it seems clear that the nascent N₂²⁺ is generated in the A¹Π_u and D³Π_g states which predominantly dissociate to form pairs of N⁺(³P) ions.

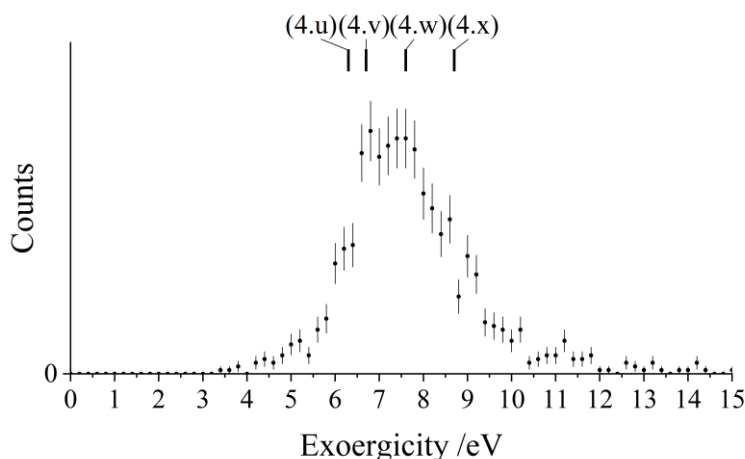


Figure 4.12: Experimental exoergicity spectrum for the dissociation of N_2^{2+} , formed in an initial DET reaction between Ar^{2+} and N_2 , to form N^+ and N^+ . The exoergicities for potential N_2^{2+} dissociation pathways calculated from literature values are also shown: (4.u) $\text{N}_2^{2+}(E = \text{Ar}^{2+}(^1\text{D})) \rightarrow \text{N}^+(^3\text{P}) + \text{N}^+(^3\text{P})$, (4.v) $\text{N}_2^{2+}(\text{A}^1\Pi_u, \nu = 7) \rightarrow \text{N}^+(^3\text{P}) + \text{N}^+(^3\text{P})$, (4.w) $\text{N}_2^{2+}(\text{D}^3\Pi_g, \nu = 0) \rightarrow \text{N}^+(^3\text{P}) + \text{N}^+(^3\text{P})$ and (4.x) $\text{N}_2^{2+}(E = \text{Ar}^{2+}(^1\text{S})) \rightarrow \text{N}^+(^3\text{P}) + \text{N}^+(^3\text{P})$. The error bars represent two standard deviation of the associated counts. See text for details.

4.4 Conclusions

Collisions between Ar^{2+} and N_2 have been studied using a coincidence technique at a CM collision energy of 5.1 eV. Four reaction channels generating pairs of monocations are observed, producing: $\text{Ar}^+ + \text{N}_2^+$, $\text{Ar}^+ + \text{N}^+$, $\text{ArN}^+ + \text{N}^+$ and $\text{N}^+ + \text{N}^+$. The formation of $\text{Ar}^+ + \text{N}_2^+$ is the most intense channel, displaying forward scattering but with a marked tail to higher scattering angles. This scattering is indicative of direct electron-transfer competing with a ‘sticky’ collision between the Ar^{2+} and N_2 reactants. After the electron-transfer, Ar^+ is generated in its ground (^2P) state and N_2^+ is primarily in the low vibrational levels of the $\text{C}^2\Sigma_u^+$ state, with contributions from the $\text{B}^2\Sigma_u^+$ state and $\text{D}^2\Pi_g$ states. The exoergicity distribution in this channel also indicates a minor contribution to the formation of N_2^+ *via* the initial population of higher energy N_2^+ states, lying above the dissociation asymptote to $\text{N}^+ + \text{N}$, which fluoresce to stable states of N_2^+ .

The formation of $\text{Ar}^+ + \text{N}^+$ results from dissociative single electron-transfer. The scattering in this channel again reveals the involvement of the two different pathways for the initial electron-transfer: a long-range direct process, and a process involving the formation of a complex, $[\text{ArN}_2]^{2+}$. Satisfyingly, the operation of these same pathways was extracted from the data for the non-dissociative channel. Despite the differing dynamics, the electronic states involved in this dissociative electron-transfer reaction appear the same for both routes. That is, the excited states of Ar^{2+} (^1D and ^1S) are involved in the initial electron-transfer, populating N_2^{+*} in its dissociative $\text{C}^2\Sigma_u^+$, $2^2\Pi_g$ and $\text{D}^2\Pi_g$ states. The nascent N_2^{+*} then quickly dissociates, primarily to the lowest energy dissociation asymptote, $\text{N}^+(^3\text{P}) + \text{N}(^4\text{S})$.

We also observe the formation of $\text{ArN}^+ + \text{N}^+$ which has not been previously reported. The scattering shows that this bond-forming reaction proceeds *via* a direct mechanism. The molecular ion ArN^+ is formed, with significant vibrational excitation, in its $\text{X}^3\Sigma^-$ state. Finally, the formation of $\text{N}^+ + \text{N}^+$ is observed, resulting from double electron-transfer that initially generates N_2^{2+} which subsequently dissociates. The exoergicity of the N_2^{2+} dissociation is in good agreement with previous studies of the dissociation of the isolated dication, formed in a vertical transition from the neutral molecule, which involve the dissociation of the $\text{A}^1\Pi_u$ and $\text{D}^3\Pi_g$ dication states.

4.5 References

- 1 S. Armenta Butt and S. D. Price, *Phys. Chem. Chem. Phys.*, 2020, **22**, 8391–8400.
- 2 D. F. Mark, F. M. Stuart and M. de Podesta, *Geochim. Cosmochim. Acta*, 2011, **75**, 7494–7501.
- 3 A. G. W. Cameron, *Space Sci. Rev.*, 1973, **15**, 121–146.
- 4 S. A. Stern, *Rev. Geophys.*, 1999, **37**, 453–491.
- 5 A. O. Nier, W. B. Hanson, A. Seiff, M. B. McElroy, N. W. Spencer, R. J. Duckett, T. C. Knight and W. S. Cook, *Science*, 1976, **193**, 786–788.
- 6 D. D. Bogard, R. N. Clayton, K. Marti, T. Owen and G. Turner, in *Space Science Reviews*, eds. R. Kallenbach, J. Geiss and W. K. Hartmann, Springer, Dordrecht, 2001, vol. 12, pp. 425–458.
- 7 R. Thissen, O. Witasse, O. Dutuit, C. S. Wedlund, G. Gronoff and J. Lilensten, *Phys. Chem. Chem. Phys.*, 2011, **13**, 18264–18287.
- 8 G. Dupeyrat, J. B. Marquette, B. R. Rowe and C. Rebrion, *Int. J. Mass Spectrom. Ion Process.*, 1991, **103**, 149–156.
- 9 W. Lindinger, E. Alge, H. Störi, M. Pahl and R. N. Varney, *J. Chem. Phys.*, 1977, **67**, 3495–3499.
- 10 H. Störi, E. Alge, H. Villinger, F. Egger and W. Lindinger, *Int. J. Mass Spectrom. Ion Phys.*, 1979, **30**, 263–270.
- 11 E. Y. Kamber, P. Jonathan, A. G. Brenton and J. H. Beynon, *J. Phys. B At. Mol. Phys.*, 1987, **20**, 4129–4142.
- 12 G. C. Shields and T. F. Moran, *J. Phys. B At. Mol. Phys.*, 1983, **16**, 3591–3607.
- 13 M. A. Parkes, J. F. Lockyear and S. D. Price, *Int. J. Mass Spectrom.*, 2009, **280**, 85–92.
- 14 B. Friedrich and Z. Herman, *Chem. Phys. Lett.*, 1984, **107**, 375–380.
- 15 P. Tosi, R. Correale, W. Lu, S. Falcinelli and D. Bassi, *Phys. Rev. Lett.*, 1999, **82**, 450–

- 452.
- 16 P. Tosi, W. Lu, R. Correale and D. Bassi, *Chem. Phys. Lett.*, 1999, **310**, 180–182.
 - 17 W. Lu, P. Tosi and D. Bassi, *J. Chem. Phys.*, 2000, **112**, 4648–4651.
 - 18 D. Ascenzi, P. Franceschi, P. Tosi, D. Bassi, M. Kaczorowska and J. N. Harvey, *J. Chem. Phys.*, 2003, **118**, 2159–2163.
 - 19 N. Lambert, D. Kearney, N. Kaltsoyannis and S. D. Price, *J. Am. Chem. Soc.*, 2004, **126**, 3658–3663.
 - 20 J. F. Lockyear, K. Douglas, S. D. Price, M. Karwowska, K. J. Fijalkowski, W. Grochala, M. Remeš, J. Roithová and D. Schröder, *J. Phys. Chem. Lett.*, 2010, **1**, 358–362.
 - 21 H. B. Niemann, S. K. Atreya, J. E. Demick, D. Gautier, J. A. Haberman, D. N. Harpold, W. T. Kasprzak, J. I. Lunine, T. C. Owen and F. Raulin, *J. Geophys. Res.*, 2010, **115**, E12006.
 - 22 O. Badr and S. D. Probert, *Appl. Energy*, 1993, **46**, 1–67.
 - 23 E. W. Schwieterman, T. D. Robinson, V. S. Meadows, A. Misra and S. Domagal-Goldman, *Astrophys. J.*, 2015, **810**, 57.
 - 24 O. Dutuit, N. Carrasco, R. Thissen, V. Vuitton, C. Alcaraz, P. Pernot, N. Balucani, P. Casavecchia, A. Canosa, S. Le Picard, J.-C. Loison, Z. Herman, J. Zabka, D. Ascenzi, P. Tosi, P. Franceschi, S. D. Price and P. Lavvas, *Astrophys. J. Suppl. Ser.*, 2013, **204**, 20.
 - 25 D. Smith, D. Grief and N. G. Adams, *Int. J. Mass Spectrom. Ion Phys.*, 1979, **30**, 271–283.
 - 26 H. M. Holzscheiter and D. A. Church, *J. Chem. Phys.*, 1981, **74**, 2313–2318.
 - 27 K. Hu and R. S. Houk, *J. Am. Soc. Mass Spectrom.*, 1993, **4**, 28–37.
 - 28 J. S. Becker, G. Seifert, A. I. Saprykin and H.-J. Dietze, *J. Anal. At. Spectrom.*, 1996, **11**, 643–648.
 - 29 S. C. Wilschefski and M. R. Baxter, *Clin. Biochem. Rev.*, 2019, **40**, 115–133.

- 30 P. Tosi, R. Correale, W. Lu and D. Bassi, *J. Chem. Phys.*, 1999, **110**, 4276–4279.
- 31 G. D. Flesch and C. Y. Ng, *J. Chem. Phys.*, 1990, **92**, 2876–2882.
- 32 M. W. Wong and L. Radom, *J. Phys. Chem.*, 1989, **93**, 6303–6308.
- 33 G. Frenking, W. Koch, D. Cremer, J. Gauss and J. F. Liebman, *J. Phys. Chem.*, 1989, **93**, 3410–3418.
- 34 S. D. Price, J. D. Fletcher, F. E. Gossan and M. A. Parkes, *Int. Rev. Phys. Chem.*, 2017, **36**, 145–183.
- 35 W.-P. Hu, S. M. Harper and S. D. Price, *Meas. Sci. Technol.*, 2002, **13**, 1512–1522.
- 36 Z. Herman, *Int. J. Mass Spectrom.*, 2015, **378**, 113–126.
- 37 M. A. Parkes, J. F. Lockyear and S. D. Price, *Int. J. Mass Spectrom.*, 2014, **365–366**, 68–74.
- 38 S. A. Rogers, S. D. Price and S. R. Leone, *J. Chem. Phys.*, 1993, **98**, 280–289.
- 39 Z. Herman, *Int. Rev. Phys. Chem.*, 1996, **15**, 299–324.
- 40 S. M. Harper, W.-P. Hu and S. D. Price, *J. Phys. B At. Mol. Opt. Phys.*, 2002, **35**, 4409–4423.
- 41 S. D. Price, *Int. J. Mass Spectrom.*, 2007, **260**, 1–19.
- 42 T. Nakamura, N. Kobayashi and Y. Kaneko, *J. Phys. Soc. Japan*, 1985, **54**, 2774–2775.
- 43 J. F. Lockyear, M. A. Parkes and S. D. Price, *J. Phys. B At. Mol. Opt. Phys.*, 2009, **42**, 145201.
- 44 A. Kramida, Y. Ralchenko, J. Reader and NIST ASD Team, Eds., *NIST Atomic Spectra Database (version 5.6.1)*, National Institute of Standards and Technology, Gaithersburg, MD, 2020.
- 45 A. J. Yench, K. Ellis and G. C. King, *J. Electron Spectros. Relat. Phenomena*, 2014, **195**, 160–173.

- 46 P. Baltzer, M. Larsson, L. Karlsson, B. Wannberg and M. Carlsson Göthe, *Phys. Rev. A*, 1992, **46**, 5545–5553.
- 47 H. R. Hrodmarsson, R. Thissen, D. Doweck, G. A. Garcia, L. Nahon and T. R. Govers, *Front. Chem.*, 2019, **7**, 222.
- 48 E. M. Bahati, J. J. Jureta, D. S. Belic, H. Cherkani-Hassani, M. O. Abdellahi and P. Defrance, *J. Phys. B At. Mol. Opt. Phys.*, 2001, **34**, 2963–2973.
- 49 X. Tang, Y. Hou, C. Y. Ng and B. Ruscic, *J. Chem. Phys.*, 2005, **123**, 074330.
- 50 L. Åsbrink and C. Fridh, *Phys. Scr.*, 1974, **9**, 338–340.
- 51 H. R. Koslowski, H. Lebius, V. Staemmler, R. Fink, K. Wiesemann and B. A. Huber, *J. Phys. B At. Mol. Opt. Phys.*, 1991, **24**, 5023–5034.
- 52 A. Ehbrecht, N. Mustafa, C. Ottinger and Z. Herman, *J. Chem. Phys.*, 1996, **105**, 9833–9846.
- 53 E. Y. Kamber, K. Akgüngör, C. P. Safvan and D. Mathur, *Chem. Phys. Lett.*, 1996, **258**, 336–341.
- 54 L. C. Lee, *J. Phys. B At. Mol. Phys.*, 1977, **10**, 3033–3045.
- 55 S. R. Langhoff and C. W. Bauschlicher, *J. Chem. Phys.*, 1988, **88**, 329–336.
- 56 A. Lofthus and P. H. Krupenie, *J. Phys. Chem. Ref. Data*, 1977, **6**, 113–307.
- 57 R. Marx, G. Mauclaire and S. Fenistein, *Chem. Phys. Lett.*, 1975, **33**, 357–361.
- 58 T. R. Govers, C. A. van de Runstraat and F. J. de Heer, *Chem. Phys.*, 1975, **9**, 285–299.
- 59 A. Ehresmann, L. Werner, S. Klumpp, P. V Demekhin, M. P. Lemeshko, V. L. Sukhorukov, K.-H. Schartner and H. Schmoranzner, *J. Phys. B At. Mol. Opt. Phys.*, 2006, **39**, L119.
- 60 C. A. van de Runstraat, F. J. de Heer and T. R. Govers, *Chem. Phys.*, 1974, **3**, 431–450.
- 61 S. M. Harper, S. W.-P. Hu and S. D. Price, *J. Chem. Phys.*, 2004, **120**, 7245–7248.

- 62 S. D. Price, M. Manning and S. R. Leone, *J. Am. Chem. Soc.*, 1994, **116**, 8673–8680.
- 63 C. L. Ricketts, D. Schröder, J. Roithová, H. Schwarz, R. Thissen, O. Dutuit, J. Žabka, Z. Herman and S. D. Price, *Phys. Chem. Chem. Phys.*, 2008, **10**, 5135–5143.
- 64 J. H. . Eland and E. . Duerr, *Chem. Phys.*, 1998, **229**, 13–19.
- 65 S. D. Price, *J. Chem. Soc., Faraday Trans.*, 1997, **93**, 2451–2460.
- 66 T. Aoto, K. Ito, Y. Hikosaka, A. Shibasaki, R. Hirayama, N. Yamamono and E. Miyoshi, *J. Chem. Phys.*, 2006, **124**, 234306.
- 67 Y. Morioka, T. Akahori, T. Hayaishi, T. Namioka, T. Sasaki and M. Nakamura, *J. Phys. B At. Mol. Phys.*, 1986, **19**, 1075–1080.
- 68 R. J. Van Brunt and L. J. Kieffer, *J. Chem. Phys.*, 1975, **63**, 3216–3221.
- 69 J. C. Lorquet and M. Desouter, *Chem. Phys. Lett.*, 1972, **16**, 136–140.
- 70 C. Nicolas, C. Alcaraz, R. Thissen, M. Vervloet and O. Dutuit, *J. Phys. B At. Mol. Opt. Phys.*, 2003, **36**, 2239–2251.
- 71 H. Yoshii, T. Tanaka, Y. Morioka, T. Hayaishi and R. I. Hall, *J. Mol. Spectrosc.*, 1997, **186**, 155–161.
- 72 B. Paulus, J. F. Pérez-Torres and C. Stemmler, *Phys. Rev. A*, 2016, **94**, 053423.
- 73 M. Hochlaf, G. Chambaud and P. Rosmus, *J. Phys. B At. Mol. Opt. Phys.*, 1997, **30**, 4509–4514.
- 74 R. Loch, J. Schopman, H. Wankenne and J. Momigny, *Chem. Phys.*, 1975, **7**, 393–404.
- 75 L. Deleanu and J. A. D. Stockdale, *J. Chem. Phys.*, 1975, **63**, 3898–3906.
- 76 C. L. Ricketts, S. M. Harper, S. W. P. Hu and S. D. Price, *J. Chem. Phys.*, 2005, **123**, 134322.
- 77 L. Broström, M. Larsson, S. Mannervik and D. Sonnek, *J. Chem. Phys.*, 1991, **94**, 2734–2740.

- 78 K. A. Newson and S. D. Price, *Chem. Phys. Lett.*, 1998, **294**, 223–228.
- 79 K. A. Newson, N. Tafadar and S. D. Price, *J. Chem. Soc., Faraday Trans.*, 1998, **94**, 2735–2740.
- 80 P. W. Burnside and S. D. Price, *Int. J. Mass Spectrom.*, 2006, **249–250**, 279–288.
- 81 D. Kearney and S. D. Price, *Phys. Chem. Chem. Phys.*, 2003, **5**, 1575–1583.
- 82 S. M. Harper, S. W. P. Hu and S. D. Price, *J. Chem. Phys.*, 2004, **121**, 3507–3514.
- 83 J. D. Fletcher, M. A. Parkes and S. D. Price, *Int. J. Mass Spectrom.*, 2015, **377**, 101–108.
- 84 M. A. Parkes, J. F. Lockyear and S. D. Price, *Int. J. Mass Spectrom.*, 2013, **354–355**, 39–45.
- 85 J. D. Fletcher, M. A. Parkes and S. D. Price, *Mol. Phys.*, 2015, **113**, 2125–2137.
- 86 M. Lundqvist, D. Edvardsson, P. Baltzer and B. Wannberg, *J. Phys. B At. Mol. Opt. Phys.*, 1996, **29**, 1489–1499.
- 87 M. Hochlaf, R. I. Hall, F. Penent, H. Kjeldsen, P. Lablanquie, M. Lavollée and J. H. D. Eland, *Chem. Phys.*, 1996, **207**, 159–165.
- 88 C. Wu, Y. Yang, Z. Wu, B. Chen, H. Dong, X. Liu, Y. Deng, H. Liu, Y. Liu and Q. Gong, *Phys. Chem. Chem. Phys.*, 2011, **13**, 18398.
- 89 N. Saito and I. H. Suzuki, *J. Phys. B At. Mol. Phys.*, 1987, **20**, L785–L790.
- 90 J. N. Bull, J. W. L. Lee and C. Vallance, *Phys. Rev. A*, 2015, **91**, 022704.
- 91 H. Iwayama, T. Kaneyasu, Y. Hikosaka and E. Shigemasa, *J. Chem. Phys.*, 2016, **145**, 034305.
- 92 W. Eberhardt, E. W. Plummer, I.-W. Lyo, R. Carr and W. K. Ford, *Phys. Rev. Lett.*, 1987, **58**, 207–210.

Chapter 5: Reactivity of S^{2+} with Ar, H_2 and N_2

5.1 Introduction

Sulphur-containing species are found throughout astrophysical environments¹⁻⁴ and on Earth, where they are ubiquitous both in nature and from anthropogenic activities.^{5,6} SF_6 is utilised in high-voltage electronics because of its electrical insulating capabilities.⁷⁻⁹ Processes involving SF_6 are also involved in the etching of semiconductors, resulting in the formation of the S^{2+} dication.⁷ Moreover, SF_6 is a very powerful greenhouse gas with a long atmospheric lifetime and therefore is relevant to atmospheric chemistry. Atmospheric sulphur compounds also contribute to the formation of acid rain and smog.¹⁰ In interstellar clouds, organic compounds containing sulphur have been detected, including species with S-X bonds where X = O, C, N, H.¹ The atomic dication, S^{2+} , has been observed in nebulae close to sources of high energy photons.¹¹⁻¹³ Furthermore, properties of the sulphur dication are relevant in the ionosphere of Io, the satellite of Jupiter, where S^{2+} has been detected by the Galileo¹⁴ and Voyager I^{15,16} spacecraft, as well as by the Hubble telescope.¹⁷ Io's sulphur rich atmosphere is derived from the satellite's intense volcanic activity which results in the expulsion of SO_2 .^{18,19} Indeed, S^{2+} is thought to be one of the major species in the Io torus.²⁰ Charged species generated in Io's ionosphere, such as S^{2+} , are transferred to Jupiter, dominating the Jovian magnetosphere,^{19,21} and the torus of Europa (another satellite of Jupiter).²² Despite this clear relevance of S^{2+} to astrophysical and anthropogenic environments, and the stability of the atomic dication once generated, to the author's knowledge, there have not been any investigations of the bimolecular reactivity of S^{2+} dications in the gas phase. Therefore, the study of the reactions of S^{2+} with neutral molecules presented here is ground-breaking and important to both astrophysical and terrestrial environments.

This chapter details the reactions of S^{2+} with Ar, N_2 and H_2 . H_2 is the most abundant molecule in the universe and is the dominant species comprising the gaseous planets, including Jupiter.²³⁻²⁵ Molecular nitrogen (N_2) is important in the atmospheres of terrestrial bodies in the solar system, especially the Earth and Titan where it is the dominant species.²⁶⁻³⁴ Argon is also often present in significant concentrations in planetary atmospheres.^{27,28,35}

The reactions resulting from dication + Ar collisions have been well studied. SET was observed where the dication was derived from a rare gas; Ne^{2+} , Ar^{2+} , Kr^{2+} or Xe^{2+} .³⁶⁻⁴¹ Collisions between N_2^{2+} and Ar also resulted in the observation of single electron-transfer

(SET) reactions.⁴² Collisions between Ar and hydrogen-containing dications, such as CHX^{2+} ($X = F, Cl, Br, I$), often result in SET and proton-transfer (PT) reactions, forming ArH^+ .^{43–45} Interactions between Ar and SF_x^{2+} ($x = 2 - 4$) or CF_y^{2+} ($y = 1 - 3$) have been the subject of several studies, with SET and collision-induced dissociation (CID) channels being observed.^{46–50} Additionally, Ar + dication reactions have been shown to occasionally produce dications resulting from new bond-formation, such as $HCCAr^{2+}$ and $ArCF_2^{2+}$, detected following collisions of Ar with $C_2H_2^{2+}$ and CF_3^{2+} respectively.^{51,52}

Dication + neutral reactions involving H_2 are relatively well studied at low collision energies (though not with S^{2+}), often resulting in SET reactions. Reactions between Ar^{2+} and H_2 resulted in non-dissociative and dissociative SET (NDSET and DSET respectively).^{36,38,53} With some H-containing dications (for example $CHCl^{2+}$) H^+ transfer is seen, producing H_3^+ *via* the formation of collision complexes.^{54–56} Direct hydride (H^-) transfer from the H_2 to the dication is also seen in some systems.^{55,57} Many other bond-forming channels have also been observed in dication + H_2 reactions, often with evidence that the reactions proceed *via* complexation.^{58–62} Some of the new bonds formed from dication + H_2 reactions include N-H,⁶² H-H,⁵⁶ C-H,^{54,55,57–60} F-H,^{59–61} Cl-H,⁵⁵ and Br-H.⁵⁴ The presence of so many bond-forming reactions in dication + H_2 systems and the prevalence of the S-H bond in nature marks H_2 as a promising candidate for the generation of new bonds following interactions with the S^{2+} dication.

The reactions resulting from dication + N_2 collisions have been the subject of several previous studies, including previous work in this thesis (Chapter 4). In the $Ar^{2+} + N_2$ system, SET, double electron-transfer (DET) and bond-forming pathways have been observed.^{36,38–40,53,63–65} SET channels were also reported from the reactions of N_2 with CO^{2+} and N_2^{2+} .^{66,67} DSET resulting from the collisions of $Ne^{2+} + N_2$ was shown to occur *via* two mechanisms including *via* a collision complex.⁶⁸ Bond-forming reactions have been observed following the interactions of N_2 with the dications $C_4H_3^{2+}$ and O_2^{2+} , resulting in the formation of N-H and N-O bonds respectively.^{56,69} Additionally, S-N bond-formation has been observed resulting from the gas-phase collisions of S^+ ions with ammonia.⁷⁰

In our experiments, we collide S^{2+} with the collision targets using the Position-Sensitive Coincidence Mass Spectrometry (PSCO-MS) apparatus, with centre-of-mass (CM) collision energies of <6 eV. The PSCO-MS apparatus combines the coincident detection of product cations with a crossed-beam collision methodology to give insight into the reactivity and

dynamics resulting from dication-neutral interactions. SET reactions were observed following the interactions of S^{2+} with Ar, N_2 and H_2 , including both non-dissociative and dissociative channels with N_2 and H_2 . The collisions of $S^{2+} + N_2$ also resulted in a bond-forming channel, generating $SN^+ + N^+$ via a collision complex. The DSET channel in the $S^{2+} + H_2$ system reveals dynamics that are evidence for the formation of a collision complex, $[SH_2]^{2+}$.

5.2 Experimental details

The S^{2+} ions used in the experiments described in this chapter were generated by electron ionization of H_2S (CKgas, 99.5 %) by 100 eV electrons in the ion source. Previous investigations show that S^{2+} ($m/z = 16$), HS^{2+} ($m/z = 16.5$), and H_2S^{2+} ($m/z = 17$) dications are all formed following the bombardment of H_2S with electrons.⁷¹ The higher m/z ions were therefore discriminated against with the velocity filter. The neutral gases used for the experiments in this chapter were Ar (BOC, 99.998 %), H_2 (BOC, > 99.995 %), and N_2 (BOC, > 99.998 %). The experiments in this work employed high (183 V cm^{-1}) TOF-MS source fields.

5.3 Results and discussion

5.3.1 The collisions of $S^{2+} + Ar$

PSCO-MS spectra were recorded following the collisions of S^{2+} with Ar at $E_{cm} = 5.3 \text{ eV}$. As with all reactions of S^{2+} , there is no prior literature with which to compare the new results. The only peak in the coincidence ‘pairs’ spectrum, $S^+ + Ar^+$, results from single electron-transfer. Figure 5.1 shows the scattering of the S^+ and Ar^+ product ions from this SET reaction. Figure 5.1 shows strong ‘forward’ scattering, where the velocity of the S^+ product is oriented in the same direction as the velocity of the reactant dication, $w(S^{2+})$. This forward scattering is indicative of a direct, long range electron-transfer, typically well defined by a Landau-Zener (LZ) formalism.^{41,72–74}

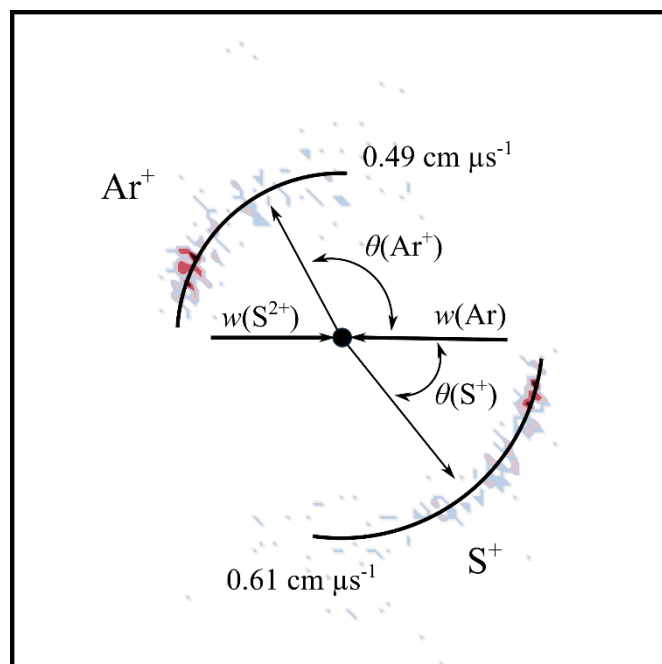


Figure 5.1: CM scattering diagram for the reaction $S^{2+} + Ar \rightarrow S^+ + Ar^+$ at a CM collision energy of 5.3 eV. The black dot indicates the position of the CM. See text for details.

Figure 5.2 shows a histogram for the exoergicities recorded in this SET channel. The bulk of the structure in this spectrum is between 4.8 eV and 7.2 eV. In order to interpret the exoergicity distribution, we must consider the possible reactant and product electronic states involved. Beams of S^{2+} ions generated by EI are not well characterised, but electronic state information is available for the S^{2+} dication from atomic spectroscopy.^{75,76} Electron impact ionization experiments of H_2S have previously reported the formation of S^{2+} , but with no information on the energetics or S^{2+} states populated.^{71,77,78} After the formation of S^{2+} from H_2S *via* electron impact in the source region, the S^{2+} dications must travel through the apparatus to the interaction region where they can collide with Ar. In the time taken to travel to the interaction region ($\sim 100 \mu s$), one would expect S^{2+} formed in unstable higher lying excited states to radiatively decay to lower energy, metastable, states. It seems reasonable that the S^{2+} ions predominantly exist in the beam in one of the $[Ne] 3s^2 3p^2$ states (3P , 1D or 1S). The ground state $S^{2+}(^3P)$ has an energy of 33.7 eV relative to S in its ground state. The excited 1D and 1S states lie 35.1 and 37.1 eV above the ground state of S respectively. S^{2+} also has some higher energy states which are potentially long-lived and could therefore also be present in the beam: the 5S state derived from the $[Ne] 3s^1 3p^3$ configuration, which lies at 41.0 eV above the ground state of S, and the 3F state, derived from the $[Ne] 3s^2 3p^1 3d^1$ configuration, lying at 48.8 eV

above the ground state of S. Emission lines attributed to decay from the 5S state of S^{2+} have been observed experimentally, including in Io.^{79–81} However, the 5S state is metastable, with estimated lifetimes on the order of $\sim 100 \mu s$, and therefore is possibly present in the S^{2+} beam.⁸² The 3F state has a shorter lifetime than 5S , but it is possible that the dication beam also contains $S^{2+}(^3F)$.^{75,82} The ground state of S^+ , 4S lies 10.4 eV above the ground state of $S(^3P)$. If solely the 3P , 1D or 1S states of S^{2+} are involved in a SET reaction with Ar, S^+ can be formed in one of four different electronic states, with energies of less than 21.3 eV above the ground state of S. However, the involvement of the 5S or 3F states of S^{2+} could result in the formation of S^+ states up to 33.1 eV in energy above the ground state of S, of which there are dozens. Ar will be in its ground electronic state, 1S . The energy required to form $Ar^+(^2P)$ from ground state $Ar(^1S)$ is 15.8 eV. If solely the 3P , 1D or 1S states of S^{2+} are involved in a SET reaction with Ar, Ar^+ can only be formed in its ground state, 2P . If the 5S state of S^{2+} is involved, Ar^+ could also be formed in its first excited state, 2S , which lies at 29.2 eV above $Ar(^1S)$. If $S^{2+}(^3F)$ is involved, Ar^+ could be formed in any state with an energy of up to 38.5 eV above the ground state of Ar, of which there are approximately 30. As will be shown below, the $[Ne] 3s^2 3p^2$ states (3P , 1D or 1S) account for most of the reactivity observed with the bimolecular reactions of S^{2+} in this study, however, evidence for the involvement of the higher lying 5S and 3F states are seen in some of the channels.

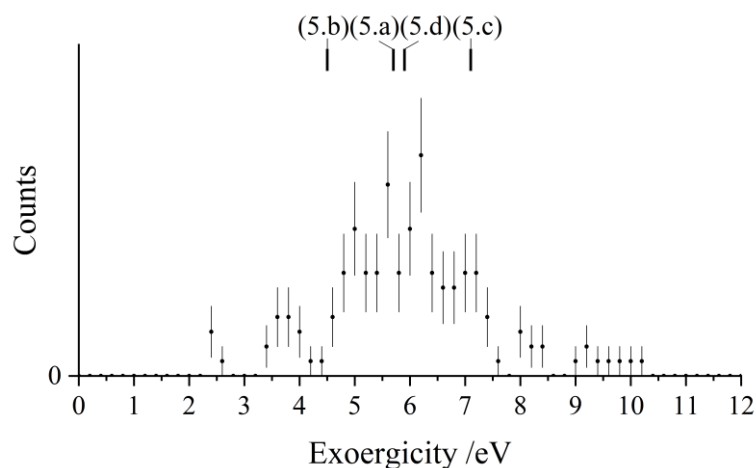
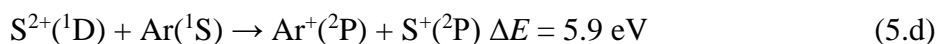
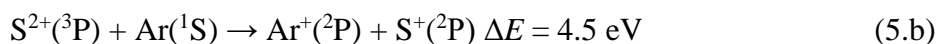


Figure 5.2: Experimental exoergicity spectrum for the reaction $S^{2+} + Ar \rightarrow S^+ + Ar^+$. Calculated exoergicities for the potential SET pathways are also shown (reactions (5.a) – (5.d), discussed in the text). The error bars represent two standard deviations of the associated counts.

Accounting for the above considerations, we find that pathways (5.a) – (5.d) match the observed exoergicity for the SET reaction between S²⁺ and Ar. All these pathways result in the formation of Ar⁺ in its ground, ²P, state. Pathways (5.a) – (5.d) are all spin allowed and their resulting exoergicities are marked in Figure 5.2. Pathway (5.a) involves S²⁺ in its ground, ³P, state and results in the formation of S^{+(2D)}, with an exoergicity of 5.7 eV. Pathway (5.b) also involves S²⁺(³P) but results in the formation of S^{+(2P)}, giving an exoergicity of 4.5 eV. Pathway (5.c) involves S²⁺ in its first excited state, ¹D, and results in the formation of S^{+(2D)}, with an exoergicity of 7.1 eV. Pathway (5.d) also involves S²⁺(¹D) but results in the formation of S^{+(2P)}, giving an exoergicity of 5.9 eV. The range of observed exoergicities in this channel is typical for a LZ governed process.^{73,83}



5.3.2 The collisions of S²⁺ + H₂

PSCO-MS spectra were recorded following the collisions of S²⁺ and H₂ at $E_{\text{cm}} = 0.71 \text{ eV}$. Two reaction channels were observed in the coincidence ‘pairs’ spectrum, both producing pairs of ions, shown in Table 5.1. The dominant channel, Rxn. 5.I, is NDSET, producing S⁺ + H₂⁺. A DSET reaction is also observed (Rxn. 5.II), resulting in the formation of S⁺ + H⁺ + H. As with all reactions of S²⁺, there is no prior literature with which to compare.

There is no peak in the coincidence spectrum resulting from DET. As discussed in Section 1.4.2.2, previous work has shown that in dication-neutral systems, DET is more likely to occur *via* a concerted mechanism in which the reactant and product asymptotes are close in energy (<1 eV).⁸⁴ Whilst the recombination energy from S²⁺ gaining two electrons is enough (> 31.7 eV) to form H⁺ + H⁺ sequentially from H₂, the (vertical) double ionization potential of H₂ is ~51 eV, significantly higher in energy than is available from even the ³F state of S²⁺.^{75,85} Therefore, it is not possible for the S²⁺ + H₂ collisions in our experiment to result in DET *via* a concerted mechanism. The absence of a DET channel in this system despite the exothermicity of such a reaction is in accordance with the idea that in dication-neutral systems, DET is more likely to occur *via* a concerted mechanism.

Table 5.1: Reaction channels following the collisions of S^{2+} with H_2 at a CM collision energy of 0.71 eV, with relative intensities. The modal experimental values of the total exoergicity ΔE from each reaction are reported.

Reaction	Products	Relative intensity / %	Modal experimental ΔE / eV
5.I	$S^+ + H_2^+$	61	5.6
5.II	$S^+ + H^+ + H$	39	12.0

It is notable that there is no peak in the coincidence spectrum corresponding to $SH^+ + H^+$, the products of a chemical bond-forming reaction. SH^+ is observed in star-forming regions⁸⁶ and diffuse interstellar clouds where it is thought to be involved in ion-neutral chemistry resulting in the formation of a range of sulphur containing species.⁸⁷ The formation of $SH^+ + H^+$ from $S^{2+} + H_2$ is exothermic by ~ 9 eV, therefore we might expect to observe $SH^+ + H^+$ in our experiment,^{75,88,89} especially considering the ubiquity of the S-H bond in biological systems, and the propensity of dication + H_2 reactions to result in bond-formation.^{54–62} The fact we do not observe the formation of $SH^+ + H^+$ in our experiment could be that in order to transition to $SH^+ + H^+$, the $S^{2+} + H_2$ system has to traverse a region of the potential energy surface dominated by SET channels. The absence of the observation of SH^+ following the collisions of S^{2+} with H_2 suggests this route is unlikely to contribute to the formation of SH^+ observed in astrophysical environments.

5.3.2.1 Non-dissociative single electron-transfer

The most intense reaction channel that produces a pair of monocations resulting from the collisions of S^{2+} and H_2 is NDSET, forming S^+ and H_2^+ . Figure 5.3 shows the CM scattering of the S^+ and H_2^+ products in this NDSET channel. Figure 5.3 shows a forward scattering pattern, the scattering of the S^+ product ion being broadly oriented with the velocity of the incident dication, $w(S^{2+})$. Conversely, the scattering of the H_2^+ product ion is oriented with $w(H_2)$, anti-parallel to $w(S^{2+})$. This type of scattering is consistent with a direct mechanism of electron-transfer occurring at a significant interspecies separation (3 Å – 6 Å). Forward scattering patterns are commonly observed for other NDSET processes and are generally well represented by a LZ formalism.^{41,72–74}

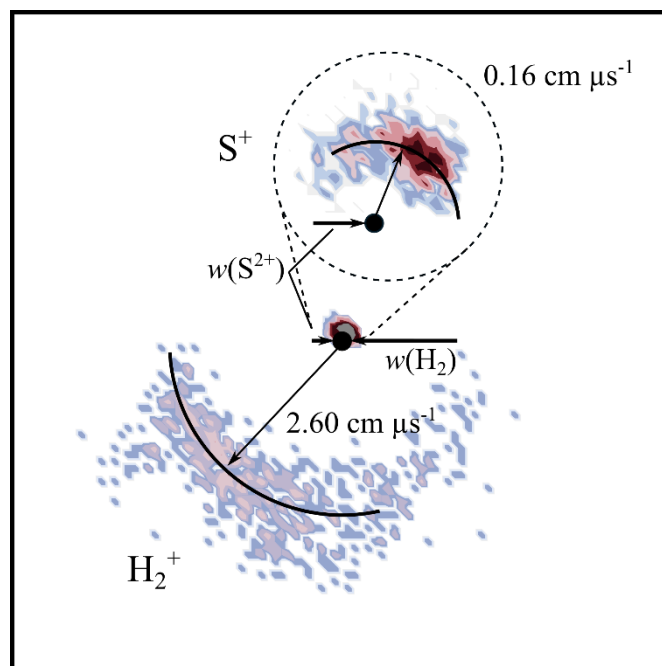


Figure 5.3: CM scattering diagram for the reaction $S^{2+} + H_2 \rightarrow S^+ + H_2^+$ at a CM collision energy of 0.71 eV. The scattering of the S^+ product ion is enlarged for a clearer view. The black dot indicates the position of the CM. See text for details.

The exoergicity distribution of this NDSET channel, shown in Figure 5.4, was determined from the product ion velocities. The exoergicity for the reaction $S^{2+} + H_2 \rightarrow S^+ + H_2^+$ is found to be centred at ~ 6.7 eV, with a full width at half maximum (FWHM) from 4.8 eV – 8.6 eV. To rationalise the exoergicity spectrum in this NDSET reaction we must consider the possible electronic states of the reactant and product species. For this collision system, energetic data are readily available. As in the previous section, looking at the reactions of S^{2+} with Ar, we will assume that dication beam is primarily comprised of S^{2+} in the $3s^2 3p^2$ states (3P , 1D and 1S).⁷⁵ The H_2 , emitted as an effusive beam, will be in its ground vibronic state, $X^1\Sigma_g^+ v = 0$. The ground state of H_2^+ ($X^2\Sigma_g^+$) lies ~ 15.4 eV in energy above $H_2(X^1\Sigma_g^+)$.^{90–92} The lowest energy dissociation asymptote of H_2^+ , the energy at which H_2^+ can dissociate and form $H^+ + H$, is at ~ 18.1 eV, determined from photoelectron and electron ionization experiments.^{93,94} If H_2^+ is formed with energy above this dissociation asymptote it is expected to dissociate within the timescale of our experiment.⁹⁰ Therefore, H_2^+ formed above 18.1 eV would not contribute to the H_2^+ counts in this NDSET channel. Photoelectron spectra show that $H_2^+(X^2\Sigma_g^+)$ has a vibrational progression reaching at least the dissociation asymptote at ~ 18.1 eV.^{95,96} There are metastable excited states of H_2^+ , however, experimental observations are limited.⁹⁷ For

example, there are three bound levels of $H_2^+(A^2\Sigma_u^+)$, lying at ~ 18 eV above the ground state of neutral H_2 , just below the $H^+ + H$ dissociation asymptote, however, the large internuclear separation means that it is not accessible from the H_2 ground state.^{98,99} There are also B and C H_2^+ states, with energies of ~ 27.1 eV and ~ 28.2 eV above H_2 .⁷⁵ These excited states of H_2^+ are not well characterised, as they can't be reached by traditional PES, therefore it is not possible to assess their involvement in this study. However, the involvement of these excited electronic states of H_2^+ would require a two-electron transition from $H_2(X^1\Sigma_g^+)$. In dication + neutral systems, ET processes involving the movement of two electrons are seen to be significantly less likely.¹⁰⁰ Therefore, the involvement of excited H_2^+ states in this channel is unlikely. With just the 3P , 1D and 1S states of S^{2+} involved, NDSET reactions resulting in the formation of S^+ in one of its six lowest energy electronic states are possible for an exothermic process.⁷⁵ The involvement of the 5S or 3F states of S^{2+} could also result in the formation of S^+ states up to 33.1 eV in energy above the ground state of S, of which there are dozens.

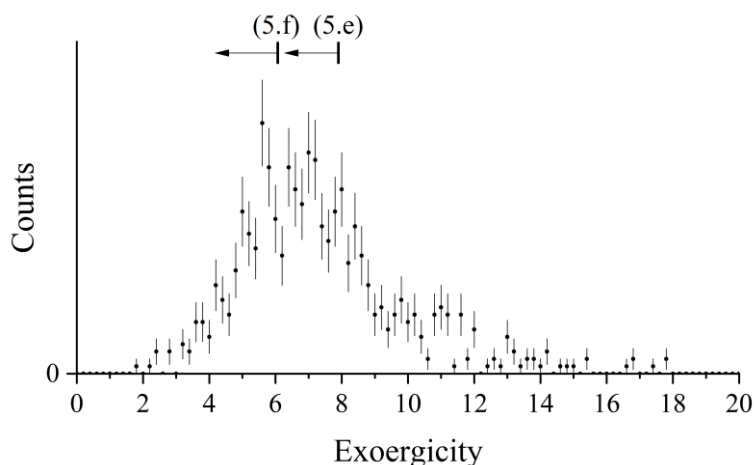
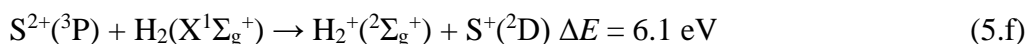
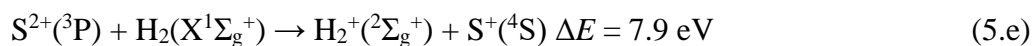


Figure 5.4: Experimental exoergicity spectrum for the reaction $S^{2+} + H_2 \rightarrow S^+ + H_2^+$. The error bars represent two standard deviations of the associated counts. The NDSET pathways indicated ((5.e) and (5.f)) are discussed in the text.

From the above energetic considerations, we find that there are many possible reaction pathways that fall within the range of the observed exoergicities. The reactant dication, S^{2+} , can be involved in any of the $S^{2+} 3s^2 3p^2$ electronic states (3P , 1D and 1S). The H_2^+ product ion is formed in ground state, $X^2\Sigma_g^+$, but could be formed with vibrational excitation, with an energy of anywhere from 15.4 eV ($X^2\Sigma_g^+ v = 0$) to the dissociation limit at ~ 18.1 eV relative to $H_2(X^1\Sigma_g^+)$. The S^+ product ion can be formed in its three lowest energy states: 4S , 2D and 2P .

Photoelectron spectra of H_2 show that H_2^+ is primarily populated from H_2 with an energy of $< \sim 17.5$ eV and therefore it is likely that the H_2^+ formed in this NDSET channel will also be formed in this energy range.^{90,91,95,96} Given this H_2^+ energy range, and the likely distribution of S^{2+} electronic states in the beam, we propose that pathways (5.e) and (5.f) are primarily involved in this NDSET channel. The exoergicities resulting from pathways (5.e) and (5.f) are marked on Figure 5.4, with arrows showing the range due to the variation in the vibrational excitation of H_2^+ . Pathways (5.e) and (5.f) are spin allowed, provide a good match to the observed exoergicity distribution (Figure 5.4) and involve S^{2+} in its ground state. Other states could be involved but we are unable to be more specific due to the large number of possible pathways, especially if the higher energy levels of S^{2+} (5S and 3F) are involved.



5.3.2.2 Dissociative single electron-transfer

The dynamics of the peak in the coincidence spectrum corresponding to the formation of $S^+ + H^+$ reveal that the channel is due to DSET. The established mechanism for dication + neutral DSET reactions is that an initial LZ style electron-transfer generates one (or both) of the product monocations in a dissociative state. The nascent dissociative states subsequently fragment to produce the observed products. Figure 5.5a shows the CM scattering diagram for the S^+ and H^+ products from this DSET channel. It should be noted that because the H^+ is significantly lighter than the S^+ fragment, it takes a large part of the energy and leads to increased uncertainty in the scattering angles of the S^+ . The S^+ is broadly forward scattered but with a tail towards higher angles. This scattering pattern is indicative of a slightly longer-lived association between the reactant species, $[SH_2]^{2+}$. Therefore, this DSET reaction does not follow the standard model of dication + neutral electron-transfer, a phenomenon that we have observed often throughout this thesis, as well as in previous work.^{68,101,102} Electron ionization experiments on H_2S show evidence for H_2S^{2+} states that are energetically accessible by the $S^{2+} + H_2$ reactants in this system, and that dissociate to form $S^+ + H_2^+$.⁷¹ These H_2S^{2+} states could be involved as a short-lived intermediates in this DSET channel.

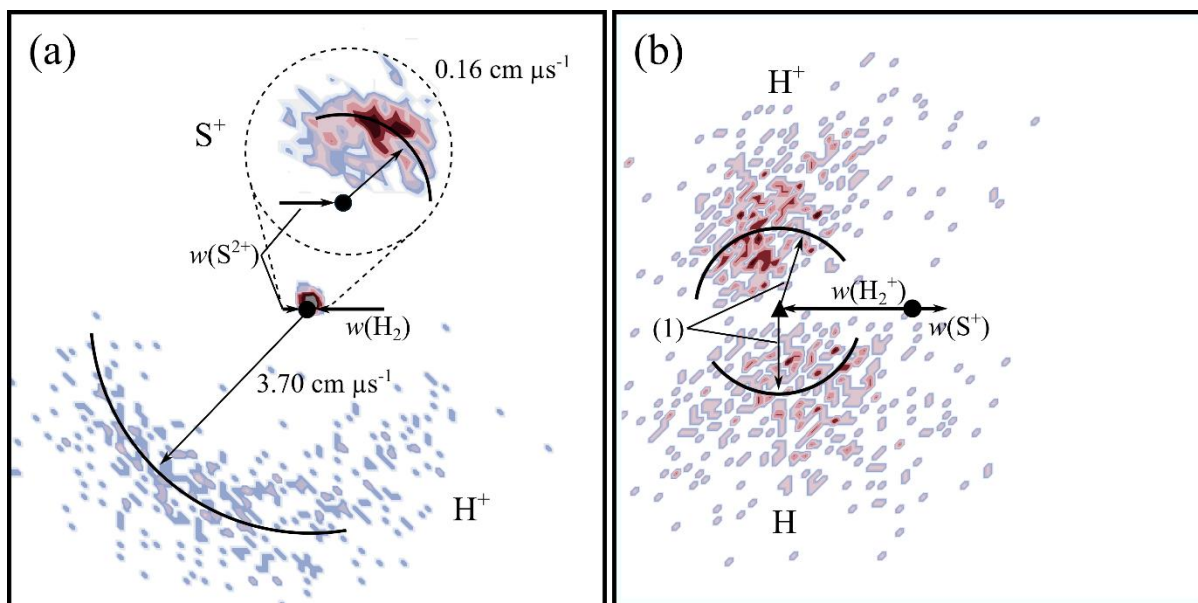


Figure 5.5: Scattering diagrams for the DSET reaction $S^{2+} + H_2 \rightarrow S^+ + H^+ + H$ at a CM collision energy of 0.71 eV. The black dot indicates the position of the CM. (a) CM scattering diagram showing the S^+ and H^+ products relative to the incident dication velocity, $w(S^{2+})$. The scattering of the S^+ product ion is enlarged for a clearer view. (b) Internal frame scattering diagram showing the scattering of H^+ and H relative to $w(S^+)$. The labelled vector (1) = $1.9 \text{ cm } \mu\text{s}^{-1}$.

Figure 5.5b shows the scattering of the H^+ and H fragments relative to the velocity of the S^+ product ion. The H^+ and H fragments are both clearly backward scattered, away from the S^+ ion. This scattering means that the $[SH_2]^{2+}$ complex dissociates into $S^+ + H_2^{+*}$ before the fragmentation of H_2^{+*} . The H^+ fragment ion distribution is slightly more backward scattered (further away from the S^+ product ion) than the H fragment distribution. The H^+ is more backward scattered because the H_2^{+*} ion fragments within the electric field of the S^+ ion, resulting in the H^+ experiencing more acceleration than the H due to Coulomb repulsion. This effect is not as pronounced as for the DSET reactions in previous sections of this thesis, such as in the $Ar^{2+} + N_2$ system.^{65,102}

The total exoergicity observed from this DSET channel is shown in Figure 5.6. The exoergicity distribution has a broad maximum, centred at ~ 10 eV, with a FWHM from 6.5 eV – 15.5 eV. In order to result in the exoergicities observed in this channel, the S^{2+} dication must be in an electronically excited state. Indeed, assuming that the highest energy electronic state of S^{2+} present in the beam is 1S , as discussed above, the maximum exoergicity possible for this

DSET channel should be 8.6 eV (marked by (5.h) in Figure 5.6). The observed exoergicity for this DSET channel clearly exceeds 8.6 eV, and therefore it is likely that S^{2+} ions in higher energy electronic states than (1S) are present in the dication beam: the involvement of $S^{2+}(^5S)$ can give exoergicities up to ~ 12.5 eV, and the involvement of 3F can give exoergicities of up to ~ 20.4 eV. The H atom is primarily formed in its ground electronic state, 2S , because the first excited state of H (2P) is more than 10 eV higher in energy and would therefore significantly reduce the available energy. H^+ only has one ‘electronic state’ because it does not have any electrons. S^+ can be formed in its lowest three energy electronic states: 4S , 2D and 2P .

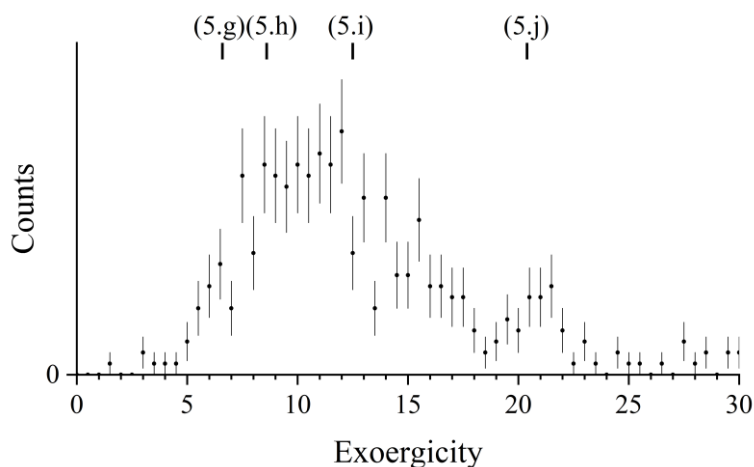
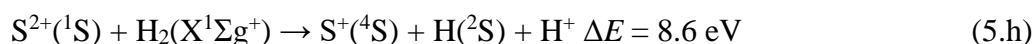
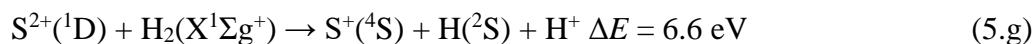
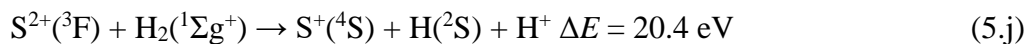
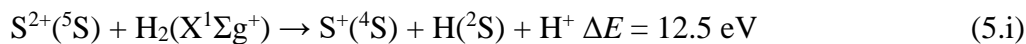


Figure 5.6: Experimental exoergicity spectrum for the reaction $S^{2+} + H_2 \rightarrow S^+ + H^+ + H$. The error bars represent two standard deviations of the associated counts.

The involvement of the electronic states discussed above result in several possible pathways that give exoergicities in the observed range for this channel, four of which are shown in pathways (5.g) – (5.j). Pathways (5.g) – (5.j) result in the formation of S^+ in its lowest electronic state, 4S , from each of the excited states of S^{2+} that could comprise the beam (1D , 1S , 5S , and 3F). The exoergicities resulting from pathways (5.g) – (5.j) are marked on the exoergicity spectrum in Figure 5.6. Of course, the excited S^+ states mentioned above, 2D and 2P , could also be involved. It should be noted that only pathways (5.i) and (5.j) are spin allowed, however, these rules can relax if the mechanism proceeds *via* complexation due to increased coupling.





Conservation of momentum can be used to determine the velocity of the precursor H_2^+ , formed in the initial SET step of this DSET reaction. This precursor velocity can be used to determine the exoergicities of the initial SET step and of the dissociation of H_2^+ . The exoergicities distribution observed from the H_2^+ dissociation, forming $H^+ + H$ is shown in Figure 5.7. The distribution has a FWHM from 0.5 eV – 5.5 eV.

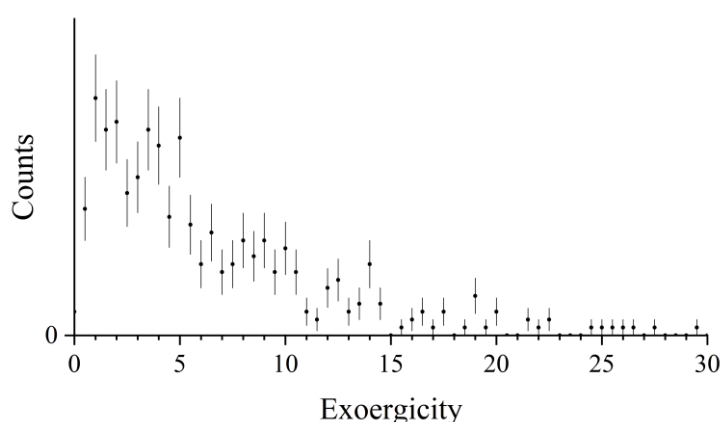


Figure 5.7: Experimental exoergicities spectrum for the dissociation of H_2^+ to form $H^+ + H$. The error bars represent two standard deviation of the counts. See text for details.

In 1986, Cordaro *et al.*⁹⁴ studied the dissociation of H_2^+ produced by electron ionization, observing exoergicities from 2 eV – 8 eV. Strathdee and Browning¹⁰³ observed similar kinetic energy releases, ranging from 4 eV – 10 eV, using 26.9 eV photons. In their study of H_2 electron ionization, Köllmann¹⁰⁴ reported H^+ kinetic energy distributions that correspond to kinetic energy releases ranging from 0 eV – 24 eV resulting from H_2^+ dissociation. The electronic states attributed to these kinetic energy releases were the high vibrational states of $H_2^+(X^2\Sigma_g^+)$ and $H_2^+(A^2\Sigma_u^+)$. Other experiments studying photo- and electron-ionization of H_2 also resulted in the observation of kinetic energy releases from H_2^+ dissociation of up to ~20 eV.^{105–107} The bulk of the exoergicities distribution resulting from H_2^+ dissociation observed in this experiment (Figure 5.7) matches well with Cordaro *et al.*⁹⁴ and Strathdee and Browning,¹⁰³ and the shoulder towards higher exoergicities is in agreement with the distributions observed by Köllmann and others.^{104–107}

As mentioned, if H_2^+ is formed with over ~ 18.1 eV above the ground state of the neutral H_2 molecule, it will dissociate.^{93,94} Our analysis above suggests that only the lowest energy H state is formed (2S). To give exoergicities in the range observed in Figure 5.7, H_2^+ therefore needs to be primarily formed with between 19 eV – 24 eV relative to $H_2(X^1\Sigma_g^+)$. The H_2^+ ion could be populated in the $A^2\Sigma_u^+$ state. However, the geometry of the $A^2\Sigma_u^+$ state in the 19 eV – 24 eV energy range is significantly different to the neutral molecule and would therefore not be expected to be formed in a vertical style transition. Moreover, the formation of $H_2^+(A^2\Sigma_u^+)$ from $H_2(X^1\Sigma_g^+)$ requires the movement of two electrons, which, as discussed above is thought to be significantly less likely.¹⁰⁰ However, both forming the H_2^+ ion with a different geometry to the neutral species, and the movement of two electrons are more feasible if the reaction proceeds *via* a collision complex, as suggested by the scattering pattern. Alternatively, H_2^+ could be formed in the continuum of the $X^2\Sigma_g^+$ state, above the 18.1 eV dissociation asymptote. The involvement of either the $H_2^+(A^2\Sigma_u^+)$ or $H_2^+(X^2\Sigma_g^+)$ states is in good agreement with the H_2^+ dissociation studies discussed above.^{94,104}

The exoergicity of the initial electron-transfer step of this DSET reaction can also be evaluated by using the precursor velocity of the H_2^+ ion. Using this method, the approximate exoergicity distribution for the initial electron-transfer step ($S^{2+} + H_2 \rightarrow S^+ + H_2^{+*}$) was determined, shown in Figure 5.8. The exoergicity distribution has a broad peak centred at ~ 7 eV with a FWHM from 1 eV – 12 eV. The observed exoergicity exceeds the range typical for LZ style processes, providing further evidence that the reaction proceeds *via* a collision complex, as indicated by the scattering.

The observed exoergicities for the initial electron-transfer step (Figure 5.8) align with the exoergicities expected from our above assessment of the likely electronic states involved in this channel. These include the excited states of S^{2+} (1D , 1S , 5S and 3F), the lowest three energy states of S^+ (4S , 2D and 2P), and $H_2^+(A^2\Sigma_u^+)$ or the continuum of the $H_2^+(X^2\Sigma_g^+)$ state. The possible involvement of all these states and the range of vibrational excitation that H_2^+ can be formed with results in too many accessible pathways to determine which specific states are involved.

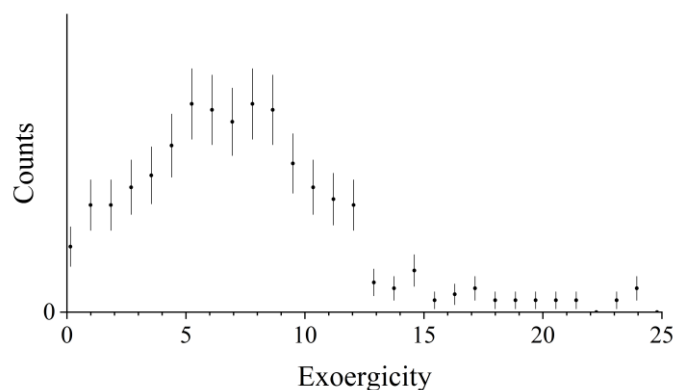


Figure 5.8: Exoergicity spectrum for the initial electron-transfer reaction in the DSET channel, $S^{2+} + H_2 \rightarrow S^+ + H_2^{+*}$. The error bars represent two standard deviations of the associated counts. See text for details.

In summary, DSET occurs following the collisions of $S^{2+} + H_2$, resulting in the formation of $S^+ + H^+$ (+ H). This channel involves S^{2+} in its electronically excited states derived from the $3s^2 3p^2$ electron configuration (1D , 1S) and also shows evidence for the presence of the higher energy S^{2+} states in the beam, 5S and 3F , resulting from the $3s^1 3p^3$ and $3s^2 3p^1 3d^1$ configurations respectively. This DSET channel results in the formation of S^+ primarily in its lowest electronic state (4S), with contributions from the first two excited states, 2D and 2P . The nascent H_2^+ ion is generated with between 19 eV and 24 eV relative to $H_2(X^1\Sigma_g^+)$ before dissociating to the lowest energy dissociation asymptote of $H^+ + H(^2S)$.

5.3.3 The collisions of $S^{2+} + N_2$

PSCO-MS spectra were recorded following the collisions of S^{2+} and N_2 at $E_{cm} = 4.7$ eV. In the coincidence ‘pairs’ spectrum three reaction channels were observed, involving four product ions: S^+ , N_2^+ , N^+ and SN^+ . The three reaction channels, each producing a pair of product ions, are shown in Table 5.2. The dominant channel, Rxn. 5.III, is NDSET, producing $S^+ + N_2^+$. A DSET reaction (Rxn. 5.IV), results in the formation of $S^+ + N^+ + N$. Finally, a bond-forming channel (Rxn. 5.V), producing $SN^+ + N^+$, is observed.

Whilst the PSCO-MS apparatus is optimised for the detection of pairs of ions, we also detect single ion spectra. We do not detect any structure present in the mass spectrum of single ions in the $m/z = 23$ region that could be indicative of SN^{2+} or the $m/z = 30$ region that could be indicative of SN_2^{2+} .

Table 5.2: Reaction channels following the collisions of S^{2+} with N_2 at a CM collision energy of 4.7 eV, with relative intensities. The modal experimental values of the total exoergicity ΔE from each reaction are reported.

Reaction	Products	Relative intensity / %	Modal experimental ΔE / eV
5.III	$S^+ + N_2^+$	98	5.6
5.IV	$S^+ + N^+ + N$	1	a
5.V	$SN^+ + N^+$	1	2.0

^aThe signal-to-noise ratio in Rxn. 5.IV is low and therefore it is difficult to extract meaningful energetic information from this channel.

It is notable that there is no peak in the coincidence spectrum corresponding to $N^+ + N^+$, the products of a dissociative DET reaction. Additionally, in the mass spectrum of single ions there is no structure indicative of a dication resolvable for N_2^{2+} ($m/z = 14$). DET between S^{2+} and N_2 would be not be exothermic with S^{2+} states with energies below $S^{2+}(^3F)$. Moreover, the polarisation of S (2.9) is greater than N_2 (1.7403),¹⁰⁸ therefore, in the concerted model of DET,^{84,102} we would not expect the $S^{2+} + N_2$ and $S + N_2^{2+}$ curves to cross if the $S^{2+} + N_2 \rightarrow S + N_2^{2+}$ reaction was exothermic.

5.3.3.1 Non-dissociative single electron-transfer

Figure 5.9 shows the CM scattering diagram for the $S^+ + N_2^+$ product ions of the NDSET reaction, $S^{2+} + N_2 \rightarrow S^+ + N_2^+$. A strong forward scattering pattern is observed, where the S^+ is oriented in the same direction as $w(S^{2+})$, whilst the N_2^+ product is oriented in the same direction as $w(N_2)$. This scattering pattern is typical of a direct electron-transfer process, occurring at a relatively large interspecies separation (3 Å – 6 Å). Such direct electron-transfer processes are well represented by a Landau-Zener formalism.^{41,72–74}

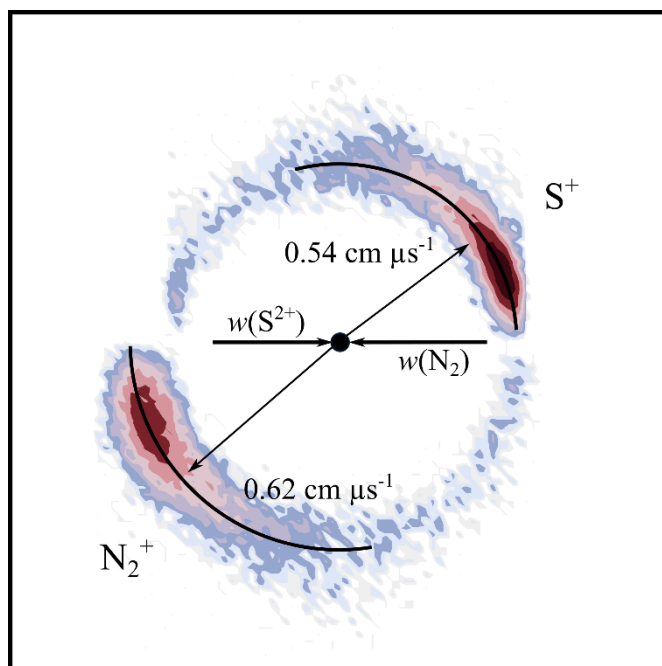


Figure 5.9: CM scattering diagram for the reaction $S^{2+} + N_2 \rightarrow S^+ + N_2^+$ at a CM collision energy of 4.7 eV. The black dot indicates the position of the CM. See text for details.

Figure 5.10 shows a histogram for the exoergicities recorded in this NDSET reaction channel. The spectrum shows a structure with a maximum at 5.6 eV, and a FWHM from 4.3 eV – 6.9 eV. The observed exoergicities are typical for such a LZ style SET reaction.^{73,83} As discussed above, we assume that the dication beam is primarily comprised of S^{2+} in the $3s^2 3p^2$ states; 3P , 1D and 1S . The N_2 reactant will be in its ground vibronic state, $X^1\Sigma_g^+ \nu = 0$. The ground state of N_2^+ , $X^2\Sigma_g^+$, has an energy of 15.58 eV relative to $N_2(X^1\Sigma_g^+)$.^{109,110} If N_2^+ is formed with energies above ~ 24.3 eV relative to $N_2(X^1\Sigma_g^+)$ (corresponding to $N_2^+(C^2\Sigma_u^+ \nu = 3)$), it will be unstable to dissociation *via* the $N^+(^3P) + N(^4S)$ asymptote.^{75,111} Photoionization studies have shown that N_2^+ states generated with more than 24.3 eV relative to $N_2(X^1\Sigma_g^+)$ have dissociation lifetimes less than the timescale of our experiment. Therefore, we do not expect any contribution to the N_2^+ counts observed in this channel from N_2^+ states formed with more than 24.3 eV of energy with respect to N_2 .^{111–114} Electron-transfer occurring between N_2 and any of the 3P , 1D and 1S electronic states of S^{2+} can result in the formation of S^+ in any of the states from the ground state (4S) up to the 4F state, derived from the $[Ne] 3s^2 3p^2 3d^1$ configuration.

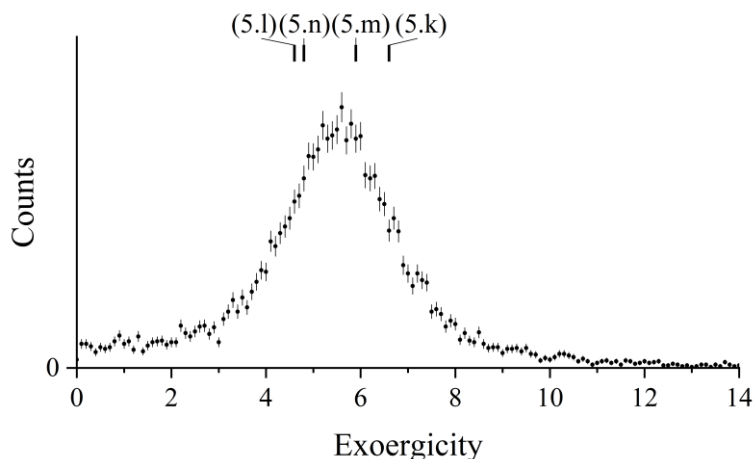
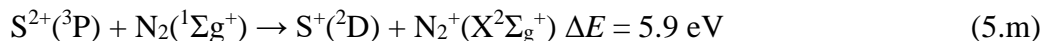
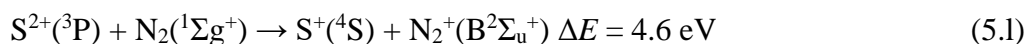


Figure 5.10: Experimental exoergic spectrum for the reaction $S^{2+} + N_2 \rightarrow S^+ + N_2^+$. The error bars represent two standard deviations of the associated counts. The exoergicities resulting from the pathways (5.k) – (5.n) are indicated. See text for details.

Considering the energetics, and accounting for the above, we find that there are many possible electronic pathways involved in the formation of $S^+ + N_2^+$. Some of the possible pathways are shown by (5.k) – (5.n), and their resulting exoergicities are shown on Figure 5.10. Pathways (5.k) – (5.n) involve S^{2+} in its ground electronic state, 3P , however, excited S^{2+} states could also be involved. N_2^+ is likely formed in one of the stable $X^2\Sigma_g^+$, $A^2\Pi_u$ or $B^2\Sigma_u^+$ states, which dominate photoelectron spectra.¹⁰⁹ The lowest two electronic states of S^+ are primarily produced; 4S and 2D . Note, pathways (5.k) – (5.n) are spin allowed.



5.3.3.2 Dissociative single electron-transfer

The peak in the coincidence ‘pairs’ spectrum corresponding to the detection of ions with $m/z = 14$ and $m/z = 32$ is due to the formation of S^+ and N^+ . The peak has very few counts and undoubtedly some result from noise, so it is only possible to see the dynamics and exoergicities involved at a low resolution. In order to discriminate against some of the counts arising from noise, the counts that gave exoergicities over 20 eV were removed.

Figure 5.11a shows the CM scattering diagram for the S^+ and N^+ products resulting from this channel. The S^+ ions are broadly forward scattered, however, there is scattering to higher angles. Conversely, the N^+ ions are broadly backscattered, with some ions scattered towards lower angles. One might expect a higher concentration of forward scattering if this channel resulted from a direct, LZ style electron-transfer. The presence of scattering to higher angles could be evidence of the involvement of a collision complex, however, due to the low intensity signal in this channel, it is difficult to be conclusive. Figure 5.11b shows the internal frame scattering of the N^+ and N products relative to the S^+ product ion. The N^+ and N ions are scattered around the expected precursor velocity of the N_2^+ intermediate, confirming the mechanism of this channel as DSET. SET occurs, producing N_2^{+*} in a dissociative state (and S^+), before dissociating to form $N^+ + N$. In Figure 5.11b the N^+ is scattered away from the S^+ with a higher velocity than the N fragment. This uneven scattering of the N^+ and N fragments is because the N_2^{+*} species dissociates quickly, within the electric field of the S^+ , where Coulomb repulsion accelerates only the N^+ ion.

The total exoergicity resulting from this DSET channel has a structure between 0.5 and 11.0 eV. Note that due to the low intensity and signal to noise ratio, the energy resolution is low, and our conclusions must be tentative. It is not common to see energy releases of less than 2 eV for reactions involving LZ style ET, however, as discussed above, the scattering could suggest a more complicated mechanism. The formation of $N^+ + S^+ + N$ resulting from the ground state of S^{2+} (3P) is endothermic, therefore the presence of this channel again confirms the existence of electronically excited states of S^{2+} in the dication beam. Indeed, the requirement of higher energy S^{2+} states accounts for the low intensity of this DSET channel. The involvement of $S^{2+}(^1S)$ can result in exoergicities in this DSET channel of up to 2.4 eV, significantly lower than the bulk of the observed exoergicity distribution. However, the involvement of the 5S and 3F states of S^{2+} can result in exoergicities of up to 6.3 eV and 14.1 eV respectively. Given the high exoergicities observed in this DSET channel, the S^+ , N^+ and N fragments are likely all formed in their ground or lower energy excited electronic states.

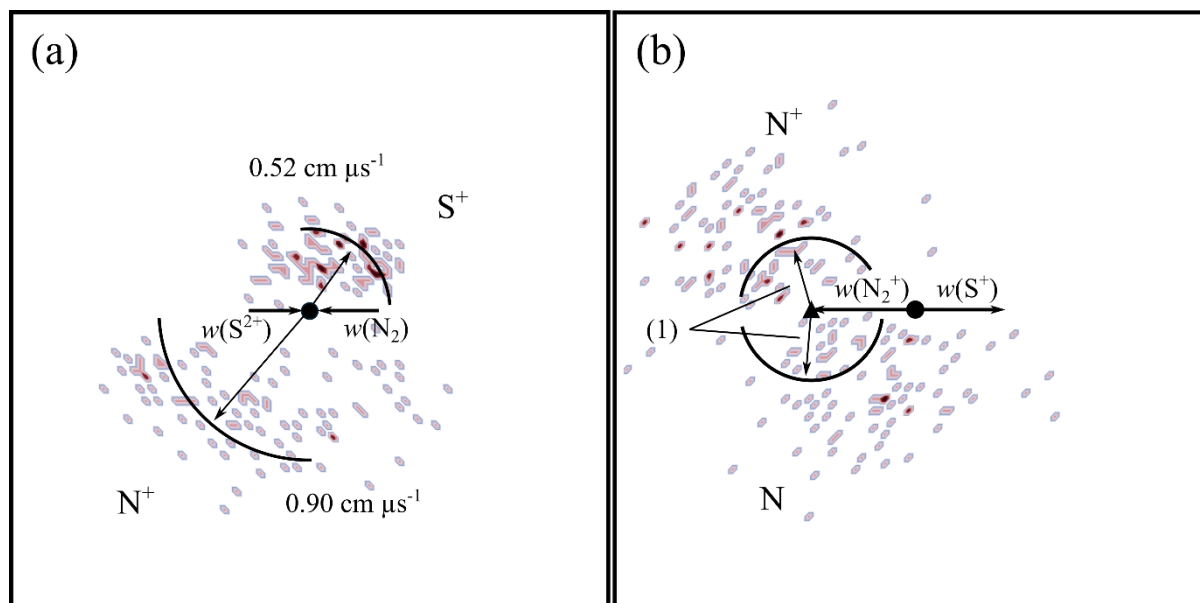


Figure 5.11: Scattering diagrams for the DSET reaction $S^{2+} + N_2 \rightarrow S^+ + N^+ + N$ at a CM collision energy of 4.7 eV. The black dot indicates the position of the CM. (a) CM scattering diagram showing the S^+ and N^+ products relative to the incident dication velocity, $w(S^{2+})$. (b) Internal frame scattering diagram showing the scattering of N^+ and N relative to $w(S^+)$. In part (b) the labelled vector, (1), represents $0.44 \text{ cm } \mu\text{s}^{-1}$.

The exoergicity of the N_2^{+*} dissociation, calculated from the N_2^+ precursor velocity, has structure from 0.3 eV – 4.0 eV. This range of exoergicities is comparable to those observed from N_2^+ dissociation in the DSET channel in our previous experiment between Ar^{2+} and N_2 (Section 4.3.2).⁶⁵ As mentioned above, N_2^+ states generated with more than 24.3 eV above $N_2(X^1\Sigma_g^+)$ are unstable to dissociation and will dissociate within the lifetime of our experiment. Considering the total exoergicity and the N_2^+ dissociation exoergicity, N_2^+ is likely formed with energies of 25 eV – 29 eV above $N_2(X^1\Sigma_g^+)$ and primarily dissociates to the lowest energy $N^+ + N$ asymptote, with both N^+ and N in their ground electronic states.

5.3.3.3 Chemical bond-formation

The peak in the ‘pairs’ spectrum corresponding to the ions $m/z = 46$ and $m/z = 14$ is due to the detection of SN^+ and N^+ , resulting from a bond-forming channel (Rxn. 5.V). The SN^+ molecular ion is relevant to a range of astrophysical environments, including in comets and nebulae.^{115–119} SN^+ is also relevant terrestrially, in manmade plasmas.¹²⁰

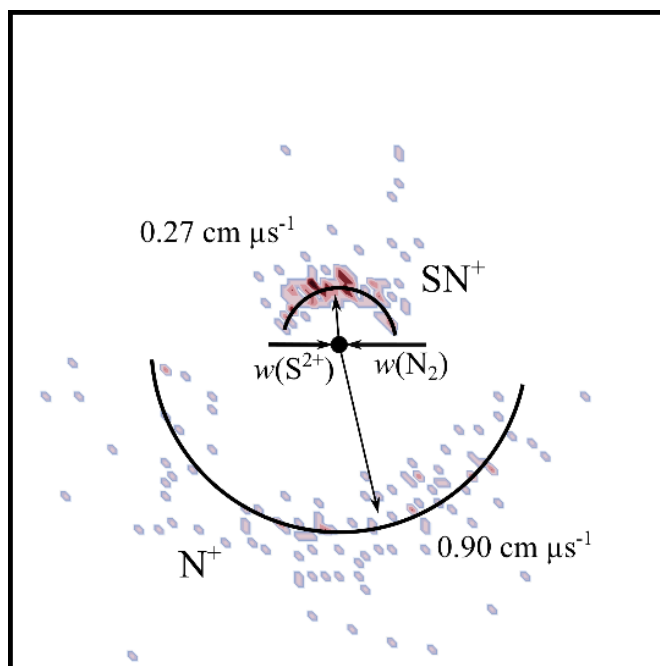
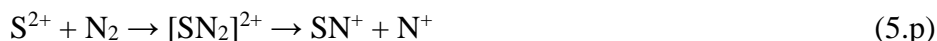


Figure 5.12: CM scattering diagram for the reaction $S^{2+} + N_2 \rightarrow SN^+ + N^+$ at a CM collision energy of 4.7 eV. The black dot indicates the position of the CM. See text for details.

Figure 5.12 shows the CM scattering for the SN^+ and N^+ product ions in this channel, showing an isotropic scattering pattern throughout 180° . Such scattering is strong evidence for the involvement of an intermediate, long-lived, collision complex, $[SN_2]^{2+}$. The collision complex exists for at least several rotations, before fragmenting into SN^+ and N^+ , as shown in (5.p). There is no structure in the mass spectrum of single ions at $m/z = 30$ that corresponds to the SN_2^{2+} collision complex, therefore it dissociates within the timescale of the experiment.



The exoergicity of Rxn. 5.V, determined from the product ion velocities, is shown in Figure 5.13. The exoergicity distribution has a maximum at 2.0 eV with a FWHM from 0.5 eV – 4.5 eV. In order to rationalise the observed exoergicities, we must consider the possible electronic states of the reactant and product species. Due to its astrophysical relevance, the SN^+ species has been the subject of experimental studies.^{118,121,122} Several theoretical studies have also investigated the electronic states of SN^+ .^{119,123–125} In this work we use the electronic state data calculated by Ben Yaghlane & Hochlaf (2009),¹¹⁹ as it provides the most comprehensive theoretical study. The SN^+ ground state ($X^1\Sigma^+$) lies ~ 6.3 eV below the lowest energy dissociation asymptote of $S^+(^4S) + N(^4S)$, and ~ 8.3 eV below the second lowest energy

dissociation asymptote of $S^+(^2D) + N(^4S)$. There are many other bound SN^+ electronic states lying below these dissociation asymptotes, several with well depths deep enough to sustain vibrational excitation. Again, we assume that the dication beam is primarily comprised of the 3P , 1D and 1S states of S^{2+} , and N_2 is in its ground vibronic state ($^1\Sigma_g^+$). N^+ can therefore be formed in any of its four lowest energy electronic states.

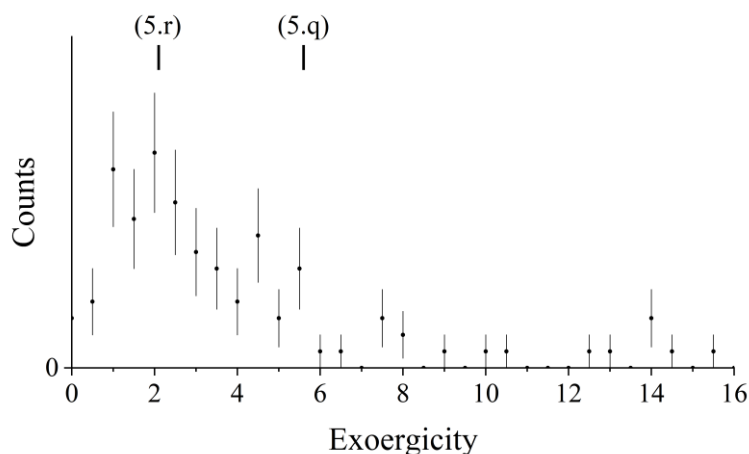
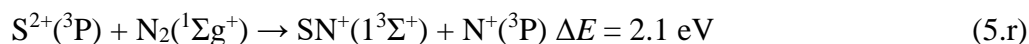
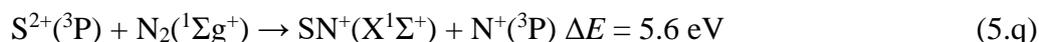


Figure 5.13: Experimental exoergicity spectrum for the reaction $S^{2+} + N_2 \rightarrow SN^+ + N^+$. The error bars represent two standard deviations of the associated counts. The exoergicities of potential reaction pathways (5.r) and (5.q) are indicated. See text for details.

Considering the above, there are a large number of pathways that match the observed exoergicity of this bond-forming channel. Two of the possible pathways are shown by (5.q) and (5.r):



These pathways involve S^{2+} in its ground (3P) state and result in the formation of N^+ in its ground (3P) state. Pathway (5.q) results in the formation of SN^+ in its ground state, $X^1\Sigma^+$, and gives an exoergicity of 5.6 eV. Pathway (5.r) results in the formation of SN^+ in its first excited electronic state, $1^3\Sigma^+$, giving an exoergicity of 2.1 eV. Note that (5.q) and (5.r) are both spin allowed. The 1D and 1S states of S^{2+} could also be involved, as well as one of the first three excited states of N^+ (1D , 1S and 5S). Moreover, it is possible that any of the electronic states of SN^+ that are stable to dissociation could be involved in this channel.

To summarise, this channel due to the formation of ions with $m/z = 46$ and $m/z = 14$ results from a chemical bond-forming reaction between $S^{2+} + N_2$, producing $SN^+ + N^+$. An isotropic scattering pattern is observed, clearly showing the involvement of a collision complex, $[SN_2]^{2+}$, typical for a bond-forming reaction. The observed exoergicity distribution is in good agreement with the energies of SN^+ calculated in other works,¹¹⁹ and the S^{2+} states that we propose comprise the dication beam.

5.4 Conclusions

In this work we have studied the reactivity of the dication S^{2+} with Ar, N_2 and H_2 . To the author's knowledge, this is the first study of the bimolecular reactivity of S^{2+} , a species relevant to planetary ionospheres and other high energy environments. The dication beam is composed predominantly by S^{2+} in a mixture of its 3P , 1D and 1S states, resulting from the $3s^2 3p^2$ electronic configuration. Most of the observed reaction channels can be accounted for with the involvement of S^{2+} in its ground state, 3P , however, counts with high associated exoergicities in the DSET channels reveal the potential involvement of higher energy S^{2+} states such as 5S and 3F ; a more detailed investigation of the S^{2+} energy states present in the dication beam is required.

The SET reaction between S^{2+} and Ar displays dynamics and energetics typical of LZ style reactions. In the reactions between $S^{2+} + H_2$, NDSET and DSET were observed. The dynamics show evidence for the formation of a long-lived association, a collision complex $[SH_2]^{2+}$, between the reactants in the DSET channel. Perhaps surprisingly, the formation of SH^+ , the product of a chemical bond-forming channel was not observed. The reactions of $S^{2+} + H_2$ are especially relevant as S^{2+} has been observed in the outer atmosphere of Jupiter, where H_2 is the dominant species. The collisions of $S^{2+} + N_2$ result in both dissociative and non-dissociative SET reactions as well as a bond-forming channel, resulting in the formation of $SN^+ + N^+$, which proceeds *via* a collision complex.

5.5 References

- 1 J. C. Laas and P. Caselli, *A&A*, 2019, **624**, A108.
- 2 C. T. Russell and M. G. Kivelson, *Science*, 2000, **287**, 1998–1999.
- 3 M. Kumar and J. S. Francisco, *Proc. Natl. Acad. Sci. U. S. A.*, 2017, **114**, 864–869.
- 4 X. Zhang, M. C. Liang, F. Montmessin, J. L. Bertaux, C. Parkinson and Y. L. Yung, *Nat. Geosci.*, 2010, **3**, 834–837.
- 5 W. W. Kellogg, R. D. Cadle, E. R. Allen, A. L. Lazrus and E. A. Martell, *Science*, 1972, **175**, 587–596.
- 6 L. A. Komarnisky, R. J. Christopherson and T. K. Basu, *Nutrition*, 2003, **19**, 54–61.
- 7 J. N. Bull, J. W. L. Lee and C. Vallance, *Phys. Rev. A*, 2017, **96**, 042704.
- 8 V. M. Donnelly and A. Kornblit, *J. Vac. Sci. Technol. A Vacuum, Surfaces, Film.*, 2013, **31**, 050825.
- 9 L. G. Christophorou and J. K. Olthoff, *J. Phys. Chem. Ref. Data*, 2000, **29**, 267–330.
- 10 M. Hochlaf, R. Linguerri, M. Cheraki, T. Ayari, R. Ben Said, R. Feifel and G. Chambaud, *J. Phys. Chem. A*, 2021, **125**, 1958–1971.
- 11 T. Barker, *Astrophys. J.*, 1980, **240**, 99–104.
- 12 S. Rappaport, E. Chiang, T. Kallman and R. Malina, *Astrophys. J.*, 1994, **431**, 237–246.
- 13 L. T. Greenberg, P. Dyal and T. R. Geballe, *Astrophys. J. Lett.*, 1977, **213**, L71–L74.
- 14 L. A. Frank, W. R. Paterson, K. L. Ackerson, V. M. Vasylunas, F. V Coroniti and S. J. Bolton, *Science*, 1996, **274**, 394–395.
- 15 D. E. Shemansky and G. R. Smith, *J. Geophys. Res.*, 1981, **86**, 9179–9192.
- 16 F. Bagenal and J. D. Sullivan, *J. Geophys. Res. Sp. Phys.*, 1981, **86**, 8447–8466.
- 17 F. Herbert, N. M. Schneider, A. R. Hendrix and F. Bagenal, *J. Geophys. Res. Sp. Phys.*, 2003, **108**, 1167.

- 18 S. Kumar, *Icarus*, 1985, **61**, 101–123.
- 19 J. R. Spencer and N. M. Schneider, *Annu. Rev. Earth Planet. Sci.*, 1996, **24**, 125–190.
- 20 P. A. Delamere and F. Bagenal, *J. Geophys. Res.*, 2003, **108**, 1276.
- 21 R. C. Allen, C. P. Paranicas, F. Bagenal, S. K. Vines, D. C. Hamilton, F. Allegrini, G. Clark, P. A. Delamere, T. K. Kim, S. M. Krimigis, D. G. Mitchell, T. H. Smith and R. J. Wilson, *Geophys. Res. Lett.*, 2019, **46**, 11709–11717.
- 22 G. Clark, B. H. Mauk, C. Paranicas, P. Kollmann and H. T. Smith, *J. Geophys. Res. Sp. Phys.*, 2016, **121**, 2264–2273.
- 23 H. B. Niemann, S. K. Atreya, G. R. Carignan, T. M. Donahue, J. A. Haberman, D. N. Harpold, R. E. Hartle, D. M. Hunten, W. T. Kasprzak, P. R. Mahaffy, T. C. Owen, N. W. Spencer and S. H. Way, *Science*, 1996, **272**, 846–849.
- 24 W. B. Hubbard and M. S. Marley, *Icarus*, 1989, **78**, 102–118.
- 25 L. Wallace, *Icarus*, 1980, **43**, 231–259.
- 26 A. G. W. Cameron, *Space Sci. Rev.*, 1973, **15**, 121–146.
- 27 S. A. Stern, *Rev. Geophys.*, 1999, **37**, 453–491.
- 28 A. O. Nier, W. B. Hanson, A. Seiff, M. B. McElroy, N. W. Spencer, R. J. Duckett, T. C. Knight and W. S. Cook, *Science*, 1976, **193**, 786–788.
- 29 D. D. Bogard, R. N. Clayton, K. Marti, T. Owen and G. Turner, in *Space Science Reviews*, eds. R. Kallenbach, J. Geiss and W. K. Hartmann, Springer, Dordrecht, 2001, vol. 12, pp. 425–458.
- 30 R. Thissen, O. Witasse, O. Dutuit, C. S. Wedlund, G. Gronoff and J. Lilensten, *Phys. Chem. Chem. Phys.*, 2011, **13**, 18264–18287.
- 31 H. B. Niemann, S. K. Atreya, J. E. Demick, D. Gautier, J. A. Haberman, D. N. Harpold, W. T. Kasprzak, J. I. Lunine, T. C. Owen and F. Raulin, *J. Geophys. Res.*, 2010, **115**, E12006.
- 32 O. Badr and S. D. Probert, *Appl. Energy*, 1993, **46**, 1–67.

- 33 E. W. Schwieterman, T. D. Robinson, V. S. Meadows, A. Misra and S. Domagal-Goldman, *Astrophys. J.*, 2015, **810**, 57.
- 34 O. Dutuit, N. Carrasco, R. Thissen, V. Vuitton, C. Alcaraz, P. Pernot, N. Balucani, P. Casavecchia, A. Canosa, S. Le Picard, J.-C. Loison, Z. Herman, J. Zabka, D. Ascenzi, P. Tosi, P. Franceschi, S. D. Price and P. Lavvas, *Astrophys. J. Suppl. Ser.*, 2013, **204**, 20.
- 35 D. F. Mark, F. M. Stuart and M. de Podesta, *Geochim. Cosmochim. Acta*, 2011, **75**, 7494–7501.
- 36 D. Smith, D. Grief and N. G. Adams, *Int. J. Mass Spectrom. Ion Phys.*, 1979, **30**, 271–283.
- 37 D. Smith, N. G. Adams, E. Alge, H. Villinger and W. Lindinger, *J. Phys. B At. Mol. Phys.*, 1980, **13**, 2787–2799.
- 38 G. Dupeyrat, J. B. Marquette, B. R. Rowe and C. Rebrion, *Int. J. Mass Spectrom. Ion Process.*, 1991, **103**, 149–156.
- 39 G. C. Shields and T. F. Moran, *J. Phys. B At. Mol. Phys.*, 1983, **16**, 3591–3607.
- 40 E. Y. Kamber, P. Jonathan, A. G. Brenton and J. H. Beynon, *J. Phys. B At. Mol. Phys.*, 1987, **20**, 4129–4142.
- 41 S. M. Harper, W.-P. Hu and S. D. Price, *J. Phys. B At. Mol. Opt. Phys.*, 2002, **35**, 4409–4423.
- 42 H. R. Koslowski, H. Lebius, V. Staemmler, R. Fink, K. Wiesemann and B. A. Huber, *J. Phys. B At. Mol. Opt. Phys.*, 1991, **24**, 5023–5034.
- 43 E. L. Zins and D. Schröder, *Int. J. Mass Spectrom.*, 2011, **299**, 53–58.
- 44 J. Roithová, Z. Herman, D. Schröder and H. Schwarz, *Chem. Eur. J.*, 2006, **12**, 2465–2471.
- 45 J. Roithová, R. Thissen, J. Žabka, P. Franceschi, O. Dutuit and Z. Herman, *Int. J. Mass Spectrom.*, 2003, **228**, 487–495.
- 46 N. Tafadar, N. Kaltsoyannis and S. D. Price, *Int. J. Mass Spectrom.*, 1999, **192**, 205–

- 214.
- 47 P. W. Burnside and S. D. Price, *Int. J. Mass Spectrom.*, 2006, **249–250**, 279–288.
- 48 W.-P. Hu, S. M. Harper and S. D. Price, *Mol. Phys.*, 2005, **103**, 1809–1819.
- 49 M. Manning, S. D. Price and S. R. Leone A, *J. Chem. Phys.*, 1993, **99**, 8695–8704.
- 50 S. D. Price, M. Manning and S. R. Leone, *Chem. Phys. Lett.*, 1993, **214**, 553–558.
- 51 D. Ascenzi, P. Tosi, J. Roithová, C. L. Ricketts, D. Schröder, J. F. Lockyear, M. A. Parkes and S. D. Price, *Phys. Chem. Chem. Phys.*, 2008, **10**, 7121–7128.
- 52 J. F. Lockyear, K. Douglas, S. D. Price, M. Karwowska, K. J. Fijalkowski, W. Grochala, M. Remeš, J. Roithová and D. Schröder, *J. Phys. Chem. Lett.*, 2010, **1**, 358–362.
- 53 H. Störi, E. Alge, H. Villinger, F. Egger and W. Lindinger, *Int. J. Mass Spectrom. Ion Phys.*, 1979, **30**, 263–270.
- 54 J. Roithová, J. Žabka, Z. Herman, R. Thissen, D. Schröder and H. Schwarz, *J. Phys. Chem. A*, 2006, **110**, 6447–6453.
- 55 J. Roithová, J. Žabka, J. Hrušák, R. Thissen and Z. Herman, *J. Phys. Chem. A*, 2003, **107**, 7347–7354.
- 56 J. Jašík, J. Roithová, J. Žabka, R. Thissen, I. Ipolyi and Z. Herman, *Int. J. Mass Spectrom.*, 2006, **255–256**, 150–163.
- 57 K. A. Newson and S. D. Price, *Chem. Phys. Lett.*, 1997, **269**, 93–98.
- 58 Z. Herman, J. Žabka, Z. Dolejšek, M. Fárník and M. Fárník, *Int. J. Mass Spectrom.*, 1999, **192**, 191–203.
- 59 N. Lambert, N. Kaltsoyannis, S. D. Price, J. Žabka and Z. Herman, *J. Phys. Chem. A*, 2006, **110**, 2898–2905.
- 60 N. Tafadar and S. D. Price, *Int. J. Mass Spectrom.*, 2003, **223–224**, 547–560.
- 61 J. Roithová, H. Schwarz and D. Schröder, *Chem. Eur. J*, 2009, **15**, 9995–9999.

- 62 J. F. Lockyear, C. L. Ricketts, M. A. Parkes and S. D. Price, *Chem. Sci.*, 2011, **2**, 150–156.
- 63 H. M. Holzscheiter and D. A. Church, *J. Chem. Phys.*, 1981, **74**, 2313–2318.
- 64 P. Tosi, R. Correale, W. Lu, S. Falcinelli and D. Bassi, *Phys. Rev. Lett.*, 1999, **82**, 450–452.
- 65 S. Armenta Butt and S. D. Price, *Phys. Chem. Chem. Phys.*, 2021, **23**, 11287–11299.
- 66 A. Ehbrecht, N. Mustafa, C. Ottinger and Z. Herman, *J. Chem. Phys.*, 1996, **105**, 9833–9846.
- 67 J. H. Agee, J. B. Wilcox, L. E. Abbey and T. F. Moran, *Chem. Phys.*, 1981, **61**, 171–179.
- 68 S. M. Harper, S. W.-P. Hu and S. D. Price, *J. Chem. Phys.*, 2004, **120**, 7245–7248.
- 69 B. K. Chatterjee and R. Johnsen, *J. Chem. Phys.*, 1989, **91**, 1378–1379.
- 70 G. Niedner-Schatteburg, T. Schindler, C. Berg, D. Wössner and V. E. Bondybey, *J. Chem. Phys.*, 1993, **99**, 9664–9669.
- 71 K. M. Douglas and S. D. Price, *Int. J. Mass Spectrom.*, 2011, **303**, 147–153.
- 72 S. A. Rogers, S. D. Price and S. R. Leone, *J. Chem. Phys.*, 1993, **98**, 280–289.
- 73 Z. Herman, *Int. Rev. Phys. Chem.*, 1996, **15**, 299–324.
- 74 S. D. Price, *Int. J. Mass Spectrom.*, 2007, **260**, 1–19.
- 75 A. Kramida, Y. Ralchenko, J. Reader and NIST ASD Team, Eds., *NIST Atomic Spectra Database (version 5.6.1)*, National Institute of Standards and Technology, Gaithersburg, MD, 2020.
- 76 W. C. Martin, R. Zalubas and A. Musgrove, *J. Phys. Chem. Ref. Data*, 1990, **19**, 821–880.
- 77 N. Imadouchene, H. Aouchiche and C. Champion, *J. Electron Spectros. Relat. Phenomena*, 2016, **210**, 36–48.

- 78 M. V. V. S. Rao and S. K. Srivastava, *J. Geophys. Res.*, 1993, **98**, 13137–13145.
- 79 S. J. Smith, J. B. Greenwood, A. Chutjian and S. S. Tayal, *Astrophys. J.*, 2000, **541**, 501–505.
- 80 H. W. Moos, S. T. Durrance, T. E. Skinner, P. D. Feldman, J.-L. Bertaux and M. C. Festou, *Astrophys. J.*, 1983, **275**, L19–L23.
- 81 P. L. Smith, C. E. Magnusson and P. O. Zetterberg, *Astrophys. J.*, 1984, **277**, L79.
- 82 L. I. Podobedova, D. E. Kelleher and W. L. Wiese, *J. Phys. Chem. Ref. Data*, 2009, **38**, 171–439.
- 83 S. D. Price, *J. Chem. Soc., Faraday Trans.*, 1997, **93**, 2451–2460.
- 84 M. A. Parkes, J. F. Lockyear and S. D. Price, *Int. J. Mass Spectrom.*, 2009, **280**, 85–92.
- 85 G. Dujardin, M. J. Besnard, L. Hellner and Y. Malinovitch, *Phys. Rev. A*, 1987, **35**, 5012–5019.
- 86 B. Godard, E. Falgarone, M. Gerin, D. C. Lis, M. De Luca, J. H. Black, J. R. Goicoechea, J. Cernicharo, D. A. Neufeld, K. M. Menten and M. Emprechtinger, *Astron. Astrophys.*, 2012, **540**, A87.
- 87 F. Lique, A. Zanchet, N. Bulut, J. R. Goicoechea and O. Roncero, *Astron. Astrophys.*, 2020, **638**, A72.
- 88 D. O. Kashinski, D. Talbi, A. P. Hickman, O. E. Di Nallo, F. Colboc, K. Chakrabarti, I. F. Schneider and J. Z. Mezei, *J. Chem. Phys.*, 2017, **146**, 204109.
- 89 P. J. Dagdigian, *J. Chem. Phys.*, 2019, **150**, 84308.
- 90 P. Bolognesi, L. Avaldi, M. A. MacDonald, C. M. A. Lopes, G. Dawber, C. E. Brion, Y. Zheng and G. C. King, *Chem. Phys. Lett.*, 1999, **309**, 171–176.
- 91 L. Åsbrink, *Chem. Phys. Lett.*, 1970, **7**, 549–552.
- 92 F. Merkt and T. P. Softley, *J. Chem. Phys.*, 1992, **96**, 4149–4156.
- 93 K. M. Weitzel, J. Mähner and M. Penno, *Chem. Phys. Lett.*, 1994, **224**, 371–380.

- 94 R. B. Cordaro, K. C. Hsieh and L. C. M. Jr, *J. Phys. B At. Mol. Phys.*, 1986, **19**, 1863–1872.
- 95 R. Stockbauer, *J. Chem. Phys.*, 1979, **70**, 2108–2114.
- 96 J. L. Gardner and J. A. R. Samson, *J. Electron Spectros. Relat. Phenomena*, 1976, **8**, 123–127.
- 97 T. E. Sharp, *At. Data Nucl. Data Tables*, 1970, **2**, 119–169.
- 98 M. Beyer and F. Merkt, *J. Mol. Spectrosc.*, 2016, **330**, 147–157.
- 99 M. Beyer and F. Merkt, *Phys. Rev. Lett.*, 2016, **116**, 093001.
- 100 M. A. Parkes, J. F. Lockyear, S. D. Price, D. Schröder, J. Roithová and Z. Herman, *Phys. Chem. Chem. Phys.*, 2010, **12**, 6233–6243.
- 101 C. L. Ricketts, D. Schröder, J. Roithová, H. Schwarz, R. Thissen, O. Dutuit, J. Žabka, Z. Herman and S. D. Price, *Phys. Chem. Chem. Phys.*, 2008, **10**, 5135–5143.
- 102 S. Armenta Butt and S. D. Price, *Phys. Chem. Chem. Phys.*, 2020, **22**, 8391–8400.
- 103 S. Strathdee and R. Browning, *J. Phys. B At. Mol. Phys.*, 1979, **12**, 1789–1804.
- 104 K. Köllmann, *Int. J. Mass Spectrom. Ion Phys.*, 1975, **17**, 261–285.
- 105 K. Ito, R. I. Hall and M. Ukai, *J. Chem. Phys.*, 1996, **104**, 8449–8457.
- 106 C. Bottcher, *J. Phys. B At. Mol. Phys.*, 1974, **7**, L352.
- 107 C. J. Latimer, J. Geddes, M. A. MacDonald, N. Kouchi and K. F. Dunn, *J. Phys. B At. Mol. Opt. Phys.*, 1996, **29**, 6113–6121.
- 108 J. R. Rumble, Ed., *CRC Handbook of Chemistry and Physics*, CRC Press/Taylor & Francis, Boca Raton, FL, 100th Edit., 2020.
- 109 A. J. Yench, K. Ellis and G. C. King, *J. Electron Spectros. Relat. Phenomena*, 2014, **195**, 160–173.
- 110 P. Baltzer, M. Larsson, L. Karlsson, B. Wannberg and M. Carlsson Göthe, *Phys. Rev. A*,

- 1992, **46**, 5545–5553.
- 111 H. R. Hrodmarsson, R. Thissen, D. Dowek, G. A. Garcia, L. Nahon and T. R. Govers, *Front. Chem.*, 2019, **7**, 222.
- 112 E. M. Bahati, J. J. Jureta, D. S. Belic, H. Cherkani-Hassani, M. O. Abdellahi and P. Defrance, *J. Phys. B At. Mol. Opt. Phys.*, 2001, **34**, 2963–2973.
- 113 X. Tang, Y. Hou, C. Y. Ng and B. Ruscic, *J. Chem. Phys.*, 2005, **123**, 074330.
- 114 L. Åsbrink and C. Fridh, *Phys. Scr.*, 1974, **9**, 338–340.
- 115 P. Rivière-Marichalar, A. Fuente, J. R. Goicoechea, J. Pety, R. Le Gal, P. Gratier, V. Guzmán, E. Roueff, J. C. Loison, V. Wakelam and M. Gerin, *Astron. Astrophys.*, 2019, **628**, A16.
- 116 T. Trabelsi, S. Ben Yaghlane, M. M. Al Mogren, J. S. Francisco and M. Hochlaf, *J. Chem. Phys.*, 2016, **145**, 084307.
- 117 M. Canaves, A. A. De Almeida, D. C. Boice and G. C. Sanzovo, *Earth, Moon Planets*, 2002, **90**, 335–347.
- 118 J. Cernicharo, B. Lefloch, M. Agúndez, S. Bailleux, L. Margulès, E. Roueff, R. Bachiller, N. Marcelino, B. Tercero, C. Vastel and E. Caux, *Astrophys. J. Lett.*, 2018, **853**, L22.
- 119 S. Ben Yaghlane and M. Hochlaf, *J. Phys. B At. Mol. Opt. Phys.*, 2009, **42**, 015101.
- 120 J. Czernek and O. Živný, *Chem. Phys.*, 2004, **303**, 137–142.
- 121 J. M. Dyke, A. Morris and I. R. Trickle, *J. Chem. Soc. Faraday Trans. 2 Mol. Chem. Phys.*, 1977, **73**, 147–151.
- 122 P. A. G. O'Hare, *J. Chem. Phys.*, 1970, **52**, 2992–2996.
- 123 A. Karpfen, P. Schuster, J. Petkov and H. Lischka, *J. Chem. Phys.*, 1978, **68**, 3884–3890.
- 124 K. A. Peterson and R. C. Woods, *J. Chem. Phys.*, 1988, **89**, 4929–4944.
- 125 D. Zhou, D. Shi, Z. Zhu and J. Sun, *J. Quant. Spectrosc. Radiat. Transf.*, 2019, **224**, 1–8.

Chapter 6: Reactivity of $\text{CH}_2\text{CN}^{2+}$ with Ar, N_2 and CO

6.1 Introduction

The atmosphere of Titan is primarily comprised of molecular nitrogen (N_2 , ~95 %) and methane (CH_4 , ~5 %).^{1,2} It follows that nitriles, organic compounds with a -CN moiety, are also relevant to the atmospheric chemistry of the satellite. Indeed, a number of nitrile compounds, including acetonitrile, have been detected in the atmosphere of Titan.^{3,4} Acetonitrile, CH_3CN , is the simplest nitrile, and has also been detected in the atmosphere of the Earth,⁵⁻⁷ as well as in the interstellar medium (ISM).^{8,9} Recent investigations (Parkes *et al.*, 2019)¹⁰ studied the EI and PI of CH_3CN , and included observations of long-lived molecular dications including, predominantly, $\text{CH}_2\text{CN}^{2+}$.

In ionospheres, dications are readily formed from their precursors by solar radiation and collisions with high energy particles.¹¹ Therefore, the $\text{CH}_2\text{CN}^{2+}$ dication is likely to be produced from CH_3CN in the ionosphere of Titan as well as the atmospheres of other planets and satellites. In addition to its relevance to ionospheres, the neutral radical species CH_2CN has been detected in the interstellar medium.^{8,12-14} This chapter presents investigations of the bimolecular reactivity of $\text{CH}_2\text{CN}^{2+}$ with the neutral species Ar, N_2 , and CO. Argon is often present in the atmospheres of planets and satellites, for example the Earth, Mars and Titan.^{2,15-20} Molecular nitrogen is the dominant species in the atmospheres of the Earth and Titan.^{11,16-19,21-24} While CO has been detected in comets,²⁵⁻²⁷ and is present in the atmospheres of planets and satellites including the Earth,²⁸ Venus,²⁹ and Titan.³⁰⁻³²

The experiments described in Chapters 3 – 5 involved the atomic dications Ar^{2+} and S^{2+} , whereas the $\text{CH}_2\text{CN}^{2+}$ dication is molecular. As well as their relevance to ionospheres, molecular dications provoke questions of a fundamental nature; for example, the stabilisation of a dipositive charge with respect to Coulomb explosion.³³ The use of a molecular dication also offers additional experimental challenges and considerations in this work, such as the presence of dicationic collision-induced dissociation (CID) channels.

To the authors' knowledge, no bimolecular reactions involving $\text{CH}_2\text{CN}^{2+}$ have previously been reported. Comparisons can be made, however, to the reactions of similar molecular dications with the neutral collision partners used in this study, particularly other dications of small hydrogen and carbon containing molecules. The reactions resulting from

dication + Ar collisions have been well studied.^{34–47} Along with other channels, proton-transfer (PT) forming ArH^+ was detected in collisions between Ar and the hydrogen-containing dications CHCl^{2+} and $\text{C}_2\text{H}_2^{2+}$.^{48,49} Additionally, Ar + CHCl^{2+} collisions generated a new dication, HCCAr^{2+} .⁴⁹ The reactions resulting from dication + N_2 collisions have been the subject of multiple previous studies, including previous work in this thesis with Ar^{2+} and S^{2+} (Chapters 4 & 5).^{34,40–42,50–57} Proton-transfer reactions have been observed following the interactions of N_2 with $\text{C}_4\text{H}_3^{2+}$, resulting in the formation of a new N-H bond.⁵⁸ CO has been used as a collision partner in several bimolecular dication reactions.^{41,55,59–62} Collisions between HCl^{2+} and CO resulted in PT with the formation of COH^+ .⁶⁰ From these studies we may hypothesise that bond-formation channels involving PT will result from $\text{CH}_2\text{CN}^{2+}$ +neutral collisions.

Roithová *et al.*³³ completed a comprehensive experimental study on the competition of PT and single electron-transfer (SET) in the reactions between the hydrogen-containing dications CHX^{2+} ($\text{X} = \text{F}, \text{Cl}, \text{Br}, \text{I}$) and several atomic, non-polar and polar neutral species including the neutral collision partners used in this study: Ar, N_2 , and CO. From their observations, Roithová *et al.*³³ proposed that if SET falls within the ‘reaction window’ (i.e. has an exothermicity of 2 eV – 6 eV) then PT is suppressed, despite often nominally resulting in energetically favoured products. Roithová’s rationale argued that ET usually occurs at long distances, rendering geometry less important, whereas PT requires at least a minimal degree of orientation of the reactants. Therefore, ET is kinetically favoured. When the neutral collision partner was polar, the relative intensity of PT increased, accounted for by the increased attractive forces between the dication and neutral resulting in an increased likelihood of a collision complex forming, thus extending the lifetime of the association and allowing more of the thermodynamic products to be formed (PT). Based on this study by Roithová *et al.*³³ we would expect that, of the neutral collision partners used in our experiments (Ar, N_2 , and CO), CO might exhibit the most intense PT channel due to its polar nature.

This chapter presents the investigation of the bimolecular reactivity of $\text{CH}_2\text{CN}^{2+}$, a dication derived from the simplest nitrile, with the neutral species Ar, N_2 and CO, relevant to the atmospheres of planets and satellites such as Titan. We find that the $\text{CH}_2\text{CN}^{2+}$ dication involved in our experiments explores a number of conformations, including a cyclic structure and a linear isocyanide structure, due to the reactivity observed and the lowest energy structures revealed by calculations. PT channels were observed in all of the collision systems and were found to be direct, long-range, processes. We report the presence of a ‘pseudo CID’ channel,

that the dynamics reveal to be mediated by the initial transfer of a proton from the dication to the neutral. The competition between PT and SET reactions does not follow the trends observed by Roithová *et al.*³³ Specifically, a SET channel was absent following the collisions between $\text{CH}_2\text{CN}^{2+}$ and Ar despite possible pathways falling within the reaction window. Additionally, the relative intensity of the PT channel in the $\text{CH}_2\text{CN}^{2+} + \text{CO}$ system was lower than in the systems with nonpolar collision partners, Ar and N_2 .

6.2 Experimental details

The $\text{CH}_2\text{CN}^{2+}$ ions used in the experiments described in this chapter were generated by electron ionization of CH_3CN (BDH, > 99.9 %, purified by the freeze-pump-thaw method using liquid nitrogen) by 100 eV electrons in the PSCO-MS ion source. Previous studies have shown that whilst several molecular dications are formed following the bombardment of CH_3CN with electrons, $\text{CH}_2\text{CN}^{2+}$ ($m/z = 20$) is the most abundant.¹⁰ The experiments in this work employed high (183 V cm^{-1}) TOF-MS source fields.

6.3 Results and discussion

The collisions of $\text{CH}_2\text{CN}^{2+}$ with Ar, N_2 and CO were investigated at CM collision energies of 5.0 eV, 4.5 eV, and 4.3 eV respectively. The observed reactions following the collisions of $\text{CH}_2\text{CN}^{2+}$ with Ar, N_2 , and CO are shown in Tables 6.1, 6.2, and 6.3 respectively. In all of the systems, a CID channel was observed that results in the formation of $\text{CH}_2\text{N}^+ + \text{C}^+$ (Rxns. 6.I, 6.IV, and 6.X). There was also a ‘pseudo CID’ (pCID) channel present that resulted from collisions of $\text{CH}_2\text{CN}^{2+}$ with all three of the neutrals, generating $\text{CHCN}^+ + \text{H}^+$ (Rxns. 6.II, 6.V, and 6.XI), where the dynamics deviate from what would be expected from simple CID. The collisions of $\text{CH}_2\text{CN}^{2+}$ with N_2 and CO result in the observation of products formed from further dissociation of the initial HC_2N^+ product formed from pCID; $\text{C}_2\text{N}^+ + \text{H}^+$ (Rxns. 6.VI and 6.XII). In all of the three systems there is a PT channel, resulting in the formation of HC_2N^+ and the protonated collision partner, XH^+ ($\text{X} = \text{Ar}, \text{N}_2, \text{CO}$) (Rxns. 6.III, 6.VII, and 6.XIII). In the reactions of $\text{CH}_2\text{CN}^{2+}$ with N_2 and CO, non-dissociative single electron-transfer (NDSET) channels are observed, resulting in the formation of $\text{CH}_2\text{CN}^{2+} + \text{X}^+$ ($\text{X} = \text{N}_2, \text{CO}$) (Rxns. 6.VIII and 6.XIV). The collisions of $\text{CH}_2\text{CN}^{2+}$ with CO and N_2 also resulted in the observation of products from dissociative single electron-transfer (DSET) pathways, involving the fragmentation of the $\text{CH}_2\text{CN}^{+*}$ initially generated by SET (Rxns. 6.IX, 6.XV, and 6.XVI).

Finally, following the collisions of $\text{CH}_2\text{CN}^{2+}$ and CO, a DSET channel was observed resulting from the fragmentation of CO^+ , generating $\text{CH}_2\text{CN}^+ + \text{C}^+$ (Rxn. 6.XVII).

Table 6.1: Reaction channels, following the collisions of $\text{CH}_2\text{CN}^{2+}$ with Ar at a CM collision energy of 5.0 eV, with associated relative intensities. See text for details.

Reaction	Products	Relative intensity / %
6.I	$\text{CH}_2\text{N}^+ + \text{C}^+$	60
6.II	$\text{HC}_2\text{N}^+ + \text{H}^+$	22
6.III	$\text{HC}_2\text{N}^+ + \text{ArH}^+$	18

Table 6.2: Reaction channels, following the collisions of $\text{CH}_2\text{CN}^{2+}$ with N_2 at a CM collision energy of 4.5 eV, with associated relative intensities. See text for details.

Reaction	Products	Relative intensity / %
6.IV	$\text{CH}_2\text{N}^+ + \text{C}^+$	41
6.V	$\text{HC}_2\text{N}^+ + \text{H}^+$	16
6.VI	$\text{C}_2\text{N}^+ + \text{H}^+$	1
6.VII	$\text{HC}_2\text{N}^+ + \text{N}_2\text{H}^+$	39
6.VIII	$\text{CH}_2\text{CN}^+ + \text{N}_2^+$	3
6.IX	$\text{HC}_2\text{N}^+ + \text{N}_2^+$	1

Table 6.3: Reaction channels, following the collisions of $\text{CH}_2\text{CN}^{2+}$ with CO at a CM collision energy of 4.3 eV, with associated relative intensities. See text for details.

Reaction	Products	Relative intensity / %
6.X	$\text{CH}_2\text{N}^+ + \text{C}^+$	21
6.XI	$\text{HC}_2\text{N}^+ + \text{H}^+$	4
6.XII	$\text{C}_2\text{N}^+ + \text{H}^+$	0 (0.4) ^a
6.XIII	$\text{HC}_2\text{N}^+ + \text{COH}^+$	15
6.XIV	$\text{CH}_2\text{CN}^+ + \text{CO}^+$	52
6.XV	$\text{CO}^+ + \text{CH}^+$	2
6.XVI	$\text{HC}_2\text{N}^+ + \text{CO}^+$	1
6.XVIII	$\text{CH}_2\text{CN}^+ + \text{C}^+$	4

^aThe relative intensity of reaction 6.XII is 0.4 %, which rounds to 0 %.

To determine the possible states of $\text{CH}_2\text{CN}^{2+}$ in the beam the lowest energy structures of the $\text{CH}_2\text{CN}^{2+}$ dication were investigated computationally. Minimum energy structures were found using an MP2 algorithm, with a cc-pVTZ basis set, using Gaussian16 (Rev. A03).⁶³ Single point energies were then calculated using CCSD(T) with the same basis set. The method is described in more detail in Appendix B.⁶⁴ Three metastable structures were discovered, each with corresponding doublet and quartet states (see Table 6.4). The lowest energy metastable conformation, is a doublet with a cyclic C-C-N arrangement (2CD), shown in Figure 6.1a, with an adiabatic double ionization energy of ~28.9 eV from the ground state neutral CH_2CN . The ground state neutral structure determined from our calculations, a doublet with a linear structure, agrees well with the literature.⁶⁵ A doublet linear dication structure (2LD), shown in Figure 6.1b, and a doublet linear isocyanide dication structure (2ID), shown in Figure 6.1c, were also calculated. Each dication conformation also has a higher energy quartet state associated with it, shown in Table 6.4. Whilst 2CD is the lowest energy conformation revealed by our calculations, the linear and linear isocyanide structures lie close in energy. It is likely that the dications in the beam are fluxional, sampling different regions on the potential energy surface (PES). Further calculations to determine the transition states involved between these different conformations are required to understand the fluxional nature of the dication.

However, one can analogue with the benzene dication which has a number of metastable minima on the potential energy surface and samples a variety of structures.^{66–68}

Table 6.4: Abbreviations and adiabatic ionization energies of the metastable $\text{CH}_2\text{CN}^{2+}$ dication structures. Minima found using MP2(fc) with cc-pVTZ basis sets, single point energies calculated using CCSD(T), with cc-pVTZ basis sets, using Gaussian16.⁶⁴

Multiplicity	Cyclic conformation (Figure 6.1a)	Linear conformation (Figure 6.1b)	Linear isocyanide conformation (Figure 6.1c)
Doublet	2CD, 28.9 eV	2LD, 30.4 eV	2ID, 29.3 eV
Quartet	4CD, 32.9 eV	4LD, 32.7 eV	4ID, 32.3 eV

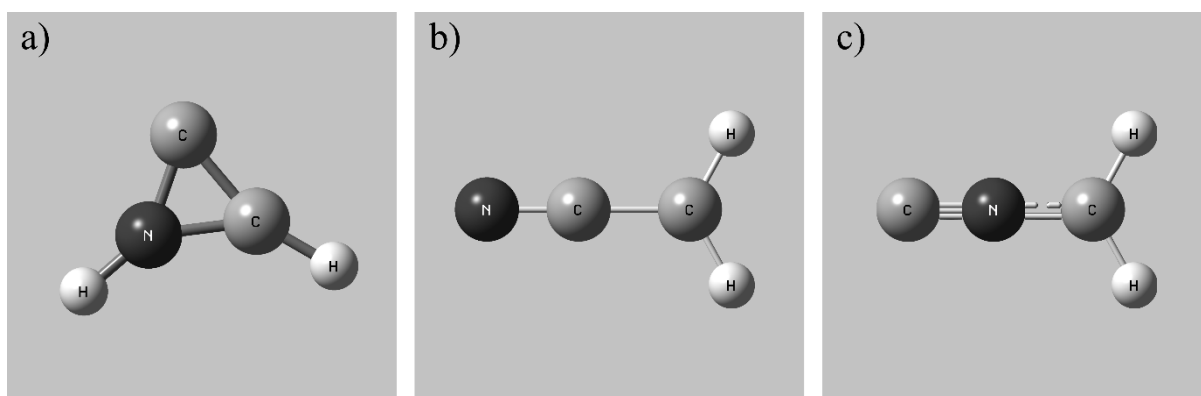


Figure 6.1: Minimum energy (metastable) structures of the reactant $\text{CH}_2\text{CN}^{2+}$ dication, calculated using MP2(fc), with VTZ basis sets, using Gaussian16.⁶⁴ a) cyclic conformation, 2CD, b) Linear conformation, 2LD, c) linear isocyanide conformation, 2ID.

The six metastable dication states revealed by the calculations (Table 6.4) have adiabatic double ionization potentials from CH_2CN of between 28.9 eV and 32.9 eV. These double ionization potentials are significantly lower than the double ionization potentials of Ar (43.39 eV),⁶⁹ N_2 (~43 eV),^{70–72} and CO (~41.5 eV).^{73–76} Therefore, as expected, there are no product peaks in any of the spectra from the $\text{CH}_2\text{CN}^{2+}$ + neutral systems resulting from DET.

Similar calculations were also undertaken to give likely structures of the CH_2CN^+ monocation, the result of the dication gaining an electron. These calculations reveal a singlet and triplet state for each of the cyclic, linear, and linear isocyanide geometries, shown in Table 6.5. The vertical ionization energies determined for the linear and linear isocyanide geometries are a good match (~ 0.1 eV difference) with experimental photoelectron spectroscopy studies.^{77–79}

Table 6.5: Abbreviations and adiabatic ionization energies of the metastable CH_2CN^+ monocation structures. Minima found using MP2(fc) with cc-pVTZ basis sets, single point energies calculated using CCSD(T), with cc-pVTZ basis sets, using Gaussian16.⁶⁴

Multiplicity	Cyclic conformation (Figure 6.1a)	Linear conformation (Figure 6.1b)	Linear isocyanide conformation (Figure 6.1c)
Singlet	1CM, 11.0 eV	1LM, 10.1 eV	1IM, 10.3 eV
Triplet	3CM, 12.9 eV	3LM, 12.1 eV	3IM, 12.3 eV

Calculations were also employed to determine the lowest energy structure of the HC_2N^+ monocation, formed when the dication loses a proton. The lowest energy state of HC_2N^+ determined from these calculations is a doublet that has a linear N-C-C geometry, with the H bonded to the terminal C slightly off the N-C-C line. This state has an adiabatic ionization energy of ~ 10.4 eV.⁶⁴ The structure of the corresponding neutral species, HCCN, was also calculated to corroborate the method and produced a staggered conformation, in accord with the geometry calculated by Nimlos *et al.*⁸⁰

In the following sections the different reaction mechanisms observed following the collisions of $\text{CH}_2\text{CN}^{2+} + \text{X}$ ($\text{X} = \text{Ar}, \text{N}_2, \text{and CO}$) will be discussed.

6.3.1 The formation of $\text{C}^+ + \text{CH}_2\text{N}^+$ (CID)

Figure 6.2 shows the CM scattering diagrams of the $\text{C}^+ + \text{CH}_2\text{N}^+$ products resulting from the reactions of $\text{CH}_2\text{CN}^{2+}$ with Ar, N_2 and CO. The scattering diagrams for each of the reactions are remarkably similar, with the C^+ and CH_2N^+ ionic products isotropically scattered around the velocity of the reactant dication. Such a scattering pattern is expected for a

unimolecular dissociation of the reactant dication. The $\text{CH}_2\text{CN}^{2+}$ dication dissociates as a result of a collision with the neutral species, forming $\text{CH}_2\text{N}^+ + \text{C}^+$, therefore, the mechanism is CID. Modelling shows that CH_2N^+ is one of the most abundant ionic species in the atmosphere of Titan.^{81–83}

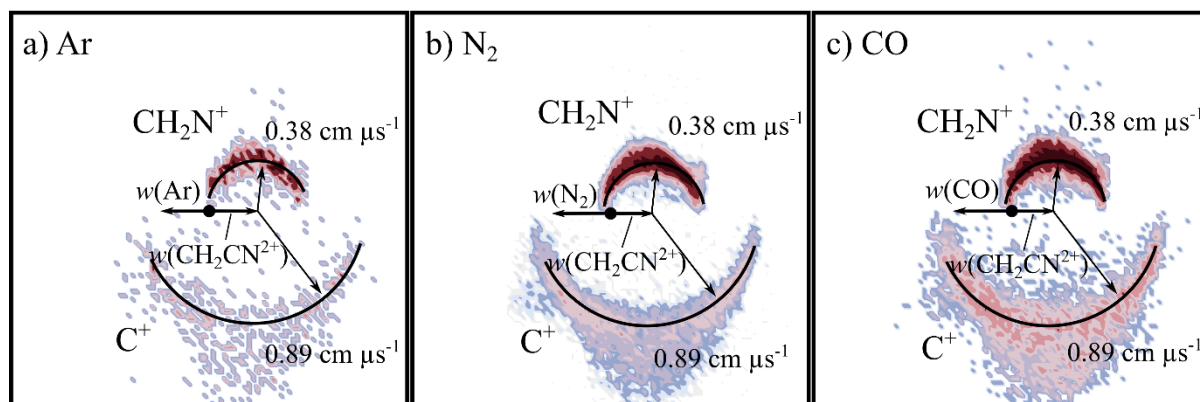


Figure 6.2: CM scattering diagrams for the CID channel producing $\text{CH}_2\text{N}^+ + \text{C}^+$ resulting from the reactions of a) $\text{CH}_2\text{CN}^{2+} + \text{Ar}$ at a CM collision energy of 5.0 eV, b) $\text{CH}_2\text{CN}^{2+} + \text{N}_2$ at a CM collision energy of 4.5 eV, and c) $\text{CH}_2\text{CN}^{2+} + \text{CO}$ at a CM collision energy of 4.3 eV.

The precursor used in this experiment to produce $\text{CH}_2\text{CN}^{2+}$ *via* EI is acetonitrile, CH_3CN . CH_3CN has a well-defined structure containing a $-\text{CH}_3$ moiety and a $-\text{CN}$, linked with a C-C bond, with a linear arrangement of the C, C, and N atoms. One might expect the formation of a dication with a similar structure. However, the presence of this CID channel resulting in the formation of $\text{CH}_2\text{N}^+ + \text{C}^+$ points to the involvement of a different dication structure. As discussed above, the minimum energy $\text{CH}_2\text{CN}^{2+}$ dication structure, 2CD, revealed from calculations has a cyclic C-C-N arrangement (Figure 6.1a), whilst slightly higher in energy is the linear isocyanide structure, 2ID (Figure 6.1c). It is easy to see how either the 2CD or 2ID $\text{CH}_2\text{CN}^{2+}$ structures could dissociate to form $\text{CH}_2\text{N}^+ + \text{C}^+$. The presence of this CID channel therefore indicates that the beam likely includes the cyclic or linear isocyanide dication. Of course, an alternative explanation could be that upon collision with the neutral, the linear dication rearranges to the cyclic or isocyanide state before dissociation. Our data cannot indicate which is most likely to occur, however, given the similarity in scattering across the three $\text{CH}_2\text{CN}^{2+} + \text{neutral}$ systems we strongly suggest that the cyclic or linear isocyanide structure is involved. The pair of ionic products generated in this channel, $\text{C}^+ + \text{CH}_2\text{N}^+$, are known to form

following the dissociative double ionization of CH_3CN , suggesting the involvement of the same dication structure.¹⁰

The experimentally observed modal velocities of the CH_2N^+ and C^+ products are the same, independent of the neutral species involved in the collision. There could be a transfer of energy between the dication and the neutral species, however, we are unable to resolve it in our experiment because we cannot determine the change in kinetic energy of the neutral product. The CID reaction is triggered by the collision between the dication and the neutral, but as far as we can see, the dissociation is effectively a unimolecular process. As well as the dominant isotropic distribution, the scattering diagrams have a slight ‘bump’ at angles near 90 degrees, where the product ions are scattered with higher velocities. This bump is also reflected in the exoergicity spectrum (Figure 6.3, discussed below), giving rise to the structure from ~8 eV – 11 eV.

Shown in Figure 6.3 are the exoergicity distributions for the dissociation of $\text{CH}_2\text{CN}^{2+}$ in the CID channels. The distributions are alike, rising sharply from ~5 eV to a maximum at ~6 eV before slowly falling. The exoergicity distributions all have FWHMs of ~5.5 eV – 7.5 eV, with a shoulder to higher exoergicities. In order to rationalise the exoergicity distribution we must determine the relative energies of the reactant and product species that could be involved in this reaction. For this system, energetic data for C^+ is readily available and the relevant energy levels for CH_2N^+ can be estimated using the proton affinity and heat of formation of HCN, which are also readily available. By combining the energy of a proton, the heat of formation of HCN and the proton affinity of HCN, we determine the limit on the heat of formation of CH_2N^+ to be 9.87 eV. We assume that any other electronic states of CH_2N^+ are not involved. For simplicity we will not consider the internal energy of the neutral species because the dissociation appears to be a unimolecular reaction. Using the double ionization energies from our calculations of $\text{CH}_2\text{CN}^{2+}$ and the heat of formation of CH_2CN (~2.5 eV),^{84–86} we estimated the exoergicities expected for this reaction. We calculate that, in an exothermic reaction, C^+ could be formed in either its ground, ^2P , or first excited state, ^4P .

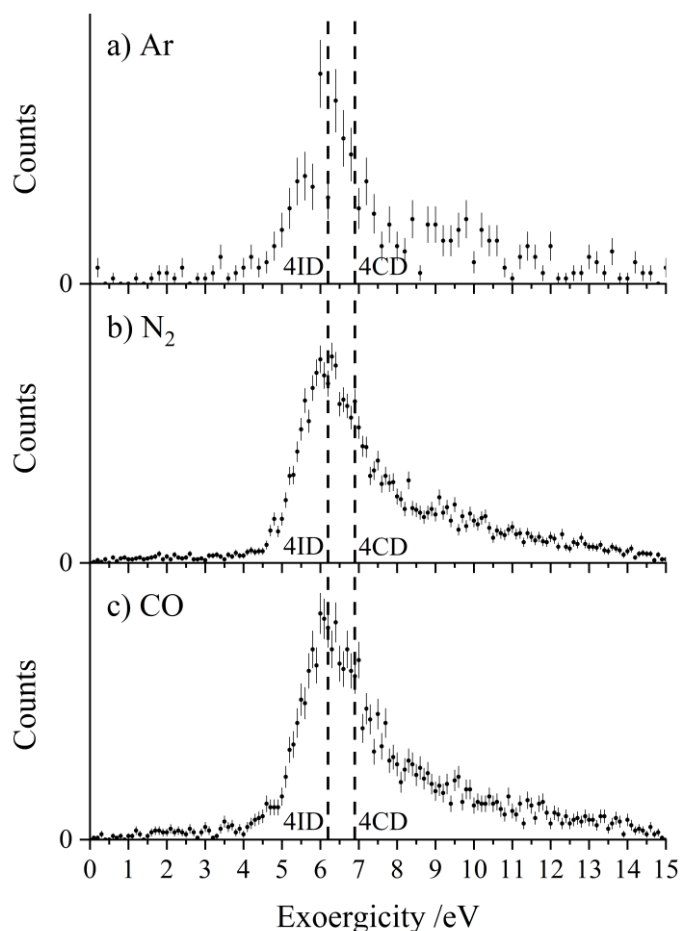


Figure 6.3: Exoergicity distributions resulting from the CID channel $\text{CH}_2\text{CN}^{2+} + \text{X} \rightarrow \text{CH}_2\text{N}^+ + \text{C}^+ + \text{X}$, where $\text{X} = \text{a) Ar, b) N}_2$, and c) CO . Dashed lines are marked at 6.2 eV and 6.9 eV in each of the distributions to show the predicted exoergicity with the involvement of the linear isocyanide dication 4ID and the cyclic quartet dication 4CD respectively. The error bars represent two standard deviations of the counts.

We find three pathways with exoergicities that fall within the FWHMs observed experimentally for these CID channels. The energy releases from 4CD and 4ID dissociating to produce $\text{C}^+ + \text{CH}_2\text{N}^+$ in their electronic ground states are 6.9 eV and 6.2 eV respectively, fitting nicely with the exoergicity distributions in Figure 6.3. The corresponding energy release from the linear quartet $\text{CH}_2\text{CN}^{2+}$ dication is 6.7 eV, also falling within the observed exoergicity. However, due to the fragments formed we think that the dication involved is not in the regular linear conformation (4LD). Both the reactant $\text{CH}_2\text{CN}^{2+}$ and product CH_2N^+ ions could be vibrationally excited, which would act to increase and decrease the observed exoergicities

respectively. If 2CD (the ground state) was involved, the expected exoergicity released from this CID channel would be 2.8 eV, clearly outside of the observed exoergicity range (Figure 6.3). If 2CD was significantly vibrationally excited (on the order of ~ 3 eV) the resulting exoergicities would be a match with the observed distribution, however, this level of vibrational excitation is not expected due to thermalisation in the ion source region. It is hard to say more about exactly which dication state is involved without more understanding of the $\text{CH}_2\text{CN}^{2+}$ dication states including their lifetimes and ability to support vibrational excitation.

To summarise, one of the dominant channels following the collisions of $\text{CH}_2\text{CN}^{2+}$ with Ar, N_2 , and CO results in the generation of $\text{CH}_2\text{N}^+ + \text{C}^+$, revealed by the dynamics to be due to CID. This CID channel is the most intense reaction channel following the collisions of $\text{CH}_2\text{CN}^{2+}$ with Ar and N_2 , whilst with CO, it is only less intense than the NDSET channel. The presence of this CID channel, resulting in the ejection of a C^+ from the reactant dication, suggests that the dication is likely not in a linear conformation directly derived from the structure of the CH_3CN precursor. The exoergicity distributions of these three channels are in excellent agreement with each other and point to the involvement of either the quartet cyclic state, 4CD, or the quartet linear isocyanide state, 4ID, of the $\text{CH}_2\text{CN}^{2+}$ dication, and result in the formation of $\text{C}^+ + \text{CH}_2\text{N}^+$ in their electronic ground states. The CH_2N^+ product is likely formed with some vibrational excitation.

6.3.2 The formation of $\text{H}^+ + \text{HC}_2\text{N}^+$ (pCID)

Each of the coincidence spectra resulting from the $\text{CH}_2\text{CN}^{2+} + \text{X}$ ($\text{X} = \text{Ar}, \text{N}_2, \text{CO}$) collisions has a peak corresponding to the formation of a pair of ions with $m/z = 39$ and $m/z = 1$, corresponding to $\text{H}^+ + \text{HC}_2\text{N}^+$. The formation of this pair of ionic products was also observed following the dissociative double ionization of CH_3CN , again suggesting that similar $\text{CH}_2\text{CN}^{2+}$ structures are involved.¹⁰ The form of the pairs spectra and the scattering diagrams from the channels generating $\text{HC}_2\text{N}^+ + \text{H}^+$ in each of the three $\text{CH}_2\text{CN}^{2+} + \text{X}$ ($\text{X} = \text{Ar}, \text{N}_2, \text{CO}$) systems look near identical, therefore, solely the $\text{CH}_2\text{CN}^{2+} + \text{N}_2 \rightarrow \text{HC}_2\text{N}^+ + \text{H}^+ + \text{N}_2$ reaction will be discussed for conciseness.

Figure 6.4 shows sub-sections of the pairs spectrum following the collisions of $\text{CH}_2\text{CN}^{2+} + \text{N}_2$. Here, Figure 6.4a shows the peak from the CID channel resulting in the formation of $\text{CH}_2\text{N}^+ + \text{C}^+$ (discussed in Section 6.3.1) and Figure 6.4b, the peak from the channel resulting in the formation of $\text{HC}_2\text{N}^+ + \text{H}^+$. Both channels display intense tails leading

up to the corresponding peaks, usually indicative of processes involving ET or CID. However, for the channel resulting in the formation of $\text{HC}_2\text{N}^+ + \text{H}^+$ there is a gap between the peak and tail (Figure 6.4b), implying that two different processes are involved. For typical CID reactions the gradient of the peak in the coincidence spectrum is approximately equal to -1 (Figure 6.4a) because the momenta of the two ionic species are correlated with each other. The peak in the coincidence spectrum for the channel forming $\text{HC}_2\text{N}^+ + \text{H}^+$ (Figure 6.4b) has a gradient of -0.1 . These factors point to the involvement of a different CID mechanism.

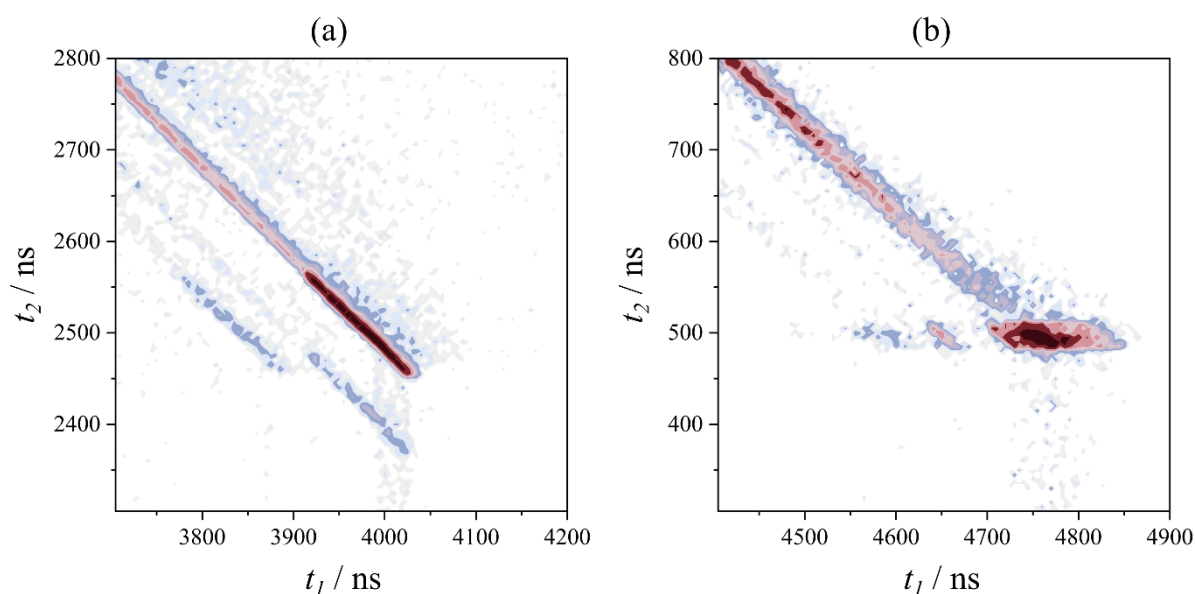


Figure 6.4: Peaks in the coincidence ‘pairs’ spectrum following the collisions of $\text{CH}_2\text{CN}^{2+} + \text{N}_2$. (a) Peak and associated tail corresponding to the formation of $\text{CH}_2\text{N}^+ + \text{C}^+$. The faint peaks in the pairs spectrum centred at (3970,2420) and (3840,2500) are not due to real counts, but due to MS artifacts due to the similarity in the drift tube potential and the MCP potential. (b) Peak and associated tail corresponding to the formation of $\text{HC}_2\text{N}^+ + \text{H}^+$. The peak in the pairs spectrum centred at (4650,500) is due to the detection of $\text{C}_2\text{N}^+ + \text{H}^+$, discussed in Section 6.3.2.1. The faint peak in the pairs spectrum centred at (4590,490) is an artifact.

It should be noted that when analysing this channel, the TOF calibration had to be modified. The other channels in these $\text{CH}_2\text{CN}^{2+} + \text{X}$ ($\text{X} = \text{Ar}, \text{N}_2$, and CO) systems were calibrated using ions from the beam with $m/z = 41$ and $m/z = 20$, however, the m/z of H^+ is 1, the extrapolation of the calibration to which was found to be inaccurate. Therefore, the TOF of

H^+ was used in the calibration for this channel. Whilst the CM moved slightly with the updated calibration, the IF scattering, including the motion of the product fragments relative to each other, did not change significantly, therefore, though the energetics are less certain for this reaction, the dynamics are clear, hence the conclusions are robust. Indeed, a range of TOF calibrations were used to check the effect of changing calibration on the IF scattering, resulting in no significant changes to the IF scattering of the product fragments across all the calibrations used.

Figure 6.5 shows each of the IF scattering diagrams of the $\text{HC}_2\text{N}^+ + \text{H}^+ + \text{N}_2$ products for the Rxn. 6.IV. In each of the IF scattering diagrams, the scattering of the two products shown appear correlated with each other relative to the third fragment. If the reaction was simple CID, such as for the formation of $\text{C}^+ + \text{CH}_2\text{N}^+$ (Section 6.3.1), we would expect the $\text{HC}_2\text{N}^+ + \text{H}^+$ products to be correlated with each other but not with the N_2 , therefore, this reaction cannot be simple CID. The scattering displayed in Figure 6.5, where all the product velocities are correlated is indicative of an association between the reactants followed by a concerted fragmentation. However, the CM scattering (Figure 6.6) reveals that the velocity of the HC_2N^+ product is broadly oriented in the direction of the incident dication velocity, implying that a complex that lives for several rotations does not form. Therefore, we propose that a short-lived association between the reactants occurs. The H^+ could start to transfer from $\text{CH}_2\text{CN}^{2+}$ to N_2 , forming a collision complex, $[\text{HC}_2\text{N-H-N}_2]^{2+}$, before fragmenting to form $\text{HC}_2\text{N}^+ + \text{H}^+ + \text{N}_2$. Therefore, this reaction can be thought of as proceeding in a ‘ H^+ mediated’ mechanism. This fragmentation mechanism explains how the HC_2N^+ fragment is broadly forward scattered in the CM frame whilst also how all of the product fragments are correlated. This channel is termed ‘pseudo CID’ (pCID).

The exoergicity distributions recorded following the $\text{CH}_2\text{CN}^{2+} + \text{X} \rightarrow \text{HC}_2\text{N}^+ + \text{H}^+ + \text{X}$ ($\text{X} = \text{Ar}, \text{N}_2, \text{CO}$) reactions are shown in Figure 6.7. The distributions have a similar structure, with a peak centred at ~ 2.5 eV and FWHM roughly from 0.5 eV to 6 eV. In order to rationalise these exoergicities, we must consider the product and reactant states involved. We consider the six metastable states of $\text{CH}_2\text{CN}^{2+}$ found from our calculations: 2CD, 2LD, 2ID, 4CD, 4LD, and 4ID. The neutral reactant species are assumed to be in their ground vibronic states. As with the CID channel, we will also initially assume that the internal energy of the neutral species does not change during the collision. The heat of formation of H is +2.26 eV, and its ionization energy is 13.60 eV.⁶⁹ The lowest energy structure of the HC_2N^+ monocation estimated by our

calculations (a doublet with a linear N-C-C geometry) has a adiabatic ionization energy of ~ 10.4 eV relative to the neutral, which has a heat of formation of 4.8 eV.⁸⁰ The theoretical exoergicity of the reaction $\text{CH}_2\text{CN}^{2+} + \text{X} \rightarrow \text{HC}_2\text{N}^+ + \text{H}^+ + \text{X}$ ($\text{X} = \text{Ar}, \text{N}_2, \text{CO}$) using the above constraints is 3.5 eV when 2CD is involved, which is marked on the exoergicity distributions in Figure 6.7. This value is a good match to the observed exoergicities, albeit at a slightly higher exoergicity than the peak maximum. The linear isocyanide structure, 2ID, could also be involved, however, the energetics are similar to 2CD, so it is not possible to differentiate between them here. If the HC_2N^+ product is formed with vibrational excitation, the theoretical exoergicity would decrease, becoming a closer match to the observed exoergicities. Considering the complex nature of the mechanism, the neutral collision partners CO and N_2 could also be vibrationally excited by the collision, further acting to reduce the observed exoergicity in this channel. If 2LD is involved in this channel the expected exoergicity is 5.0 eV, also marked on Figure 6.7 for reference. There is a shoulder to higher exoergicities in the distributions that could be explained by the involvement of the 2LD state. Additionally, if the 4CD and 4LD states of the dication are involved this would result in exoergicities of 7.6 eV and 7.4 eV respectively. However, the low intensity of the exoergicity distribution at these higher values makes a large contribution from these higher energy dication states unlikely. Of course, the involvement of a range of vibrationally excited dication states in the beam would act to increase the spread of observed exoergicities.

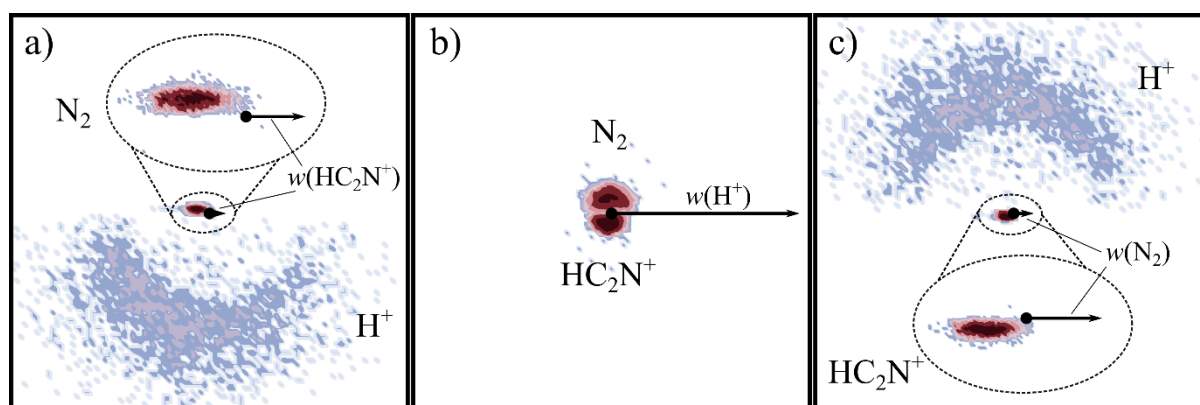


Figure 6.5: IF scattering diagrams for the channel $\text{CH}_2\text{CN}^{2+} + \text{N}_2 \rightarrow \text{HC}_2\text{N}^+ + \text{H}^+ + \text{N}_2$ at a CM collision energy of 4.5 eV. a) The scattering of the H^+ and N_2 product fragments relative to the velocity of HC_2N^+ . b) The scattering of the N_2 and HC_2N^+ fragments relative to H^+ . c) The scattering of H^+ and HC_2N^+ relative to N_2 .

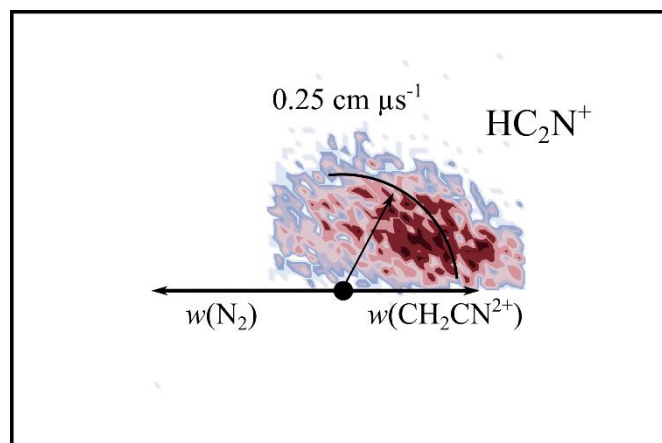


Figure 6.6: CM scattering of the HC_2N^+ product for the channel $\text{CH}_2\text{CN}^{2+} + \text{N}_2 \rightarrow \text{HC}_2\text{N}^+ + \text{H}^+ + \text{N}_2$ at a CM collision energy of 4.5 eV.

To summarise, the peak in the coincidence spectrum observed corresponding to the formation of $\text{HC}_2\text{N}^+ + \text{H}^+$ following the collisions of $\text{CH}_2\text{CN}^{2+} + \text{X}$ ($\text{X} = \text{Ar}, \text{N}_2, \text{CO}$) is due to a complex mechanism, mediated by the transfer of a H^+ from the dication to the neutral reactant. The dynamics and energetics of each of the three $\text{CH}_2\text{CN}^{2+} + \text{X} \rightarrow \text{HC}_2\text{N}^+ + \text{H}^+ + \text{X}$ reactions ($\text{X} = \text{Ar}, \text{N}_2, \text{CO}$) are in excellent agreement with each other. The dynamics reveal that the velocities of the HC_2N^+ , H^+ , and X ($\text{X} = \text{Ar}, \text{N}_2, \text{CO}$) fragments are all highly correlated, contrary to the expected mechanism for a typical CID channel. The exoergicities indicate the involvement of predominantly the cyclic 2CD state and linear isocyanide 2ID state of the dication, resulting in the formation of the products in their ground electronic states. The HC_2N^+ product is likely formed with vibrational excitation. Additionally, the structure in the exoergicity spectra extending to higher exoergicities suggests the involvement of the linear dication 2LD. Further investigations utilising the deuterated dication, $\text{CD}_2\text{CN}^{2+}$, could reveal more information about the nature of this reaction. For example, this channel could be suppressed, or the dynamics may change if the initial proposed H^+/D^+ transfer step is altered.^{87,88}

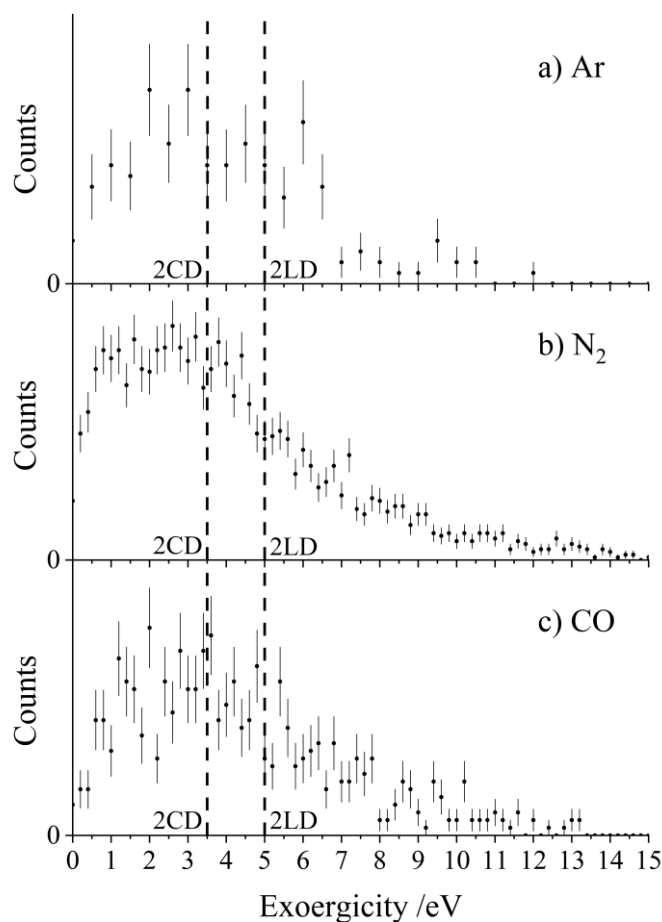


Figure 6.7: Exoergicity distributions resulting from the channel $\text{CH}_2\text{CN}^{2+} + \text{X} \rightarrow \text{HC}_2\text{N}^+ + \text{H}^+ + \text{X}$, where X = a) Ar, b) N_2 , and c) CO. Lines are marked at 3.5 eV and 5.0 eV in each of the distributions to show the predicted exoergicity with the involvement of the cyclic doublet dication 2CD and linear doublet dication 2LD respectively. The error bars represent two standard deviations of the counts.

6.3.2.1 The formation of $\text{H}^+ + \text{C}_2\text{N}^+$

The coincidence spectra recorded following the collisions of $\text{CH}_2\text{CN}^{2+} + \text{N}_2/\text{CO}$ reveal an additional peak corresponding to C_2N^+ ($m/z = 38$) + H^+ ($m/z = 1$). This channel likely also results in the formation of the neutrals $\text{N}_2/\text{CO} + \text{H}$. The velocities of the ionic products are similar to those for the pCID reactions, indicating a similar mechanism is responsible, however, in our setup it is not possible to be certain of the dynamics of a reaction that results in the formation of more than one neutral species. We therefore tentatively suggest that these channels proceed *via* ‘pseudo CID’ followed by the dissociation of HC_2N^+ to form $\text{C}_2\text{N}^+ + \text{H}$.

6.3.3 Proton-transfer channels

In all three $\text{CH}_2\text{CN}^{2+}$ + neutral systems in this investigation, PT is observed, resulting in the formation of HC_2N^+ and the protonated target. PT is often observed following the collisions of hydrogen-containing dications with neutrals, and has been seen before in different reactive systems with each of the neutral species used in this investigation: N_2 ,⁵⁸ CO ,⁶⁰ and Ar.^{33,38,48,49} The argonium ion, ArH^+ , is an example of a molecular species involving a rare gas and has been detected in the ISM,^{89,90} including in other galaxies.⁹¹ N_2H^+ has been detected in the interstellar medium,⁹² protoplanetary disks,⁹³ and in the atmosphere of Titan, where modelling also predicts the presence of N_2H^{2+} , which can be formed *via* a number of processes.⁹⁴ COH^+ has also been detected in the ISM.^{95,96}

Shown in Figure 6.8 are the scattering diagrams of the ionic products resulting from the PT reactions. In each of the scattering diagrams, strong forward scattering is observed. Such a scattering pattern is indicative of a long-range mechanism. If a proton transfers from the dication to the neutral at a large interspecies separation, the deflection of the reactant species is minimal and therefore the product velocities are oriented with the velocities of their corresponding reactants. As discussed throughout this thesis, dication-neutral reactions that involve the formation of new bonds are thought to more commonly occur *via* the formation of a collision complex, where the reactants form an association in order for new bonds to be made.^{97–100} However, yet again, we see evidence for bond-forming reactions occurring *via* a direct mechanism.^{101,102} Dication-neutral PT reactions have been clearly observed to occur *via* direct mechanisms previously.^{58,103}

In the coincidence spectra the NDSET and PT channels are partially overlapping. Therefore, the counts close to the CM in Figure 6.8b are in fact due to NDSET, demonstrated by the low velocities (being close to the CM) when the assumptions of the PT products fragment masses are applied. These counts due to NDSET are not present in the exoergicity spectrum (Figure 6.9) because they result in exoergicities of less than 0 eV when the constraints of the PT fragment masses are applied. One of the advantages of single event counting using coincidence coupled with position-sensitive detection is that we can differentiate between these counts resulting from two different processes despite any overlap in the spectra.

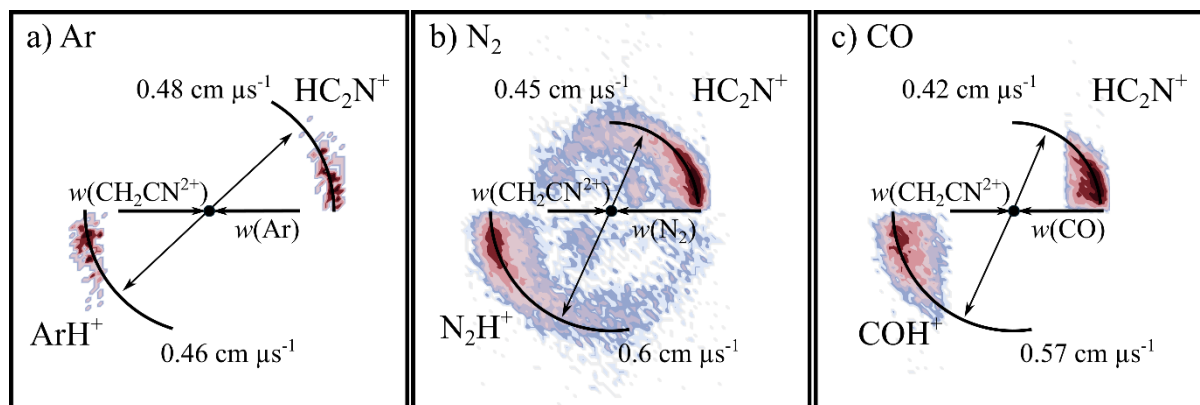


Figure 6.8: CM scattering diagrams for the PT channel $\text{CH}_2\text{CN}^{2+} + \text{X} \rightarrow \text{HC}_2\text{N}^+ + \text{XH}^+$. a) $\text{X} = \text{Ar}$ at a CM collision energy of 5.0 eV, b) $\text{X} = \text{N}_2$ at a CM collision energy of 4.5 eV, and c) $\text{X} = \text{CO}$ at a CM collision energy of 4.3 eV.

The exoergicities recorded for the PT channels are shown in Figure 6.9. The distributions have similar shapes, with maxima at ~ 5 eV. In order to rationalise the exoergicities spectra we must consider the reactant and product electronic states that could be involved. We will consider the six $\text{CH}_2\text{CN}^{2+}$ dication states obtained from our calculations; 2CD, 2LD, 2ID, 4CD, 4LD, and 4ID. We will again use the adiabatic ionization energy determined from our calculations of lowest energy structure of the HC_2N^+ monocation, and the heat of formation from Nimlos *et al.*⁸⁰ The energetics of the protonated species ArH^+ , N_2H^+ , and COH^+ are easily determined from proton affinities that are readily available, giving heats of formation of 12.0 eV, 10.7 eV, and 12.6 eV respectively.⁶⁹

Using the energetics information discussed above, the projected exoergicities for the PT reactions involving the cyclic doublet dication 2CD, resulting in the formation of both the XH^+ and HC_2N^+ products in their ground states are 4.2 eV, 5.5 eV and 5.4 eV for the reactions with Ar, N_2 and CO respectively. These exoergicities are marked on the corresponding distributions in Figure 6.9. Of course, if the linear isocyanide structure was involved, similar exoergicities (~ 0.4 eV higher) would result. Therefore, for simplicity, only 2CD is discussed. If the reactant dication was vibrationally excited, this would act to increase the observed exoergicities. Conversely, if the product HC_2N^+ or XH^+ ions were formed with vibrational excitation, the observed exoergicities would be lower. The projected exoergicities from the involvement of 2CD are a good fit with the experimental data (Figure 6.9), especially when the effects of vibrational excitation of the reactant and product species are considered.

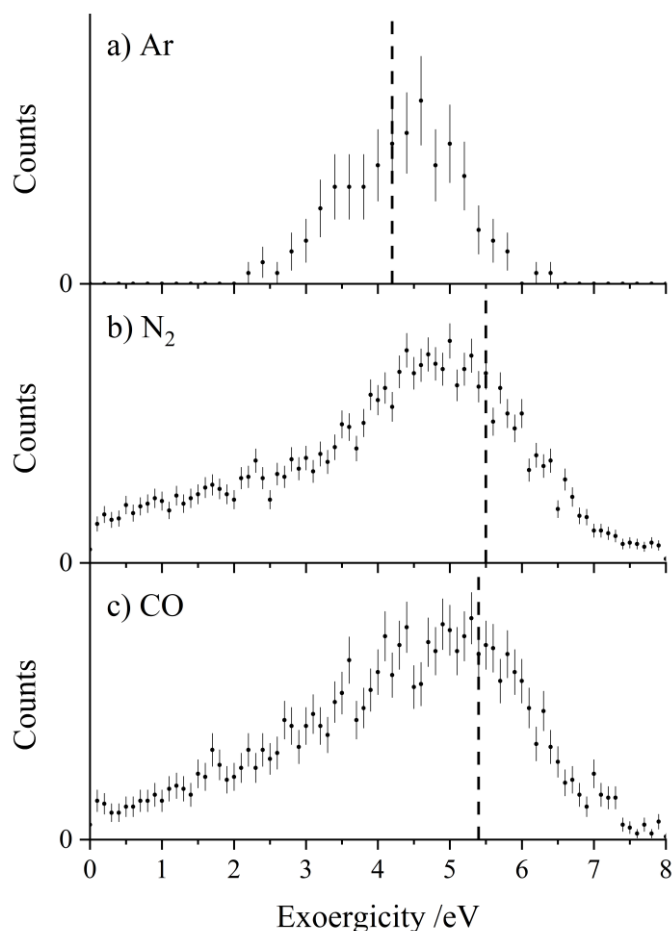


Figure 6.9: Exoergicity distributions resulting from the PT reactions $\text{CH}_2\text{CN}^{2+} + \text{X} \rightarrow \text{HC}_2\text{N}^+ + \text{XH}^+$. a) $\text{X} = \text{Ar}$, b) $\text{X} = \text{N}_2$, c) $\text{X} = \text{CO}$. Lines are marked on each distribution corresponding to the expected exoergicity from forming $\text{XH}^+ + \text{HC}_2\text{N}^+$ in their ground states from the ground state dication, 2CD. The error bars represent two standard deviations of the counts.

To summarise, PT reactions occur in each of the $\text{CH}_2\text{CN}^{2+} + \text{X}$ ($\text{X} = \text{Ar}, \text{N}_2$ and CO) systems, resulting in the formation of HC_2N^+ and XH^+ . The dynamics show that PT occurs *via* a direct, long-range, mechanism. The exoergicity distributions reveal that the 2CD and 2ID dication states are involved, producing the ionic products in their ground electronic states.

6.3.4 Non-dissociative single electron-transfer channels

In each of the $\text{CH}_2\text{CN}^{2+} + \text{X}$ ($\text{X} = \text{Ar}, \text{N}_2, \text{CO}$) systems there is a clear tail in the coincidence spectra that results from SET reactions occurring in the acceleration region, where E_{cm} is greater than in the interaction region. With N_2 , there is a small peak associated with the

NDSET channel occurring in the interaction region, whereas, for CO, NDSET is the most intense reaction channel observed following collisions with $\text{CH}_2\text{CN}^{2+}$. For the $\text{CH}_2\text{CN}^{2+} + \text{Ar}$ system, there is no significant peak associated with counts from SET reactions happening in the interaction region. In the coincidence spectra, the events from the NDSET and PT channels are close together and even overlapping in parts. However, the actual peaks, due to those reactions occurring in the interaction region, can be robustly isolated.

Figure 6.10 shows the CM scattering diagrams for the NDSET reactions $\text{CH}_2\text{CN}^{2+} + \text{X} \rightarrow \text{CH}_2\text{CN}^+ + \text{X}^+$, for $\text{X} = \text{N}_2$ and CO. Strong forward scattering is observed for both reactions. That is, the velocity of the CH_2CN^+ product ion is oriented with the velocity of the reactant dication, $\text{CH}_2\text{CN}^{2+}$. Such a scattering pattern is typical for NDSET reactions in dication-neutral systems and is indicative of a direct electron-transfer process occurring at a significant interspecies separation of $\sim 3 \text{ \AA} - 6 \text{ \AA}$.^{43,47,101,104,105} For the NDSET reaction with N_2 , in the coincidence spectrum only the forward scattered counts could be isolated from counts from the PT channel, hence the lack of a tail to higher angles in the scattering diagram (Figure 6.10a).

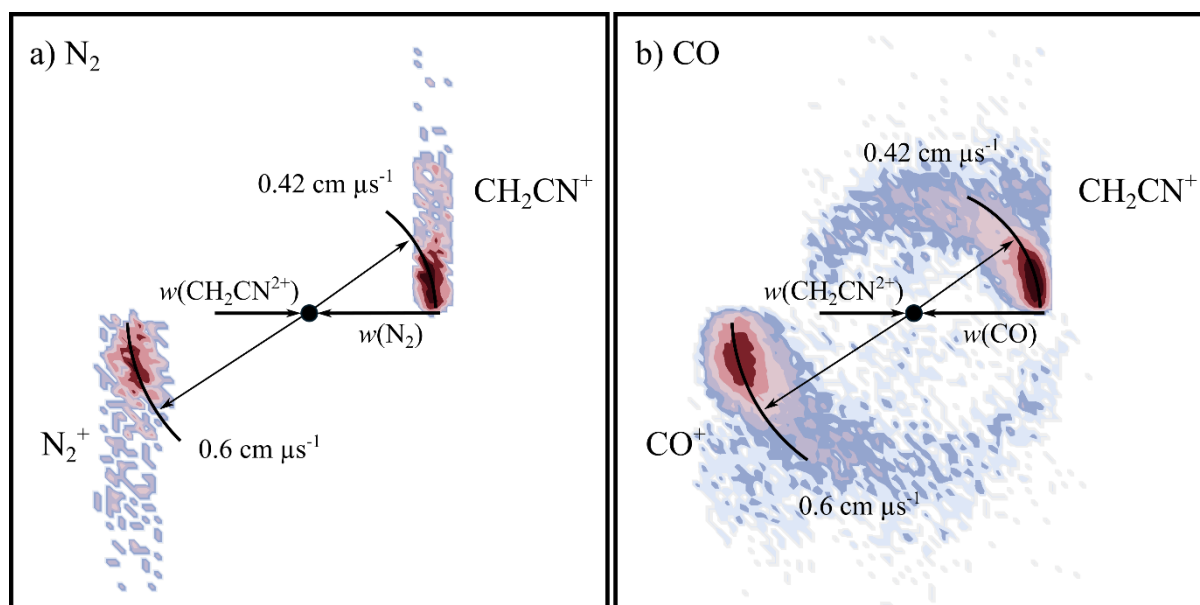


Figure 6.10: CM scattering diagrams for the NDSET channel $\text{CH}_2\text{CN}^{2+} + \text{X} \rightarrow \text{CH}_2\text{CN}^+ + \text{X}^+$. a) $\text{X} = \text{N}_2$ at a CM collision energy of 4.5 eV b) $\text{X} = \text{CO}$ at a CM collision energy of 4.3 eV.

Figure 6.11 and Figure 6.12 show the exoergic distributions recorded following the NDSET reactions of $\text{CH}_2\text{CN}^{2+}$ with N_2 and CO respectively. In order to rationalise the exoergic spectra we must first consider the reactant and product states that could be involved.

We consider the six metastable states of $\text{CH}_2\text{CN}^{2+}$ found with our calculations: 2CD, 2LD, 2ID, 4CD, 4LD, and 4ID. The neutral reactants are assumed to be in their ground vibronic states. Calculations undertaken to give likely structures of the CH_2CN^+ monocation resulted in the discovery of a singlet and triplet state for the each of cyclic, linear, and linear isocyanide geometries (See Table 6.5): 1CM, 1LM, 1IM, 3CM, 3LM, and 3IM. The lowest energy CH_2CN^+ state is the singlet linear conformation (1LM). The ground state of N_2^+ ($X^2\Sigma_g^+$) is 15.58 eV higher in energy than the ground state of N_2 .^{71,106} The lowest energy dissociation asymptote of N_2^+ ($\text{N}^+(^3\text{P}) + \text{N}(^4\text{S})$) lies at ~24.3 eV above N_2 . The energy of this dissociation asymptote corresponds to the energy of $\text{N}_2^+(\text{C}^2\Sigma_u^+ \nu = 3)$.^{69,107} Photoionization studies of N_2 show that N_2^+ states generated with an energy higher than 24.3 eV have dissociation lifetimes significantly less than the timescale of our experiment and therefore will not contribute to the observed N_2^+ counts in this channel.¹⁰⁷⁻¹¹⁰ The ground state of CO^+ ($X^2\Sigma^+$) lies 14.0 eV above $\text{CO}(X^1\Sigma^+)$.^{111,112} The lowest energy dissociation asymptote of CO^+ , corresponding to $\text{C}^+(^2\text{P}) + \text{O}(^3\text{P})$, lies at 22.4 eV above $\text{CO}(X^1\Sigma^+)$.⁶⁹ Photoionization investigations of CO show that if CO^+ is formed with an energy of greater than 22.4 eV, it will dissociate within the lifetime of the experiment and therefore will not contribute to the counts observed in this reaction channel.¹¹²⁻¹¹⁴

To determine the states involved in these NDSET channels we will also make the assumptions that the transitions will be spin allowed, and that the conformation of the dication will not change (electron-transfer is a vertical process), for example, a cyclic dication must result in the formation of a cyclic monocation.

The exoergicity distribution for the NDSET reaction with N_2 (Figure 6.11) has a maximum at 4.0 eV, with a FWHM from 3.6 eV – 5.2 eV. We find that there are 9 pathways fulfilling the above assumptions that result in exoergicities within the observed range, shown in Table 6.6. The exoergicities associated with these pathways are marked on Figure 6.11. Whilst there are possible pathways with the 4CD, 2LD, 4LD, 2ID, and 4ID states, the lowest energy dication state 2CD results in exoergicities that are lower than the FWHM and is therefore likely not involved in this channel.

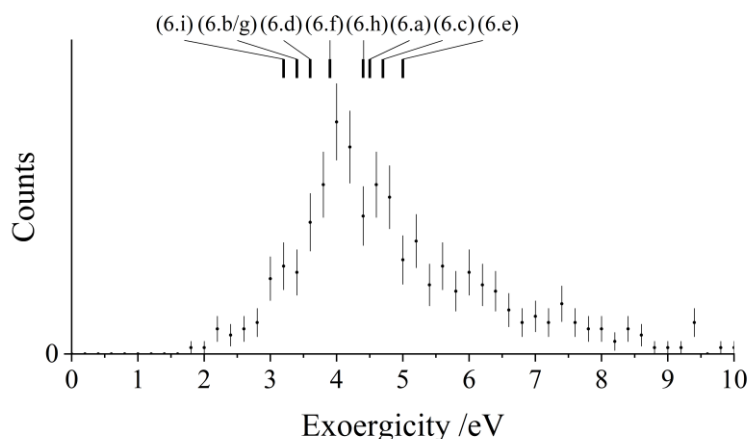


Figure 6.11: Exoergicity distributions resulting from the NDSET reaction between $\text{CH}_2\text{CN}^{2+} + \text{N}_2$, resulting in the formation of $\text{CH}_2\text{CN}^+ + \text{N}_2^+$. The exoergicities resulting from pathways (6.a) – (6.i) are marked, see Table 6.6 for details. The error bars represent two standard deviations of the counts.

Table 6.6: Electronic states involved, with associated exoergicities, for the reaction $\text{CH}_2\text{CN}^{2+} + \text{N}_2 \rightarrow \text{CH}_2\text{CN}^+ + \text{N}_2^+$. (N_2 is assumed to be in its ground vibronic state $X^1\Sigma_g^+$.)

Pathway	Reactant $\text{CH}_2\text{CN}^{2+}$ state	Product CH_2CN^+ state populated	Product N_2^+ state populated	Exoergicity
(6.a)	4CD	3CM	$X^2\Sigma_g^+$	4.5 eV
(6.b)	4CD	3CM	$A^2\Pi_u$	3.4 eV
(6.c)	2LD	1LM	$X^2\Sigma_g^+$	4.7 eV
(6.d)	2LD	1LM	$A^2\Pi_u$	3.6 eV
(6.e)	4LD	3LM	$X^2\Sigma_g^+$	5.0 eV
(6.f)	4LD	3LM	$A^2\Pi_u$	3.9 eV
(6.g)	2ID	1IM	$X^2\Sigma_g^+$	3.4 eV
(6.h)	4ID	3IM	$X^2\Sigma_g^+$	4.4 eV
(6.i)	4ID	3IM	$A^2\Pi_u$	3.2 eV

The exoergicity distribution for the NDSET reaction with CO, shown in Figure 6.12, has a maximum at 4.4 eV, with a FWHM from 3.4 eV – 5.5 eV. Using the energetics information discussed above, and constrained by the same assumptions as for N_2 , we find that there are 12 pathways for the NDSET reaction with $\text{CH}_2\text{CN}^{2+}$ and CO that give exoergicities within the experimentally observed range, shown in Table 6.7. For the reactions with CO, any of the six reactant dication states can be involved to give exoergicities within the observed range.

Table 6.7: Electronic states involved, with associated exoergicities, for the reaction $\text{CH}_2\text{CN}^{2+} + \text{CO} \rightarrow \text{CH}_2\text{CN}^+ + \text{CO}^+$. (CO is assumed to be in its ground vibronic state $\text{X}^1\Sigma^+$.)

Pathway	Reactant $\text{CH}_2\text{CN}^{2+}$ state	Product CH_2CN^+ state populated	Product CO^+ state populated	Exoergicity
(6.j)	2CD	1CM	$\text{X}^2\Sigma^+$	3.8 eV
(6.k)	4CD	3CM	$\text{X}^2\Sigma^+$	6.1 eV
(6.l)	4CD	3CM	$\text{A}^2\Pi$	3.5 eV
(6.m)	2LD	1LM	$\text{X}^2\Sigma^+$	6.3 eV
(6.n)	2LD	1LM	$\text{A}^2\Pi$	3.7 eV
(6.o)	2LD	3LM	$\text{X}^2\Sigma^+$	4.3 eV
(6.p)	4LD	3LM	$\text{X}^2\Sigma^+$	6.6 eV
(6.q)	4LD	3LM	$\text{A}^2\Pi$	4.0 eV
(6.r)	2ID	1IM	$\text{X}^2\Sigma^+$	5.0 eV
(6.s)	2ID	3IM	$\text{X}^2\Sigma^+$	3.0 eV
(6.t)	4ID	3IM	$\text{X}^2\Sigma^+$	5.9 eV
(6.u)	4ID	3IM	$\text{A}^2\Pi$	3.3 eV

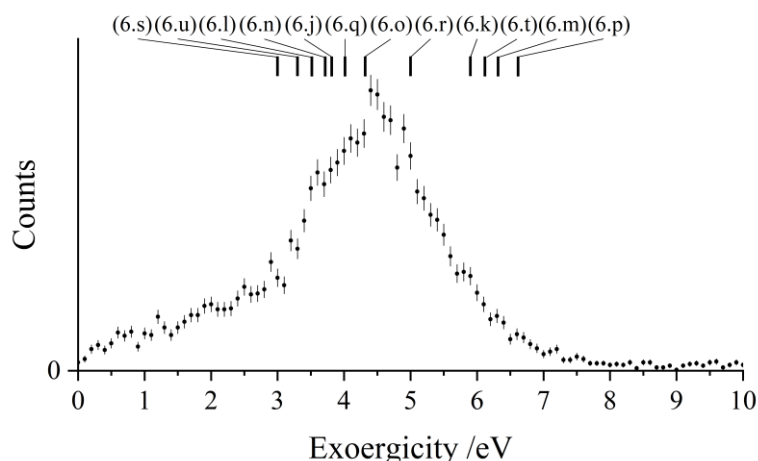


Figure 6.12: Exoergicity distributions resulting from the NDSET reaction between $\text{CH}_2\text{CN}^{2+} + \text{CO}$, resulting in the formation of $\text{CH}_2\text{CN}^+ + \text{CO}^+$. The exoergicities resulting from pathways (6.j) – (6.u) are marked, see Table 6.7 for details. The error bars represent two standard deviations of the counts.

As mentioned above, there is no distinct peak in the coincidence spectrum that results from the NDSET reaction between $\text{CH}_2\text{CN}^{2+}$ and Ar, despite the presence of a tail in the coincidence spectrum that results from SET reactions occurring in the acceleration region of the TOF-MS. The absence of a SET reaction is surprising as there are several possible pathways that would result in exoergicities that fall within the 2 eV – 6 eV LZ reaction window. These pathways adhere to the same assumptions considered for the energetic analyses of the NDSET reactions with N_2 and CO including the likely reactant and product electronic states that could be formed from a SET reaction. These NDSET pathways with Ar include all of the six metastable dication states revealed by calculations. Therefore, one would expect an NDSET reaction to occur following collisions of $\text{CH}_2\text{CN}^{2+} + \text{Ar}$. The signals due to SET reactions occurring in the acceleration region show that the SET reaction is more efficient at higher collision energies, implying the presence of a barrier in the potential energy surface to the NDSET products. Further experimental studies of this system at different collision energies could help us understand why SET is suppressed in this system. The model generally used to account for dication-neutral ET reactivity, LZRW, assumes a two-body system where each species occupies a single point in space, an obvious oversimplification. The behaviour we see could point to subtleties in the form of the crossing between the potential energy surfaces. The PES of the NDSET reaction could be significantly different with Ar compared to the other neutral species. On dication-neutral potential energy surfaces, ‘Coulomb barriers’ are thought

to exist to account for the stability of molecular dications or collision complexes, preventing charge separation in the form of CID and SET.¹¹⁵ However, in this case, whilst SET appears to be suppressed, PT is efficient, and also involves charge separation, meaning it should also have a ‘Coulomb barrier’. One possible rationale for the lack of a SET reaction occurring in the $\text{CH}_2\text{CN}^{2+} + \text{Ar}$ system could be that the Coulomb barrier in the PT channel is significantly reduced compared to the SET channel. Another possible explanation could be that in this system the coupling between reactant and product states is low, resulting in a low transition probability. It is difficult to explain this lack of reactivity without further investigation.

6.3.4.1 Dissociative single electron-transfer channels with CO and N_2

Examination of the dynamics of the counts from other peaks in the coincidence spectra recorded following the collisions of $\text{CH}_2\text{CN}^{2+}$ with N_2 and CO, reveal that there are four channels resulting from DSET. There are peaks for $\text{N}_2^+ / \text{CO}^+ (m/z = 28) + \text{HC}_2\text{N}^+ (m/z = 39)$, where the CH_2CN^+ ion formed following SET fragments, losing an H. There is a peak for $\text{CO}^+ (m/z = 28) + \text{CH}^+ (m/z = 13)$, also due to fragmentation of CH_2CN^+ after its formation. Additionally, there is a channel due to the formation of $\text{C}^+ (m/z = 12) + \text{CH}_2\text{CN}^+ (m/z = 40)$, where the CO^+ generated by SET fragments into $\text{C}^+ + \text{O}$ after its formation. These DSET channels have low intensities, with the DSET channel in the $\text{CH}_2\text{CN}^{2+} + \text{N}_2$ system contributing just 1.1 % of the total counts, and the three DSET channels in the $\text{CH}_2\text{CN}^{2+} + \text{CO}$ system combined contributing 7.4 % of the total counts.

In order to dissociate, accessing the $\text{C}^+ + \text{O}$ asymptote, CO^+ must be formed with an energy of at least 22.4 eV relative to CO. Using the energies of the $\text{CH}_2\text{CN}^{2+}$ dication states and CH_2CN^+ monocation states determined computationally, we calculate that forming CO with over 22.4 eV relative to CO is possible, but, requires the formation of either the cyclic or linear singlet monocation states from the corresponding cyclic or linear quartet dication states, which is spin forbidden. The spin forbidden nature of these transitions undoubtedly accounts for the low intensity of the channel. In order for CO^+ to fragment to produce $\text{O}^+ + \text{C}$, CO^+ must be formed with at least 24.6 eV relative to CO. It is not possible to form CO^+ with over 24.6 eV given the $\text{CH}_2\text{CN}^{2+}$ and CH_2CN^+ states we believe to be involved. Satisfyingly, there is no structure in the coincidence spectrum resulting from the formation of $\text{CH}_2\text{CN}^+ + \text{O}^+$, corroborating our assessment of the likely $\text{CH}_2\text{CN}^{2+}$ and CH_2CN^+ states.

6.4 Competition between proton-transfer and single electron-transfer

Roithová *et al.*³³ reported an investigation comparing PT and SET for collisions between CHX^{2+} ($\text{X} = \text{F}, \text{Cl}, \text{Br}, \text{I}$) and various neutrals, at similar CM collision energies to this study. Roithová *et al.* proposed that if there are SET channels with exothermicities lying within the reaction window (2 eV – 6 eV) then these SET processes will dominate, suppressing PT. However, in our experiment we do not see a SET reaction with Ar despite the presence of several possible pathways that result in exoergicities in the correct range. The lack of SET in the $\text{CH}_2\text{CN}^{2+} + \text{Ar}$ system, despite the presence of several possible pathways, could point to a barrier in the PES preventing SET. Additionally, Roithová *et al.* propose that the involvement of polar neutral collision partners increases the chance of PT reactions occurring due to an increase in attraction between the dication and neutral. However, in the experiments outlined in this chapter, the only system with a polar neutral, CO, though it only has a small dipole, in fact exhibits the highest intensity ratio of SET to PT reactions. Instead our results follow the trend of the difference in exothermicity between PT and SET. When the exoergicities of PT and SET are similar, SET dominates. For example, in the $\text{CH}_2\text{CN}^{2+} + \text{CO}$ system, assuming 2CD is involved, PT is only ~1.6 eV more exothermic than SET, and SET is dominant. For the analogous system with N_2 , PT is ~3.2 eV more exothermic than SET, and PT is the most intense channel. The energetics of the two competing reactions therefore appear to be very important. Further experiments could be undertaken that use the deuterated dication, $\text{CD}_2\text{CN}^{2+}$, to reveal more information regarding the balance between SET and PT reactions in these dication-neutral systems.

6.5 Conclusions

In this chapter we have detailed the reactivity of the molecular dication $\text{CH}_2\text{CN}^{2+}$ with Ar, N_2 , and CO. To the author's knowledge, this is the first study of the bimolecular reactivity of $\text{CH}_2\text{CN}^{2+}$, a species relevant to the ionospheres of planets and satellites including Titan.

Calculations of the lowest energy electronic states of $\text{CH}_2\text{CN}^{2+}$ reveal six metastable electronic states, both doublet and quartet states for cyclic (2CD & 4CD), linear (2LD & 4LD), and linear isocyanide (2ID & 4ID) geometries. The lowest energy electronic state was determined to be the doublet cyclic dication, 2CD.

All of the collision systems displayed an intense CID channel resulting in the formation of $\text{C}^+ + \text{CH}_2\text{N}^+$, with similar dynamics and exoergicity distributions. The formation of a C^+ fragment suggests the involvement of the cyclic or linear isocyanide dication states, and the exoergicity distributions confirm the involvement of 4CD or 4ID.

Each $\text{CH}_2\text{CN}^{2+} + \text{neutral}$ collision system resulted in a reaction generating $\text{H}^+ + \text{HC}_2\text{N}^+$, with similar dynamics and exoergicity distributions. The dynamics reveal that the mechanism of this reaction is not typical for a dication-neutral CID reaction; the reaction is ‘mediated’ by the initial transfer of a proton from the dication to the neutral before a rapid dissociation. The exoergicity distributions primarily point to the involvement of the 2CD and 2ID dication states, with 2LD also involved. Evidence for channels involving further dissociation of the HC_2N^+ product, forming $\text{H}^+ + \text{CCN}^+$, were also detected in the $\text{CH}_2\text{CN}^{2+} + \text{N}_2 / \text{CO}$ systems. Further studies, using the deuterated dication could confirm the nature of the mechanism in this channel. For example, one might expect the reaction to be suppressed if the process is initiated by a H^+ transfer.

PT occurs in all three of the systems *via* a direct mechanism, adding further evidence that H-containing dications are effective proton donors. The exoergicities resulting from PT firmly point to the involvement of 2CD or 2ID. Finally, there are channels resulting from SET in the $\text{CH}_2\text{CN}^{2+} + \text{N}_2$ and CO systems. The exoergicity distributions show that the NDSET channels could involve the dication in any of the possible states in the beam. Our findings deviate from the trends observed by Roithová *et al.*,³³ perhaps suggesting these trends are less general across dication-neutral systems than the earlier authors hoped. Specifically, in this work SET channels only dominate over PT following the collisions between $\text{CH}_2\text{CN}^{2+}$ and the polar CO, where three DSET channels are also observed. Additionally, we are unable to explain the absence of an expected and allowed SET channel following collisions between $\text{CH}_2\text{CN}^{2+} + \text{Ar}$.

The involvement of all three dication conformations indicated by the exoergicity distributions points to rearrangement processes following the dissociative double ionization of CH_3CN . More information on the $\text{CH}_2\text{CN}^{2+}$ PES, including barrier heights between the states, could show us if the dications in the beam are continuously sampling different conformations as appears likely from experiments. Future investigations could also reveal more metastable dication states that could be involved.

6.6 References

- 1 R. L. Hudson and M. H. Moore, *Icarus*, 2004, **172**, 466–478.
- 2 H. B. Niemann, S. K. Atreya, S. J. Bauer, G. R. Carignan, J. E. Demick, R. L. Frost, D. Gautier, J. A. Haberman, D. N. Harpold, D. M. Hunten, G. Israel, J. I. Lunine, W. T. Kasprzak, T. C. Owen, M. Paulkovich, F. Raulin, E. Raaen and S. H. Way, *Nature*, 2005, **438**, 779–784.
- 3 M. A. Cordiner, M. Y. Palmer, C. A. Nixon, P. G. J. Irwin, N. A. Teanby, S. B. Charnley, M. J. Mumma, Z. Kisiel, J. Serigano, Y.-J. Kuan, Y.-L. Chuang and K.-S. Wang, *Astrophys. J.*, 2015, **800**, L14.
- 4 A. Coustenis, B. Schmitt, R. K. Khanna and F. Trotta, *Planet. Space Sci.*, 1999, **47**, 1305–1329.
- 5 S. Hamm, G. Helas and P. Warneck, *Geophys. Res. Lett.*, 1989, **16**, 483–486.
- 6 H. Böhringer and F. Arnold, *Nature*, 1981, **290**, 321–322.
- 7 E. Murad, W. Swider, R. A. Moss and S. Toby, *Geophys. Res. Lett.*, 1984, **11**, 147–150.
- 8 P. M. Solomon, K. B. Jefeerts, A. A. Penzias and R. W. Wilson, *Astrophys. J.*, 1971, **168**, L107–L110.
- 9 B. E. Turner, P. Friberg, W. M. Irvine, S. Saito and S. Yamamoto, *Astrophys. J.*, 1990, **355**, 546.
- 10 M. A. Parkes, K. M. Douglas and S. D. Price, *Int. J. Mass Spectrom.*, 2019, **438**, 97–106.
- 11 R. Thissen, O. Witasse, O. Dutuit, C. S. Wedlund, G. Gronoff and J. Lilensten, *Phys. Chem. Chem. Phys.*, 2011, **13**, 18264–18287.
- 12 C. Vastel, S. Yamamoto, B. Lefloch and R. Bachiller, *Astron. Astrophys.*, 2015, **582**, L3.
- 13 M. Agúndez, J. P. Fonfría, J. Cernicharo, J. R. Pardo and M. Guélin, *Astron. Astrophys.*, 2008, **479**, 493–501.
- 14 E. Herbst and C. M. Leung, *Astron. Astrophys.*, 1990, **233**, 177–180.
- 15 D. F. Mark, F. M. Stuart and M. de Podesta, *Geochim. Cosmochim. Acta*, 2011, **75**, 7494–7501.

- 16 A. G. W. Cameron, *Space Sci. Rev.*, 1973, **15**, 121–146.
- 17 S. A. Stern, *Rev. Geophys.*, 1999, **37**, 453–491.
- 18 A. O. Nier, W. B. Hanson, A. Seiff, M. B. McElroy, N. W. Spencer, R. J. Duckett, T. C. Knight and W. S. Cook, *Science*, 1976, **193**, 786–788.
- 19 D. D. Bogard, R. N. Clayton, K. Marti, T. Owen and G. Turner, in *Space Science Reviews*, eds. R. Kallenbach, J. Geiss and W. K. Hartmann, Springer, Dordrecht, 2001, vol. 12, pp. 425–458.
- 20 D. F. Strobel, D. T. Hall, X. Zhu and M. E. Summers, *Icarus*, 1993, **103**, 333–336.
- 21 H. B. Niemann, S. K. Atreya, J. E. Demick, D. Gautier, J. A. Haberman, D. N. Harpold, W. T. Kasprzak, J. I. Lunine, T. C. Owen and F. Raulin, *J. Geophys. Res.*, 2010, **115**, E12006.
- 22 O. Badr and S. D. Probert, *Appl. Energy*, 1993, **46**, 1–67.
- 23 E. W. Schwieterman, T. D. Robinson, V. S. Meadows, A. Misra and S. Domagal-Goldman, *Astrophys. J.*, 2015, **810**, 57.
- 24 O. Dutuit, N. Carrasco, R. Thissen, V. Vuitton, C. Alcaraz, P. Pernot, N. Balucani, P. Casavecchia, A. Canosa, S. Le Picard, J.-C. Loison, Z. Herman, J. Zabka, D. Ascenzi, P. Tosi, P. Franceschi, S. D. Price and P. Lavvas, *Astrophys. J. Suppl. Ser.*, 2013, **204**, 20.
- 25 D. Bockelée-Morvan, V. Debout, S. Erard, C. Leyrat, F. Capaccioni, G. Filacchione, N. Fougere, P. Drossart, G. Arnold, M. Combi, B. Schmitt, J. Crovisier, M.-C. de Sanctis, T. Encrenaz, E. Kührt, E. Palomba, F. W. Taylor, F. Tosi, G. Piccioni, U. Fink, G. Tozzi, A. Barucci, N. Biver, M.-T. Capria, M. Combes, W. Ip, M. Blecka, F. Henry, S. Jacquino, J.-M. Reess, A. Semery and D. Tiphene, *Astron. Astrophys.*, 2015, **583**, A6.
- 26 M. A. DiSanti, M. J. Mumma, N. Dello Russo and K. Magee-Sauer, *Icarus*, 2001, **153**, 361–390.
- 27 M. J. Mumma, M. A. DiSanti, N. Dello Russo, M. Fomenkova, K. Magee-Sauer, C. D. Kaminski and D. X. Xie, *Science*, 1996, **272**, 1310–1314.
- 28 P. C. Novelli, L. P. Steele and P. P. Tans, *J. Geophys. Res.*, 1992, **97**, 20731–20750.
- 29 A. C. Vandaele, A. Mahieux, S. Chamberlain, B. Ristic, S. Robert, I. R. Thomas, L. Trompet, V. Wilquet and J. L. Bertaux, *Icarus*, 2016, **272**, 48–59.

- 30 D. O. Muhleman, G. L. Berge and R. T. Clancy, *Science*, 1984, **223**, 393–396.
- 31 B. L. Lutz, C. De Bergh and T. Owen, *Science*, 1983, **220**, 1374–1375.
- 32 B. Fleury, N. Carrasco, T. Gautier, A. Mahjoub, J. He, C. Szopa, E. Hadamcik, A. Buch and G. Cernogora, *Icarus*, 2014, **238**, 221–229.
- 33 J. Roithová, Z. Herman, D. Schröder and H. Schwarz, *Chem. Eur. J*, 2006, **12**, 2465–2471.
- 34 D. Smith, D. Grief and N. G. Adams, *Int. J. Mass Spectrom. Ion Phys.*, 1979, **30**, 271–283.
- 35 D. Smith, N. G. Adams, E. Alge, H. Villinger and W. Lindinger, *J. Phys. B At. Mol. Phys.*, 1980, **13**, 2787–2799.
- 36 M. Manning, S. D. Price and S. R. Leone A, *J. Chem. Phys.*, 1993, **99**, 8695–8704.
- 37 S. D. Price, M. Manning and S. R. Leone, *Chem. Phys. Lett.*, 1993, **214**, 553–558.
- 38 E. L. Zins and D. Schröder, *Int. J. Mass Spectrom.*, 2011, **299**, 53–58.
- 39 J. F. Lockyear, K. Douglas, S. D. Price, M. Karwowska, K. J. Fijalkowski, W. Grochala, M. Remeš, J. Roithová and D. Schröder, *J. Phys. Chem. Lett.*, 2010, **1**, 358–362.
- 40 G. Dupeyrat, J. B. Marquette, B. R. Rowe and C. Rebrion, *Int. J. Mass Spectrom. Ion Process.*, 1991, **103**, 149–156.
- 41 G. C. Shields and T. F. Moran, *J. Phys. B At. Mol. Phys.*, 1983, **16**, 3591–3607.
- 42 E. Y. Kamber, P. Jonathan, A. G. Brenton and J. H. Beynon, *J. Phys. B At. Mol. Phys.*, 1987, **20**, 4129–4142.
- 43 S. M. Harper, W.-P. Hu and S. D. Price, *J. Phys. B At. Mol. Opt. Phys.*, 2002, **35**, 4409–4423.
- 44 H. R. Koslowski, H. Lebius, V. Staemmler, R. Fink, K. Wiesemann and B. A. Huber, *J. Phys. B At. Mol. Opt. Phys.*, 1991, **24**, 5023–5034.
- 45 N. Tafadar, N. Kaltsoyannis and S. D. Price, *Int. J. Mass Spectrom.*, 1999, **192**, 205–214.
- 46 P. W. Burnside and S. D. Price, *Int. J. Mass Spectrom.*, 2006, **249–250**, 279–288.

- 47 W.-P. Hu, S. M. Harper and S. D. Price, *Mol. Phys.*, 2005, **103**, 1809–1819.
- 48 J. Roithová, R. Thissen, J. Žabka, P. Franceschi, O. Dutuit and Z. Herman, *Int. J. Mass Spectrom.*, 2003, **228**, 487–495.
- 49 D. Ascenzi, P. Tosi, J. Roithová, C. L. Ricketts, D. Schröder, J. F. Lockyear, M. A. Parkes and S. D. Price, *Phys. Chem. Chem. Phys.*, 2008, **10**, 7121–7128.
- 50 B. K. Chatterjee and R. Johnsen, *J. Chem. Phys.*, 1989, **91**, 1378–1379.
- 51 S. Armenta Butt and S. D. Price, *Phys. Chem. Chem. Phys.*, 2021, **23**, 11287–11299.
- 52 H. Störi, E. Alge, H. Villinger, F. Egger and W. Lindinger, *Int. J. Mass Spectrom. Ion Phys.*, 1979, **30**, 263–270.
- 53 H. M. Holzscheiter and D. A. Church, *J. Chem. Phys.*, 1981, **74**, 2313–2318.
- 54 P. Tosi, R. Correale, W. Lu, S. Falcinelli and D. Bassi, *Phys. Rev. Lett.*, 1999, **82**, 450–452.
- 55 A. Ehbrecht, N. Mustafa, C. Ottinger and Z. Herman, *J. Chem. Phys.*, 1996, **105**, 9833–9846.
- 56 J. H. Agee, J. B. Wilcox, L. E. Abbey and T. F. Moran, *Chem. Phys.*, 1981, **61**, 171–179.
- 57 S. M. Harper, S. W.-P. Hu and S. D. Price, *J. Chem. Phys.*, 2004, **120**, 7245–7248.
- 58 J. Jašík, J. Roithová, J. Žabka, R. Thissen, I. Ipolyi and Z. Herman, *Int. J. Mass Spectrom.*, 2006, **255–256**, 150–163.
- 59 J. D. Fletcher, M. A. Parkes and S. D. Price, *Mol. Phys.*, 2015, **113**, 2125–2137.
- 60 P. W. Burnside and S. D. Price, *Phys. Chem. Chem. Phys.*, 2007, **9**, 3902–3913.
- 61 P. Tosi, W. Lu, R. Correale and D. Bassi, *Chem. Phys. Lett.*, 1999, **310**, 180–182.
- 62 M. W. Wong and L. Radom, *J. Phys. Chem.*, 1989, **93**, 6303–6308.
- 63 M. J. Frisch, G. W. Trucks, H. B. Schlegel, G. E. Scuseria, M. a. Robb, J. R. Cheeseman, G. Scalmani, V. Barone, G. a. Petersson, H. Nakatsuji, X. Li, M. Caricato, a. V. Marenich, J. Bloino, B. G. Janesko, R. Gomperts, B. Mennucci, H. P. Hratchian, J. V. Ortiz, a. F. Izmaylov, J. L. Sonnenberg, Williams, F. Ding, F. Lipparini, F. Egidi, J. Goings, B. Peng, A. Petrone, T. Henderson, D. Ranasinghe, V. G. Zakrzewski, J. Gao,

- N. Rega, G. Zheng, W. Liang, M. Hada, M. Ehara, K. Toyota, R. Fukuda, J. Hasegawa, M. Ishida, T. Nakajima, Y. Honda, O. Kitao, H. Nakai, T. Vreven, K. Throssell, J. a. Montgomery Jr., J. E. Peralta, F. Ogliaro, M. J. Bearpark, J. J. Heyd, E. N. Brothers, K. N. Kudin, V. N. Staroverov, T. a. Keith, R. Kobayashi, J. Normand, K. Raghavachari, a. P. Rendell, J. C. Burant, S. S. Iyengar, J. Tomasi, M. Cossi, J. M. Millam, M. Klene, C. Adamo, R. Cammi, J. W. Ochterski, R. L. Martin, K. Morokuma, O. Farkas, J. B. Foresman and D. J. Fox, *Gaussian 16, Revision A.03*, Gaussian, Inc., Wallingford CT, 2016.
- 64 S. D. Price, Personal communication, 2021.
- 65 H. G. Cho and L. Andrews, *J. Phys. Chem. A*, 2011, **115**, 8638–8642.
- 66 W. Wolff, A. Perlin, R. R. Oliveira, F. Fantuzzi, L. H. Coutinho, F. de A Ribeiro and G. Hilgers, *J. Phys. Chem. A*, 2020, **124**, 9261–9271.
- 67 S. Anand and H. B. Schlegel, *J. Phys. Chem. A*, 2005, **109**, 11551–11559.
- 68 J. Jašík, D. Gerlich and J. Roithová, *J. Am. Chem. Soc.*, 2014, **136**, 2960–2962.
- 69 A. Kramida, Y. Ralchenko, J. Reader and NIST ASD Team, Eds., *NIST Atomic Spectra Database (version 5.6.1)*, National Institute of Standards and Technology, Gaithersburg, MD, 2020.
- 70 M. Lundqvist, D. Edvardsson, P. Baltzer and B. Wannberg, *J. Phys. B At. Mol. Opt. Phys.*, 1996, **29**, 1489–1499.
- 71 A. J. Yench, K. Ellis and G. C. King, *J. Electron Spectros. Relat. Phenomena*, 2014, **195**, 160–173.
- 72 M. Hochlaf, R. I. Hall, F. Penent, H. Kjeldsen, P. Lablanquie, M. Lavollée and J. H. D. Eland, *Chem. Phys.*, 1996, **207**, 159–165.
- 73 L. H. Andersen, J. H. Posthumus, O. Vahtras, H. Agren, N. Elander, A. Nunez, A. Scrinzi, M. Natiello and M. Larsson, *Phys. Rev. Lett.*, 1993, **71**, 1812–1815.
- 74 F. Penent, R. I. Hall, R. Panajotović, J. H. D. Eland, G. Chaplier and P. Lablanquie, *Phys. Rev. Lett.*, 1998, **81**, 3619–3622.
- 75 J. H. D. Eland, M. Hochlaf, G. C. King, P. S. Kreynin, R. J. LeRoy, I. R. McNab and J.-M. Robbe, *J. Phys. B At. Mol. Opt. Phys.*, 2004, **37**, 3197–3214.

- 76 M. Lundqvist, P. Baltzer, D. Edvardsson, L. Karlsson and B. Wannberg, *Phys. Rev. Lett.*, 1995, **75**, 1058–1061.
- 77 B. Gans, S. Hartweg, G. A. Garcia, S. Boyé-Péronne, O. J. Harper, J. C. Guillemin and J. C. Loison, *Phys. Chem. Chem. Phys.*, 2020, **22**, 12496–12501.
- 78 R. P. Thorn, P. S. Monks, L. J. Steif, S. C. Kuo, Z. Zhang, S. K. Ross and R. B. Klemm, *J. Phys. Chem. A*, 1998, **102**, 846–851.
- 79 G. A. Garcia, J. Krüger, B. Gans, C. Falvo, L. H. Coudert and J. C. Loison, *J. Chem. Phys.*, 2017, **147**, 13908.
- 80 M. R. Nimlos, G. Davico, C. M. Geise, P. G. Wenthold, W. C. Lineberger, S. J. Blanksby, C. M. Hadad, G. A. Petersson and G. B. Ellison, *J. Chem. Phys.*, 2002, **117**, 4323–4339.
- 81 D. B. Milligan, C. G. Freeman, R. G. A. R. Maclagan, M. J. McEwan, P. F. Wilson and V. G. Anicich, *J. Am. Soc. Mass Spectrom.*, 2001, **12**, 557–564.
- 82 V. Vuitton, R. V. Yelle and M. J. McEwan, *Icarus*, 2007, **191**, 722–742.
- 83 C. N. Keller, V. G. Anicich and T. E. Cravens, *Planet. Space Sci.*, 1998, **46**, 1157–1174.
- 84 J. Berkowitz, G. B. Ellison and D. Gutman, *J. Phys. Chem.*, 1994, **98**, 2744–2765.
- 85 D. F. McMillen and D. M. Golden, *Annu. Rev. Phys. Chem.*, 1982, **33**, 493–532.
- 86 J. L. Holmes and P. M. Mayer, *J. Phys. Chem*, 1995, **99**, 1366–1370.
- 87 K. A. Newson and S. D. Price, *Chem. Phys. Lett.*, 1997, **269**, 93–98.
- 88 K. A. Newson and S. D. Price, *Chem. Phys. Lett.*, 1998, **294**, 223–228.
- 89 P. Schilke, D. A. Neufeld, H. S. P. Müller, C. Comito, E. A. Bergin, D. C. Lis, M. Gerin, J. H. Black, M. Wolfire, N. Indriolo, J. C. Pearson, K. M. Menten, B. Winkel, Á. Sánchez-Monge, T. Möller, B. Godard and E. Falgarone, *Astron. Astrophys.*, 2014, **566**, 29.
- 90 M. J. Barlow, B. M. Swinyard, P. J. Owen, J. Cernicharo, H. L. Gomez, R. J. Ivison, O. Krause, T. L. Lim, M. Matsuura, S. Miller, G. Olofsson and E. T. Polehampton, *Science*, 2013, **342**, 1343–1345.
- 91 H. S. P. Müller, S. Muller, P. Schilke, E. A. Bergin, J. H. Black, M. Gerin, D. C. Lis, D.

- A. Neufeld and S. Suri, *Astron. Astrophys.*, 2015, **582**, 4.
- 92 F. Daniel, M. L. Dubernet, M. Meuwly, J. Cernicharo and L. Pagani, *Mon. Not. R. Astron. Soc.*, 2005, **363**, 1083–1091.
- 93 V. N. Salinas, M. R. Hogerheijde, E. A. Bergin, L. Ilseidore Cleeves, C. Brinch, G. A. Blake, D. C. Lis, G. J. Melnick, O. Panic, J. C. Pearson, L. Kristensen, U. A. Yllidz and E. F. Van Dishoeck, *Astron. Astrophys.*, 2016, **591**, 122.
- 94 V. Brites and M. Hochlaf, *J. Phys. Chem. A*, 2009, **113**, 11107–11111.
- 95 E. Herbst, J. M. Norbeck, P. R. Certain and W. Klemperer, *Astrophys. J.*, 1976, **207**, 110–112.
- 96 Y. Yamaguchi, C. A. Richards and H. F. Schaefer, *J. Chem. Phys.*, 1994, **101**, 8945–8954.
- 97 Z. Herman, *Int. J. Mass Spectrom.*, 2015, **378**, 113–126.
- 98 S. D. Price, *Int. J. Mass Spectrom.*, 2007, **260**, 1–19.
- 99 M. A. Parkes, J. F. Lockyear and S. D. Price, *Int. J. Mass Spectrom.*, 2014, **365–366**, 68–74.
- 100 C. L. Ricketts, S. M. Harper, S. W. P. Hu and S. D. Price, *J. Chem. Phys.*, 2005, **123**, 134322.
- 101 S. Armenta Butt and S. D. Price, *Phys. Chem. Chem. Phys.*, 2020, **22**, 8391–8400.
- 102 J. D. Fletcher, M. A. Parkes and S. D. Price, *Int. J. Mass Spectrom.*, 2015, **377**, 101–108.
- 103 J. Roithová, J. Žabka, J. Hrušák, R. Thissen and Z. Herman, *J. Phys. Chem. A*, 2003, **107**, 7347–7354.
- 104 K. Yamasaki and S. R. Leone, *J. Chem. Phys.*, 1989, **90**, 964–976.
- 105 Z. Herman, *Int. Rev. Phys. Chem.*, 1996, **15**, 299–324.
- 106 P. Baltzer, M. Larsson, L. Karlsson, B. Wannberg and M. Carlsson Göthe, *Phys. Rev. A*, 1992, **46**, 5545–5553.
- 107 H. R. Hrodmarsson, R. Thissen, D. Dowek, G. A. Garcia, L. Nahon and T. R. Govers, *Front. Chem.*, 2019, **7**, 222.

- 108 E. M. Bahati, J. J. Jureta, D. S. Belic, H. Cherkani-Hassani, M. O. Abdellahi and P. Defrance, *J. Phys. B At. Mol. Opt. Phys.*, 2001, **34**, 2963–2973.
- 109 X. Tang, Y. Hou, C. Y. Ng and B. Ruscic, *J. Chem. Phys.*, 2005, **123**, 074330.
- 110 L. Åsbrink and C. Fridh, *Phys. Scr.*, 1974, **9**, 338–340.
- 111 B. Wannberg, D. Nordfors, K. L. Tan, L. Karlsson and L. Mattsson, *J. Electron Spectros. Relat. Phenomena*, 1988, **47**, 147–166.
- 112 Y. Zhao, M. Cao, Y. Li, X. Shan, F. Liu, L. Sheng, L. Li and W. Liu, *J. Electron Spectros. Relat. Phenomena*, 2014, **196**, 181–186.
- 113 P. Baltzer, M. Lundqvist, B. Wannberg, L. Karlsson, M. Larsson, M. A. Hayes, J. B. West, M. R. F. Siggel, A. C. Parr and J. L. Dehmer, *J. Phys. B At. Mol. Opt. Phys.*, 1994, **27**, 4915–4932.
- 114 R. C. Shiell, M. Evans, S. Stimson, C.-W. Hsu, C. Y. Ng and J. W. Hepburn, *Chem. Phys. Lett.*, 1999, **315**, 390–396.
- 115 J. Roithová and D. Schröder, *Angew. Chemie Int. Ed.*, 2009, **48**, 8788–8790.

Chapter 7: Conclusions and Further Work

7.1 Conclusions

The PSCO-MS technique has been used in this thesis to investigate the collisions between various dications and neutral targets. The coincident detection of pairs of ions allows for the unambiguous identification of reaction channels in which two or three products are formed. Coupled with position-sensitive ion detection, this technique allows for the determination of comprehensive dynamic and energetic information for each reaction. The technique has been used here to study the previously investigated collision systems, $\text{Ar}^{2+} + \text{O}_2$, and $\text{Ar}^{2+} + \text{N}_2$, revealing new, detailed, information on the dynamics and energetics involved, as well as observing new reactions. Collisions involving the S^{2+} and $\text{CH}_2\text{CN}^{2+}$ dications with a number of neutral partners, collision systems which have not been studied before, have also been presented. These dications are especially important to the ionospheres of Io and Titan respectively.

Chapter 3 presents detailed insights into the collisions of Ar^{2+} and O_2 at a collision energy of 4.4 eV. Four bimolecular reaction channels are observed: NDSET generating $\text{Ar}^+ + \text{O}_2^+$, DSET generating $\text{Ar}^+ + \text{O}^+$, a chemical bond-forming channel generating $\text{ArO}^+ + \text{O}^+$, and dissociative DET generating $\text{O}^+ + \text{O}^+$. Our experimental results reveal dynamics clearly showing that a short-lived collision complex $[\text{ArO}_2]^{2+}$ is involved in the formation of $\text{Ar}^+ + \text{O}^+ + \text{O}$, rather than being a direct SET process followed by dissociation of O_2^{+*} . In contrast, the bond-forming reaction, generating $\text{O}^+ + \text{ArO}^+$, involves direct abstraction of O^- from O_2 by Ar^{2+} with no evidence of the involvement of a collision complex in this reaction.

The reactions following collisions between Ar^{2+} and N_2 at a CM collision energy of 5.1 eV have also been analysed in depth, with the results presented in Chapter 4. Again, four reaction channels are observed: NDSET generating $\text{Ar}^+ + \text{N}_2^+$, DSET generating $\text{Ar}^+ + \text{N}^+$, a chemical bond-forming channel $\text{ArN}^+ + \text{N}^+$, and dissociative DET generating $\text{N}^+ + \text{N}^+$. As with the $\text{Ar}^{2+} + \text{O}_2$ collision system, our results show that the generation of $\text{Ar}^+ + \text{N}^+$ involves the formation of a $[\text{ArN}_2]^{2+}$ collision complex. Additionally, this same collision complex is also involved in the NDSET channel, which results in the generation of N_2^+ in its $\text{C}^2\Sigma_u^+$ state. The previously unreported bond-forming channel resulting in the generation of $\text{ArN}^+ + \text{N}^+$ occurs *via* a direct mechanism without the involvement of a collision complex.

These investigations of the $\text{Ar}^{2+} + \text{O}_2$ and $\text{Ar}^{2+} + \text{N}_2$ systems reveal marked dynamic similarities. Both systems exhibited evidence for the formation of collision complexes in ET channels whilst bond-formation, generating rare gas molecular species, occurred *via* direct processes, in contrast to typical dication-neutral bond-forming reactions.

In Chapter 5, the reactivity of the S^{2+} dication with Ar, N_2 and H_2 was investigated. This work being the first study of the bimolecular reactivity of S^{2+} , a species detected in planetary ionospheres and other high energy environments.^{1–8} Generated from electron ionization of H_2S , the dications in the beam are predominantly S^{2+} in a mixture of its ^3P , ^1D and ^1S states, resulting from the $3s^2 3p^2$ electronic configuration. The dynamics show evidence for the formation of a long-lived a collision complex, $[\text{SH}_2]^{2+}$, between the reactants in the dissociative SET channel, generating $\text{S}^+ + \text{H}^+$. Perhaps surprisingly, the formation of SH^+ *via* a chemical bond-forming channel was not observed, despite the exothermic nature of the reaction, the prevalence of SH^+ in nature and astrophysical environments, and the propensity for other dication + H_2 reactions to result in bond-formation.^{9–19} Conversely, the collisions of $\text{S}^{2+} + \text{N}_2$ did result in a bond-forming channel, generating $\text{SN}^+ + \text{N}^+$, a reaction which proceeds *via* a collision complex.

Finally, in Chapter 6, the reactivity of the molecular dication $\text{CH}_2\text{CN}^{2+}$ with Ar, N_2 , and CO was studied. Formed from the ionization of acetonitrile, $\text{CH}_2\text{CN}^{2+}$ is relevant to the ionospheres of planets and satellites, including Titan.^{20–25} From electronic structure calculations there are potentially 6 dicationic electronic states, both doublet and quartet states for cyclic, linear, and linear isocyanide conformations in the reactant beam. The lowest energy electronic state is a doublet cyclic dication. Exoergicity distributions from the different reaction channels suggest the involvement of all six dication states, pointing to a range of rearrangement processes following the dissociative double ionization of CH_3CN . All of the collision systems display intense CID channels, which follow the generally expected pattern for a non-reactive collision. The formation of $\text{H}^+ + \text{HC}_2\text{N}^+$ was shown to be atypical for a dication-neutral CID reaction. The dissociation is ‘mediated’ by the initial transfer of a proton from the dication to the neutral before a rapid dissociation of the protonated neutral. PT occurs in all three of the collision systems *via* a direct mechanism. This observation adds strong further evidence that these H-containing dications are effective proton donors, and again provides an example of dication-neutral chemical bond-formation occurring *via* a direct process. Finally, there are channels resulting from SET in the $\text{CH}_2\text{CN}^{2+} + \text{N}_2$ and CO systems. SET channels only dominated over PT following the collisions between $\text{CH}_2\text{CN}^{2+}$ and the polar CO molecule, where three DSET

channels are also observed, in contrast to the trends observed by Roithová *et al.*²⁶ The absence of an expected and allowed SET channel following collisions between $\text{CH}_2\text{CN}^{2+} + \text{Ar}$ is curious, and potentially indicates the presence of a barrier to SET in the PES.

These investigations of atmospherically relevant species are vital in building a database of known dication reactions and aiding understanding and control of processes occurring in high energy environments such as ionospheres and plasmas. Many reactions were observed involving the formation of new chemical bonds, including those that resulted in the generation of molecular species with Ar: ArH^+ , ArO^+ , ArN^+ . The observation of these ions demonstrates that the bimolecular reactivity of dications displays unusual chemistry and is a viable source of species involving rare gas bonds. Many of the bond-forming reactions observed in this thesis have been shown to occur *via* direct mechanisms, whilst the formation of collision complexes has also been, surprisingly, often in reactions that are apparently due to SET. Both findings are contrary to the orthodoxy and emphasise that much of dication reactivity is still poorly understood – a point which should not be understated. The appraisal of these dynamics and the determination of the electronic states involved in the reactions studied demonstrates the power of the PSCO-MS technique.

7.2 Further work

Further theoretical and experimental investigations to enhance the work in this thesis would benefit the field. Computational studies to determine the geometries of minima on the $[\text{ArO}_2]^{2+}$ and $[\text{ArN}_2]^{2+}$ potential energy surfaces may explain the observation of collision complexes observed in the reactions of Ar^{2+} with O_2 and N_2 . Additionally, further computational studies of the $\text{CH}_2\text{CN}^{2+}$ dication potential energy surface could tell us more about the fluxional nature of the dication formed after electron ionization of acetonitrile. The use of the deuterated analogue in PSCO-MS experiments, $\text{CD}_2\text{CN}^{2+}$, could reveal isotope effects in the PT and pCID channels, shedding further light on the mechanisms involved and the competition between SET and PT. The composition of the S^{2+} and $\text{CH}_2\text{CN}^{2+}$ dication beams could be analysed by a systematic study of collisions with simple atomic species. Such a systematic study would confirm the dication states involved in reactions and allow for firmer conclusions about the energetics to be drawn.

The experiments in this thesis contribute to the overall picture of dication-neutral reactions. The development of this database should be continued, especially involving species

relevant to high energy environments such as the ionospheres of planets or satellites. Encouragingly, there is increasing public interest in space exploration, with the possibility of extra-terrestrial colonisation slowly becoming more realistic. If humans are to spread their influence on other planets and satellites in the solar system it is vital to understand the chemistry of these environments to aid exploration and reduce the destructive effects of anthropogenic activity such as those seen on Earth.²⁷⁻²⁹ The bimolecular reactivity of the atomic dications O^{2+} and N^{2+} , both species being directly detected in ionospheres, would be a next logical step. The recent detection of the molecular CO_2^{2+} dication in the ionosphere of Mars, and the coma of a comet, is encouraging.³⁰ This detection will hopefully be followed by the detection of more molecular dications in these environments and should stimulate investigations on the bimolecular reactivity of species such as CO_2^{2+} , N_2^{2+} , and O_2^{2+} .

The results of dication-neutral experiments are fundamentally interesting and other avenues should also be explored, such as reactions involving the He^{2+} dication. The He^{2+} dication is essentially an alpha particle, ubiquitous in radioactive processes and also present in solar wind. Other intriguing studies could involve the C^{2+} dication, which has been observed in the ISM, and Xe^{2+} , which could be generated as a product of ion drives in spacecraft propulsion.

7.3 References

- 1 F. Herbert, N. M. Schneider, A. R. Hendrix and F. Bagenal, *J. Geophys. Res. Sp. Phys.*, 2003, **108**, 1167.
- 2 L. A. Frank, W. R. Paterson, K. L. Ackerson, V. M. Vasyliunas, F. V Coroniti and S. J. Bolton, *Science*, 1996, **274**, 394–395.
- 3 D. E. Shemansky and G. R. Smith, *J. Geophys. Res.*, 1981, **86**, 9179–9192.
- 4 F. Bagenal and J. D. Sullivan, *J. Geophys. Res. Sp. Phys.*, 1981, **86**, 8447–8466.
- 5 J. N. Bull, J. W. L. Lee and C. Vallance, *Phys. Rev. A*, 2017, **96**, 042704.
- 6 T. Barker, *Astrophys. J.*, 1980, **240**, 99–104.
- 7 S. Rappaport, E. Chiang, T. Kallman and R. Malina, *Astrophys. J.*, 1994, **431**, 237–246.
- 8 L. T. Greenberg, P. Dyal and T. R. Geballe, *Astrophys. J. Lett.*, 1977, **213**, L71–L74.
- 9 K. A. Newson and S. D. Price, *Chem. Phys. Lett.*, 1997, **269**, 93–98.
- 10 J. Roithová, J. Žabka, J. Hrušák, R. Thissen and Z. Herman, *J. Phys. Chem. A*, 2003, **107**, 7347–7354.
- 11 B. Godard, E. Falgarone, M. Gerin, D. C. Lis, M. De Luca, J. H. Black, J. R. Goicoechea, J. Cernicharo, D. A. Neufeld, K. M. Menten and M. Emprechtinger, *Astron. Astrophys.*, 2012, **540**, A87.
- 12 Z. Herman, J. Žabka, Z. Dolejšek, M. Fárník and M. Fárník, *Int. J. Mass Spectrom.*, 1999, **192**, 191–203.
- 13 N. Lambert, N. Kaltsoyannis, S. D. Price, J. Žabka and Z. Herman, *J. Phys. Chem. A*, 2006, **110**, 2898–2905.
- 14 N. Tafadar and S. D. Price, *Int. J. Mass Spectrom.*, 2003, **223–224**, 547–560.
- 15 J. Roithová, H. Schwarz and D. Schröder, *Chem. Eur. J*, 2009, **15**, 9995–9999.
- 16 J. F. Lockyear, C. L. Ricketts, M. A. Parkes and S. D. Price, *Chem. Sci.*, 2011, **2**, 150–

- 156.
- 17 J. Jašik, J. Roithová, J. Žabka, R. Thissen, I. Ipolyi and Z. Herman, *Int. J. Mass Spectrom.*, 2006, **255–256**, 150–163.
- 18 J. Roithová, J. Žabka, Z. Herman, R. Thissen, D. Schröder and H. Schwarz, *J. Phys. Chem. A*, 2006, **110**, 6447–6453.
- 19 F. Lique, A. Zanchet, N. Bulut, J. R. Goicoechea and O. Roncero, *Astron. Astrophys.*, 2020, **638**, A72.
- 20 M. A. Cordiner, M. Y. Palmer, C. A. Nixon, P. G. J. Irwin, N. A. Teanby, S. B. Charnley, M. J. Mumma, Z. Kisiel, J. Serigano, Y.-J. Kuan, Y.-L. Chuang and K.-S. Wang, *Astrophys. J.*, 2015, **800**, L14.
- 21 A. Coustenis, B. Schmitt, R. K. Khanna and F. Trotta, *Planet. Space Sci.*, 1999, **47**, 1305–1329.
- 22 S. Hamm, G. Helas and P. Warneck, *Geophys. Res. Lett.*, 1989, **16**, 483–486.
- 23 H. Böhringer and F. Arnold, *Nature*, 1981, **290**, 321–322.
- 24 E. Murad, W. Swider, R. A. Moss and S. Toby, *Geophys. Res. Lett.*, 1984, **11**, 147–150.
- 25 M. A. Parkes, K. M. Douglas and S. D. Price, *Int. J. Mass Spectrom.*, 2019, **438**, 97–106.
- 26 J. Roithová, Z. Herman, D. Schröder and H. Schwarz, *Chem. Eur. J.*, 2006, **12**, 2465–2471.
- 27 S. A. Montzka, G. S. Dutton, P. Yu, E. Ray, R. W. Portmann, J. S. Daniel, L. Kuijpers, B. D. Hall, D. Mondeel, C. Siso, J. D. Nance, M. Rigby, A. J. Manning, L. Hu, F. Moore, B. R. Miller and J. W. Elkins, *Nature*, 2018, **557**, 413–417.
- 28 N. Butt, H. L. Beyer, J. R. Bennett, D. Biggs, R. Maggini, M. Mills, A. R. Renwick, L. M. Seabrook and H. P. Possingham, *Science*, 2013, 342, 425–426.
- 29 R. Cassia, M. Nocioni, N. Correa-Aragunde and L. Lamattina, *Front. Plant Sci.*, 2018, **9**, 273.
- 30 H. Gu, J. Cui, D. Niu, L. Dai, J. Huang, X. Wu, Y. Hao and Y. Wei, *Earth Planet. Phys.*,

2020, **4**, 396–402.

Chapter 8: Appendix A

Table 8.1: Exoergicities of reaction pathways for the reaction $\text{Ar}^{2+} + \text{O}_2 \rightarrow \text{Ar}^+ + \text{O}_2^+$, calculated from literature values.^{1,2} O_2 is assumed to be in its ground state, $^3\Sigma_g^-$. Highlighted in bold are the pathways with exoergicities between 3 eV and 6.5 eV.

Product states		Reactant (Ar^{2+}) states	Total exoergicity
Ar^+ state, relative to the ground state of Ar, (^1S)	O_2^+ state, relative to the ground state of O_2 , ($^3\Sigma_g^-$)	Ar^{2+} state, relative to the ground state of Ar, (^1S)	Reactant states – total product states
^2P , 15.76 eV	$\text{X}^2\Pi_g$, 12.07 eV	^3P , 43.39 eV	15.56 eV
^2P , 15.76 eV	$\text{a}^4\Pi_u$, 16.10 eV	^3P , 43.39 eV	11.53 eV
^2P , 15.76 eV	$\text{b}^4\Sigma_g^-$, 18.17 eV	^3P , 43.39 eV	9.46 eV
^2P , 15.76 eV	$\text{B}^2\Sigma_g^-$, 20.30 eV	^3P , 43.39 eV	7.33 eV
^2P, 15.76 eV	$\text{c}^4\Sigma_u^-$, 24.58 eV	^3P, 43.39 eV	3.05 eV
^2P , 15.76 eV	$\text{X}^2\Pi_g$, 12.07 eV	^1D , 45.13 eV	17.30 eV
^2P , 15.76 eV	$\text{a}^4\Pi_u$, 16.10 eV	^1D , 45.13 eV	13.27 eV
^2P , 15.76 eV	$\text{b}^4\Sigma_g^-$, 18.17 eV	^1D , 45.13 eV	11.20 eV
^2P , 15.76 eV	$\text{B}^2\Sigma_g^-$, 20.30 eV	^1D , 45.13 eV	9.07 eV
^2P, 15.76 eV	$\text{c}^4\Sigma_u^-$, 24.58 eV	^1D, 45.13 eV	4.79 eV
^2P , 15.76 eV	$\text{X}^2\Pi_g$, 12.07 eV	^1S , 47.51 eV	19.68 eV
^2P , 15.76 eV	$\text{a}^4\Pi_u$, 16.10 eV	^1S , 47.51 eV	15.65 eV
^2P , 15.76 eV	$\text{b}^4\Sigma_g^-$, 18.17 eV	^1S , 47.51 eV	13.58 eV
^2P , 15.76 eV	$\text{B}^2\Sigma_g^-$, 20.30 eV	^1S , 47.51 eV	11.45 eV
^2P , 15.76 eV	$\text{c}^4\Sigma_u^-$, 24.58 eV	^1S , 47.51 eV	7.17 eV
^2S , 29.24 eV	$\text{X}^2\Pi_g$, 12.07 eV	^3P , 43.39 eV	2.08 eV
^2S , 29.24 eV	$\text{a}^4\Pi_u$, 16.10 eV	^3P , 43.39 eV	-1.95 eV
^2S , 29.24 eV	$\text{b}^4\Sigma_g^-$, 18.17 eV	^3P , 43.39 eV	-4.01 eV

2S , 29.24 eV	$B^2\Sigma_g^-$, 20.30 eV	3P , 43.39 eV	-6.15 eV
2S , 29.24 eV	$c^4\Sigma_u^-$, 24.58 eV	3P , 43.39 eV	-10.43 eV
2S, 29.24 eV	$X^2\Pi_g$, 12.07 eV	1D, 45.13 eV	3.82 eV
2S , 29.24 eV	$a^4\Pi_u$, 16.10 eV	1D , 45.13 eV	-0.21 eV
2S , 29.24 eV	$b^4\Sigma_g^-$, 18.17 eV	1D , 45.13 eV	-2.28 eV
2S , 29.24 eV	$B^2\Sigma_g^-$, 20.30 eV	1D , 45.13 eV	-4.41 eV
2S , 29.24 eV	$c^4\Sigma_u^-$, 24.58 eV	1D , 45.13 eV	-8.69 eV
2S, 29.24 eV	$X^2\Pi_g$, 12.07 eV	1S, 47.51 eV	6.2 eV
2S , 29.24 eV	$a^4\Pi_u$, 16.10 eV	1S , 47.51 eV	2.17 eV
2S , 29.24 eV	$b^4\Sigma_g^-$, 18.17 eV	1S , 47.51 eV	0.10 eV
2S , 29.24 eV	$B^2\Sigma_g^-$, 20.30 eV	1S , 47.51 eV	-2.03 eV
2S , 29.24 eV	$c^4\Sigma_u^-$, 24.58 eV	1S , 47.51 eV	-6.31 eV
4D , 32.17 eV	$X^2\Pi_g$, 12.07 eV	3P , 43.39 eV	-0.85 eV
4D , 32.17 eV	$a^4\Pi_u$, 16.10 eV	3P , 43.39 eV	-4.88 eV
4D , 32.17 eV	$b^4\Sigma_g^-$, 18.17 eV	3P , 43.39 eV	-6.95 eV
4D , 32.17 eV	$B^2\Sigma_g^-$, 20.30 eV	3P , 43.39 eV	-9.08 eV
4D , 32.17 eV	$c^4\Sigma_u^-$, 24.58 eV	3P , 43.39 eV	-13.36 eV
4D , 32.17 eV	$X^2\Pi_g$, 12.07 eV	1D , 45.13 eV	0.89 eV
4D , 32.17 eV	$a^4\Pi_u$, 16.10 eV	1D , 45.13 eV	-3.14 eV
4D , 32.17 eV	$b^4\Sigma_g^-$, 18.17 eV	1D , 45.13 eV	-5.21 eV
4D , 32.17 eV	$B^2\Sigma_g^-$, 20.30 eV	1D , 45.13 eV	-7.34 eV
4D , 32.17 eV	$c^4\Sigma_u^-$, 24.58 eV	1D , 45.13 eV	-11.62 eV
4D, 32.17 eV	$X^2\Pi_g$, 12.07 eV	1S, 47.51 eV	3.28 eV
4D , 32.17 eV	$a^4\Pi_u$, 16.10 eV	1S , 47.51 eV	-0.75 eV
4D , 32.17 eV	$b^4\Sigma_g^-$, 18.17 eV	1S , 47.51 eV	-2.83 eV
4D , 32.17 eV	$B^2\Sigma_g^-$, 20.30 eV	1S , 47.51 eV	-4.95 eV
4D , 32.17 eV	$c^4\Sigma_u^-$, 24.58 eV	1S , 47.51 eV	-9.24 eV

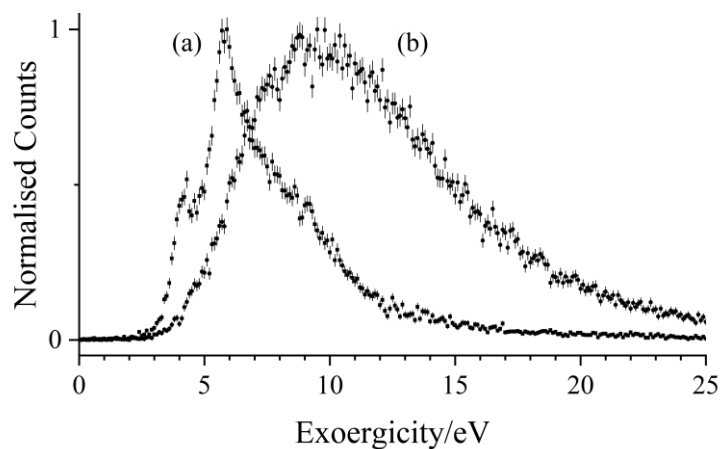


Figure 8.1: Experimental exoergic spectra for the reaction $\text{Ar}^{2+} + \text{O}_2 \rightarrow \text{Ar}^+ + \text{O}_2^+ \rightarrow \text{Ar}^+ + \text{O}^+ + \text{O}$ with source fields of (a) 28.5 V cm^{-1} and (b) 183 V cm^{-1} . The error bars represent two standard deviations of the counts.

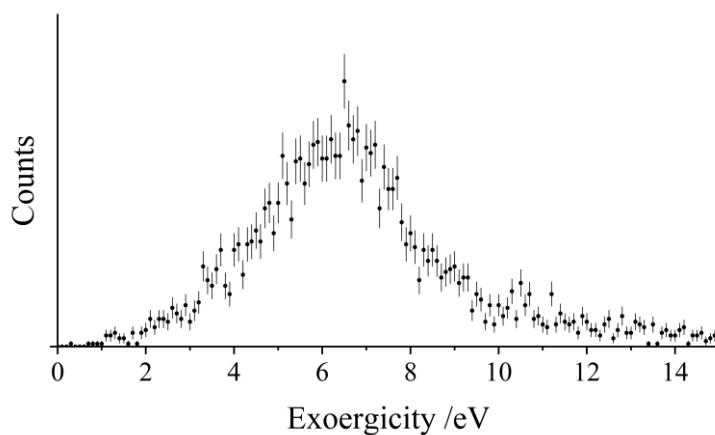


Figure 8.2: Total exoergic spectrum for the DSET reaction, $\text{Ar}^{2+} + \text{N}_2 \rightarrow \text{Ar}^+ + \text{N}^+ + \text{N}$. The error bars represent two standard deviations of the associated counts.

8.1 References

- 1 O. Edqvist, E. Lindholm, L. E. Selin and L. Asbrink, *Phys. Scr. Phys. Scr.*, 1970, **1**, 25–30.
- 2 A. Kramida, Y. Ralchenko, J. Reader and NIST ASD Team, Eds., *NIST Atomic Spectra Database (version 5.6.1)*, National Institute of Standards and Technology, Gaithersburg, MD, 2020.

Chapter 9: Appendix B

The equilibrium geometries and corresponding adiabatic and vertical ionization energies were determined for the species of interest. These quantities were calculated for the lowest energy states of each of the relevant multiplicities. Stationary points were located using the MP2 algorithm with a cc-pVTZ basis set and the frequencies were analysed to determine minima. The energetics of these minima were then calculated using single-point CCSD(T) calculations with the cc-pVTZ basis set. Zero-point energies were corrected for using vibrational information from the MP2 geometry optimisations. For the quartet isocyanide dication (4ID), where one MP2 frequency appeared unreliable, a B3LYP determination of the frequencies was used, the B3LYP algorithm converging to essentially the same geometry as the MP2 algorithm. This methodology has previously been successfully used to determine the geometries and energetics of dications.¹

9.1 References

- 1 J. D. Fletcher, M. A. Parkes and S. D. Price, *Mol. Phys.*, 2015, **113**, 2125–2137.